République Algérienne Démocratique et Populaire
Ministère de l'Enseignement Supérieur et de la Recherche Scientifique
Université A.MIRA-BEJAIA
جامعة بجاية
Tasdawit n Bgayet
Université de Béjaïa
Faculté des Sciences Exactes
Département de physique
Laboratoire de Physique Théorique

THÈSE

EN VUE DE L'OBTENTION DU DIPLOME DE DOCTORAT

Domaine : Science de la Matière Filière : Physique
Spécialité : Physique des Matériaux et Nano-composites

Présentée par

AGGOUNE WAHIB

Thème

Optical excitations of selected van der Waals heterostructures investigated by many-body perturbation theory

Soutenue le : 05 Mai 2018 **Devant le Jury composé de :**

Nom et Prénom	Grade		
Mahtout Sofiane	Professeur	Univ. de Bejaia	Président
Belkhir Mohamed-Akli	Professeur	Univ. de Bejaia	Rapporteur
Zenia Hand	MCA	Univ. de Bejaia	Examinateur
Rezouali Karim	MCA	Univ. de Bejaia	Examinateur
Draxl Claudia	Professeur	Univ. Humboldt (Allemagne)	Examinatrice
Bouhemadou Abdelmadjid	Professeur	Univ. de Setif 1	Examinateur
Cocchi Caterina	Professeur	Univ. Humboldt (Allemagne)	Invitée

Année Universitaire : **2017/2018**

Contents

Abstract **5**

Acknowledgment **6**

Introduction and motivations **8**

1 From two-dimensional materials to van der Waals heterostuctures **11**
- **1.1 Two-dimensional materials** 11
  - 1.1.1 Graphene 12
  - 1.1.2 Hexagonal boron nitride 14
- **1.2 Van der Waals heterostuctures** 16
  - 1.2.1 Graphene/h-BN vdW heterostructures 17

2 Theoretical methods **20**
- **2.1 The many-body problem** 20
- **2.2 Density functional theory (DFT)** 22
  - 2.2.1 The Kohn-Sham (KS) equations 23
  - 2.2.2 Exchange-correlation functionals 25
  - 2.2.3 Limitations 25
- **2.3 Many-body perturbation theory (MBPT)** 27
  - 2.3.1 The one-particle Green's function 28
  - 2.3.2 Hedin's equations 30
  - 2.3.3 The GW approximation 30
  - 2.3.4 The two-particles Green's function 31
  - 2.3.5 Effective two-particles Bethe-Salpeter equation (BSE) 33
- **2.4 Numerical methods and computational details** 36
  - 2.4.1 Numerical methods within the `exciting` code 36
  - 2.4.2 Computational details 37

3 Tuning optical excitations in bulk hexagonal boron nitride by layer patterning . 43
3.1 Structural properties ... 43
3.1.1 Stacking arrangements ... 44
3.1.2 Lattice parameters ... 45
3.1.3 Hybridization and electronic charge density ... 46
3.1.4 Interplay between layer patterning, interlayer distance, and stability . 47
3.2 Electronic properties and optical excitations in bulk h-BN ... 50
3.2.1 Electronic band structure ... 50
3.2.2 Character of the bands ... 52
3.2.3 Electronic distribution of Kohn-Sham states ... 52
3.2.4 Absorption spectrum including excitonic effects ... 54
3.2.5 Excitons in bulk h-BN ... 56
3.3 Effect of layer patterning in bulk h-BN ... 60
3.3.1 Tunable character and size of the band gap ... 60
3.3.2 Absorption spectra vs. stacking arrangement ... 63
3.3.3 Stacking-exciton relationship ... 64
3.4 Tunability in other vdW layered materials ... 72

4 Graphene/h-BN vdW heterostructures ... 73
4.1 Structures ... 73
4.1.1 Lattice parameters ... 75
4.1.2 Electronic charge density ... 76
4.1.3 Stability ... 77
4.2 Electronic properties ... 78
4.2.1 From building blocks to vdW heterostructures ... 79
4.2.2 Electronic band structure vs. stacking arrangement ... 80
4.3 Semi-conducting configurations ... 82
4.3.1 Tuning the size of the band gap by layer patterning ... 83
4.3.2 Quasi-particle band structure ... 83
4.3.3 Distribution of Kohn-Sham states ... 86
4.4 Optical properties ... 88
4.4.1 From constituents to vdW heterostructures ... 88
4.4.2 Stacking arrangement vs. absorption spectra ... 90
4.4.3 Excitons in graphene/h-BN vdW heterostructures ... 90
4.5 Stacking effects on the electron-hole distribution ... 96

5 Conclusions and outlooks ... 100

A Convergence tests of bulk h-BN calculations ... 102

B Computational details of graphene/h-BN vdW heterostructures ... 106

Bibliographie **113**

Papers **123**

List of communications **172**

Abstract in French, English, and Arabic **173**

Abstract

Light-matter interaction in van der Waals (vdW) materials, formed by vertically stacked two-dimensional (2D) sheets, displays fascinating characteristics, making them ideal candidates for the next generation of opto-electronic devices. Nowadays, these materials are intensively investigated in order to understand the main parameters that can affect, tune and customize their resulting properties.

In this thesis we address how the vdW combinations of these vertically stacked 2D materials can give rise to peculiar optical excitations that are not present in the individual constituents. Focusing on the structure-property relation, we investigate the impact of layer arrangement on the resulting character and distribution of the electron-hole (e-h) pairs. With the example of bulk hexagonal boron-nitride (h-BN), we first demonstrate that the electronic and optical properties of h-BN multilayers can be tuned through layer stacking. By modifying the layer arrangement, energy, intensity, and character of the e-h pairs can be selectively modulated. Focusing on the dimensionality of the excitons, we summarize the conditions that have to be fulfilled in order to obtain excitons with purely 2D distribution, charge-transfer, or three-dimensional character. Second, by combining graphene and h-BN to form periodic vdW heterostructures, we find that the gap opening in graphene is strongly related to the layer patterning. Focusing on the semiconducting configurations, we show that such heterostructures absorb light over a broad frequency range, from the near-infrared (IR) up to the ultraviolet (UV). The low-energy part of the spectrum is dominated by delocalized e-h pairs in the graphene layer, while strongly bound excitons in h-BN layers dominate the near-UV range. Besides these intrinsic features of the constituents, charge-transfer excitations appear across the visible region. Notably, the spatial distribution of e-h pairs can be selectively tuned through a controlled modulation of the stacking arrangement of the individual building blocks.

Our results, obtained within a first-principles density functional theory (DFT) and many-body perturbation theory (MBPT), open a fascinating perspectives to benefit from the structure-property relationship for designing vdW materials and heterostructures with tailored opto-electronic properties.

Acknowledgment

I would like to express special appreciation to my advisor Prof. Mohamed-Akli Belkhir for the continuous support of my Ph.D study, for his patience, motivation, and availability. His guidance helped me in all the time of research. My profound gratitude goes to Dr. Karim Rezouali for opening the wonderful world of the theoretical spectroscopy for me. You have been a tremendous mentor and without your precious support it would be not possible to conduct this research. Half of my Ph.D project was done within the solid-state theory group at Humboldt-Universität Berlin and has been funded by " Le Ministère Algérien de L'enseignement Supérieur et de la Recherche Scientifique".

Firstly, I express my sincere gratitude to Prof. Claudia Draxl, leader of this group, for providing me an opportunity to joint his team, all research facilities, support, and for the appreciated social group. Your guidance was the main key in achieving this work. I am very grateful to Prof. Caterina Cocchi for the countless constructive discussions during my Ph.D. This work must not be done without your support, encouraging, and fruitful discussions. Thank you very much for supporting me, availability, and for the critical reading of my thesis, and for all the helps. A special thank goes to Dr. Dmitrii Nabok for supporting this work. His patience and experience helped me to solve all the computational problems. Many thanks to Pasquale Pavone for his nice lectures in solid state physics, and to Andris Gulans for the technical helps. Finally, I would like to thank Helen, Ronaldo, Marzieh, Benjamin, Cristian, Martin, Svan, Albin, Hong, Qiang, Sebastian, Lorenzo, and all the members of solid-state theory group at Humboldt-Universität Berlin.

I would like to thank the members of my thesis committee: the president Prof. Sofiane Mahtout, Prof. Abdelmadjid Bouhemadou, and Dr. Hand Zenia for their insightful comments and fruitful questions which incited me to widen my research from various perspectives, and also for the encouragement in my scientific career. Many thanks to Profs. Fatiha Barka, Kamel Louzazna, Kassa Adel, Farid Rezgui, Abdeslame Houari, Yazid Kasri, Salim Ouhnia, Noual Amatousse, Hakim Guarbi, Mostapha Amaouche, Bo-

ufala Khaled, Bouda Ahmed, Nacer Bezzi, Hakim Ait-Amokhtar, Boukhalfa Bellache, and all my teachers at the Department of Physics of Bejaia University. I would like to thank Safer Sofiane, Foudil Zaabar, Faysel Mahrouche, Youcef Benzemouri, Doubal Ahmed, Abdellah Adnane and all my friends master and PhD students at "Laboratoire de physique theorique, University de Bejaia" and "Laboratoire de physico-chimie des matériaux", specifically, Lydia, Chahra, Nadia, Djoudi, Sara, Salma, Lynda, Ghilass, Wafa, Fares, Rbiha and Farida. Many thanks to Ourdani Djoudi for encouraging and for learning me several scientific tools.

Deg tazwara ad buddeγ amahil-a i yemma d vava yellan γer yidis-iw aten-yiḥrez Rebbi. I Nanna ad yesγezf Rebbi di leεmer-is i Jeddi fellas yeεfu Rebbi. I watmaten-iw d yisetma akked d tmeṭṭut n gemma. I Σemmi akked d tmeṭṭut-is. I Σmumti, Xwali d Xwalti akked twaculin-nsen. I Lemzien-neγ akken ma llan ladγa, Amin, Masnsen, d Litisya, d yigurdan Midu, Badis, ilina, Sirin, Randa, Milina, Tiziri, Σabdella, Hiba, akked Silin. At buddeγ i twacult n wat Σagun akken ma llan.

At buddeγ daγen i yemdukal-iw akken ma llan, i yimezdaγ n tγiwant n Kendira sumata, i widak d wacu i γriγ seg γerbaz amzewaru n Lmerj, ar uγerbaz alemmas n Tizi, d Tesnawit n yiberbacen, akked tseddawit n Bgayet. I yiselmaden-iw akken ma llan. Mebla ma ttuγ wid i qedcen deg tsedawit n Bgayt ama d iselmaden neγ d inelmaden d kra n win iqedcen γef tussna.

Wahib Σagun

Introduction and motivations

The van der Waals (vdW) materials and heterostructures [1] are promising candidates for the next generation of nanotechnologies in terms of efficiency and size. As such, they represent one of the new frontiers of materials science. Starting from three-dimensional (3D) layered systems, the exfoliation of graphene sheet in 2004 [2] demonstrated that it is possible to isolate a stable single layer. Due to its exceptional physical properties, graphene has attracted tremendous attention for the opportunity it offers in several promising applications [3]. The intensive studies devoted to graphene are extended to other layered materials, such as hexagonal boron-nitride (h-BN) [4–6], transition metal dichalcogenides (TMDs) [7–11], and black-phosphorous [12–14] in order to access new unique properties [15–18]. In addition, several elementary 2D materials analogue of graphene have been synthesized, such as silicene [19] and germanene [20]. The family of 2D materials includes also many other elements such as hydoxides [21, 22] and perovskites [23–27]. The wealth physical properties of these materials opens the path to many promising applications in several fields [10, 18, 28–30].

Nowadays, the research is oriented towards the vertical combination of these 2D constituents to build vdW heterostructures (bilayers, few-layers or multi-layers) where they are held together by vdW forces [1, 31–36]. These assemblies basically preserve the individual properties of the building blocks and additionally give access to novel intriguing features that are not present in the isolated constituents. Focusing on the electronic and optical properties, the diversity of 2D materials has opened unprecedented and vast opportunities to create vdW combinations with customized characteristics in the field of optoelectronics. As presented in Fig. 1, one can design an infinity of vdW combinations by changing the order of the layers, stacking sequence, and the type of the constituents. For these reasons, the necessity to understand and control the main parameters and conditions that can impact the resulting properties in such combinations requests an independent investigation of each parameter.

The first part of this thesis consists of a comprehensive study of the mechanisms that rule the electronic structure, including excitonic effects in relation with the stacking ar-

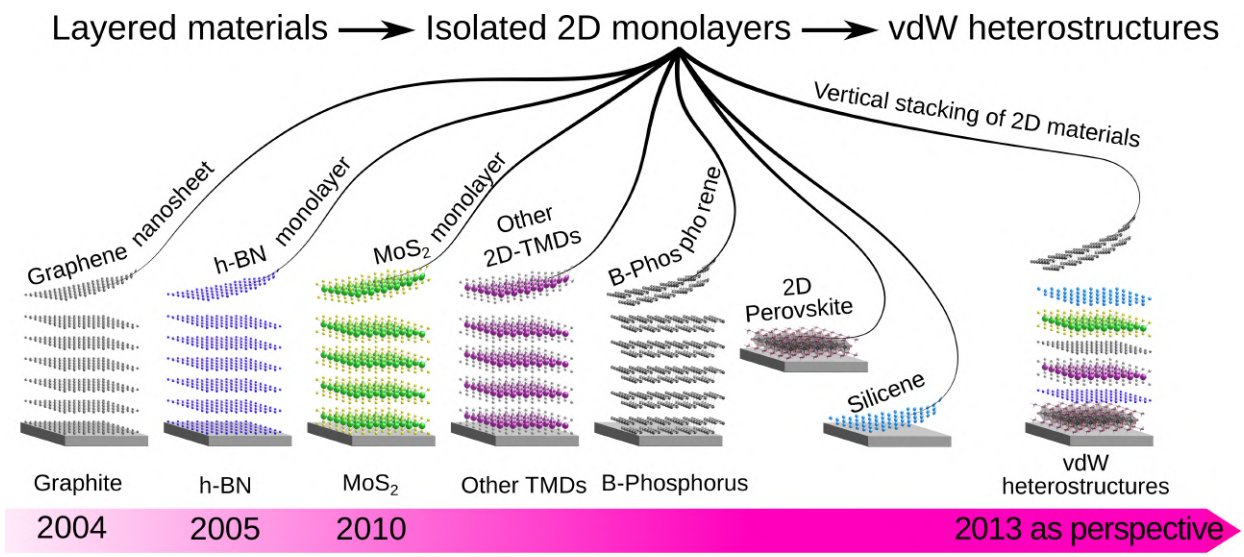

Figure 1: Schematic representation of the isolation of 2D materials from 3D layered systems. Nowadays, the combination of the different fascinating 2D layers in vdW heterostructures [1] grows as the most promising way to benefit from the characteristic of 2D constituents and access new features.

rangement. For this purpose, in the framework of density-functional theory (DFT) and many-body perturbation theory (MBPT), we select the bulk h-BN as a prototypical vdW material. This choice is motivated by the fact that bulk h-BN is formed by the same layer constituents and exhibits unique optical properties in the near-UV range [4, 37], related to the presence of strongly bound excitons [38–41]. These conditions allow to investigate, independently, the impact of the stacking arrangement on the resulting electronic and optical excitations in such material. In addition to the typical 2D distribution of the h-BN monolayer [42], we discuss the different e-h pair distributions that can appear in vdW bulk material. By considering different stacking arrangements, we study how such a layer patterning affects the structural, electronic, and optical properties focusing on the energy, intensity, and spatial distribution of the resulting e-h pairs.

The second part of the thesis is devoted to vdW heterostructures formed by two different building blocks in order to investigate the impact of the different constituents on the resulting properties. To do so, we select graphene and h-BN monolayers as ideal candidates for this propose. This choice is motivated by the similarity between their structural parameters, as they exhibit a small lattice mismatch ($\sim$1.6%) and by the opportunity that h-BN offers to open the graphene band gap [43–45]. In addition to the intrinsic electronic and optical properties of these constituents, we present the new features that appear in such heterostructures. Focusing on the resulting excitations, we discuss how the stacking arrangement of these 2D constituents leads to a significant enhancement of light-matter interaction.

The thesis is organized as follows. The first chapter describes the 2D materials and vdW heterostructures in a general context focusing on the selected systems. In the second

chapter, we introduce the theoretical methods (DFT and MBPT) and present the computational scheme and details. In chapter 3 and 4, we discuss our results on the structural, electronic, and optical properties including excitonic effects of stacked bulk h-BN and graphene/h-BN vdW heterostructure, respectively, focusing on the effect of layer patterning on the e-h pairs distribution. Finally, in chapter 5, we present our conclusions and perspectives.

1

From two-dimensional materials to van der Waals heterostuctures

1.1 Two-dimensional materials

In the interaction with light two-dimensional materials display fascinating characteristics. Their unique properties, such as quantum confinement, low screening, and tunable electronic structure, as well as their easy interface with substrates [30, 46–48] make them ideal candidates for the next generation of opto-electronic devices [10, 15, 18, 28–30, 35, 49–51].

The resulting electron-hole (e-h) pairs in 2D materials, are generally confined within the plane and typically exhibit enhanced binding strength compared to the bulk [9, 52–54] (see Fig. 1.1). This is an effect of the interplay between increased spatial confinement of the excitons and reduced screening due to the large amount of vacuum surrounding the atomically-thin materials [50, 55–57]. The resulting excitations localized within a single layer [58–62] have triggered intensive research about the possibility to exploit these systems in the next generation of opto-electronic and photonic devices [35, 46, 51, 63, 64].

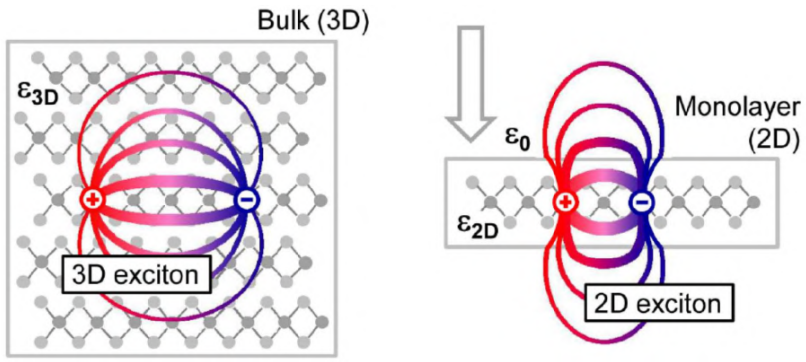

Figure 1.1: Schematic representation of the reduced dielectric screening in 2D materials with respect to their bulk counterpart. The resulting e-h pair are confined within the plane with strong binding energy. Fig. reproduced from Ref. [55].

The diversity of the 2D materials in terms of atomic constituents and structural arrangements is reflected in their rich electronic and optical properties. According to their

band gap that fulfills all the energy ranges (metals, semi-metals, semiconductors and insulators), each 2D material absorbs light in a specific energy range [51, 65] as shown in Fig. 1.2. In our case, we have selected graphene and h-BN as building blocks for our heterostructures. As we can see, they exhibit a complementary behavior when interacting with light since graphene absorbs the light in the near IR region and the h-BN in the near UV range. We expect a large variety of optical features when combining these materials to build vdW heterostructures. In the following we present the intrinsic characteristic of these two constituents.

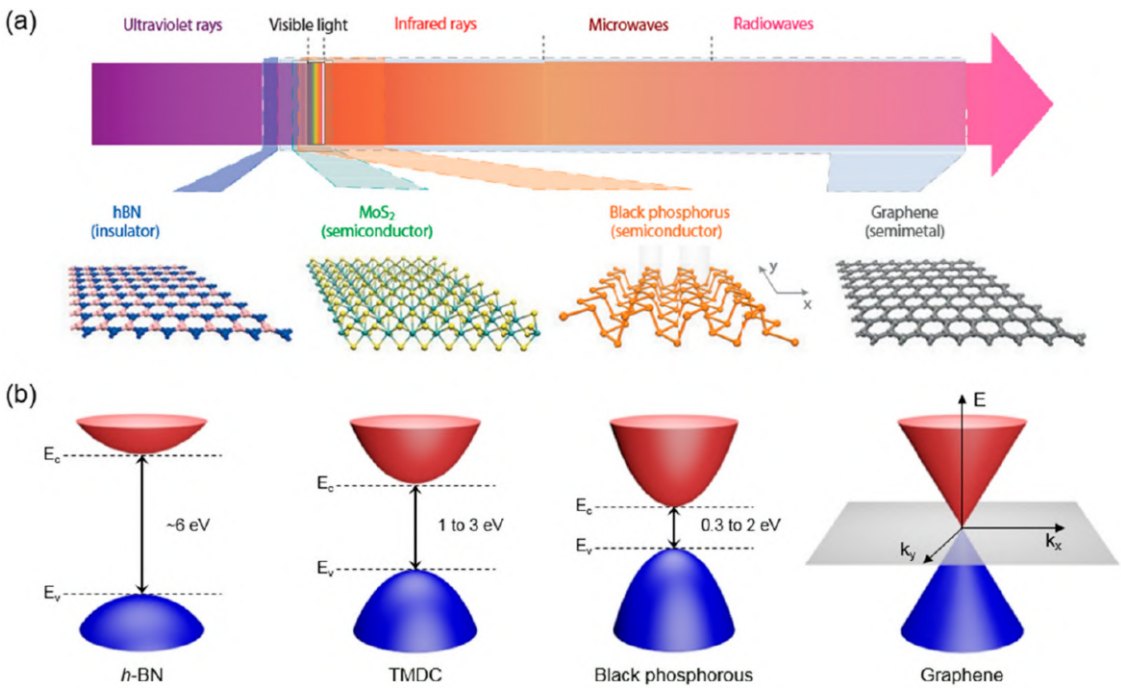

Figure 1.2: **a**: Schematic of the large variety of the 2D materials which absorb light in specific energy range according to their band gap. **b**: The corresponding size and dispersion of the band gab. Fig. is reproduced from Ref. [65].

1.1.1 Graphene

In a graphene sheet, the C atoms are regularly distributed over two-dimensional hexagonal honeycomb lattice (see Fig. 1.3.a). Graphene presents unique physical properties, such as high carrier mobility (up to 10000 $\mathrm{cm^2V^{-1}s^{-1}}$ at room temperature) [2, 66], strong mechanical properties (breaking strength is 42 $\mathrm{Nm^{-1}}$ with Young's modulus of 1.0 TPa) [67], transparency to the visible light (absorb only 2.3%) [68], high thermal conductivity (up to 5000 $\mathrm{Wm^{-1}k^{-1}}$) [69] and many other fascinating properties [3, 28, 70]. Consequently, several promising applications have been designed, investigated and explored in order to benefit from this unique material [28, 70–79]. To achieve this goal, several synthetic methods have been developed to elaborate less expensively [80] a large scale and high quality graphene sheet. In addition to the mechanical exfoliation (cleav-

age) which is used to isolate a monolayer graphite initially [2], epitaxial growth, chemical vapor deposition (CVD), and liquid phase exfoliation show their highest quality and efficiency [80, 81]. These qualified methods of elaboration represent also the main condition that enhanced the way to discover other 2D materials.

For the optoelectronic applications, the vanishing band gap in graphene limits its uses in such devices. As shown in Fig. 1.3, the optical spectrum of graphene is dominated by a zero-energy resonance, reflecting its semi-metallic character, while it is rather featureless in the visible region. For this reason, several methods are proposed to open a band gap in graphene such as cutting graphene into nanoribbons [82], chemical functionalization (adsorbed atoms and molecules) [83–89], uniaxial strain [90], and substrate-effect [91, 92]. We notice that the band gap problem represents another main motivation to go beyond graphene towards the discovery of other 2D materials presented above.

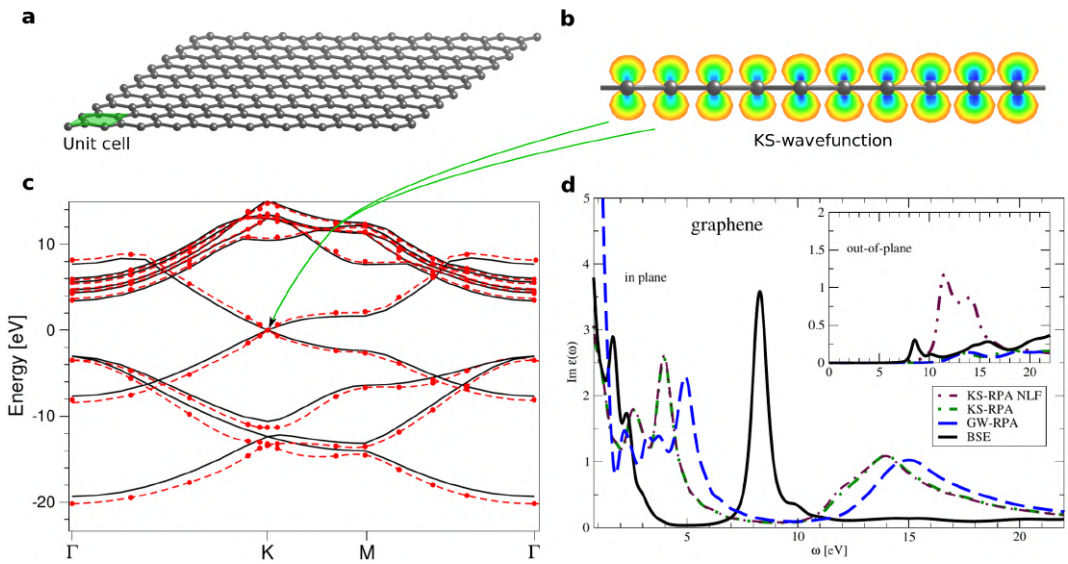

Figure 1.3: **a**: 2D structure of graphene where the unit cell contains two carbon atoms. **b**: Electronic distribution of the top of valence band and the bottom of the conduction band at K point (Dirac cone). **c**: Electronic band structure of graphene along the high symmetry points given by DFT (black) and quasi-particle GW (red). Fig. reproduced from Ref. [93]. **d**: Absorption spectrum of graphene at different level of approximation. The black spectrum, given by solving the Bethe-Salpeter equations, is the more accurate ones, which take into account the excitonic effects. Fig. reproduced from Ref. [94].

Recently, a new exciting way to open a band gap in graphene without modifying or destroying the structure has been proposed [1, 43, 45, 91, 92, 95]. By combining graphene with other 2D materials to form a vdW heterostructure a small gap can be induced while its intrinsic properties are basically preserved. This way allows the use of graphene in several optoelectronic devices on one side and benefit from its unique features, such as mechanical and thermal properties on the other side [28, 35, 43, 96–98].

1.1.2 Hexagonal boron nitride

Hexagonal boron nitride is a widely studied material [4, 37, 99] exhibiting the same vdW layered structure as graphite. In this case, the layers are composed of B and N atoms, distributed over hexagonal honeycomb lattice. The resulting in-plane lattice parameter is closer to that of graphene. In contrast to graphite where the layers are staggered with AB Bernal arrangement [100], in h-BN material the layers are eclipsed with B over N, making the AA' stacking arrangement (see Fig. 1.4.a). In addition to its attractive properties, such as chemical stability, high thermal conductivity, and easy layer sliding (lubricant applications), the unique electronic and optical properties of h-BN have been extensively investigated in the last 15 years [4, 37–41, 101, 102].

Owing to its large band gap, ($\sim$ 6 eV) [4, 38, 102], h-BN absorbs light in the UV region. Moreover, due to the low dielectric screening, the optical response of bulk h-BN is dominated by strong excitonic effects in the near-UV region (see Fig. 1.4.b,c,d). These properties make h-BN a promising candidate for optoelectronic applications [70] as demonstrated for deep-ultraviolet light emitting devices [37]. Due to the necessity to estimate the size and the nature of the band gap for such applications, bulk h-BN have been widely investigated by different experimental techniques and theoretical methods. As shown in Table 1.1, the reported experimental band gap in h-BN ranges between 3.6 and 7.1 eV with direct or indirect nature. This diversity reflects the different measurement techniques and the quality of the sample used. The reported theoretical band gap based on the MBPT range between 5 and 6 eV with indirect nature.

Table 1.1: Theoretical and experimentally measured band gap of bulk h-BN.

Exp. gaps(Author)	(year)[Ref]	Band gap (eV)	Nature
Fomichev.	(1971) [104]	3.6	
Zupan et al.	(1972) [105]	4.3	
Zunger et al.	(1976) [105]	5.8	Direct
Carpenter et al.	(1982) [106]	7.1$\pm$0.1	
Tarrio et al.	(1989) [107]	5.9$\pm$0.2	
Lukomskii et al.	(1993) [108]	5.89	
Solozhenko et al.	(2001) [109]	4.02$\pm$0.01	
Watanabe et al.	(2004) [4]	5.97	Direct
Evans et al.	(2008) [110]	5.96$\pm$0.04	Quasi-direct
Edgar et al.	(2014) [111]	5.8	Indirect
Cassabois et al.	(2016) [102]	5.955	Indirect
Theo. gaps(MBPT)	**(year)[Ref]**	**Band gap (eV)**	**Nature**
Blase et al.	(1995) [112]	5.4	Indirect
Wirtz et al.	(2005) [113]	5.53	Indirect
Arnaud et al.	(2006) [38]	5.95	Indirect
Gao et al.	(2012) [114]	5.84	Indirect

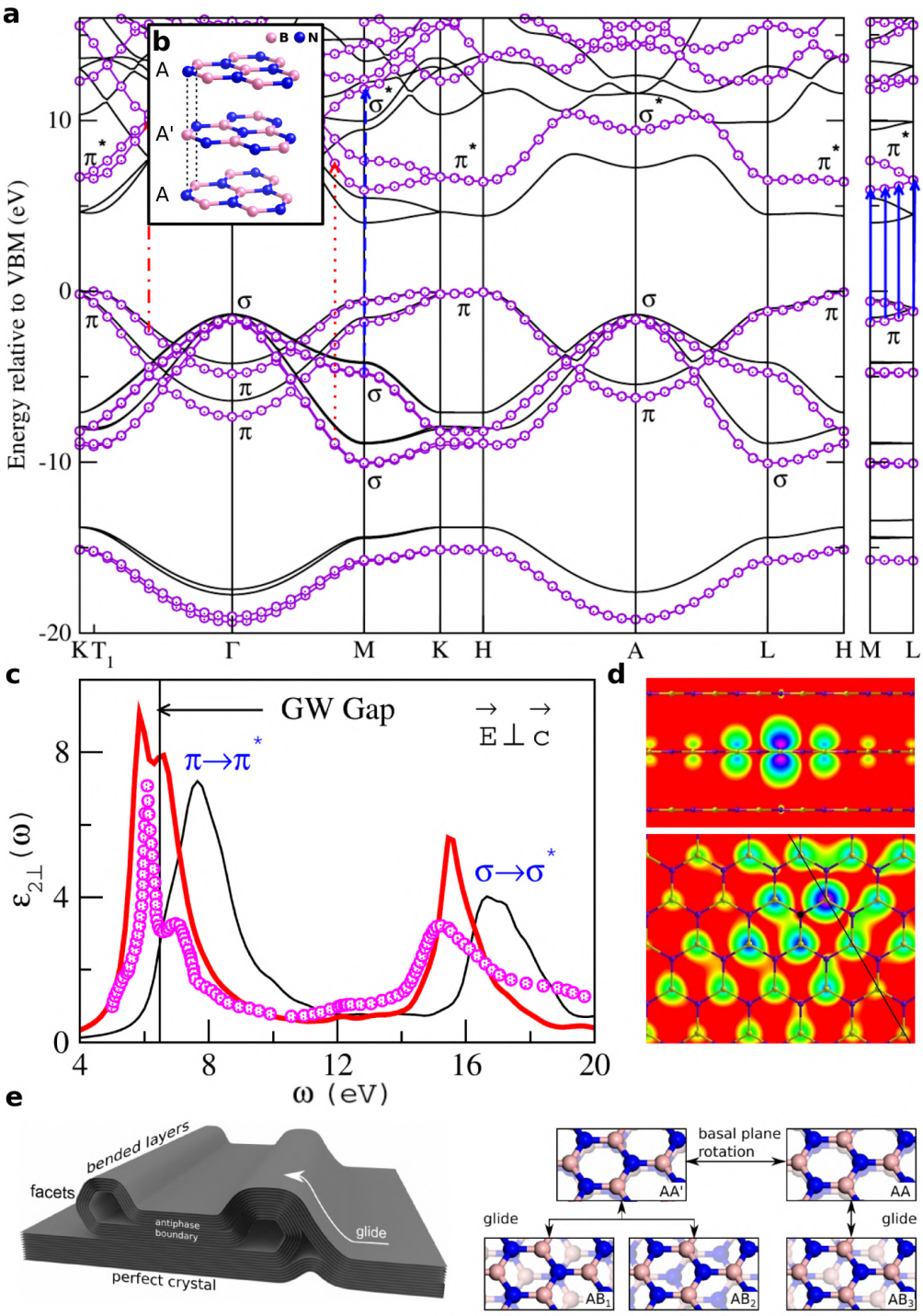

Figure 1.4: **a**: Electronic band structures of bulk h-BN given by DFT (black line) and quasi-particle GW (pink circles) where the top valance band is set to zero. **b**: Sketch of the experimentally known h-BN structures (AA′ staking arrangement). **c**: Absorption spectrum of bulk h-BN given by the BSE calculation (red line) which include the excitonic effects and without excitonic effects (black line) together with the experimental measurement spectrum (pink circles). **d**: In and out of plane projection of the e-h pairs distribution of the main exciton that dominate the sharp peak at the onset. **e**: The morphological deformation of bulk h-BN (left) may promote transitions between different stacking sequences (right). Figs. (**b**,**c**,**d**) are reproduced from Ref. [38] and Fig. **e**, from Ref. [103].

Focusing on the recent theoretical and experimental band gaps we can see a very close agreement in terms of nature and size of the reported band gaps which turn around 5.95 eV. As shown in (see Fig. 1.4.c), this agreement can be also seen by comparing the computed (red line) and measured (pink circles) absorption spectra, reflecting the accuracy of the MBPT approach that includes the excitonic effects (the details are shown in Chapter 2). As mentioned above, the most commonly realized stacking in experiments, corresponds to the AA' arrangement (see Fig. 1.4.a). However, we notice that the AB stacking arrangement can be favorably formed in bilayer h-BN, as reported in Ref. [115]. In addition, the other possible arrangements shown in Fig. 1.4.e have been probed experimentally in few-layer h-BN structures [116–120]. In Ref. [103], it has been also suggested that a morphological deformation may promote transitions between different stacking arrangements which can impacts the physical properties in bulk h-BN (see Fig. 1.4.e). The presence of layer patterns represents one of the reasons of the diversity in the size and nature of the experimental band gap (see Table 1.1) as reported in Refs. [103, 121, 122].

Today, the tunability of the electronic and optical properties in h-BN and other layered materials by layer patterning represent a new fascinating topic in order to access new features [103, 119, 121–135]. In the first part of this thesis, the effect of the staking arrangement on the electronic structures including excitonic effects in bulk h-BN will be investigated in details.

1.2 Van der Waals heterostuctures

VdW heterostructures are promising candidates for the next generation of nanotechnologies [1]. By combining 2D materials in the vertical direction vdW heterostructures can be formed. The in-plane structure of 2D constituents are preserved in such combination since they are held together by only vdW forces [1] (see Fig. 1.5). Consequently, these vdW combinations preserve the intrinsic characteristic of the 2D constituent while the weak interlayer interaction gives rise to new characteristic that are absent in the building blocks.

The diversity of 2D materials library in terms of physical properties, structural arrangement, and atomic constituent allows an endless possibilities of vdW combinations. Starting from the choice of the constituents one have to take into consideration the lattice mismatch, any possible chemical interactions, band alignment at the interface, the desirable properties, and so on in order to build vdW heterostructures [1, 50, 136–138]. Taking the optical excitations as example, the vdW combination of MoS_2 and WSe_2 monolayers gives rise to novel features represented by charge transfer e-h pair at the interface. This type of exciton is favorably formed in vdW heterostructures where the band gaps of the constituents are staggered at the interface (band alignment type II) [139].

Furthermore, the way how to combine these 2D materials such as vertical order, stacking arrangements, lattice mismatch, and rotations represent other sensitive parameters

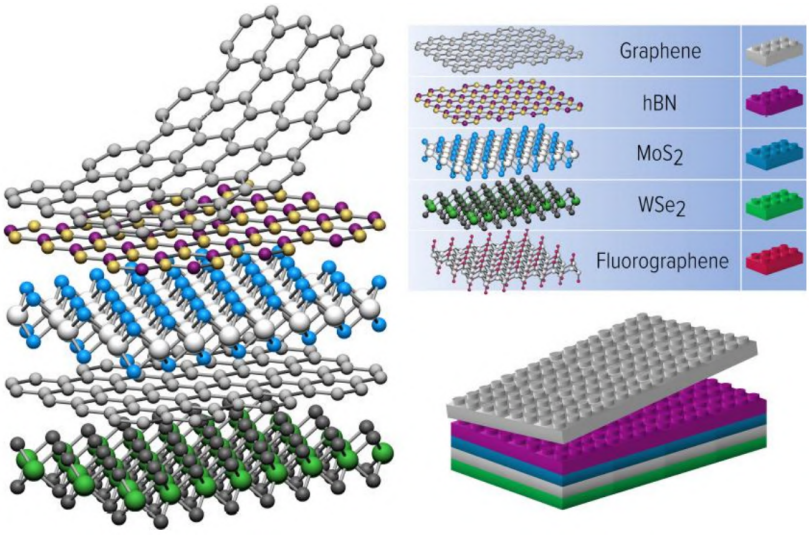

Figure 1.5: Schematic representation of the vdW heterostructures formed by vertical stacking of different 2D materials. Fig. reproduced from Ref. [1]

that should be considered when building of such heterostructures [123, 124, 126–135]. As an example, it is found that the charge transfer exciton in bulk TMDs can exist only in the presence of inversion symmetry that links the layers, as demonstrated in Ref. [138].

To sum up, all the parameters cited above request to be investigated independently in each layered materials in order to understand their importance and impact.

1.2.1 Graphene/h-BN vdW heterostructures

Hexagonal boron nitride is reported as the best substrate for graphene sheet in order to benefit from its unique properties [140]. Moreover, encapsulation between h-BN layers makes graphene insusceptible to the external environment [141]. The possibility to induce a band gap in graphene by h-BN substrate or by intercalating graphene between h-BN layers has already triggered a number of pioneering studies in this direction [43–45, 92, 95, 142, 143] for optoelectronic applications [45, 70, 144–148]. The ability for such vdW combination reflects the similar structural parameters between graphene and h-BN such as flat structures and small lattice mismatch $\sim 1.6\%$ [45, 70, 144, 145, 147].

By combining graphene and h-BN layers we address in the second part of this thesis how the vdW assemblies of these 2D materials can induce to peculiar optical excitations that are not present in the individual constituents.

Focusing now on the differences in the structural parameters, the small lattice mismatch between graphene and h-BN ($\sim 1.6\%$) leads to a significant Moiré pattern [149–154]. As shown in Fig. 1.6, the deposition of graphene on h-BN exhibits several possibilities of twist angles which change the periodicity of the Moiré pattern. In Fig. 1.7 we present the graphene/h-BN heterobilayer neglecting (left) and including (right) the lattice mismatch. In order to simulate such heterobilayer, one needs to consider a supercell to

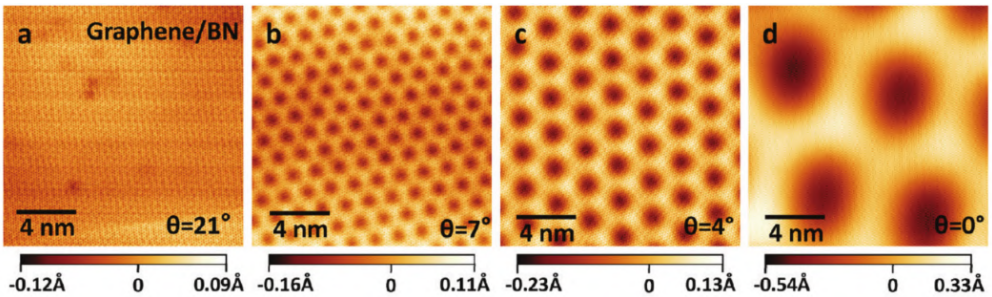

Figure 1.6: Experimental observation of Moiré pattern in graphene/h-BN interface given by their lattice mismatch (**d**) or by different twist angle (**a**, **b**, **c**). This combinations allows several orientations (rotation of graphene with respect to h-BN) which reduce the Moiré periodicity. The Fig. is reproduced from Ref. [149].

cover the non uniform stacking of the layers (incommensurate layers). The periodicity of the Moiré pattern which represents the length of the supercell is approximately 15.3 nm without rotation, in agreement with the reported experimental one (15$\pm$ 1 nm with zero rotation angle) in Ref. [155]. This supercell is equivalent to $\sim$ 62x62 unit cell of graphene. On the other hand, the incommensurate layers can be considered as locally commensurate with specific stacking arrangement (see Fig. 1.7.a, right). For this reason, instead of using the supercell, in chapter 4 we consider a simple commensurate graphene/h-BN unit cell (see Fig. 1.7.a, left) in order to avoid the deal with supercell containing 62x62x2 atoms for each layer. Thus, by investigating different stacking arrangements the systems are more or less close to the locally realistic combination [149, 150, 155].

The resulting size of the supercell can be reduced by including rotations, as shown in Fig. 1.7.b, being consistent with the realistic experimental observation reported in Fig. 1.6 at different twist angle [149]. Since the layer rotations allows infinite arrangement possibilities, in this thesis we avoid the twist angle also and focus only on the eclipsed or staggered layers where the atoms are vertically aligned and/or occupy the *hollow* site of the neighboring layers. This choice allows us to investigated the ideal materials where interlayer interaction is maximized and to understand the phenomenon in the simplest cases. This ideal configurations pave a way through the understanding of the complex realistic combination.

In the next chapter we present the theoretical methods and computation details used to achieve our goal.

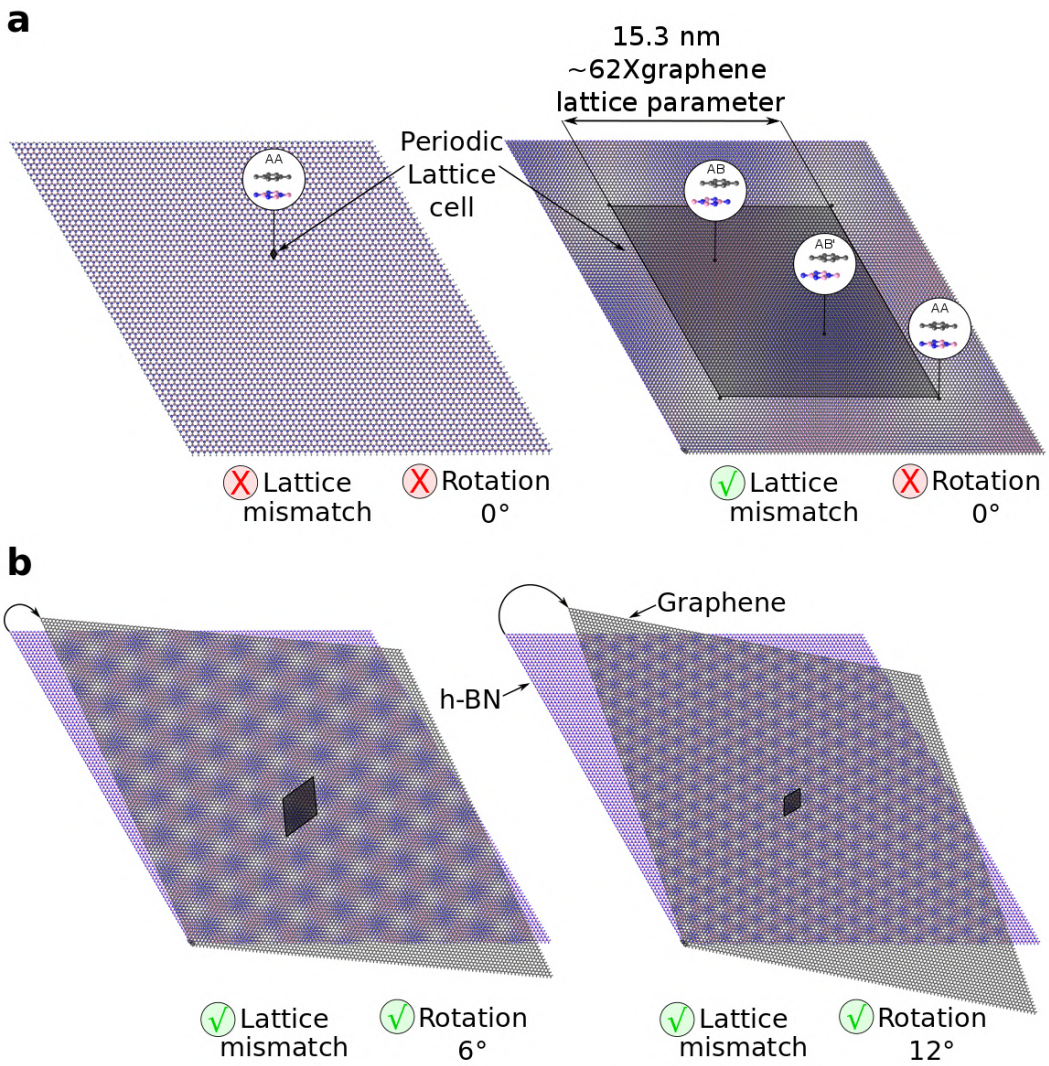

Figure 1.7: **a**: Schematic representation of graphene/h-BN heterobilayer neglecting (left) and including (right) lattice mismatch which leads to the Moiré pattern. The local commensurate stacking is indicated inside the white circles. **b**: This combination allows infinity of twist angle (rotation) which reduces the Moiré periodicity (supercell).

2 Theoretical methods

The traditional subject of theoretical solid state physics consists of studying the physical properties of periodic crystals by solving the Schrödinger equation. However, due to the many-body nature of the system, where electrons interact with each other and with the nuclei, the exact solution of this equation is not possible. Consequently, several methods and approximations are proposed in order to get access to the physical properties of materials. Starting from the Born-Oppenheimer approximation, the many-body problem (electrons and nuclei) is reduced to the many-electron system. The density functional theory (DFT) approach has been successfully applied for determining the physical properties of the systems. It is based on the fact that these properties can be described by the electronic density. Owing to non interacting approach of the DFT method, the excited-state properties cannot be determined. Consequently, the many-body perturbation theory (MBPT) is introduced to provide an efficient alternative for accessing these properties. In this chapter, we introduce these methods in a general context, together with the corresponding computational details.

2.1 The many-body problem

The physical properties of systems made up of nuclei and electrons can be determined by solving the time-independent Schrödinger equation:

$$\hat{H}\psi = E\psi, \tag{2.1}$$

where $\hat{H}$ is the Hamiltonian of the system, ψ and E are the wave-function and energy of the system, respectively.

For example, a system consisting of N_n atomic nuclei and N_e electrons interacting with each other, the corresponding Hamiltonian is expressed in the following form:

$$\hat{H} = \hat{T}_{\mathrm{e}} + \hat{T}_{\mathrm{n}} + \hat{V}_{\mathrm{e-e}} + \hat{V}_{\mathrm{e-n}} + \hat{V}_{\mathrm{n-n}}, \tag{2.2}$$

with:

- $\hat{T}_{\mathrm{e}}$ and $\hat{T}_{\mathrm{n}}$ are the kinetic energy operator of electrons and nuclei, respectively.
- $\hat{V}_{\mathrm{ee}}$, $\hat{V}_{\mathrm{e-n}}$ and $\hat{V}_{\mathrm{n-n}}$ are the electrostatic interactions between electrons, electrons-nuclei, and between nuclei, respectively.

From the Born-Oppenheimer approximation the many-body Hamiltonian is simplified. Owing to the large mass difference between the electron and the nucleus ($m_e \approx M_n/1800$, where, m_e and M_n are the electron and nucleus masses, respectively), the nuclei are considered fixed, reflecting their very slow motion with respect to that of the electrons. As a result, the nuclei positions can be treated as a simple parameter in the resolution of the Schrödinger equation. With this consideration, the kinetic term of the nuclei $\hat{T}_{\mathrm{n}}$ will be set to zero and the nucleus-nucleus repulsion term $\hat{V}_{\mathrm{nn}}$ will be as constant added to the total energy.

The Hamiltonian is reduced to describe the interacting electrons under an external potential generated by the nuclei, as follow:

$$\hat{H}_{\mathrm{e}} = \hat{T}_{\mathrm{e}} + \hat{V}_{\mathrm{e-e}} + \hat{V}_{\mathrm{ext}}. \tag{2.3}$$

Noting $\mathbf{R}_k$ the vector position of the kth nucleus and $\mathbf{r}_i$ that of the ith electron, we have[1]:

$$\begin{cases} \hat{T}_{\mathrm{e}} = -\sum_{i=1}^{N_e} \frac{\Delta_i}{2}, \\ \hat{V}_{\mathrm{e-e}} = \frac{1}{2}\sum_{i\neq j}^{N_e} \frac{1}{|\mathbf{r}_i - \mathbf{r}_j|}, \\ \hat{V}_{\mathrm{ext}} = \sum_{i,k}^{N_e,N_n} \frac{-Z_k}{|\mathbf{r}_i - \mathbf{R}_k|} = \sum_i^{N_e} \hat{v}_{ext}(\mathbf{r}_i), \end{cases} \tag{2.4}$$

where $\hat{v}_{\mathrm{ext}}(\mathbf{r}_i)$ is the external potential acting on each electron i (=1,...,N_e), with:

$$v_{\mathrm{ext}} = \sum_k^{N_n} \frac{-Z_k}{\mid \mathbf{r}_i - \mathbf{R}_k \mid}, \tag{2.5}$$

and:

$$\hat{H}_{\mathrm{e}} = \sum_i^{N_e} \left\{ -\frac{\Delta_i}{2} + v_{ext}(\mathbf{r}_i) \right\} + \hat{V}_{\mathrm{e-e}}. \tag{2.6}$$

This problem is simpler than the initial many-body problem, but still not solvable since the Hamiltonian contains usually 10^{23} electron/cm^3. In the following we introduce the alternative way given by the density functional theory to solve this problem.

[1]From now on, we will be using atomic unites (a.u.), with $\hbar = 1$, $e = 1$, $4\pi\epsilon_0 = 1$ and $m_e = 1$, which give the energies in Hartree (1 Ha =27.21138602 eV).

2.2 Density functional theory (DFT)

The density functional theory is based on the fact that the electronic density of materials contains the information about their ground-state properties. It allows for solving the Schrödinger equation from a different physical and mathematical point of view. The many-electron problem is reformulated into a simple electronic density problem. Historically, the original idea of this theory was born in the works of Thomas and Fermi in 1927 [156, 157], while the first bases were laid in 1964 by Hohenberg and Kohn [158], and in 1965, by Kohn and Sham [159] who demonstrated the possibility of determining the properties of a system using the electronic density as a sole input. It is based on the two following theorems by Hohenberg and Kohn [158]:

- The first states that for any bounded system of interacting particles in an external potential $\mathrm{V}_{ext}(\mathbf{r})$, except for a constant, this potential is determined uniquely by the ground-state particle density $n(\mathbf{r})$.
- The second stipulates that we can define a universal functional $E[n]$ for the energy in terms of the density n, valid for any external potential $\mathrm{V}_{ext}(\mathbf{r})$. The exact ground-state energy $E_{GS}[n_{GS}(\mathbf{r})]$ of the system is the global minimum of the functional $E[n]$, for a given $\mathrm{V}_{ext}(\mathbf{r})$, while, the density $n_{GS}(\mathbf{r})$ that minimizes this functional corresponds to the exact ground-state density.

Using a *reductio ad absurdum* argumentation, Hohenberg and Kohn [158] proved the one-to-one correspondence between the external potentials, ground-state wave-functions, and ground-state densities as shown in Fig. 2.1. As mentioned in the second theorem, the total energy can be written as functional of the density:

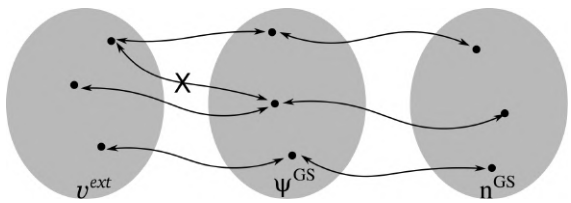

Figure 2.1: Representation of the one-to-one correspondence described in the first Hohenberg and Kohn theorem.

$$
\begin{aligned}
E[n] =< \psi|\hat{H}|\psi >=< \psi|\hat{T}_{\mathrm{e}}+\hat{V}_{\mathrm{ee}}|\psi > + < \psi|\hat{V}_{\mathrm{ext}}|\psi >, \\
= T[n(\mathbf{r})] + V[n(\mathbf{r})] + \int v_{\mathrm{ext}}(\mathbf{r})n(\mathbf{r})d^3r, \\
= F[n(\mathbf{r})] + \int v_{\mathrm{ext}}(\mathbf{r})n(\mathbf{r})d^3r,
\end{aligned} \tag{2.7}
$$

where the universal functional $F[n(\mathbf{r})]$ is independent of the external potential. Thanks to the variational principle and the one-to-one correspondence between the density and the wave-functions, the ground-state energy can be written as:

$$
E_{GS} = E[n_{GS}] = \underset{n(\mathbf{r})}{min} E[n(\mathbf{r})] = \underset{n(\mathbf{r})}{min}\{F[n(\mathbf{r})] + \int v_{\mathrm{ext}}(\mathbf{r})n(\mathbf{r})d^3r\}. \tag{2.8}
$$

Based on the unique correspondence (potentials-densities) and the universality of the functional, as well as the variational principle, Hohenberg and Kohn describe the ground-state properties of the many-body system as a functional of the density. However, the lack of a clear expression of this functional presents a hurdle to use these theorems in practice. For this reason, Kohn and Sham proposed, in 1965 [159], another viable path to access the ground-state properties trough these theorems.

2.2.1 The Kohn-Sham (KS) equations

Nowadays, the success of the DFT is due to the practical approach proposed by Kohn and Sham (KS) [159]. Instead of the fully interacting system, they considered a "fictitious" non interacting system of particules in an effective potential, such that it has the same density as the real system (see Fig. 2.2). This approach presents a practical way to determine the ground-state properties by solving a single-particle problem instead of the many body problem. The energy functional of the non interacting system can be written as:

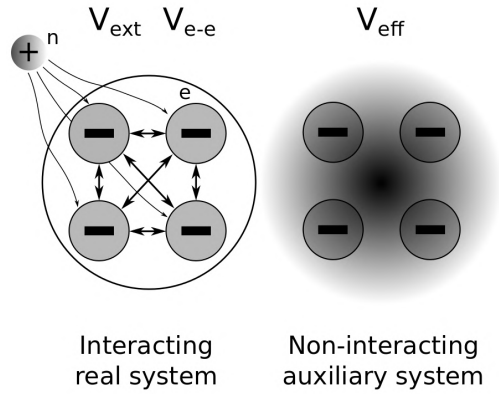

Figure 2.2: Schematic representation of the real interacting system and the corresponding "fictitious" auxiliary system.

$$E[n] = T_{\text{ind}}[n(\mathbf{r})] + \int v_{\text{eff}}(\mathbf{r})n(\mathbf{r})d^3r, \tag{2.9}$$

where the effective potential (v_{eff}) contains all the interaction acting on the single-particle. Starting from the energy of the interacting system:

$$E[n] = T[n] + V[n] + \int v_{\text{ext}}(\mathbf{r})n(\mathbf{r})d^3r, \tag{2.10}$$

$$E[n] = T[n] + V[n] + T_{\text{ind}}[n] - T_{\text{ind}}[n] + V_{\text{ind}}[n] - V_{\text{ind}}[n] + \int v_{\text{ext}}(\mathbf{r})n(\mathbf{r})d^3r, \tag{2.11}$$

can be written as:

$$E[n] = T_{\text{ind}}[n] + E_{\text{H}}[n] + E_{\text{XC}}[n] + V_{\text{ext}}[n], \tag{2.12}$$

where, $T_{\text{ind}}[n]$ is the kinetic energy of the non interacting system, $E_{\text{H}}[n]$ represents the Hartree potential energy (corresponds to the classical Coulomb interaction between electrons, $V_{\text{ind}}[n]$). $E_{XC}[n]$ is the exchange-correlation term which contains the difference between the kinetic energy of the interacting and non interacting systems and the difference between the full e-e interaction and the classic Coulomb energy. The $V_{\text{ext}}[n]$ term repre-

sents the external potential energy, with:

$$\begin{cases} E^{XC}[n] = T[n] - T_{\text{ind}}[n] + V[n] - V_{\text{ind}}[n], \\ \\ E_{\text{H}}[n] = V_{\text{ind}}[n] = \frac{1}{2}\int \frac{n(\mathbf{r})n(\mathbf{r}')}{|\mathbf{r}-\mathbf{r}'|} d^3r\, d^3r', \\ \\ V_{\text{ext}}[n] = \int v_{\text{ext}}(\mathbf{r})n(\mathbf{r})d^3r. \end{cases} , \tag{2.13}$$

The functional derivative of Eq. 2.12 gives:

$$\frac{\delta E[n(\mathbf{r})]}{\delta n(\mathbf{r})} = \frac{\delta T_{\text{ind}}[n(\mathbf{r})]}{\delta n(\mathbf{r})} + \underbrace{\int \frac{n(\mathbf{r}')}{|\mathbf{r}-\mathbf{r}'|} d^3r'}_{v_{\text{H}}(\mathbf{r})} + \underbrace{\frac{\delta E_{\text{XC}}[n(\mathbf{r})]}{\delta n(\mathbf{r})}}_{v_{\text{XC}}(\mathbf{r})} + v_{\text{ext}}(\mathbf{r}), \tag{2.14}$$

let

$$v_{\text{eff}}(\mathbf{r}) = v_{\text{H}}(\mathbf{r}) + v_{\text{XC}}(\mathbf{r}) + v_{\text{ext}}(\mathbf{r}), \tag{2.15}$$

represents the effective potential where the non interacting particles move. The problem now is reduced from many-electrons to single particle Schrödinger equation, as follows:

$$\left[-\frac{\Delta}{2} + v_{\text{eff}}(\mathbf{r})\right] \phi_i^{KS}(\mathbf{r}) = \varepsilon_i \phi_i^{KS}(\mathbf{r}). \tag{2.16}$$

The corresponding ground-state density of the non interacting system (which is the same as that of the interacting system) is constructed from the Kohn-Sham lowest-energy eigenstates ϕ_i^{KS}, as follows:

$$n(\mathbf{r}) = \sum_{i=1}^{N_e} |\phi_i^{KS}(\mathbf{r})|^2. \tag{2.17}$$

Since $v_{\text{eff}}(\mathbf{r})$ depends on the ground-state density (specifically $v_{\text{H}}(\mathbf{r})$ and $v_{\text{XC}}(\mathbf{r})$ potentials), all DFT calculations are based on the iterative resolution of (2.15) (2.16) (2.17) KS equations. The calculation procedure starts by making a guess for the initial density and constructing v_{eff}. By solving the single particle KS equation (Eq. 2.16), the resulting wave-functions are used to calculate the ground-state density, as shown in Eq. 2.17. This process is repeated in a self-consistent way until reaching a given convergence criterion (for example on the total energy or the density). The resulting ground-state energy is expressed as follows:

$$E[n] = -\sum_{i=1}^{N_e} \int d^3r \phi_i^*(\mathbf{r}) \frac{\nabla^2}{2} \phi_i(\mathbf{r}) + \frac{1}{2}\int \frac{n(\mathbf{r})n(\mathbf{r}')}{|\mathbf{r}-\mathbf{r}'|} d^3r\, d^3r' + \int v_{\text{ext}}(\mathbf{r})n(\mathbf{r})d^3r + E_{XC}[n]. \tag{2.18}$$

We notice that at this level no approximations have been made, $v_{\text{eff}}(\mathbf{r})$ contains all many-body interactions, and the resulting energy is the exact ground-state energy of the

system. However, since the exchange-correlation term is unknown, an approximation is therefore necessary.

2.2.2 Exchange-correlation functionals

Despite the small contribution of the $E_{XC}[n]$ to the total energy with respect to the kinetic term, the quality of the ground-state calculations is determined by the precise knowledge of the earlier. Consequently, several approximations are proposed in order to estimate this exchange-correlation term.

The local density approximation (LDA)

The local-density approximation is the first level and the simplest approach to the exchange-correlation term for systems with slowly varying electron density. The basic principle is to consider an inhomogeneous system as locally homogeneous (this means that the density varies slowly as a function of position) through its division into elementary volumes of local and uniform densities. The exchange-correlation is then expressed as follows:

$$E_{XC}^{LDA}[n] = \int n(\mathbf{r})\varepsilon_{XC}(n(\mathbf{r}))d^3r. \tag{2.19}$$

So the exchange-correlation energy $E_{XC}^{LDA}[n]$ is the integral over all space, assuming that ε_{XC} is the exchange-correlation energy per particle of a homogeneous electron gas of density $n(\mathbf{r})$. While the form of the exchange part is exactly known ($\varepsilon_X[n(\mathbf{r})] = -\frac{3}{4}\left(\frac{3}{\pi}n(\mathbf{r})\right)^{\frac{1}{3}}$), the expression of the correlation term is not known and can be computed accurately using the quantum Monte-Carlo method proposed by Ceperley and Alder [160, 161].

The generalized gradient approximation (GGA)

In case where the inhomogeneities of the density are important, the LDA is extended to include the gradient of the density. The resulting approximation, named "generalized gradient approximation", is expressed as follows:

$$E_{XC}^{GGA}[n] = \int n(\mathbf{r})\varepsilon_{XC}(n(\mathbf{r}), |\nabla(n(\mathbf{r}))|)d^3r. \tag{2.20}$$

Now, the exchange energy functional ε_{XC} depends also on the gradient $\nabla(n(\mathbf{r}))$. The most used and accurate parametrization is the GGA-PBE, proposed by J. P. Perdew et al. [161].

2.2.3 Limitations

Despite the simplicity of the LDA, the ground-state properties of many systems (covalent systems and simple metals for which the electronic density varies slowly) have been

successfully predicted. The LDA generally underestimates bond distances and overestimates the cohesive energies. The inclusion of the gradient of the density, allows GGA to be more accurate in predicting the structural parameters, such as the bond length and angles, with a tendency to overestimating them. In this thesis, we use this parametrization for the exchange-correlation term to study the ground-state properties of our system (stacked bulk h-BN and graphene/h-BN vdW heterostructures) since the in-plane bonds of h-BN exhibit a polar nature.

The limitations of the LDA and GGA approximations (and other functionals based on the local density and its derivatives) when calculating the structural parameters, is the treatment of systems in which non-local correlations are important. This is typically the case for Van der Waals interactions. In this thesis, additional methods to account for vdW forces will be used (see subsection 2.4.2).

Band-gap

The knowledge of the size and the nature of the band gap is the first requested information for optoelectronic applications of any material. The fundamental band gap is given by the different between the smallest removal energy (ionization) and the largest addition energy (affinity) of an electron. They can be experimentally measured by photoemission and inverse photoemission techniques, respectively. As a shown in Fig. 2.3, the gap is expressed as follows:

$$E_{gap} = I(N) - A(N) = E(N+1) - 2E(N) + E(N-1), \tag{2.21}$$

In one hand, the minimal ionization energy in an N-electron system is given by the highest occupied Kohn-Sham eigenvalue ε_N [162–164]. On the other hand, the first ionization energy of N+1 system is equivalent to the maximal electron affinity energy of an N electron system. As result, the fundamental band gap can be expressed as:

$$\begin{aligned}
&E_{gap} = I(N) - I(N+1), \qquad \text{with}: \quad \varepsilon_N^{KS}(N) = -I(N), \\
&E_{gap} = \varepsilon_{N+1}^{KS}(N+1) - \varepsilon_N^{KS}(N), \\
&E_{gap} = \varepsilon_{N+1}^{KS}(N+1) \underbrace{-\varepsilon_N^{KS}(N) + \varepsilon_{N+1}^{KS}(N)}_{E_{gap}^{KS}} - \varepsilon_{N+1}^{KS}(N), \\
&E_{gap} = E_{gap}^{KS} + \triangle_{XC}.
\end{aligned} \tag{2.22}$$

While the difference between the highest occupied and the lowest unoccupied Kohn-Sham states represent the E_{gap}^{KS}, the $\triangle_{XC}$ term shows that the E_{gap}^{KS} cannot be the fundamental band gap of the system. This term reflects also the discontinuity of the exchange-correlation functional with respect to the particle number. In general, depending on the system, the resulting band gaps from DFT calculations (using LDA or GGA) are usually

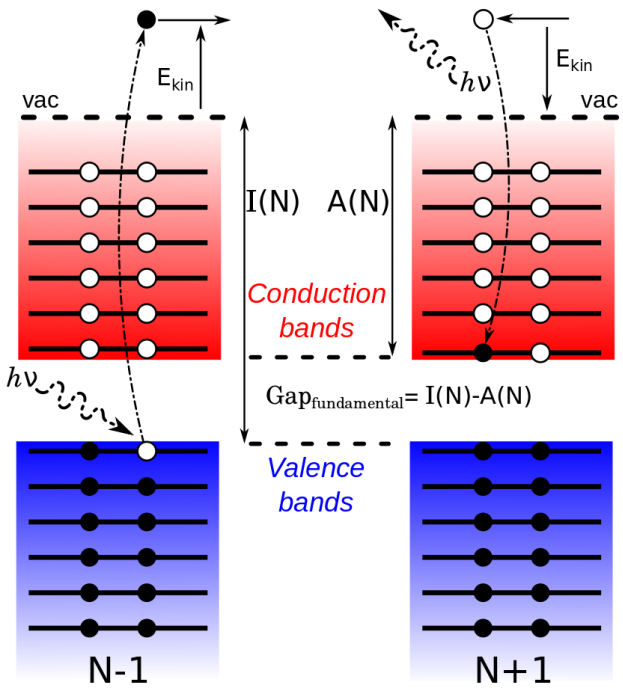

Figure 2.3: Schematic representation of the relationship between the fundamental gap and the photo-emission processes, direct (N-1) and inverse (N+1).

underestimated by up to 80% with respect to the experimental ones. This problem of the band-gap is directly related to the K-S formalism. To overcome such a problem one has to go beyond the DFT, to the many-body perturbation theory.

2.3 Many-body perturbation theory (MBPT)

Nowadays, the many-body perturbation theory presents a powerful way to describe the excited-state properties of materials. Instead of the non-interacting system as in DFT, the MBPT approach introduces the quasi-particle concept where the interactions with the neighboring particles are taken into account. The excited-state properties are successfully described by the Green's function method. In case of charged systems, the single-particle Green's function is successfully used to characterize the direct and inverse photo-emission processes, giving access to the quasiparticle excitation energies. The Green's function is also used to describe the neutral excitation. In this case the absorbed photon excites the quasi-electron to the higher states without leaving the interacting system, making the optical absorption process. The interaction with the remaining quasi-hole, which represents the empty valence state, is described by the two-particles Green's function. Finally, the solution of the single and two-particles' equations of motion, which are the Dyson and Bethe-Salpeter equations, respectively, give access to the excited-state properties (band gap, quasi-particle band structures, absorption spectra, excitons wave-functions, etc).

In this section, we introduce briefly the one- and the two-particles Green's function. In addition, we present the practical resolution of their equations of motion (GW approximation, Bethe-Salpeter equation, respectively) while the details can be found in Refs. [165–170]. These tools are used in this thesis to investigate the excited-state properties of our systems.

2.3.1 The one-particle Green's function

The single particle Green's function is defined as follows:

$$G(1,2) = -i\langle\Phi_0|\hat{T}\left[\hat{\psi}(1)\hat{\psi}^\dagger(2)\right]|\Phi_0\rangle, \tag{2.23}$$

$$\text{with :} \quad \begin{cases} \Phi_0 : \text{is the many} - \text{body N particle gound} - \text{state}, \\ (1,2) : \text{compact notation of } (\mathbf{r}_1, t_1, \mathbf{r}_2, t_2), \end{cases}$$

$\hat{T}$ is the time ordering operator, such that the first operator is the one at later time.

$$\hat{T}\left[\hat{\psi}(1)\hat{\psi}^\dagger(2)\right] = \begin{cases} \hat{\psi}(1)\hat{\psi}^\dagger(2) & t_1 > t_2, \\ -\hat{\psi}^\dagger(2)\hat{\psi}(1) & t_1 < t_2. \end{cases} \tag{2.24}$$

$\hat{\psi}^\dagger$ and $\hat{\psi}$ are the creation and annihilation field operators, respectively, and the one-particle Green's function $G(1,2)$ represents the probability amplitude for propagating electron (hole) from position $\mathbf{r}_2$ ($\mathbf{r}_1$) at time t_2 (t_1) to the position $\mathbf{r}_1$ ($\mathbf{r}_2$) at time t_1 (t_2) for $t_1 > t_2$ ($t_1 < t_2$). This propagation describes the inverse photoemission (direct photoemission) processes, since it represents the probability to find an electron (hole) at position $\mathbf{r}_1$ ($\mathbf{r}_2$) at time t_1 (t_2) when an electron is added (removed) in $\mathbf{r}_2$ ($\mathbf{r}_1$) position at time t_2 (t_1). By considering the charged systems with N+1 (N-1) electrons, we show how the excitation energies are related to the one-particle Green's function. After Fourier transformation with respect to time, the Lehman presentation [171] of the Green's function is written as follows:

$$G(\mathbf{r}_1, \mathbf{r}_2, \omega) = \sum_i \frac{\phi_i(\mathbf{r}_1)\phi_i^*(\mathbf{r}_2)}{\omega - \varepsilon_i + i\eta\,\mathrm{sgn}(\varepsilon_\mathrm{i} - \mu)}, \tag{2.25}$$

$$\text{with :} \quad \phi_i(\mathbf{r}) = \begin{cases} \langle\Phi_0|\hat{\psi}(\mathbf{r})|\Phi^i_{N+1}\rangle, & \varepsilon_i = E^i_{N+1} - E^0_N, \quad \text{if} \quad \varepsilon_i > \mu, \\ \langle\Phi^i_{N-1}|\hat{\psi}(\mathbf{r})|\Phi_0\rangle, & \varepsilon_i = E^0_N - E^i_{N-1}, \quad \text{if} \quad \varepsilon_i < \mu. \end{cases} \tag{2.26}$$

Here, $E^i_{N\pm1}$ and $\langle\Phi^i_{N\pm1}|$ correspond to the i$-th$ state of the $N \pm 1$ particle system. The excitation energies ε_i of the N particle system due to the addition or removal of a particle represent the poles Green's function. The term η is a positive infinitesimal and μ represents the Fermi energy of the system. The equation of motion of the one-particle Green's

function is given by the time-evolution $\frac{\partial G(1,2)}{\partial t}$ as follows [165]:

$$\left[i\frac{\partial}{\partial t_1} - h_0(\mathbf{r}_1)\right] G(1,2) = \delta(1,2) - i\int d3\, v(1,3) G_2(1,3^+;2,3^{++}), \tag{2.27}$$

$$\text{with :} \quad \begin{cases} h_0(\mathbf{r}_1) = -\frac{1}{2}\nabla_1^2 + v_{ext}(\mathbf{r}_1) & \text{is the independent particle Hamiltonian,} \\ + & \text{positive and infinitesimal additional time,} \\ v & \text{is the Coulomb potential,} \\ G_2 & \text{is the two} - \text{particles Green function.} \end{cases}$$

In this way, the one-particle Green's function G depends on the two-particles Green's function (G_2), and the G_2 depends on three-particles Green's function (G_3) and so on. Since in this part we are interested in the one-particle Green's function, the *self-energy* operator Σ is introduced to express approximately the two-particles Green's function G_2 in terms of the one-particle Green's function and to cut the hierarchy of the Green's functions [165]. This operator contains the electron-electron interaction part (exchange and correlation). Consequently, the resulting equation of motion depends only on the one-particle Green's function:

$$\left[i\frac{\partial}{\partial t_1} - h_0(\mathbf{r}_1) - v_H(1)\right] G(1,2) = \delta(1,2) - i\int d3\Sigma(1,3) G(3,2). \tag{2.28}$$

In case where $\Sigma = 0$, this equation describe the motion of independent particle as follows:

$$\left[i\frac{\partial}{\partial t_1} - h_0(\mathbf{r}_1) - v_H(1)\right] G_0(1,2) = \delta(1,2), \tag{2.29}$$

with $G_0(1,2)$ representing the independent particle Green's function. The resulting equation of motion of the one-particle Green's function, called the *Dyson equation*, is expressed as:

$$G(1,2) = G_0(1,2) + \int d3d4\, G_0(1,3)\Sigma(3,4)G(4,2). \tag{2.30}$$

Using the Lehman representation of the Green's function, the quasi-particle Schrödinger-like equation is written as follows:

$$\left[h_0(\mathbf{r}_1) + v_H(\mathbf{r}_1)\right]\phi_i^{QP}(\mathbf{r}_1) + \int \Sigma(\mathbf{r}_1, \mathbf{r}_2, \varepsilon_i^{QP})\phi_i^{QP}(\mathbf{r}_2) d\mathbf{r}_2 = \varepsilon_i^{QP}\phi_i^{QP}(\mathbf{r}_1), \tag{2.31}$$

where ε_i^{QP}, ϕ_i^{QP} are the quasi-particle eigenvalue and wave-function, respectively. This expression looks like the Kohn-Sham equation (see Eq. 2.16), however, instead the v_{XC}, in this case it contains the *self-energy* operator Σ. This operator is non-local and includes the many-body exchange and correlation interactions with other electrons in the system. In the following, we present briefly the Hedin's equations [168] which describe the Σ operator, and the practical scheme G_0W_0 approximation.

2.3.2 Hedin's equations

Hedin's equations allow us to describe the *self-energy* operator Σ exactly in order to solve the full interacting Green's function. In addition to the Dyson equation (Eq. 2.30), Hedin's scheme contains four other equations [168], which are: the *self-energy* Σ, irreducible polarizability P, screened Coulomb potential W and the vertex function Γ.

$$G(1,2) = G_0(1,2) + \int d(34) G_0(1,3)\Sigma(3,4)G(4,2), \tag{2.32}$$

$$\Sigma(1,2) = i\int d(34) G(1,4)W(1^+,3)\Gamma(4,2;3), \tag{2.33}$$

$$W(1,2) = v(1,2) + \int d(34) v(1,3)P(3,4)W(4,2), \tag{2.34}$$

$$\Gamma(1,2;3) = \delta(1,2)\delta(1,3) + \int d(4567)\frac{\delta\Sigma(1,2)}{\delta G(4,5)}G(4,6)G(7,5)\Gamma(6,7;3), \tag{2.35}$$

$$P(1,2) = -i\int d(34) G(1,3)G(4,1)\Gamma(3,4;2). \tag{2.36}$$

With:

- G, G_0 are the one-particle and independent particle Green's function, respectively.
- P is the irreducible polarizability which represents the variation of the electronic density with respect to the total classical (external and Hartree) potential ($P(1,2) = \frac{\delta n(1)}{\delta v_{tot}(2)}$).
- W represent the screened Coulomb interaction.

The Hedin's equations (Eq. 2.32-2.36) are presented in Fig. 2.4 as an interconnected pentagon. The exact solution can be reached by solving these equations self-consistently starting with an initial guess for one of these equations. However, this iterative resolution is not possible in practice, and approximations are needed.

2.3.3 The GW approximation

The GW approximation consists of setting the vertex function to unity ($\Gamma(1,2,3) \approx \delta(1,3)\delta(1,2)$), see Fig. 2.4. The self-consistent calculation of the reduced cycle (scGW) is still a hard task. In practice, in many cases DFT provides already a good approximation for the quasiparticle wave-functions. In this case, one can treat Σ operator as a perturbation and obtain the quasiparticle energies after first iteration (see G_0W_0 scheme in Fig. 2.4) [172–174]. The resulting Hedin's equations are expressed as following:

$$\begin{cases} P_0(1,2) = -iG_0(1,2)G_0(2,1), \\ W_0(1,2) = v(1,2) + \int d(34) v(1,3)P_0(3,4)W_0(4,2), \\ \Sigma(1,2) = iG_0(1,2)W_0(1^+,2). \end{cases} \tag{2.37}$$

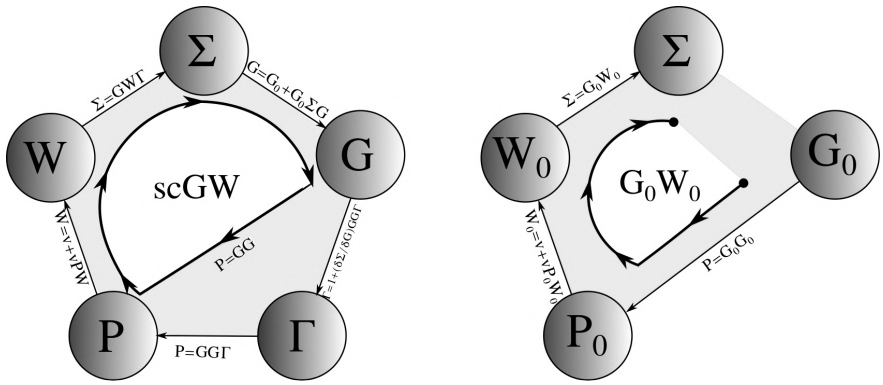

Figure 2.4: (Left): Pentagon schematic of Hedin's equations and the self-consistent GW approximation where the vertex Γ is set to the unity. (Right) sketch of the first GW cycle, named G_0W_0, which starts from the Kohn-Sham Green's function G_0.

Starting from the Kohn-Sham energies and wave-functions (ε_i^{KS}, ϕ_i^{KS}), G_0 is constructed, using Eq. (2.25). Then, following the (2.37) cycle, *self-energy* is evaluated. The resulting G_0W_0 eigenvalue [174, 175] are obtained by:

$$\varepsilon_i^{QP} = \varepsilon_i^{KS} + \langle \phi_i^{KS} | \Sigma(\varepsilon_i^{QP}) - v_{XC}^{KS} | \phi_i^{KS} \rangle. \tag{2.38}$$

For the v_{XC}^{KS}, in this thesis, we use the one given by GGA-PBE [176]. The dependence of the *self-energy* on the ε_i^{QP} is given by the first order expansion of the Σ around ε_i^{KS} as follows:

$$\Sigma(\varepsilon_i^{QP}) = \Sigma(\varepsilon_i^{KS}) + (\varepsilon_i^{QP} - \varepsilon_i^{KS}) \frac{\partial \Sigma(\omega)}{\partial \omega}\Big|_{\omega=\varepsilon_i^{KS}}, \tag{2.39}$$

As discussed in the last sections, the DFT formalism cannot be accurate in predicting the excitation energies and the band gap. However, the quasi-particle picture in the many-body perturbation theory provide a valid approach (Green's functions) to access the excitation energies. By introducing the non-local self-energy operator, the many-body exchange and correlation interactions with other electrons in the system are included. Nowadays, the G_0W_0 approximation is successfully applied to predict the excitation energies of materials [173, 174]. In this thesis, in order to calculate the electronic properties (excitation energies, band gap), in stacked bulk h-BN and graphene/h-BN vdW heterostructures, we use the G_0W_0 approximation starting from the GGA-PBE calculations (ε_i^{KS}, ϕ_i^{KS}) [174].

2.3.4 The two-particles Green's function

The one-particle Green's function (electron or hole propagator), as shown in the previous section, allows to describe the photoemission, and the inverse photoemission processes, and access the excitation energies. However, in case of a neutral excitation where the excited electron (leaving a hole in the valence state) occupies a previously empty state (energetically higher), the phenomenon cannot be described by the one-particle Green's

function, since we have two different particles (electron and hole) simultaneously. This phenomenon is known as the absorption process where the excited electron interacts with the remaining hole to create an exciton (excitonic effects). Consequently, in order to describe this effect, the two-particles Green's function G_2 is introduced as a two-particles propagator which accounts for the electron-hole interaction and their individual motions, as follows:

$$G_2(1,2;1^{'},2^{'}) = -\langle\Phi_0|\hat{T}\left[\hat{\psi}(1)\hat{\psi}(2)\hat{\psi}^{\dagger}(2^{'})\hat{\psi}^{\dagger}(1^{'})\right]|\Phi_0\rangle. \tag{2.40}$$

However, to describe only the electron-hole interaction, the two-particles correlation function L is introduced such that the individual motion of the two-particles (GG product) is excluded from the G_2 Green's function, written as:

$$L(1,1^{'},2,2^{'}) = G_2(1,1^{'},2,2^{'}) - L_0(1,1^{'},2,2^{'}), \tag{2.41}$$

with $L_0(1,1^{'},2,2^{'}) = G(1^{'},2^{'})G(1,2)$ represent the independent e-h polarizability which describes their uncorrelated motions. The Dyson-like equation of motion of the two-particles Green's function in this case, called "Bethe-Salpeter equation", is expressed as follow:

$$L(1,1^{'},2,2^{'}) = L_0(1,1^{'},2,2^{'}) + i\int d(33^{'}44^{'})L_0(1,1^{'},3,3^{'})\Xi(3,3^{'},4,4^{'})L(4,4^{'},2,2^{'}). \tag{2.42}$$

This equation describes the propagation of the interacting e-h pair in a many-body system. The kernel Ξ, which relates the non-interacting quasiparticle L_0 and the interacting one L, contains the interacting part of the two-particles (e-h) system. It is given by the functional derivative of the *self-energy*[2] Σ and the Hartree energy with respect to the one-particle Green's function, as follows:

$$\Xi(3,3^{'},4,4^{'}) = \frac{\delta[v_H(4,4^{'}) + \Sigma(4,4^{'})]}{\delta G(3,3^{'})},$$

$$= -i\,\delta(3,3^{'})\,\delta(4,4^{'})\,v(3,4) + \frac{\delta\Sigma(4,4^{'})}{\delta G(3,3^{'})}, \tag{2.43}$$

$$= \underbrace{-i\,\delta(3,3^{'})\,\delta(4,4^{'})\,v(3,4)}_{\text{Exchange term (repulsive)}} + \underbrace{i\,\delta(3,4)\,\delta(3^{'},4^{'})W(3,3^{'})}_{\text{Correlation term (attractive)}} + \underbrace{iG(1,2)\frac{W(1,2)}{\delta G(4,3)}}_{neglected}. \tag{2.44}$$

The first term (exchange) is the e-h repulsion interaction due to the unscreened Coulomb potential (represents the independent motion of the particles, electron and hole, in an effective potential). The second term is the attractive e-h correlation corresponding to the screened Coulomb potential which is responsible for the formation of the bound e-h pair (exciton). As an approximation, the third term which describes the variation of the self-energy with respect to the Green's function is neglected.

[2]In this thesis, the *self-energy* Σ is given by the G_0W_0 approximation discussed previously ($\Sigma = iGW$).

2.3.5 Effective two-particles Bethe-Salpeter equation (BSE)

In this part we present the solution of the previous BSE equation, where all details (ingredients, approximations and procedure) can be found in Ref. [165–167, 169, 170, 172]. The resulting BSE eigenvalue problem is expressed as follows:

$$\sum_{v'c'\mathbf{k}'} H^{e-h}_{vc\mathbf{k},v'c'\mathbf{k}'} A^{\lambda}_{v'c'\mathbf{k}'} = E^{\lambda} A^{\lambda}_{vc\mathbf{k}}, \tag{2.45}$$

where, c and v are the valence and conduction band states, respectively. The resulting eigenvalues E^{λ} are the excitation energies for each λth exciton (e-h pair). As discussed in the following, all information about the exciton (oscillator strengths, exciton weight, exciton wave-function, etc) as well as the absorption spectrum depends on the eigenvectors A^{λ}.

Now, the resulting effective two-particles (e-h) BSE Hamiltonian is written as follows:

$$H^{e-h} = H^{diag} + \gamma_{dir} H^{dir} + \gamma_x H^x. \tag{2.46}$$

With:

$$\begin{cases} H^{diag}_{vc\mathbf{k},v'c'\mathbf{k}'} = (\varepsilon^{QP}_{c\mathbf{k}} - \varepsilon^{QP}_{v\mathbf{k}})\delta_{vv'}\delta_{cc'}\delta_{\mathbf{k}\mathbf{k}'}, \\ H^{dir}_{vc\mathbf{k},v'c'\mathbf{k}'} = -\int d\mathbf{r}d\mathbf{r}'\psi_{v\mathbf{k}}(\mathbf{r})\psi^*_{c\mathbf{k}}(\mathbf{r}')W(\mathbf{r},\mathbf{r}')\psi^*_{v'\mathbf{k}'}(\mathbf{r})\psi_{c'\mathbf{k}'}(\mathbf{r}'), \\ H^{x}_{vc\mathbf{k},v'c'\mathbf{k}'} = \int d\mathbf{r}d\mathbf{r}'\psi_{v\mathbf{k}}(\mathbf{r})\psi^*_{c\mathbf{k}}(\mathbf{r})\bar{v}(\mathbf{r},\mathbf{r}')\psi^*_{v'\mathbf{k}'}(\mathbf{r}')\psi_{c'\mathbf{k}'}(\mathbf{r}'). \end{cases} \tag{2.47}$$

The H^{diag} contains only the differences between quasiparticle energy ε^{QP}_i of the valence (v) and conduction (c) states (account for vertical transitions) which gives the independent quasiparticle approximation (IQPA) spectrum. The direct term H^{dir}, labeled also H^c for the correlation, contains the e-h attractive term given by the screened Coulomb interaction W. The third term (H^x) represents the repulsive exchange part of the e-h pairs which is given by the bare Coulomb interaction without the long-range part ($\bar{v}$).

In the next chapters, in order to analyze the optical absorption of our systems, we present the absorption spectrum given by the IQPA ($\gamma_{dir} = \gamma_x = 0$ in Eq. 2.46) which explicitly ignores the e-h interactions (excitonic effects) together with the one given by the full BSE Hamiltonian H^{e-h} ($\gamma_{dir} = \gamma_x = 1$ in Eq. 2.46) which takes into account the excitonic effects.

The absorption spectrum, represented by the imaginary part of the macroscopic dielectric function, is defined as following:

$$\mathrm{Im}\varepsilon_M = \frac{8\pi^2}{\Omega}\sum_{\lambda} |\mathbf{t}_{\lambda}|^2 \delta(\omega - E^{\lambda}), \tag{2.48}$$

with Ω is the unit cell volume. The oscillator strength is given by the the square modulus

of $\mathbf{t}_\lambda$ as follows:

$$\mathbf{t}_\lambda = \sum_{vc\mathbf{k}} A^\lambda_{vc\mathbf{k}} \frac{\langle v\mathbf{k}|\widehat{\mathbf{p}}|c\mathbf{k}\rangle}{\epsilon_{c\mathbf{k}} - \epsilon_{v\mathbf{k}}}. \tag{2.49}$$

where the eigenvectors A^λ provide information about the intensity of the excitations. In the reciprocal space, the $\mathbf{k}$-resolved contributions of individual quasi-particle bands to the electron-hole pairs are given also by the eigenvectors A^λ. The *weight* of each transition between valence and conduction states at a given $\mathbf{k}$-point, is defined as:

$$w^\lambda_{v\mathbf{k}} = \sum_c |A^\lambda_{vc\mathbf{k}}|^2, \;\; w^\lambda_{c\mathbf{k}} = \sum_v |A^\lambda_{vc\mathbf{k}}|^2, \tag{2.50}$$

these equations allow to determine the origin of each exciton in band structures. The eigenvectors A^λ indicate also the character and the composition of excitations, being the coefficients of the two-particles (e-h) wave-function:

$$\Psi^\lambda(\mathbf{r}_h, \mathbf{r}_e) = \sum_{vc\mathbf{k}} A^\lambda_{vc\mathbf{k}} \psi_{v\mathbf{k}}(\mathbf{r}_h)\psi^*_{c\mathbf{k}}(\mathbf{r}_e), \tag{2.51}$$

it depends on both positions of the two-particles (e-h), $\mathbf{r}_h$ and $\mathbf{r}_e$. In order to visualize the spatial distribution of the excited electron (probability to find the electron), we plot the square modulus of the e-h wave-function by fixing the hole position. We notice that, in contrary the Kohn-Sham states that retain the crystal periodicity, excitonic wave-functions are non-periodic. Therefore, one must consider a large supercell for such visualization.

DFT vs. MBPT approach

To summarize the two last approaches (DFT and MBPT) and their degrees of success, in Fig. 2.5 we compare the resulting physical quantities of these approaches. We have seen that the DFT, as a ground-state theory, is not suitable to produce reliable band structures. At this level, the resulting spectrum from the inter-band transitions of independent particles starts from the DFT gap (see Fig. 2.5.a). However, the one-particle Green's function allows to access the excited-state energies taking into account the weak interaction with the surrounding electrons (quasi-particle). We have shown that this consideration is practical within the GW approximation which allows to access the fundamental gap (in agreement with experimental results) and band structure, within the quasi-particle picture. We notice that the G_0W_0 approach shows a small underestimation on the band gap with respect to the experimental one due to the considered approximations discussed above. In this case the inter-band transitions spectrum of the independent quasi-particle states is blue-shifted to the GW gap (see Fig. 2.5.b). Finally, the two-particles Green's function allows to account for the interaction between the quasi-electron and its remaining quasi-hole. At this level the considered excitonic effects red-shifts the absorption spectrum below the GW gap, where bound exciton (e-h pair) is formed. The excitation

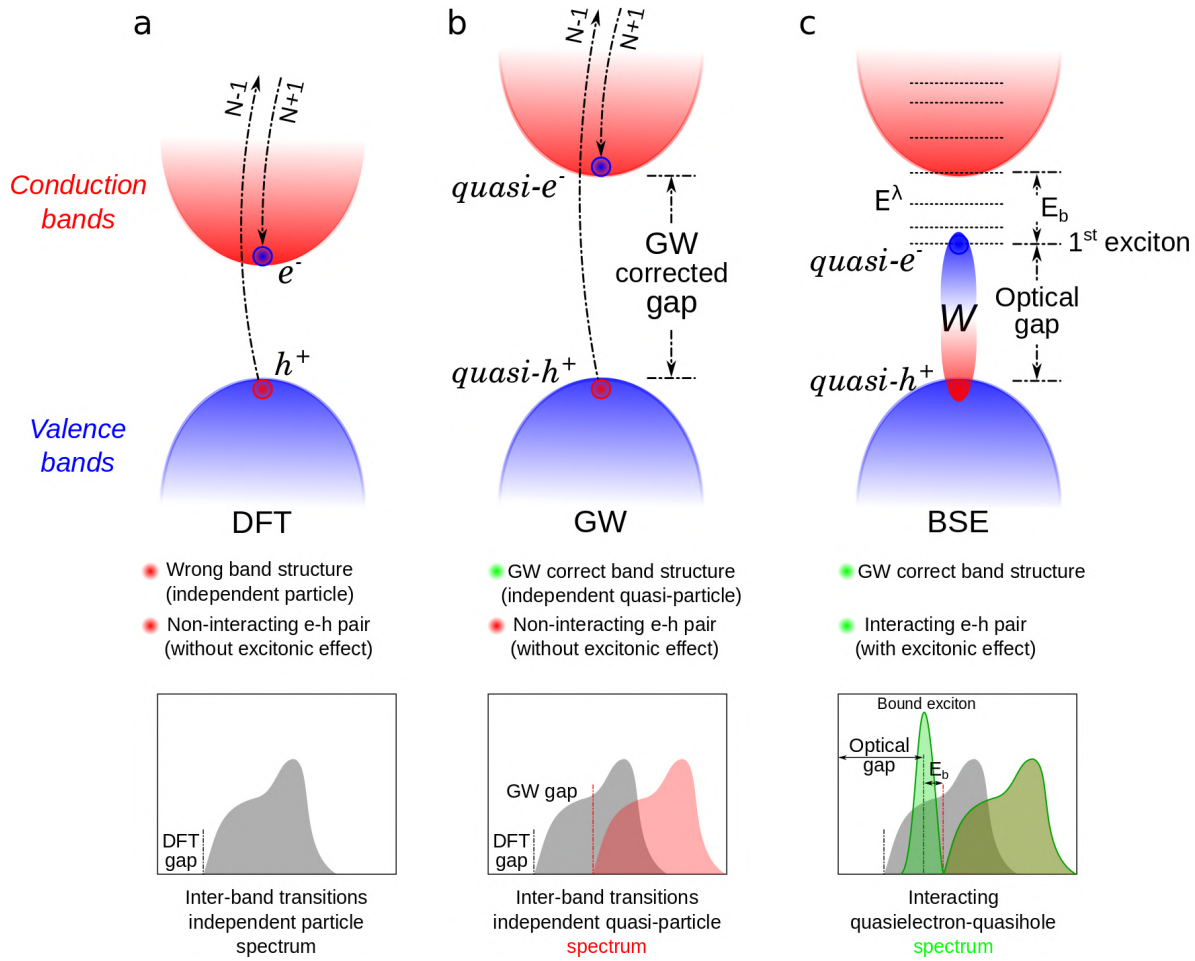

Figure 2.5: Schematic representation of the three level of approximations and their degree of success, from: (a) Independent particle DFT approach which underestimate the band gap to the (b) independent quasi-particle GW approximation where the corrected band gap agree with the experimental results. (c) The correlated quasi-electron and quasi-hole in BSE calculation provide a closer approach to the many-body system which is successfully applied to describe the absorption spectra with good agreement with the experimental counterpart.

energy of this exciton represents the optical gap, while the red-shift with respect to the GW gap (minimum direct gap) represents the e-h binding energy (see Fig. 2.5.c). The resulting spectra from the BSE solutions shows a very good agreement with the experimental measurements since most many body effect are basically included [177].

Starting from the ground-state DFT calculation, in this thesis, we investigate the excited-state properties of our systems through the presented MBPT (GW and BSE) approach. In the following section, we present the numerical methods within the `exciting` code as well as the computational scheme and details.

2.4 Numerical methods and computational details

2.4.1 Numerical methods within the `exciting` code

All calculation, in this thesis, are performed using `exciting`, an all-electron full-potential code implementing the family of linearized augmented plane-wave plus local orbitals, (L)APW+lo, methods [178]. (L)APW+lo is known as one of the most accurate methods for solving the Kohn-Sham equations. [179]. In addition to the ground-state DFT calculations, `exciting` allows access to the excited-state properties within the MBPT (G_0W_0 and BSE) approach [169, 174].

(L)APW+lo bases

To solve the Kohn-Sham equation (Eq. 2.16) in practice, the wave-functions are expanded as follows:

$$\psi_i^{KS}(\mathbf{r}) = \sum_G C_{i\mathbf{G}}^{\mathbf{k}} \phi_{\mathbf{G}+\mathbf{k}}(\mathbf{r}). \tag{2.52}$$

APW approach

Since the wave-functions varies rapidly near the nuclei (core region) and more smooth and slowly between the atoms, the APW method [180] defines two different region in the unit cell: (i) the interstitial (I) zone between atoms and (ii) *muffin-tin* (MT) sphere around the nuclei (see Fig. 2.6). The basis functions of these zone are described by: (i) planewaves and (ii) a linear combination of the atomic-like orbitals, as follows:

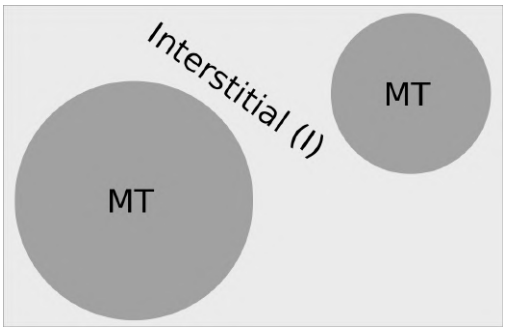

Figure 2.6: Separation into interstitial (I) and *muffin-tin* (MT) region of the unit cell.

$$\phi_{\mathbf{G}+\mathbf{k}}^{APW}(\mathbf{r}) = \begin{cases} \sum_{lm} A_{lm\alpha}^{\mathbf{G}+\mathbf{k}} u_{l\alpha}(r_\alpha, \varepsilon) Y_{lm}(\hat{\mathbf{r}}_\alpha), & r_\alpha \leq R_{MT}^\alpha, \\ \frac{1}{\sqrt{\Omega}} e^{i(\mathbf{G}+\mathbf{k})\mathbf{r}}, & \mathbf{r} \in I, \end{cases} \tag{2.53}$$

with R_{MT}^α is the *muffin-tin* radius of the atoms α positioned at R_α, the matching coefficients $A_{lm\alpha}^{\mathbf{G}+\mathbf{k}}$ are constructed to ensure the continuity of the wave-functions at the boundary between the I and MT regions. The augmented planwaves in the MT region are formed by the radial function $u_{l\alpha}(r_\alpha)$, which depends on the energy, and the spherical harmonics $Y_{lm}(\hat{\mathbf{r}}_\alpha)$. The main drawback of APW approach is this dependence on energy which leads to the non-linear eigenvalue problem. To remedy this, the linearized augmented planewaves (LAPW) method is introduced [181].

(L)APW and APW+lo methods

The LAPW method consider the energies ε as parameters and expand the radial function $u_{l\alpha}(r_\alpha)$ around ε_l, defined as:

$$u_{l\alpha}(r_\alpha,\varepsilon) = u_{l\alpha}(r_\alpha,\varepsilon_l) + \dot{u}_{l\alpha}(r_\alpha,\varepsilon_l)(\varepsilon-\varepsilon_l), \quad \text{with}: \quad \dot{u}_{l\alpha}(r_\alpha,\varepsilon_l) = \frac{\partial u_{l\alpha}(r_\alpha,\varepsilon_l)}{\partial\epsilon}|_{\varepsilon=\varepsilon_l} \tag{2.54}$$

The resulting LAPW basis is written as following:

$$\phi^{LAPW}_{\mathbf{G+k}}(\mathbf{r}) = \sum_{lm}\left[A^{\mathbf{G+k}}_{lm\alpha}u_{l\alpha}(r_\alpha,\varepsilon_{l\alpha}) + B^{\mathbf{G+k}}_{lm\alpha}\,\dot{u}_{l\alpha}(r_\alpha,\varepsilon_{l\alpha})\right]Y_{lm}(\hat{\mathbf{r}}_\alpha), \qquad r_\alpha \leq R^\alpha_{MT}, \tag{2.55}$$

with $A^{\mathbf{G+k}}_{lm\alpha}$ and $B^{\mathbf{G+k}}_{lm\alpha}$ to ensure the continuity of the wave-functions at the boundary between the I and MT regions. In addition to the LAPW method, `exciting` code implement also the APW+lo method [182] where local orbitals are added to the APW functions (Eq. 2.53) in the MT region, as follows:

$$\psi^{KS}_i(\mathbf{r}) = \sum_G C^{\mathbf{k}}_{i\mathbf{G}}\phi_{\mathbf{G+k}}(\mathbf{r}) + \sum_\mu C^{\mathbf{k}}_{i\mu}\phi_\mu(\mathbf{r}), \tag{2.56}$$

where, $\phi_{\mathbf{G+k}}(\mathbf{r})$ and $\phi_\mu(\mathbf{r})$ are the APW bases and the local orbitals, respectively. More detail about these methods as well as the procedure to solve the KS equation can be found in Ref. [178].

2.4.2 Computational details

In order to investigate the ground- and excited-state properties of our systems, lattice optimization and atomic relaxation are needed. The vdW nature of the investigated systems request to account for the vdW interaction during the minimization of the total energy of the systems. Then, the resulting Kohn-Sham energies and wave-functions are used as starting point for the electronic G_0W_0 correction. Finally, the optical properties (absorption spectra, exciton wave-functions, etc) are given by solving the BSE equation using the quasi-particle G_0W_0 results. In this section we present the computational details of each steps, summarized in Fig. 2.7. We notice that the detail of each parameter (meaning and how to converge) can be found in the `exciting` website [183] and in Ref. [178].

DFT calculations

Ground-state properties are computed in the framework of density functional theory (DFT), within the generalized gradient approximation for the exchange-correlation functional (Perdew-Burke-Ernzerhof parameterization [176]). Lattice constants and internal coordinates are optimized until the residual forces on each atom are smaller than 0.003

eV/Å. The Broyden–Fletcher–Goldfarb–Shanno (BFGS) method [184] is used for the atomic relaxations during the optimization of the in- and out-of plane lattice parameters. Owing to the vdW nature of our systems, in this thesis we use the different vdW methods implemented in `exciting` code. The DFT-D2 proposed by S. Grimme [185] is used for minimizing energy in graphene/h-BN vdW heterostructures system which account for the vdW interaction between layers. In case of h-BN, the structural parameters have obtained using the vdW-TS [186] and the binding energies by using the DFT-D2 [185], to account for vdW interaction. We notice that this choice is due to the accuracy of the vdW-TS in predicting the interlayer distance. However, this method is known to overestimate the binding energy [194]. For this reason we use the DFT-D2 method in order to evaluate it in bulk h-BN. More details about the vdW-TS and DFT-D2 methods can be found in these Refs. [185, 186, 194, 197]. As shown in Fig.2.7, the optimization procedure (e.g., to optimize c-parameter) is as follows: (i) the BFGS method is used to relax the internal coordinate of the atoms for each c value, (ii) the resulting total energy of each KS cycle during the BFGS relaxation is corrected by one of these vdW methods, then (iii) collecting the minimized energies for different c value, we found the optimized structure.

In the ground-state calculations, a converged basis-set cutoff $R_{MT}G_{max}$=7 is used. For all atomic species involved in our systems, namely boron (B), nitrogen (N), and carbon (C), a *muffin-tin* radius R_{MT}=1.3 bohr is adopted. Within the (L)APW+lo method the 1s electrons of these atomic species are treated as core electrons, while the 2s2p electrons represent the valence part. The sampling of the Brillouin zone (BZ) is performed with a $36 \times 36 \times 14$ **k**-grid for the stacked bulk h-BN and with $30 \times 30 \times 8$ **k**-grid in case of the graphene/h-BN vdW heterostructures.

G_0W_0 correction

Calculations of the QP correction to the Kohn-Sham eigenvalues within the G_0W_0 approximation [174] are performed with 250 empty states and a BZ sampling with a $18 \times 18 \times 6$ shifted **k**-mesh is adopted for the stacked bulk h-BN (see convergence tests in Appendix A) and $18 \times 18 \times 4$ shifted **k**-mesh for the graphene/h-BN vdW heterostructures (see convergence tests in Appendix B). It is worth noting that the GW results presented in the manuscript are obtained by shifting the k-mesh from the Γ point, in order to improve the quality of the BZ sampling (avoid any reduction in the number of k-point for symmetry reason) also in the subsequent BSE calculations. The resulting quasi-particle energies and wave-functions are then used to build the main parts of the BSE calculation (the non interacting quasiparticle L_0, the Kernel Ξ,...), see Fig. 2.7.

BSE calculation

For the solution of the BSE [187] within the Tamm-Dancoff approximation a cutoff $R_{MT}G_{max}$=6 and a $24 \times 24 \times 8$ shifted **k**-point mesh are used for the stacked bulk h-BN systems (see

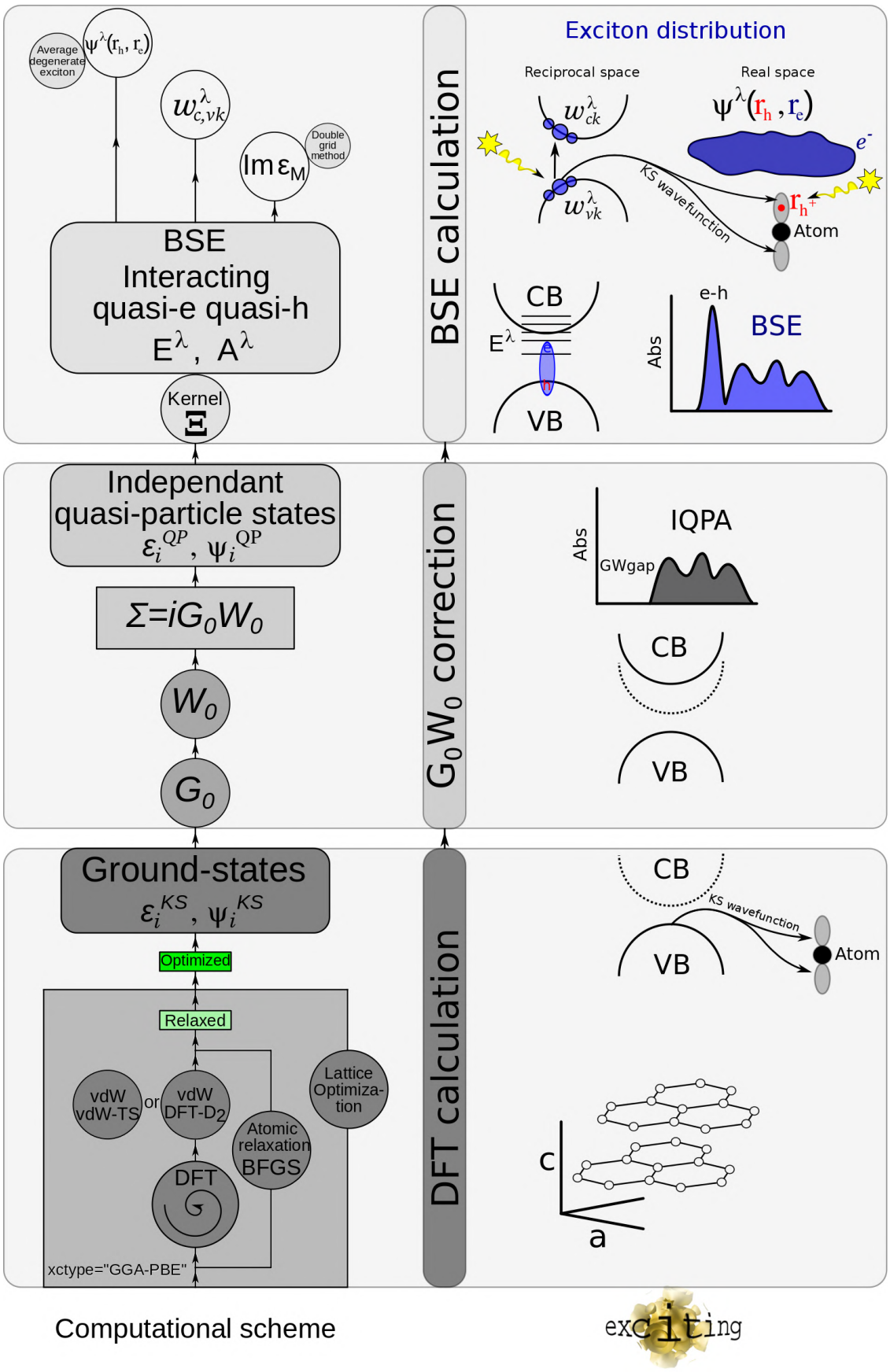

Figure 2.7: Schematic representation of the followed computational scheme and the resulting physical quantities, while most details are presented in this subsection.

convergence tests in Appendix A, Fig. A.1). Likewise, in order to converge the absorption spectra of the graphene/h-BN vdW heterostructures, a cutoff $R_{MT}G_{max}$=6 and a 30 $\times$ 30 $\times$ 4 shifted **k**-point mesh are adopted. Owing to the high dispersion around the graphene Dirac-cone, the latter sampling is interpolated onto a 60 $\times$ 60 $\times$ 4 mesh, using the so-called double grid technique [188, 189] (see convergence tests and detail about the used interpolation in Appendix B). In the calculation of the response function and of the screened Coulomb potential 100 empty bands are included.

In the construction and diagonalization of the BSE Hamiltonian 4 occupied and 4 unoccupied bands are considered in the stacked bulk h-BN systems (see Fig. A.1 in Appendix A). In case of graphene/h-BN vdW heterostructures, a 3 occupied and 3 unoccupied bands are taken into consideration to converge the spectra within the desired energy window (see Appendix B). Local-field effects are taken into account by including 25 $|\mathbf{G}+\mathbf{q}|$ vectors (for stacked bulk h-BN) and 41 $|\mathbf{G}+\mathbf{q}|$ vectors for the graphene/h-BN vdW heterostructures. The main result of the BSE calculation (see Fig. 2.7) are discussed in the following.

- **Absorption spectra**

  As mentioned in subsection 2.3.5, we plot both spectra (Eq. 2.48) with (BSE spectrum, see Eq. 2.46) and without (IQPA spectrum, see Eq. 2.47) the excitonic effects, in order to ease the analysis of the main peaks of the absorption spectrum (see Fig. 2.7). A Lorentzian broadening of 0.1 eV is applied to the resulting spectra.

- **Exciton binding energy**

  The binding energy of the e-h pairs represent the energy needed to dissociate/separate the two quasiparticle (electron and hole) which are held together by attractive Coulomb interaction. In Fig. 2.8 we summarize how this energy can be evaluated in different cases. As example, the exciton labeled *b* is found above the direct QP gap in the spectrum, and stems from transitions between the QP states far from the gap (green circles). Consequently, the binding energy can be evaluated as the difference between the excitation energy E_b^λ with respect the energy difference between involving QP states (green arrow in Fig. 2.8). This energy difference represent the independent QP transition (IQPA). We notice that, in this case, the precision on the value of the binding energy depends on the localization of the exciton weight (green circle) such that in case where this exciton arises from mixed character between different bands and regions in the reciprocal space, this evaluation become complicate. Within the `exciting` code [178], the value of the excitation energy and the corresponding value of the IQPA transition of each exciton are accessible from our calculations, and following the discussion above the binding energy can be evaluated.

  The exciton labeled *a* that dominates the absorption onset arises from transitions between the QP gap states (blue circles), and this can be seen by plotting the exciton

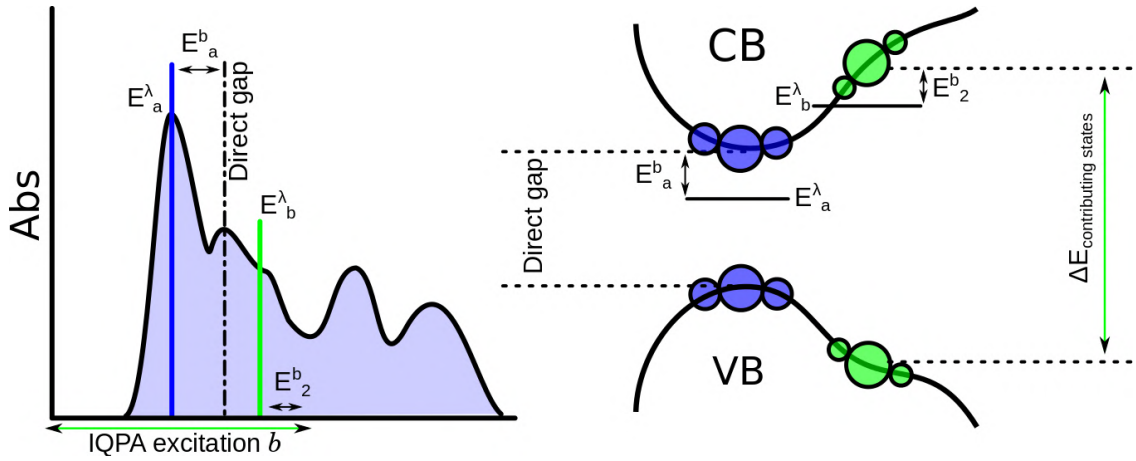

Figure 2.8: (left): Example of BSE spectrum where the different types of excitations (a and b) are highlighted. The dotted-dashed line indicates the direct QP gap. The green arrow estimate the energy of excitation b given by IQPA approximation. (right): Schematic representation of the excitonic distribution in the reciprocal space (colored circles). The color code of the circles correspond to that of the excitations highlighted in the spectrum. The green arrow indicates the difference between the green QP states contributed to excitation b.

weight presented above. In this case the binding energy E^b_a is given, simply, by the difference between the value of the excitation energy E^λ_a given by BSE solution and the direct QP gap. We notice that, in case of the stacked bulk h-BN presented in the next chapter, the considered excitations arise from transitions within the QP gap. Consequently, the binding energy is evaluated with respect to the direct QP gap. In case of the graphene/h-BN vdW heterostructures, shown in chapter 4, the binding energy of the excitons cannot be evaluated with respect to the band gap given by graphene. In this case, by comparing the peaks given by BSE and IQPA spectra the binding energy can be estimated.

- **Exciton weight**

  As shown in Eq. 2.50, the BSE eigenvectors A^λ contain information about the **k**-resolved contributions of individual QP bands to the electron-hole pairs. This analysis provides us the origin of each exciton and allows us to determine the physical position (atoms and orbital) where the remaining hole is located (see Fig. 2.7). In the next chapter, these quantities (Eq. 2.50) are plotted as circles, whose size is representative of the **k**-resolved band contributions, which represent the key information for visualizing the spacial distribution of the electron-hole as discussed in the following.

- **Electron-hole distribution**

  In order to visualize the excitons, we plot the square modulus of the e-h wave-functions (Eq. 2.51). Since this wave-function depends on both the electron the hole coordinates, the probability to find the electron can be visualized by fixing the

hole position. This position can be determined by plotting the KS wave-functions of the contributing valence states (see Fig. 2.7). In our systems, most valence states contributing to the main excitons are dominated by one atomic species with π-like character (see Fig. 2.7). Consequently, we fix the position of the hole at the corresponding atomic species with slight shift along the z direction. This shift is determined by moving the hole in this direction such that the physical shift gives the maximal probability (or isovalue) to find the electron. In this case the physical value is ≈ 0.4 a.u. In Fig. B.5 in Appendix B, we show how the moving of the hole position in the in-plane direction impact the resulting electronic distribution.

All atomic structures and isosurfaces are visualized with the VESTA software [190].

3

Tuning optical excitations in bulk hexagonal boron nitride by layer patterning

To fully exploit the potential of vdW materials and heterostructures, it is essential to rationalize the mechanisms that rule the electronic structure including excitonic effects, in relation with stacking arrangement of the 2D constituents. For this purpose, in this chapter we select bulk hBN as ideal candidate since it is formed by vertical stacking of 2D constituents (in this case only h-BN layers). In addition, bulk h-BN exhibits attractive optical properties, related to the presence of pronounced bound excitons in the near-UV region [4, 37–41, 103]. This choice collects all ingredients to investigate independently the impact of the stacking arrangements on its rich properties. To do so, we consider the five possible stacking arrangements given by relative displacement of the layers and by swapping the positions of the two atomic species (B and N) in the unit cell. In the framework of DFT and MBPT, we investigate the structural, stability, electronic and optical properties including excitonic effects, discussing the interplay between these properties and the layers arrangement. We discuss the importance of the layer patterning in h-BN and how this can be extended to other vdW layered materials and heterostructures as an exciting way to tune their properties.

3.1 Structural properties

Similar to graphite, hexagonal boron nitride is formed by vertical stacking of 2D monolayers which are held together by van der Waals forces. In such materials the layers are strongly bound in the in-plane direction and allow several stacking arrangement. The latter defines how the layers are combined in the vertical direction. In graphite, the monoatomic layers (formed by only carbon, C, atoms) allow two different stacking arrangements. The layers can be eclipsed in AA stacking (the atoms of different layers are vertically aligned) or staggered in AB *Bernal* configuration (every second atom lies on the *hollow* site) [100]. These are the two possible simple stackings given by a relative sliding of the inequivalent layers by one bond length while the realistic one is the AB ar-

rangements. We notice that by non-relative sliding and/or layers rotating one can design infinity of layer arrangements. In h-BN, in addition to the AA and AB configurations, stacking arrangements can be further modulated by swapping the positions of the two atomic species (B and N) as shown in the following.

3.1.1 Stacking arrangements

In bulk h-BN the eclipsed layers allow two different stacking arrangements, which are the AA and AA' configurations. In AA stacking, atoms of the same species are vertically aligned (B over B and N over N). However, in AA' configuration, the atoms of different species are vertically aligned (B over N and N over B) as shown in Fig. 3.1. This configuration is the one known for the realistic bulk h-BN [191].

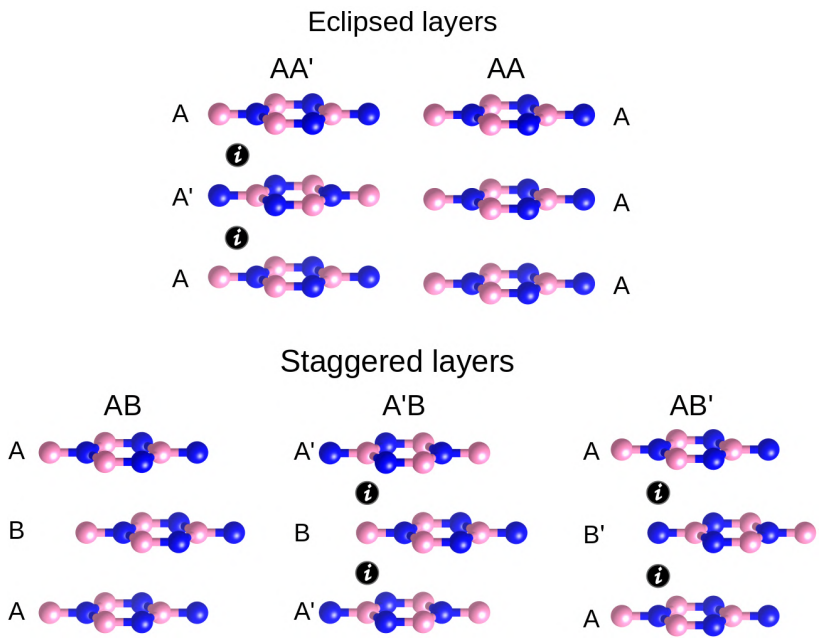

Figure 3.1: Sketch of the five stacking arrangements of bulk h-BN. The black circle indicate the presence and position of inversion symmetry between layers.

The staggered h-BN layers allow three different stacking arrangements which are the AB, A'B and AB' configurations (see Fig. 3.1). In AB stacking, B and N atoms alternately occupy the *hollow* site (B over N, N over *hollow*, B over *hollow*). In the A'B (AB') arrangement, all N (B) atoms occupy the hollow position and B (N) atoms are vertically aligned. In Fig. 3.1, we indicate also the configurations where the layers are linked by inversion symmetry. We notice that the used nomenclature of these stackings is based on the order of the atoms and layers. The A (B) is referred to the first (second) in-plane position of h-BN layer in the unit cell. We add (remove) the prime , ' , if it starts by the N (B) atom. It should be noticed that the proposed configurations are the simplest and the higher-symmetry ones ignoring any complex patterning. The atoms are either vertically aligned (which maximize the vertical interactions between the atomic species) and/or occupy the

hollow position of the neighboring layers.

3.1.2 Lattice parameters

In order to simulate the considered stackings of bulk h-BN, we consider a unit cell containing 4 atoms (2 B and 2 N atoms) forming the 2 basal h-BN layers with in-plane hexagonal symmetry, as shown in Fig.3.2 for the AA′ configuration. We notice that the AA arrangement can be simulated by only one h-BN layer per unit cell. However, in order to study the effects of stacking consistently with all other arrangements, we consider a unit cell with two h-BN layers.

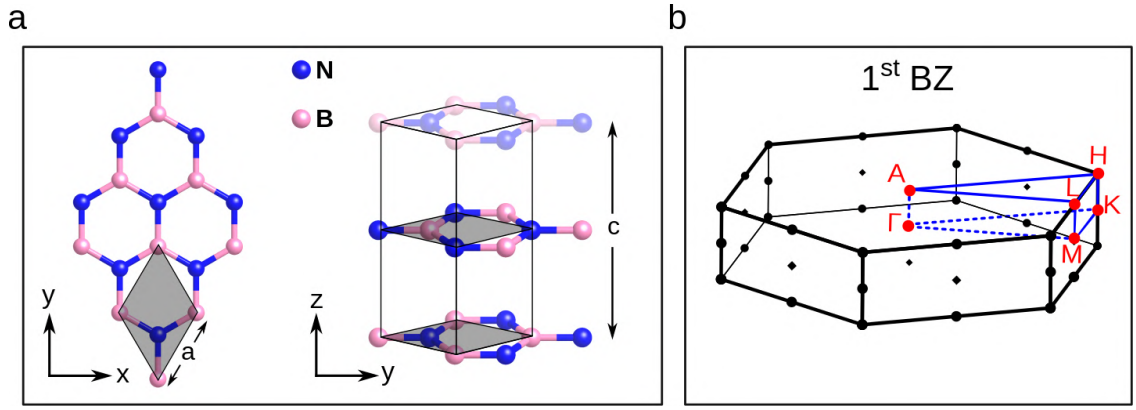

Figure 3.2: (**a**): In- and out-of-plane view of h-BN unit cell in AA′ stacking arrangements. The two layers included in the unit cell are shown in the foreground, while periodic images are shaded. The B (N) atoms are pink (blue). (**b**): The corresponding 1st Brillouin zone including the higher symmetry points.

As it is known in layered materials, the role of the vdW forces is to anchor the layers at fixed distance [192]. In our system in order to optimize the in- and out-of-plane lattice parameters we use the vdW-TS [186] and DFT-D2 [185], to account for vdW interaction. First, we compare the resulting structural parameters of AA′ stacking with the previous theoretical and experimental results. Thus, the more accurate method will be considered to optimize the other stacking arrangements.

In-plane lattice constant

In Table 3.1, we report the resulting in- and out-of-plane lattice parameters of stacked bulk h-BN given by different methods. The in-plane lattice parameter "a" of the AA′ configuration given by GGA approximation together with vdW-TS method is 2.50 Å, in good agreement with the reported experimental value (2.50 Å) in Ref. [193]. Owing to the non-uniform charge density distribution along the B-N bond (see subsection 3.1.3), we notice that LDA approximation underestimates the in-plane lattice parameter, being 2.48 Å. Considering the other arrangements the in-plane lattice parameter (given by the GGA approximation together with vdW-TS or DFT-D2 method) remains constant for all

considered configurations (a=2.50Å). Due to the strong in-plane bonding with respect to the weak interlayer interaction, this parameter is unaffected by the layer patterning. This is also confirmed since the resulting "a" parameters given by vdW-TS and DFT-D2 methods are equal (a=2.50 Å).

Out-of-plane lattice constant

The resulting "c" parameters given by different vdW methods are shown in Table 3.1. In AA′ configuration the more accurate value of interlayer distances is given by vdW-TS approach, being 6.60 Å. This value is in close agreement with the reported theoretical (6.64 Å in Ref. [194]) and the experimental result (c=6.66 Å in Ref. [193]). We notice that the DFT-D2 underestimate the c parameter to 6.12 Å, with respect to the experimental value, which shows a good agreement with reported value using the same method in Ref. [194]. Due to its accuracy with respect to LDA and DFT-D2 results [186, 194], from now on we will use the vdW-TS method to account for vdW interaction in other stackings.

Analyzing the vdW-TS results (see Table 3.1), the smallest c parameters are found in the AA′, AB and A′B arrangements, being 6.60 Å, 6.58 Å and 6.48 Å, respectively. The common point in these arrangements is that the N atoms never lie on top of each others. However, the largest "c" parameters are found in the AA and AB′ configurations with values of 6.84 Å and 6.86 Å , respectively. In these arrangements the N atoms are vertically aligned. In the following, in order to understand the relationship between the vertical alignment of the atomic species and the interlayer distance, we visualize the electronic charge density in bulk h-BN.

Table 3.1: Lattice parameters of h-BN in the considered stacking arrangements given by different methods. The binding energies of the corresponding stacking are given by the DFT-D2 method.

bulk h-BN	methods	AA′	AB	A′B	AB′	AA
Lattice parameter a (Å)	GGA+vdWTS	2.50	2.50	2.50	2.50	2.50
	GGA+DFT-D2	2.50	2.50	2.50	2.50	2.50
Lattice parameter c (Å)	GGA+vdWTS	6.60	6.58	6.48	6.86	6.84
	GGA+DFT-D2	6.17	6.12	6.25	6.66	6.75
Binding energy (eV)	E_b	0.355	0.360	0.340	0.270	0.260

3.1.3 Hybridization and electronic charge density

By sp^2 hybridization ($1s^2 2s^1 2p_x^1 2p_y^1$), B atoms can form three covalent bonds with N atoms which exhibit $2s^2 2p_x^1 2p_y^1 2p_z^1$ configuration. As a result, we have three covalent σ bonds within the h-BN layer leading to the hexagonal structure. In case of N atom, one electron

from $2s^2$ fills the $2p_z$ orbital and the second $2s^2$ electron contributes to the sp^2 σ bond. Consequently, the electronic configuration of N atoms become ($2s^1 2p_x^1 2p_y^1 2p_z^2$).

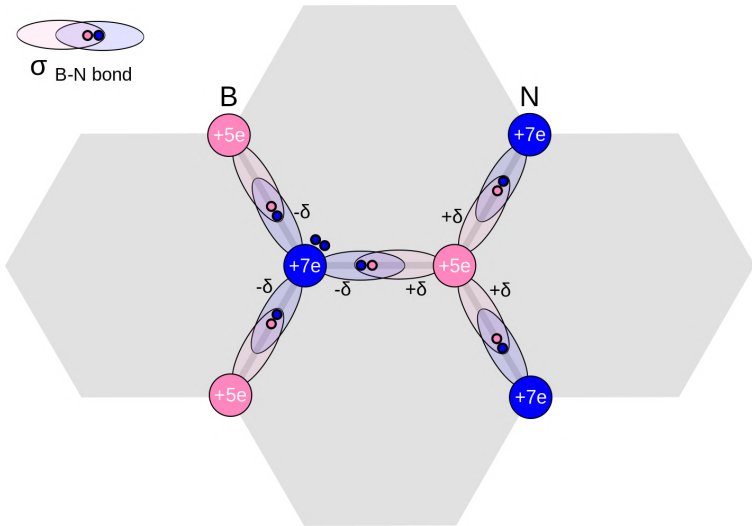

Figure 3.3: Schematic representation of the σ bonds that lead to the hexagonal structures in h-BN. The atomic centers of B (N) are pink (blue) and the $\pm\delta$ reflect the difference in the electronegativity between B and N atoms, which gives rise to the localization of the electrons pair around the N atoms.

On the other hand, the N atoms exhibit a larger nuclear charge than the B atoms (+7e, +5e, respectively). As a result, electrons forming the σ bonds are more attracted to the N atoms (large electronegativity then the B atoms). To schematize this effect in Fig.3.3, we add $-\delta$ and $+\delta$ for each bond to N and B atoms, respectively.

In order to visualize the charge distribution in bulk h-BN, we plot the in- and the out-of-plane projection of the electronic charge density in the AA′ configuration (see Fig. 3.4.b). As discussed above, the excess of electronic charge in the vicinity of the N atoms is due to the enhanced electronegativity compared to the B atoms. As a result, the atomic centers of N (B) atoms are negatively (positively) partially charged. Consequently, the B-N bond exhibits a polar-like character [122, 192, 195, 196].

While the vdW forces in our systems are responsible for keeping the layers at a fixed distance [192], in the following we discuss how the nature of the atoms that are vertically aligned play a crucial role in determining the interlayer distances in different stackings.

3.1.4 Interplay between layer patterning, interlayer distance, and stability

In order to study the relationship between the interlayer distance, stability, and stacking arrangements, we analyze the resulting c parameter and binding energy of the different stacking arrangement, given by the DFT-D2 approach [185] (see Table 3.1). This method is expected to be more accurate to estimate the bonding energy in relation with the stacking arrangements [194, 197]. By increasing the out-of-plane "c" parameter until 60 Å, we plot

the total energy per unit cell as function of the *c* parameter for each stacking (see Fig. 3.4). The total energy of the *c*=60 Å is set to zero and considered as the energy corresponds to the isolated layers since the interlayer distance is 30 Å between.

AA′, AB and A′B stacking arrangements

In the AA′ stacking the h-BN layers are eclipsed with B over N and N over B. The resulting "*c*" parameter given by DFT-D2 is about 6.17 Å in good agreement with that reported in Ref. [194]. In the AB configuration where the h-BN layers are staggered with B over N stacking, the interlayer distance is 6.12 Å. From the electrostatic point of view the small interlayer distance in the AA′ and AB configurations with respect to other stackings is due to the attractive interaction between the vertically aligned and the oppositely partially charged atomic centers of B and N atoms [192, 196, 198]. Furthermore, since both h-BN layers are eclipsed, the attractive interaction in AA′ stacking is larger than in the AB arrangement. For this reason the AA′ stacking is the most favorable configuration which is also most commonly realized in experiments [199]. The reported result in Table 3.1 shows that the binding energy of the AB configuration (0.36 eV) is larger than that of AA′ stacking (about 0.355 eV). This result reflects the accuracy limitation of our method, as demonstrated in Refs [192, 196, 198]. By using more accurate methods [198], the more favorable stacking is the AA′ configuration, in agreement with the experimental finding. Beside this comparison, in addition to the AA′ arrangement, the AB stacking is predicted to be the most stable configuration with respect to the other three arrangements (see Fig. 3.4). The possibility to find the AB arrangement as defect in bulk h-BN is expected due to the different size and nature of the experimentally reported band gaps [200]. Moreover, the appearance of this arrangement in realistic systems is reported for bilayer h-BN [115].

In A′B arrangement where the layers are staggered with B over B atoms, the interlayer distance (6.25 Å) is larger than that found for the AA′ stacking. This result reflects the electrostatic repulsion between the vertically aligned and the positively partially charged atomic centers of B atoms. Consequently, this stacking is less stable (E_b=0.34 eV) than the AA′ and the AB configurations where the attractive interaction is significant, consistently with the stability order given by DFT-D2 method in Fig. 3.4.

AB′ and AA stacking arrangements

In AB′ arrangement where the h-BN layers are staggered with N over N, the interlayer distance given by DFT-D2 method is 6.66 Å. This large interlayer distance with respect to the previous stackings discussed above is due to the electrostatic repulsion between the vertically aligned and the negatively partially charged atomic centers of N atoms.

The common points between the AB′ and A′B stacking is that the layers are staggered with vertical alignment of similar atomic species (N over N in the AB′ and B over B in A′B stacking). As a result, both configurations exhibit an electrostatic repulsion between

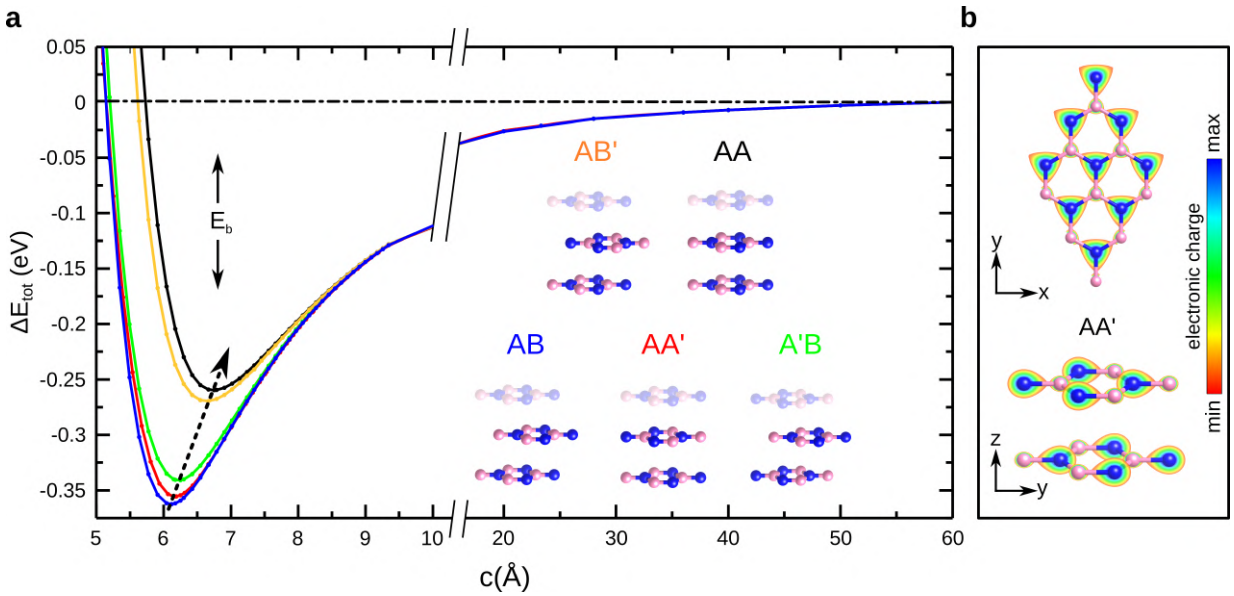

Figure 3.4: (**a**): Binding energies curves of the five considered h-BN stackings evaluated as the total energy per unit cell at different interlayer distances along the c direction. The zero energy referred to the c=60 Å, where the interlayer interaction is negligible. (**b**): In- and out-of-plane projection of the electronic charge density in h-BN (AA′ stacking).

the same partially charged atomic centers. Since B and N atoms exhibit a similar partial charge with different sign, positive and negative, respectively (see Figs. 3.3 and 3.4.b), the interlayer distance of the A′B and AB′ should be the same. However, in addition to the electrostatic repulsion, the enhanced Pauli repulsion between the more delocalized overlapping electron clouds of the N atoms [196, 201] gives rise to the larger interlayer distance in AB′ stacking than in the A′B arrangement. This is also reflected in the binding energy where AB′ is predicted to be an unfavorable configuration with respect to A′B stacking (see Fig. 3.4).

In the AA arrangement where the h-BN layers are eclipsed with B over B and N over N, the interlayer distance is 6.75 Å. In this case the electrostatic interaction is given by the repulsion forces between the negatively (positively) partially charged atomic centers of N (B) atoms which are vertically aligned. As a result the interlayer distance in the AA configuration is larger than in the AB′ stacking and all other considered configurations (see the corresponding "c" values in the "x" axes in Fig 3.4 and DFT-D2 results in Table 3.1). Focusing on the binding energy (see the y axes in Fig 3.4), this arrangement is the most unstable stacking (E_b=0.26 eV). It reflects the large electrostatic repulsion with respect to all other arrangements.

To summarize this subsection, the binding energy or the stability of these systems can be deduced by comparing their interlayer distances. The dotted-dashed arrow in Fig 3.4 shows that the more favorable stackings exhibit a smaller interlayer distances (see also Table 3.1). In addition, we have shown that the nature of the atoms that are vertically aligned plays a crucial role in determining such distance in different stackings. In the

following, in order to study the electronic and optical properties of different stackings, we consider the structural parameter given by vdW-TS (see Table 3.1 and Fig. 3.5). As mentioned before, this choice is motivated by the fact that the resulting c parameter of the AA' stacking given by vdW-TS method is in agreement with the experimental value [193].

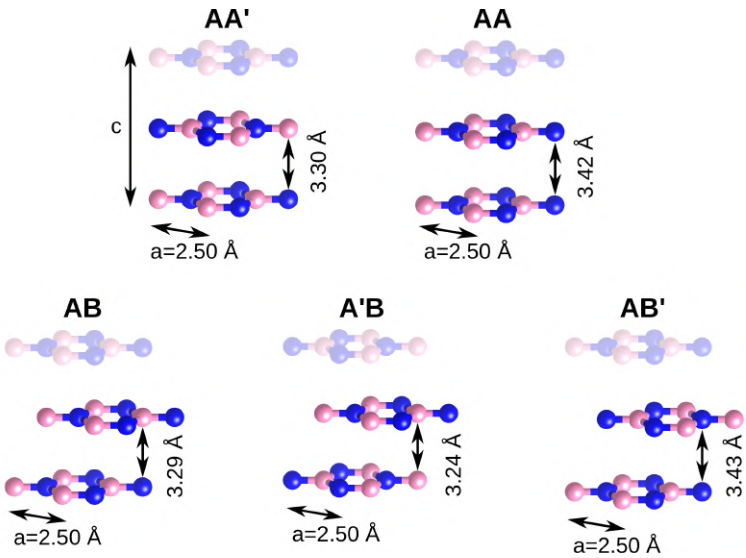

Figure 3.5: Structural parameters of the five considered stacking arrangements of h-BN given by vdW-TS method. In the following, we investigate the electronic and optical properties using these parameters.

3.2 Electronic properties and optical excitations in bulk h-BN

In order to study the effect of the layer patterning, we first present the electronic and optical properties of bulk h-BN (AA' arrangements). Moreover, in this section we provide a comparison with the previous theoretical and experimental results. The resulting e-h pairs that can appear in bulk h-BN will be also investigated and classified according to their spatial distribution.

3.2.1 Electronic band structure

The electronic properties of hexagonal boron nitride are extensively investigated in order to estimate the size and nature of the band gap. This is motivated by the controversy between the theoretical and experimental results as discussed in section 1.1.2. Starting from the structural parameter given by vdW-TS method (see Fig. 3.5), we compute the electronic band structure of bulk h-BN in the AA' stacking arrangement using the DFT method and the G_0W_0 approximation introduced in chapter 2.

First, from DFT ground-states calculation using the GGA-PBE functional for the exchange correlation term, we have found that the band gap of the AA' stacking is 4.22 eV

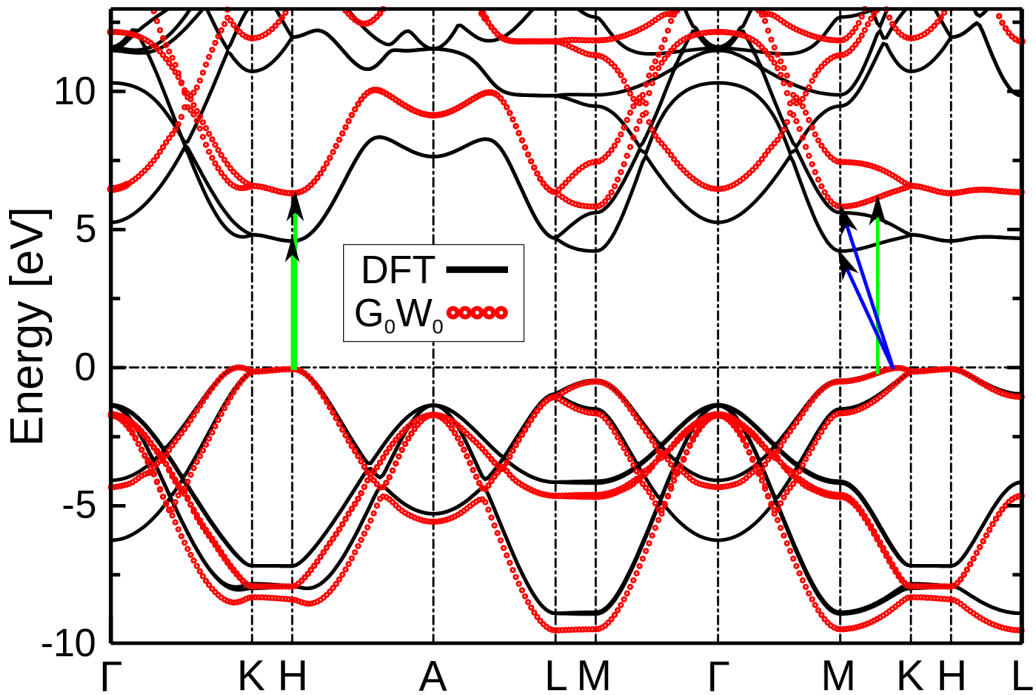

Figure 3.6: Electronic band structures of bulk h-BN along the full path indicated in Fig. 3.2 which are given by DFT-GGA (black line) and by QP G_0W_0 approximation (red circles). The blue (green) arrow indicates the indirect (direct) gaps. The valence-band maximum is set to zero.

with indirect character. The valence band maximum (VBM) is located near the K point and the conduction band minimum (CBM) is at M point in the BZ. Our finding is in agreement with previous theoretical results based on ground-state calculations [38, 103, 112, 114, 122]. The DFT method underestimates the band gap with respect to the experimental value (see Table 1.1). In order to be more accurate in estimating the band gap we employ the G_0W_0 method shown in Chapter 2.

The G_0W_0 correction increases the band gap from 4.22 eV at DFT level to 5.83 eV. Due to the poor screening effect in h-BN, the QP gap is increased by such a large value ($\sim$1.6 eV), reflecting the significant e-e interaction in h-BN. The nature (indirect gap between VBM near K point and CBM at M point in the BZ) and the size (5.83 eV) of the band gap are in good agreement with the previous theoretical works based on MBPT [38, 112, 114]. Moreover, our results are in close agreement with the recent experimental results reported in Ref. [102, 110, 111] with small underestimation (see Table 1.1). In addition to the experimental error that usually arises from the measurement technique and sample quality (see section 1.1.2), we ascribe this discrepancy to the intrinsic underestimation of the gap given by the single-shot G_0W_0 method compared to including any degree of self-consistency [177, 202].

In Fig 3.6, we plot the electronic band structure given by the DFT-GGA (black line) together with the G_0W_0 quasiparticle one (red circles) along the full path in the BZ. The blue (green) arrow shows the DFT and the QP indirect (minimum direct) gap. The minimum

direct DFT gap (4.63 eV) is located at H point in the BZ in agreement with Ref. [38, 114] and the minimum direct QP gap (6.33 eV) can be found in the vicinity of the M point which is comparable to that at the H point in the BZ. The QP correction shifts up the CB bands by 1.56 eV at gamma point and by around 1.77 eV at K point in the BZ. This means that the scissor operator which is defined, in this case, as the value needed to shift the DFT bands to QP ones cannot be used since this shift depends on the k-point in the BZ and on the band index. For this reason, the optical properties will be computed, in the following, using the G_0W_0 QP electronic states.

3.2.2 Character of the bands

The B and N atoms have 3 and 5 electrons in the valence orbitals, respectively. In our case the unit cell contains 2 N and 2 B atoms which means that we have in total 16 electrons. Consequently, the h-BN exhibits 8 filled bands (valence bands). To analyze the character of these bands, we plot the partial density of states projected on the DFT band structure (see Fig. 3.7). The bands that are dominated by a mixture of B and N orbitals reflect their σ like character. On the other hand, the well-defined N-like VB-1/VB and B-like CB/CB+1 bands exhibit a π, π^* character along the K-H path in the BZ, respectively. As discussed in the subsection 3.1.3, this character is related to the atomic structure of the constituting species (the p_z orbital in the N (B) atoms is filled (empty)). We notice that in this stacking the two VB/VB-1 and the CB/CB+1 are energetically very close to each other due to the presence of two atoms of the same species in the unit cell. The degeneracy of these bands along the K-H path in the BZ is a direct consequence of the vertical alignment of the atomic species. Since N atoms are not on top of each other, they avoid any vertical electrostatic interaction. In addition, they are in identical environments (both have the same neighboring atoms in the vertical direction). Consequently, the N-like VB-1/VB bands exhibit the same energy along the K-H path in the BZ. The same thing happens for CB/CB+1 bands. They are degenerated along the K-H path in the BZ, since the B atoms are not vertically aligned.

3.2.3 Electronic distribution of Kohn-Sham states

The indirect and the minimum direct gap in h-BN are located around the K-H path in the BZ. All excitations that arise from this region are expected to dominate the absorption onset as shown in the next section. For this reason, the understanding of the character of the degenerated VB-1/VB (CB/CB+1) bands along the K-H path in relation with the structural arrangements is requested. To do so, we visualize the Kohn-Sham electronic states distribution for these bands at high symmetry K and H points (see in Fig. 3.8). The character of the bands is indicated using the color code of the atomic species. At the K point the electronic distribution of the VB/VB-1 bands exhibit a π-like character and spread over N atoms of both h-BN layers in the unit cell, as shown in Fig. 3.8 (left).

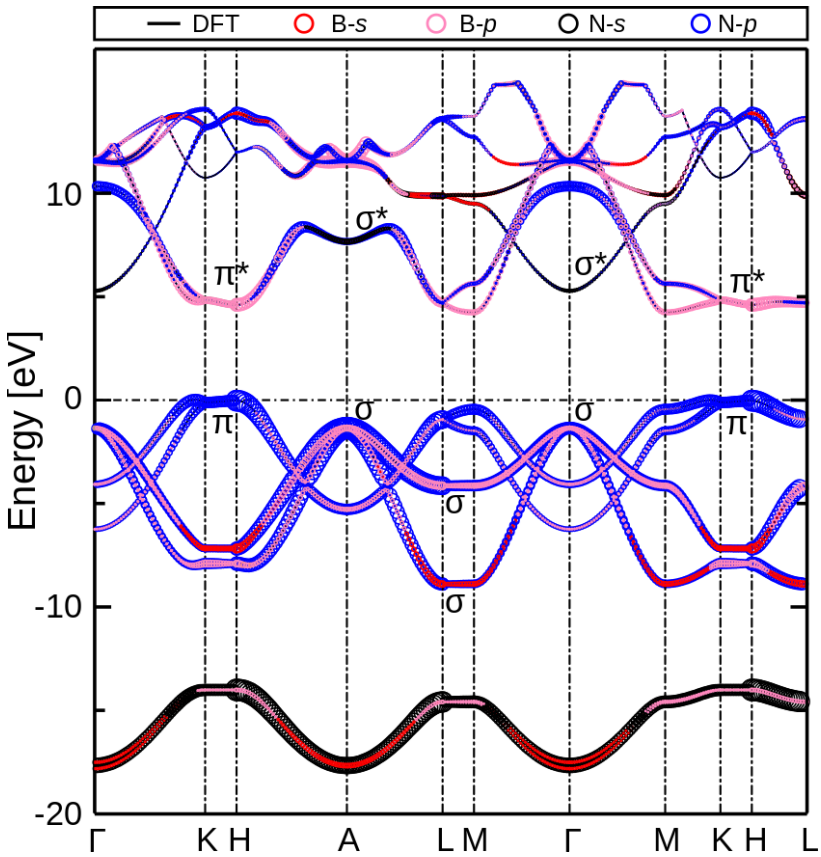

Figure 3.7: Character of the bands in bulk h-BN (AA′ configuration), indicated by colored circles on top of the band structure given by DFT-GGA method along the full path in the BZ. The corresponding orbital of the colored circles are indicated on the top of this figure. The valence-band maximum is set to zero.

This distribution is valid also along the K-H path in the BZ. However, at the H point, the electronic distribution of each band spread over N atoms of only one inequivalent h-BN layer in the unit cell, in good agreement with Ref. [112], see Fig. 3.8 (right).

The same is happen for the B-like CB/CB+1 bands. At K point the electronic distribution of these bands exhibit a π^*-like character and spread over B atoms of both h-BN layers in the unit cell, which is valid along the K-H path. However, at H point the electronic distribution of each band spread over B atoms of only one inequivalent h-BN layers in the unit cell (see Fig. 3.8). To summarize, focusing on the QP gap states, the N-like VB-1/VB and the B-like CB/CB+1 bands are degenerate and their corresponding wave-functions distribution spreads over both (only one inequivalent) atoms in the unit cell along the K-H path (at H point) in the BZ. The electronic distribution of these bands and their overlap play a crucial role in determining the intensity and the spatial distribution of the resulting excitations as discussed in the following.

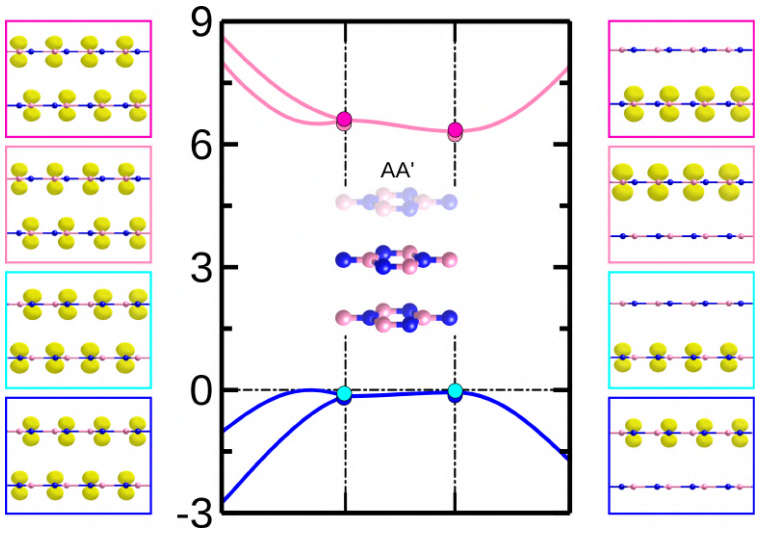

Figure 3.8: QP band structures in the vicinity of K-H path of the AA′ stacking arrangements (inset) and real-space distribution of the two highest occupied and the two lowest unoccupied bands at the K (left) and at the H (right) points in the BZ. The band character is indicated by the color code of the corresponding atomic species (B: pink, N: blue), while the box frame points to the corresponding electronic states marked in the band structures. The valence-band maximum is set to zero.

3.2.4 Absorption spectrum including excitonic effects

In the last subsections we have shown in detail the electronic properties of bulk h-BN. Now, by solving the BSE equation staring from the electronic QP states given by the G_0W_0 approximation, we investigate the optical properties of the bulk h-BN with and without including excitonic effects (see details in Chapter 2). We focus on the excitation and binding energies of the resulting e-h pairs as well as their distribution in the real and the reciprocal space.

In Fig. 3.9, we show the optical absorption spectra given by the imaginary part of the macroscopic dielectric function computed by including excitonic effects (BSE: solid line for the in-plane component and dotted-dashed line for the out-of-plane one) and neglecting them within the IQPA approximation (shaded area). A Lorentzian broadening of 0.1 eV is applied to all spectra. The resulting IQPA spectrum is formed by the band-to-band transitions between the QP states (see Eq. 2.47). It is characterized by a broad hump in the UV region where the onset coincides with the direct QP gap. The inclusion of the e-h interaction (BSE) leads to redshift the spectrum below the direct QP gap by around 0.7 eV. Such a large value is due the low dielectric screening in h-BN, which enhances the e-h binding strength. Consequently, the sharp peak within the direct QP gap exhibits an excitonic character. The BSE solutions (E^{λ} eigenvalues in Eq. 2.45) are indicted by red bares while the intensity indicate their oscillator strength (see Eq. 2.49). We notice that most excitons are doubly degenerate reflecting the in-plane hexagonal symmetry as reported in Ref. [40]. The sharp peak is characterized by doubly degenerate bound exciton at 5.6 eV indicating its excitonic nature. The sharp peak is followed by a broad

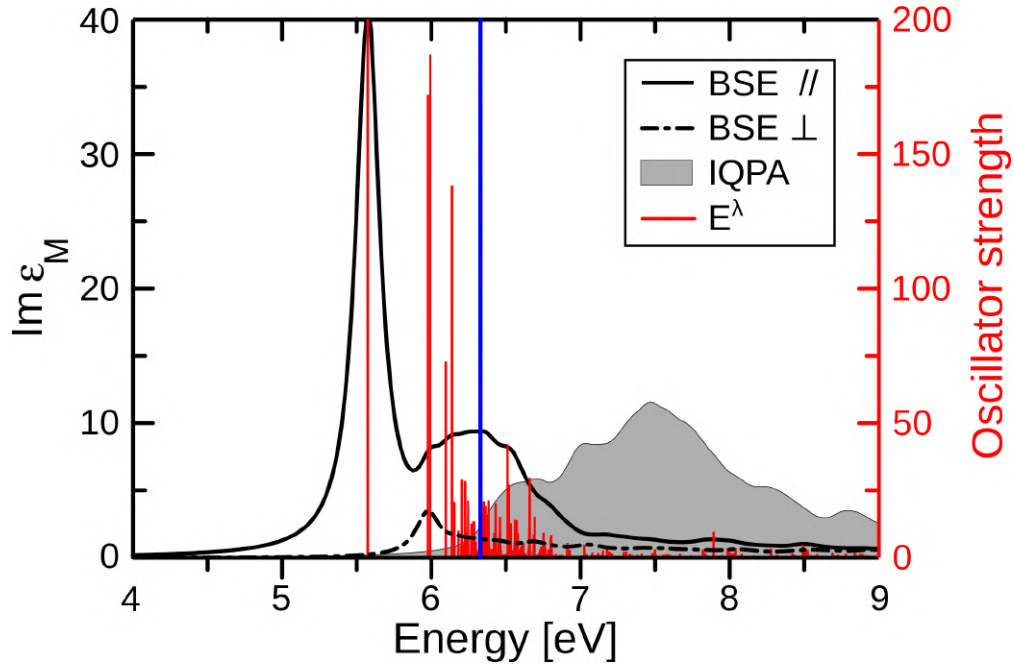

Figure 3.9: Optical spectra computed by including excitonic effects (BSE: solid line for the in-plane component and dotted-dashed line for the out-of-plane one) and neglecting them within the independent QP approximation (IQPA, shaded area). Red bars indicate the oscillator strength of the BSE solutions E^{λ}. The blue line indicates the direct QP gap.

hump formed by inter-band transitions, and thus visible also in the IQPA spectra. The out-of plane component of the spectrum is rather featureless in the relevant energy region for this study. The relatively intense peak appears around 6 eV correspond to the non-degenerate charge-transfer exciton, discussed in the following subsection.

Comparison to the experimental data

Before analyzing the resulting e-h pairs of each region, we compare our calculated BSE spectrum to the available experimental datasets for assessment of the quality of our results. The experimental datasets shown in Fig. 3.10 are obtained with different measurement techniques and covering different energy ranges. The intensity of the first bright peak of the computed spectrum is renormalized to match the measured ones. As we can see, in Fig. 3.10.b, our computed spectrum shows a very good agreement with the experimental data found in Ref. [107]. The sharp peak and broad hump are correctly reproduced as reported also in other theoretical works using similar method [113, 177].

The experimental data shown in Fig. 3.10.a are obtained by optical absorption measurements [203] and span up to 18 eV. Our result shows a very good agreement including the weak peak around 12 eV. Owing to the intrinsic underestimation of the band gap given by the G_0W_0 approach (see subsection 3.2.1), our computed spectrum is blue-shifted by 0.4-0.5 eV to match both experimental onsets shown in Fig. 3.10. This blue-shift reflect also the experimental error of $\pm$ 0.2 eV in the band gap reported in Ref. [107].

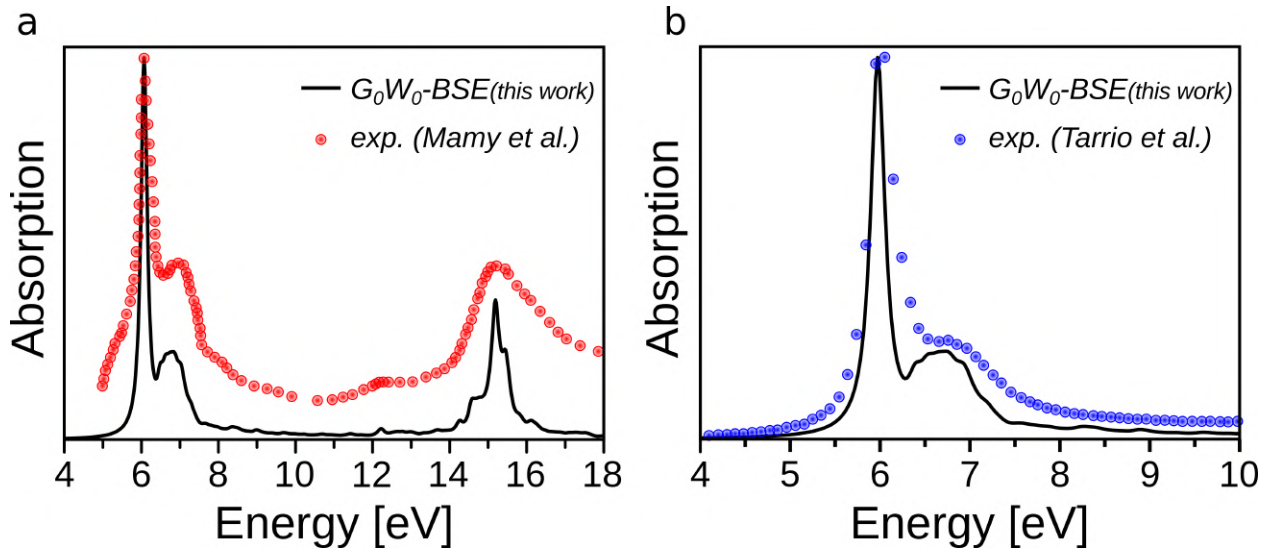

Figure 3.10: Calculated optical spectrum of bulk h-BN in the AA′ stacking, compared with experimental data from: (**a**) Mamy et al. [203] and (**b**) Tarrio and Schnatterly [107]. Our computed spectrum is blue-shifted by 0.495 eV in (**a**) and by 0.4 eV in (**b**) to align with the measured position of the first peak. The spectral intensity is aligned to the height of the first peak. We notice that the experimental data in (**b**) are obtained with inelastic X-ray scattering at finite q=0.13Å^{-1}. However, its similarity to the one at q=0 (as ours), discussed in the original reference [107] makes this comparison consistent.

We notice that the BSE calculation can be done on top of the electronic ground-states with applying scissor operator. The scissor allows to adjust the DFT gap to the experimental one. However, as mentioned in subsection 3.2.1, the scissor depends on the k-point and the bands index in h-BN. Consequently, even if the first peak of the BSE spectrum can be adjusted to the experimental one, the positions of the following peaks cannot be reproduced correctly. In addition, owing to the diversity of the reported experimental gap of bulk h-BN (see Table 1.1) and to the lack of the experimental gaps of other investigated stackings, we opt in this chapter to use the QP electronic states given by G_0W_0 as a starting point. Since this choice correctly reproduces experimental data (see Fig. 3.10.a,b), we rule out any artifact results in the following investigated stackings.

3.2.5 Excitons in bulk h-BN

By analyzing the resulting excitons in bulk h-BN (AA′ stacking), in Fig. 3.11, we report the absorption spectrum including excitonic effects together with the real and the reciprocal distribution of selected prototypes e-h pairs. The reciprocal space distribution (also called here exciton weights) contains information about the k-resolved contributions of individual QP bands to the e-h pairs (see Eq. 2.50). This information is indicated by the green circles drawn on top of the QP band structures (see Fig. 3.11.b). Their size is representative of the contribution of a specific transition to the corresponding exciton. The real space distribution of the main excitons shown in Fig. 3.11.c, is given by the elec-

tronic distribution surrounding a fixed position of the hole. Since most excitations are double-degenerate for symmetry reasons. As such, the correlated probability density associated to the electron, with the hole being fixed, is a linear combination of the single contributions of degenerate BSE solutions. With the excitonic spatial distribution given by the square modulus of the electron-hole wave-functions (see Eq. 2.51), here, we report the corresponding averaged densities, consistent with the results reported in Ref. [40]. The details about the used supercell and isovalues to plot such excitons can be found in Appendix A.

2D distribution

The intense peak centered at 5.57 eV is dominated by a double-degenerate exciton with binding energy of ~ 0.75 eV [1] (see Fig. 3.11). This result is in agreement with previous works based on MBPT [38, 103]. It stems from VB-1 $\rightarrow$ CB+1 and VB $\rightarrow$ CB transitions along the K-H path in the BZ (see Fig. 3.11.b). As shown in Fig. 3.8, these bands are degenerate along the K-H path, and uniformly spread over both layers in the unit cell. As a result, by fixing the hole on top of N atom [2] the corresponding electronic distribution spread over the neighboring B atoms in the in-plane direction. We refer to this type by 2D distribution since the hole and the associated electron sit on the same layer. Its extension up to three lattice parameters reflects the strongly bound character (see Fig. 3.11.c).

The trigonal shape of the excitonic wave-function reflects the hexagonal symmetry of the h-BN. This distribution is the most know in h-BN material which have been found to exhibit basically the same character and extension in monolayers [42], few-layers [204] and bulk [38, 40] systems at the absorption onset. As mentioned above, such e-h pair is twofold degenerate and its shape results from the averaged densities of the two degenerate contributions [40]. The first e-h pair at 5.50 eV, indicated in Fig. 3.11.a by a red arrow, arises from VB-1 $\rightarrow$ CB+1 and VB $\rightarrow$ CB transitions along the M-K-H path in the BZ. This exciton is also double-degenerate with a 2D distribution. Since the electronic distributions of the VB-1/VB and CB/CB+1 bands along the K-H path spread over all layers (see Fig. 3.8), these 2D excitons can appear uniformly in both h-BN layer in the unit cell. Their parity with respect to the inversion symmetry that links the h-BN layers gives rise

[1] We define this quantity as the difference between the excitation energy computed including the e-h interaction, from the full solution of the BSE, and neglecting it within the so-called independent QP approximation (IQPA), where excitation energy and spectra are obtained only from matrix elements between QP states. Both are accessible from our calculations. The excitation energy including excitonic effects can be determined by the solution of the BSE equation. On the other hand, the energy separation between the QP states contribute to each excitation (green circle in Fig. 3.11) allows to estimate the independent QP excitation energy. This definition is generally applicable and does not depend on the position of a given excitation in the spectrum. In case the first exciton is bright and formed by transition between the VBM and the CBM, the binding energy can be determined as the difference between the excitation energy given by BSE solution and the direct QP gap (dotted line in Fig. 3.11).

[2] The VB-1/VB bands, where most excitons arise, exhibit a π character and spread over N atoms. For this reason, we fix the hole on top of N atom using the same in-plane coordinate (see the test shown in Appendix B, Fig. B.5). However, we shift the out-of-plane coordinate of the hole by 0.4 a.u. from the N atom in order to fix it on the p_z orbital, as discussed in subsection 2.4.2

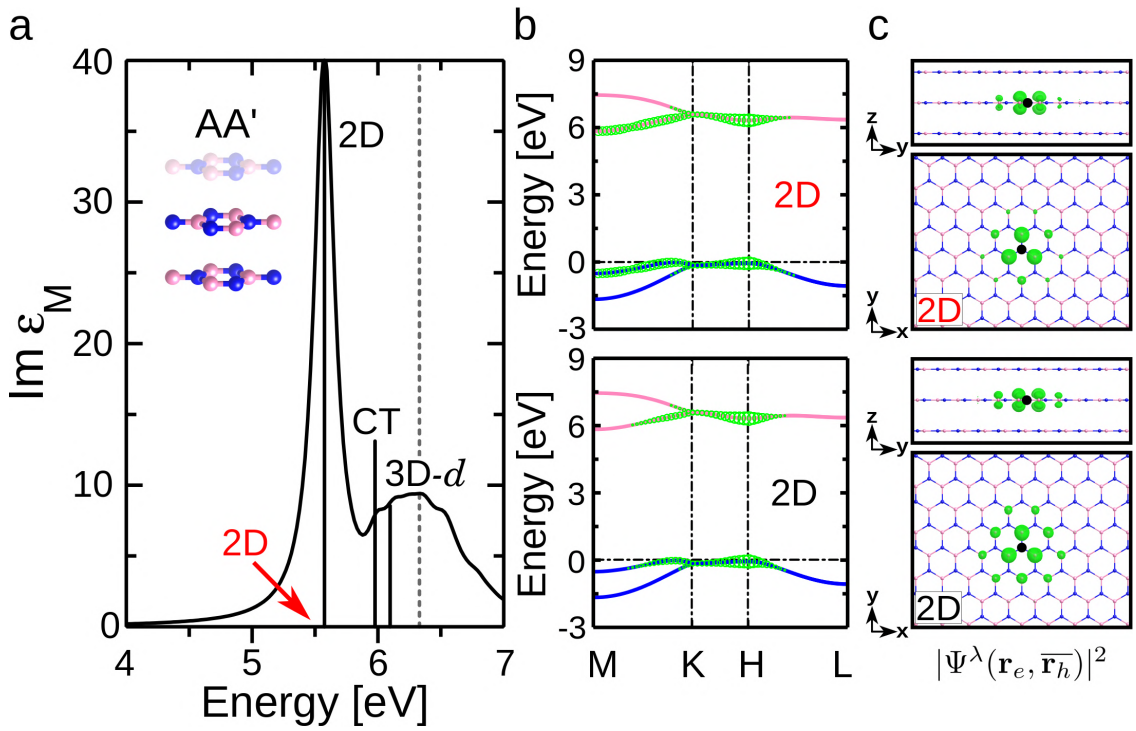

Figure 3.11: (**a**): Optical spectra of the AA'stacking of h-BN (structures shown in the inset), computed by including excitonic effects (BSE). A Lorentzian broadening of 100 meV is included. The dotted line indicates the direct QP gap. (**b**): Band contributions to the excitations marked in the spectra: The size of the green circles is representative of the weights (Eq. 2.50) of the involved QP states. The band character is indicated by the color code of the atomic species (B: pink, N: blue). The valence-band maximum is set to zero. (**c**): Three-dimensional projections of the electron component of the e-h wave-functions highlighted in the spectrum, with the position of the fixed hole marked by the black dot.

to the dark lowest energy exciton (red arrow) and bright (intense) one highlighted in Fig. 3.11.a, as reported in Ref. [40, 204]. In addition to the in-plane 2D distribution, in bulk h-BN e-h pairs can be extended also in the vertical direction with the electron and/or the hole spreading over neighboring layers.

Charge transfer CT exciton

Around 6 eV, charge-transfer e-h pair distribution appears in bulk h-BN, named CT exciton. It arises from VB-1 → CB+1 and VB → CB transitions at the H point in the BZ. Owing to the electronic distribution of these bands at H points (see Fig 3.8) the electron and the hole sit on different h-BN layers making CT like exciton. The in-plane extension of this exciton is limited to a few (up to four) lattice parameters with hexagonal symmetry (see Fig. 3.12). This exciton is dipole-allowed only in the perpendicular polarization direction and corresponds to the relative intense peak found in the out-of plane spectrum (see Fig. 3.9). As a result, this exciton does not exhibit any degeneracy and its in-plane distribution differs from the trigonal shape of the 2D exciton.

As shown in the side view, the remaining hole sits in one layer and the excited electron

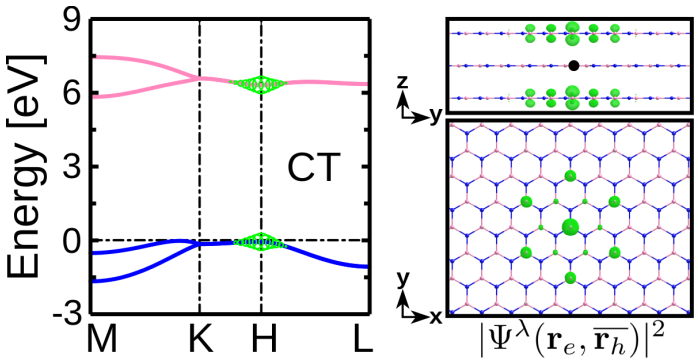

Figure 3.12: (Left): Band contributions to the CT exciton marked in the spectra of Fig. 3.11.a. The size of the green circles is representative of the weights (Eq. 2.50) of the involved QP states. The band character is indicated by the color code of the atomic species (B: pink, N: blue). The valence-band maximum is set to zero. (Right): Three-dimensional projections of the electron component of the CT e-h wave-functions highlighted in the spectrum, with the position of the fixed hole marked by the black dot.

localize uniformly on the two neighboring h-BN layers (see Fig. 3.12). The binding energy of this exciton evaluated as the difference between its excitation energy and the direct QP gap, is smaller than the 2D exciton, being 0.35 eV (see Fig. 3.11).

3D distribution

Above 6 eV where a number of inter-band transitions take place, we find a delocalized three dimensional e-h pair distribution, named 3D$-d$ exciton. This new feature can be found by considering multilayer or bulk h-BN. This exciton arises from transitions between the VB and the CB in the vicinity of M point. Here the bands are energetically split and spatially spread over both inequivalent h-BN layers in the unit cell.

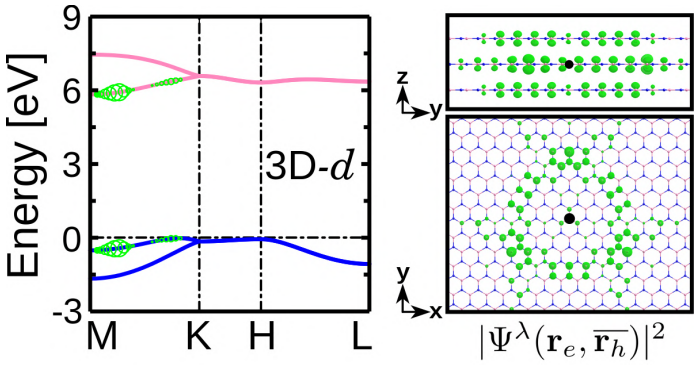

Figure 3.13: (Left): The same analysis, as in Fig. 3.12, is done for the 3D$-d$ exciton.

The electronic distribution in this case overlaps with the hole position and extends uniformly and symmetrically in the vertical direction to the nearest neighbouring h-BN layers forming 3D$-d$ distribution (see Fig. 3.13). Its in-plane distribution preserves the trigonal symmetry, similar to typical in-plane distribution of higher-energy excitons in

monolayer [42]. The delocalized character reflects the weak binding strength with respect to the 2D and CT excitons (around 0.23 eV).

Delocalized 3D excitation

It is worth noting that excitons with a very delocalized 3D distribution appear in the high-energy range (1 eV above the absorption onset) in bulk h-BN. They are due to a number of mixed and very localized transitions between states outside the QP gap (see Fig. 3.14. left). Due to their resonant character of band-to-band transitions, their distribution resembles that of delocalized Kohn-Sham states (see Fig. 3.14. right). The details about the suppercell used to visualize such delocalized exciton is shown in Fig. A.3 in Appendix A.

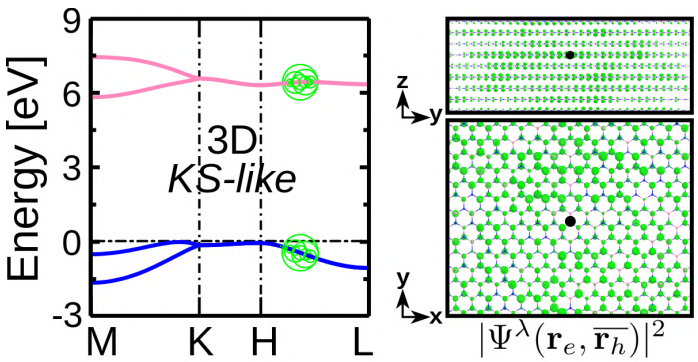

Figure 3.14: (Left): The same analysis, as in Fig. 3.12, is done for the K-S like delocalized 3D exciton.

3.3 Effect of layer patterning in bulk h-BN

By considering the other stacking arrangement shown in Fig. 3.5, we investigate the effect of the layer patterning on the electronic and optical properties of bulk h-BN (AA' stacking) presented in the last section. We focus on the character and the spatial distribution of the resulting e-h pairs.

3.3.1 Tunable character and size of the band gap

We start our analysis on the layer patterning effect from the electronic properties. In Fig. 3.15, we show a sketch of the five considered stackings together with their corresponding QP band structures along the full path in the BZ, shown in Fig. 3.2. The electronic wave-functions distribution of the VB-1/VB and CB/CB+1 at K and H points are also shown together with the QP band structure in the vicinity of the K-H path in the BZ. The electronic properties of the AA' stacking, discussed in the last chapter, are included in

Fig. 3.15 for comparison. The QP band structures of different stackings look quite similar to each other. The main important differences are in the character and the size of the band gap. These differences reflect the degeneracy or the splitting of the VB-1/VB and CB/CB+1 along the K-H path in the BZ. In Table 3.2 we report the resulting electronic and minimum direct band gaps of all stacking arrangement given by DFT-GGA method and by G_0W_0 correction on top of the GGA-PBE results.

Table 3.2: Electronic and minimum direct gaps of bulk h-BN in the five considered stacking arrangements

h-BN bulk	method	AA′	AA	AB	A′B	AB′
Electronic gap (eV)	GGA-PBE	4.22	3.30	4.35	3.48	3.43
	G_0W_0@ *GGA-PBE*	5.83	4.84	6.00	5.03	4.96
Min. direct gap (eV)	GGA-PBE	4.63	4.16	4.46	3.50	4.00
	G_0W_0@ *GGA-PBE*	6.33	5.89	6.16	5.05	5.64

We notice that the reported band gaps of other stackings are in good agreement with the GW results in Ref. [114]. The large difference between the DFT and the QP direct gap (around 1.7 eV), which reflects the significant e-e interaction in h-BN, is unaffected by the layer stacking. However, the difference between the electronic and the direct QP gap can be more or less pronounced depending on the stacking arrangement. All configurations exhibit an indirect gap except the A′B where the gap is quasi-direct (with difference less than 20 meV). The layer patterning in h-BN has a strong impact on the band gap (see Table 3.2). Depending on the stacking arrangements, the reported direct QP gap ranges between 5 and 6.33 eV with a relevant decrease in those stackings where atoms of the same species are vertically aligned. In contrast to the AA′ and AB stacking, the electrostatic interaction between the vertically aligned N (B) atoms in AB′ (A′B) stacking leads to split the VB-1/VB (CB/CB+1) bands along the K-H path in the BZ (see Fig. 3.15.b,c). As a result the band gaps are smaller in these stackings with respect to AA′ and AB configurations. We notice that, despite the N atoms are not vertically aligned in AB arrangement (as in AA′ stacking) the VB-1/VB bands are split along the K-H path. Since the N atoms of different h-BN layers have different neighboring atoms in the vertical direction, they are not in identical environment. Consequently, the N-like VB-1/VB bands exhibit different energy along the K-H path in the BZ. The same thing happens for CB/CB+1 bands. They are not degenerate along the K-H path in the BZ, since the B atoms are in different environment. As mentioned in subsection 3.1.2, we simulate the AA configuration by including two layers in the unit cell to be consistent with the other structures. As a result of band folding the reported minimum direct QP in Table 3.2 is 5.89 eV, corresponding to the difference between the VB-1 and the CB at the high-symmetry point K. This result is in agreement with the reported value in Ref. [103] and consistent with that given by the IQPA spectrum, as shown in the following. In this case the band gap is also smaller than the one reported for the AA′ and AB stackings. To sum up, the N-like

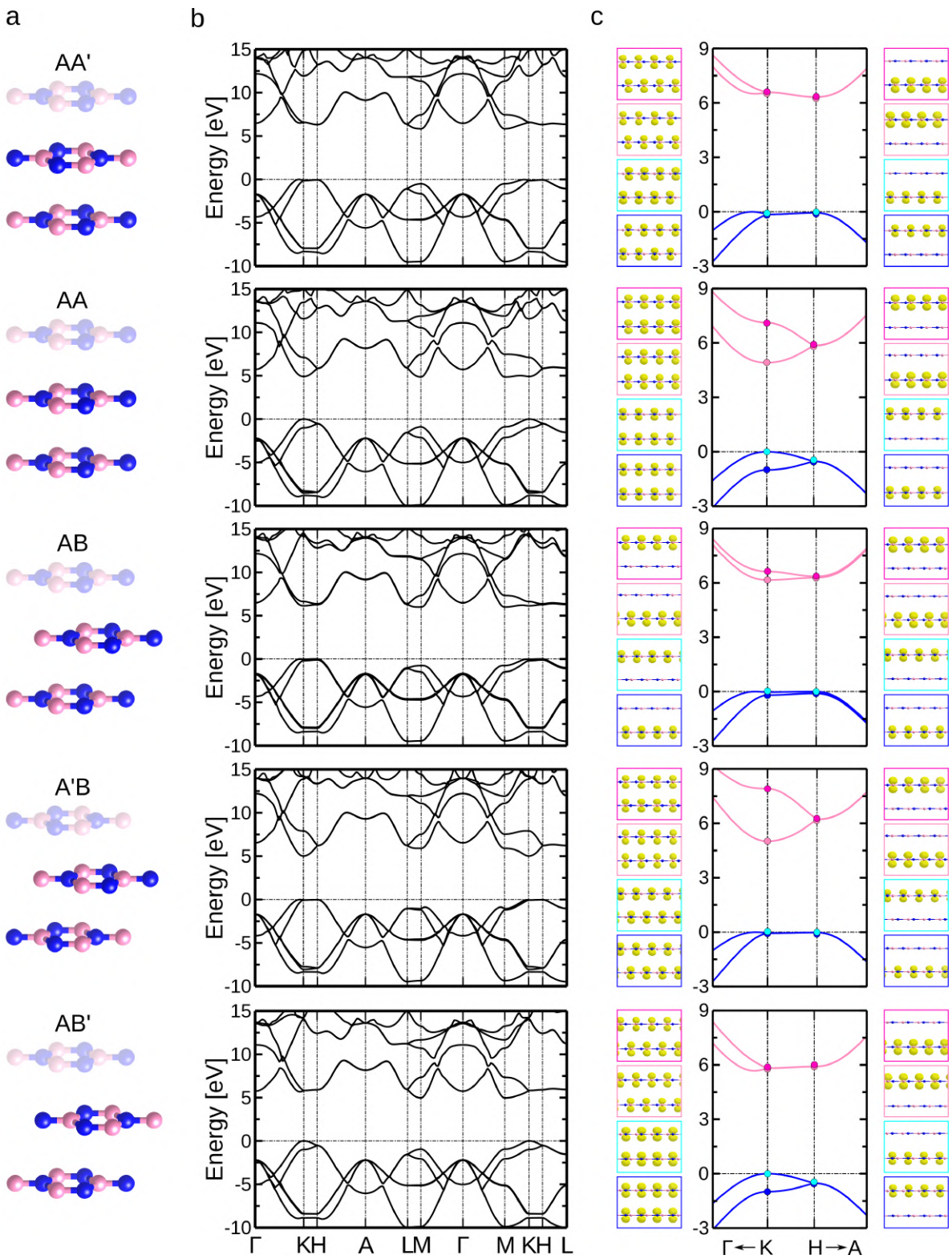

Figure 3.15: (**a**): Sketch of the five considered stacking arrangements of h-BN (including the AA′ stacking for comparison). (**b**): Quasi-particle band structures along the full symmetrical path shown in Fig. 3.2 in the BZ, with the valence-band maximum set to zero. (**c**): QP band structures in the vicinity of K-H path of the five considered stacking arrangements and real-space distribution of the two highest occupied and the two lowest unoccupied bands at the K (left) and at the H (right) point in the BZ. The band character is indicated by the color code of the corresponding atomic species (B: pink, N: blue), while the box frame points to the corresponding electronic states marked in the band structures. The valence-band maximum is set to zero.

bands (VB-1/VB) and the B-like bands (CB/CB+1) are split (degenerate) along the K-H path when the atoms of the same species in unit cell are (not) on top of each other (see Fig. 3.15). This energy splitting reflects the weak electrostatic interaction between atoms of the same species.

In Fig. 3.15.c, we plot the real-space distribution of the VB-1/VB and CB/CB+1 at the K and H points in order to visualize the effect of the stacking on the QP gap states. As in AA′ stacking, the VB-1/VB and the CB/CB+1, with N- and B-like character, respectively, are degenerate in all stackings at H point in the BZ. The corresponding electronic distribution of each band is spread over only one h-BN layer in unit cell. However, at the K point the VB-1/VB and the CB/CB+1 are either energetically degenerate or split as mentioned above. The electronic distribution of these bands spreads uniformly over both h-BN layers in the unit cell of all stackings as in AA′ configuration. This distribution is valid also along the K-H path. Except for the AB arrangement, the VB-1/VB and the CB/CB+1 are almost split along the K-H path in the BZ and are therefore spread over only one h-BN layer in unit cell, like at the H point. These different electronic distributions will lead to several e-h pair extensions since the absorption onset basically arises from these QP gap states.

3.3.2 Absorption spectra vs. stacking arrangement

The absorption spectra of the five considered stackings given by including(BSE) and neglecting (IQPA) the e-h interaction are shown in Fig. 3.16. c. The BSE solutions are indicated by red bars, while their intensity represent the oscillator strength. The corresponding stackings and band structures in the vicinity of the K-H path are also presented in order to ease the comparison and the discussion of the relationship between the structural, electronic, and optical properties. The sharp excitonic peak found in bulk h-BN (AA′ stacking) is preserved in all stackings. This is due to the poor screening effect in h-BN which enhance the e-h interaction, and thus independent of the stacking arrangements. This peak is followed by a broad hump formed by band-to-band transitions as can be seen in the independent QP spectra. While the excitonic character of the absorption onset is preserved, its intensity and excitation energy depend on the layer patterning. This is a direct consequence of the differences in the structural and the electronic properties.

As example, the intensity of the absorption onset in AA′, AA, and AB arrangements are quite similar while their energies differ due to the varying direct QP gap (see Table 3.2). In this arrangements most excitations are either very intense or forbidden (see red bares in Fig. 3.16. c).

In the A′B and AB′ stackings, the spectrum is red-shifted compared to the other structures. This shift reflects their small gaps (see Table 3.3) with respect to the AA′ arrangement. Concomitantly, the lower symmetry of these two configurations and the reduced wave-function overlap between the contributing QP states are responsible for the larger number of weak and allowed excitations (see red bares in Fig. 3.16.c).

Table 3.3: Excitation energy of the first and the second doubly degenerate (x2) excitons. The sharp excitonic peak in each stacking is dominated and centered by the second (x2) exciton, expect in the AA stacking where the first (x2) dominate its sharp peak. The first (x2) exciton is optically forbidden (allowed) in those stackings where inversion symmetry is present (absent).

	minimum direct	$E_{excitation}$ (eV)		Inversion sym
	QP-gap	1st exciton (x2)	2nd exciton (x2)	
AA′	6.33	**5.50**	5.57	√
AA	5.89	5.34	5.71	X
AB	6.16	5.48	5.59	X
A′B	5.05	**4.73**	4.74	√
AB′	5.64	**5.04**	5.14	√

Focusing on the absorption onset, the sharp peak is dominated by a double degenerate exciton in all stackings (see red bares in Fig. 3.16. c). We notice that in the AA′, AB′ and A′B arrangements where the layers are linked by inversion symmetry (see Fig. 3.1), the first twofold degenerate exciton is optically forbidden (dark). In these cases the absorption onset is dominated by the second doubly-degenerate exciton. However, in the AA and AB arrangement where the inversion symmetry is absent, the first doubly-degenerate exciton is optically allowed (bright). The absorption onset in the latter cases embraces also this lowest-energy bright exciton. To sum up, the layer patterning in h-BN strongly impacts the resulting excitation's energy and intensity, reflecting the diversity in the electronic properties (see subsection 3.3.1). Moreover, the presence of the inversion symmetry in such layered material leads to switching off the lowest-energy exciton.

3.3.3 Stacking-exciton relationship

In order to provide a clear rationale between exciton character and layer stacking, in the following we analyze the different types of e-h pairs that can appear in the considered configurations with respect to those found in the AA′ arrangement of bulk h-BN (see last section). We focus on their spatial distribution in relation with the character of contributing QP states and discuss their appearance by symmetry considerations.

AA and AB stacking arrangements

In Fig. 3.17 we display the optical spectra of the AA and AB arrangements together with the real and reciprocal distribution of highlighted main excitons.

The sharp excitonic peak in AB stacking is centered at 5.60 eV. Owing to the lack of inversion symmetry, the lowest-energy excitons is bright. The sharp excitonic peak in this case embraces both first and second doubly degenerate excitons at 5.48 and 5.60 eV. They exhibit a 2D like distribution (see Fig. 3.17) with binding energy of 0.67 and 0.57 eV, respectively. By examining the electronic structures one can see that the lowest energy

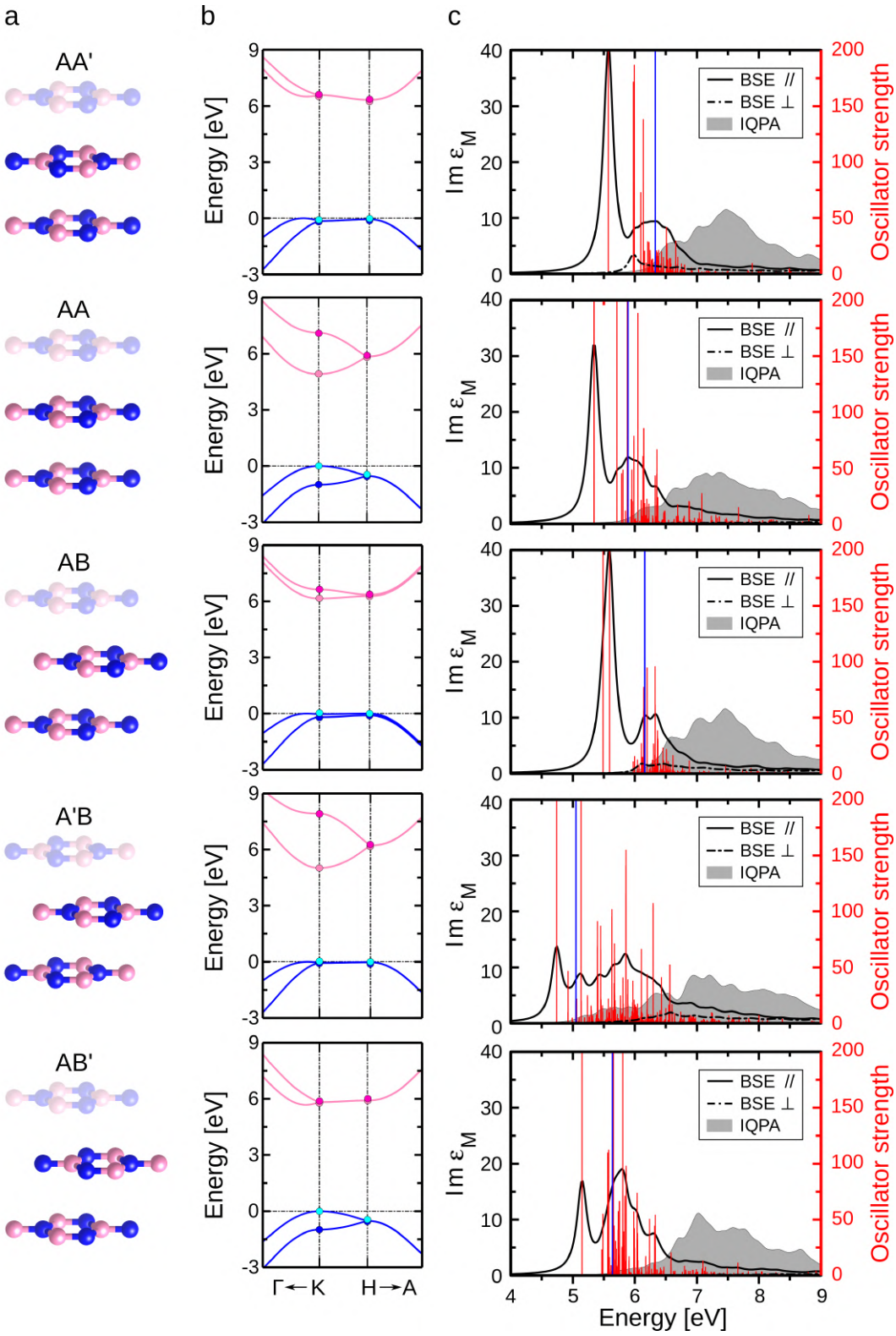

Figure 3.16: (**c**): Optical spectra computed by including excitonic effects (BSE: solid line for the in-plane component and dotted-dashed line for the out-of-plane one) and neglecting them within the independent QP approximation (IQPA, shaded area) of the considered stacking arrangements. Red bars indicate the oscillator strength of the BSE solutions. The direct QP gap is indicated by blue line. The corresponding stacking and QP band structure along the K-H path in the BZ are shown, respectively, in (**a**) and (**b**).

and the second 2D excitons arises from VB-1 → CB and VB → CB+1 transitions, respectively, along the K-H path in the BZ. Consequently, in contrast to the AA′ arrangement where the 2D excitons can appear uniformly in both h-BN layer in the unit cell (see subsection 3.2.5), in AB stacking they can appear only on specific h-BN layer according to the electronic distribution of the involved bands (see Fig. 3.15.c). In case of transitions between the VB → CB and/or VB-1 → CB+1, charge transfer excitons can be formed (see Fig. 3.15.c).

As example, at 5.76 eV we found a doubly degenerate CT exciton with in-plane polarization and binding energy of 0.4 eV. It originates from VB → CB transition at the K point in the BZ (see Fig. 3.17). As discussed above, the hole and the associated electron sit on different inequivalent h-BN layers according to the wave-function distribution of the contributing bands, making CT exciton. The weak wave-function overlap of these bands is responsible for the reduced oscillator strength of these excitations with respect to that of the 2D exciton (see Fig. 3.15.c). In contrast to the CT exciton found in AA′ stacking, this exciton is doubly degenerate. The resulting in-plane distribution exhibits a trigonal shape as 2D exciton, extending up to five lattice parameters.

At higher energy, excitons with delocalized 2D distribution appear, dominating the broad hump above 6 eV. They exhibit a triangular-like shape and extended within h-BN layer up to ten lattice parameter as typical of higher-energy excitons in monolayer h-BN [42]. The layer selectivity of the contributing bands (see Figs. 3.17 and 3.15.c) prevents the vertical extension of this exciton as in 3D$-d$ one in AA′ stacking (see subsection 3.2.5). It is worth noting that this layer-selective localization of the K-S states observed in the AB stacking can be exploited to modulate the distribution of excitons. Specifically in case where h-BN is intercalated with other materials to form vdW heterostructure as shown in the next chapter.

As in AB configuration, the lack of inversion symmetry in AA stacking makes the twofold degenerate first exciton optically allowed. This exciton is located at 5.35 eV with binding energy of 0.55 eV, dominating the sharp peak at the onset (see Ref.3.17). It arises from VB-1 → CB transitions[3] around the K point in the BZ with a 2D like character as in AA′ and AB arrangements. Owing to the electronic distribution of the involved bands around the K point (see Fig.3.15), the 2D exciton can appear uniformly in both h-BN layers in contrast to the AB stacking. In the broad hump slightly below 6 eV, exciton with delocalized 2D character appears. It arises from VB-1 → CB transition around the H point in the BZ. The electronic distribution of the contributing bands in this case prevents the vertical extension, as in the AB stacking (see Fig. 3.8.c).

Finally, at the higher energy range (∼1.2 eV above absorption onset), excitons with

[3]For consistency with the other structures, also the AA stacking is represented in a unit cell containing two layers. On account of the resulting band folding, the transitions between VB and CB are optically forbidden and the first allowed transition is between VB-1 and CB at K point in the BZ. The latter transition gives the value of minimum direct QP gap (5.89 eV) shown in Tables 3.2 and 3.3, which coincide with the one given by IQPA spectrum in Fig. 3.16.c).

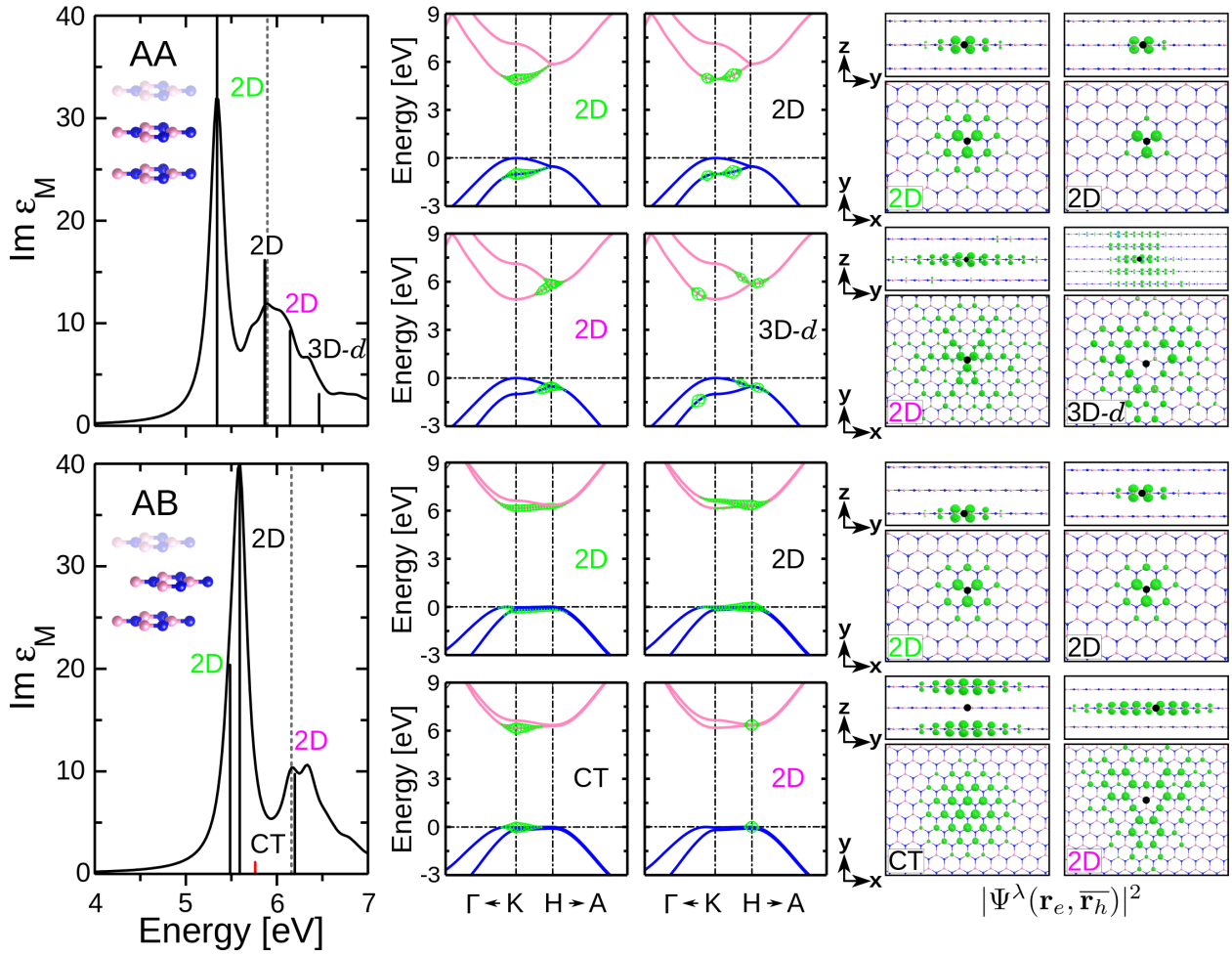

Figure 3.17: (Left): Optical spectra of the AA and AB stackings of h-BN (structures shown in the inset), computed by including excitonic effects (BSE). A Lorentzian broadening of 0.1 eV is included. The dotted line indicates the direct QP gap. (Center): Band contributions to the excitations marked in the spectra: The size of the green circles is representative of the weights (Eq. 2.50) of the involved QP states. The band character is indicated by the color code of the atomic species (B: pink, N: blue). The valence-band maximum is set to zero. (Right): Three-dimensional projections of the electron component of the e-h wave-functions highlighted in the spectrum, with the position of the fixed hole marked by the black dot.

very delocalized 3D distribution appear as found in higher energy range in the AA′ spectrum (see Fig. 3.14). To summarize, we have shown that the layer-selectivity of the electronic wave-functions in AB stacking strongly impact and enhance the localization of the e-h pairs on specific h-BN layer. In addition, the lack of the inversion symmetry in AA and AB configurations allows to switch on the corresponding lowest-energy dark exciton in the AA′ stacking. Moreover, in these stacking (AA and AB), delocalized 2D exciton dominates the broad hump above the sharp excitonic peak, preventing formation of 3D$-d$ exciton.

A'B and AB' configurations

To explore other stacking arrangements, in Fig. 3.18 we report the same analysis done in the last stackings for the highlighted excitons in the absorption spectrum of the A'B and AB' configurations. Their corresponding spectra differ from those of the last three arrangements (AA', AA and AB). As discussed in subsection 3.3.2, the red-shifted spectrum reflects the reduced minimum direct QP gap (5.05 eV in A'B and 5.64 eV in AB'). The electronic distribution of the QP states where the absorption onset arises (along the K-H path in the BZ) are spread over both h-BN layers in the unit cell as shown in Fig. 3.8.c. Since the layers are staggered in these two configurations (A'B and AB'), the wave-function overlap between the QP states is reduced. Consequently, the intensity of the excitonic peaks is quenched with respect to their counterparts in previously discussed stackings (AA', AA and AB).

Starting from the A'B stacking, the sharp peak is dominated by the second doubly degenerate exciton at 4.74 eV. This exciton stems from (VB-1 and VB) $\rightarrow$ CB transitions at the K point in the BZ. It is worth noting that in this system (B over B with inversion symmetry) the two highest-occupied bands which have N-like character, are degenerate and therefore uniformly distributed over both layers in the unit cell. Consequently, the electron and the hole distribution overlaps within the same layer as 2D exciton in AA' stacking. In addition they further extend uniformly and symmetrically to the two neighboring h-BN layers forming the 3D localized distribution (3D$-l$). This new type of exciton is not found in the last considered stackings (AA', AA and AB). The electron probability density is significantly enhanced in the layer where the hole resides, preserving the trigonal shape (see Fig. 3.18). The extended distribution of the e-h pair reflects the reported weak binding energy of 0.3 eV with respect to that of 2D one in the AA' stacking. We notice that the 3D$-l$ exciton appears regardless of the layer where the hole is pinned, due the wave-function distribution of the N-like VB-1/VB bands (see Fig. 3.8).

Owing to its parity with respect to the inversion symmetry, the lowest energy exciton at 4.73 eV in A'B configuration is optically forbidden. It originates from (VB-1 and VB) $\rightarrow$ CB transitions at the K point in the BZ. The corresponding electronic distribution looks similar to the 3D$-l$ bright exciton that dominates the sharp peak (see Fig. 3.18). Above 5 eV, the broad hump is mainly characterized by a number of delocalized excitations with 3D$-d$ distribution. Their in-plane distribution preserves the trigonal symmetry, similar to higher-energy excitons in monolayer h-BN [42]. Furthermore, the 3D$-d$ exciton extends uniformly and symmetrically over the nearest neighboring layers, as in AA' stacking. These excitons arises from VB-1/VB $\rightarrow$ CB/CB+1 transitions outside the K-H path in the BZ (see Fig. 3.18). In this region, the bands are split and their corresponding wave-functions are spread over both h-BN layers in the unit cell.

Similar behaviors, as in A'B configurations, are found in the AB' stacking (see Fig. 3.18). In both configurations A'B (AB') the staggered h-BN layers are linked by inversion symmetry, with B (N) atoms vertically aligned. Consequently, the resulting intensity of

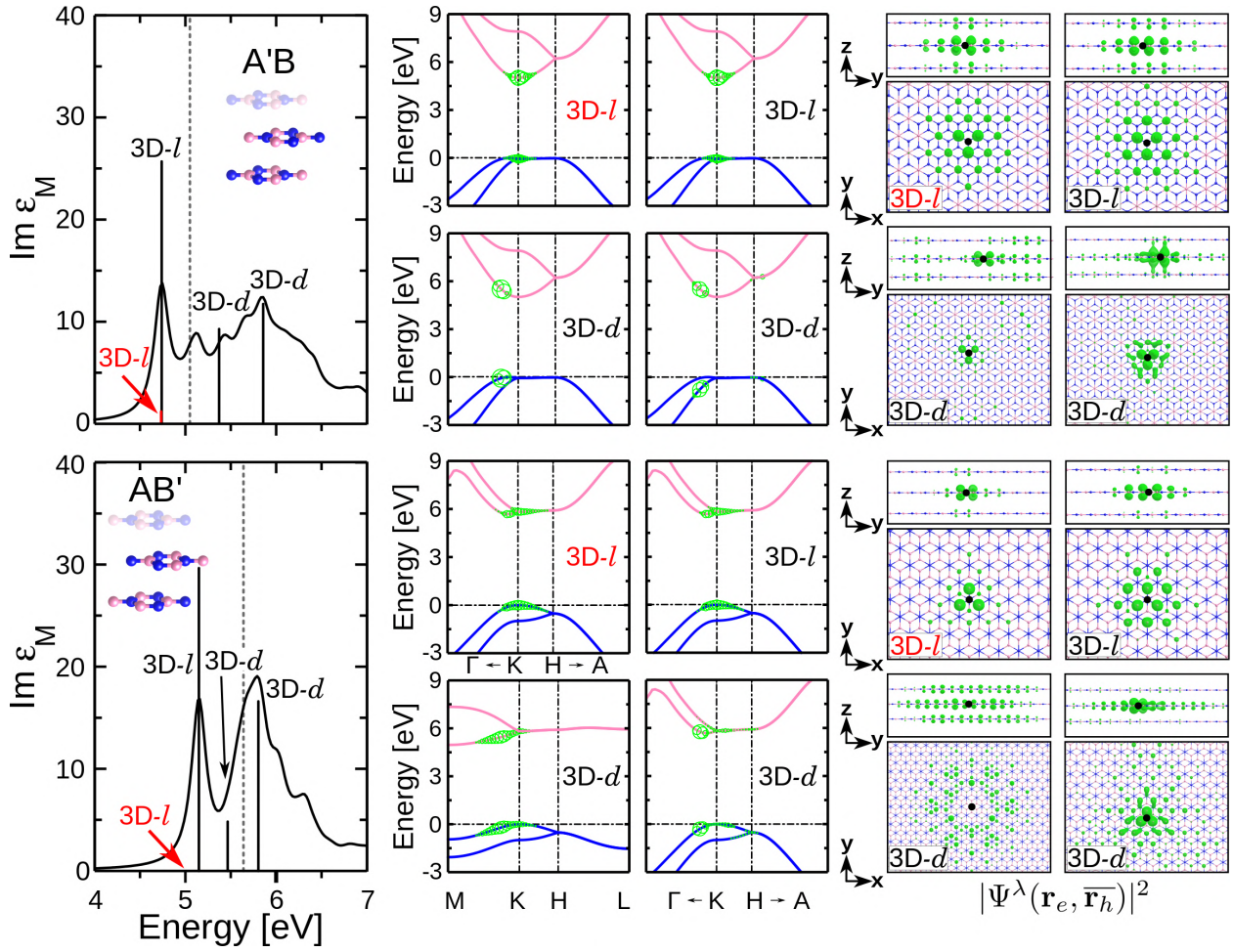

Figure 3.18: (Left): Optical spectra of the A'B and AB' stackings of h-BN (structures shown in the inset), computed by including excitonic effects (BSE). A Lorentzian broadening of 0.1 eV is included. The dotted line indicates the direct QP gap. (Center): Band contributions to the excitations marked in the spectra: The size of the green circles is representative of the weights (Eq. 2.50) of the involved QP states. The band character is indicated by the color code of the atomic species (B: pink, N: blue). The valence-band maximum is set to zero. (Right): Three-dimensional projections of the electron component of the e-h wavefunctions highlighted in the spectrum, with the position of the fixed hole marked by the black dot.

the peaks is also reduced with respect to that of the AA' stacking, as in A'B configuration. The main difference is the degeneracy of the CB/CB+1 in AB' stacking instead of VB-1/VB as in A'B arrangement. As a result, the direct QP gap as well as the excitation energy of the onset are different. The lowest energy exciton at around 5 eV is optically forbidden owing to its parity with respect to the inversion symmetry. The latter and the second doubly degenerate exciton that dominates the sharp peaks at 5.14 eV exhibit a 3D$-l$ distribution as in A'B stacking (see Fig. 3.18). The broad hump above 5.5 eV embraces several 3D$-d$ excitons. We notice that the different in-plane shape of the 3D$-d$ excitons reported in AA', A'B , and AB' is due to their atomic arrangements.

To sum up, in these two configurations, the splitting of the VB-1/VB or CB/CB+1 which reflect the vertical alignment of the atomic species leads to reducing the direct QP

gap and accordingly the energy of the absorption onset. Moreover, the overlap of the wave-functions distributed over staggered h-BN layers is reduced. Consequently, the intensity of the peaks is reduced with respect to the AA′, AA and AB configurations. Under all these conditions the 2D exciton in the AA′ stacking is extended in the vertical direction to form the 3D$-l$ distribution. The presence of inversion symmetry makes lowest-energy exciton optically forbidden, in both A′B and AB′ configurations.

In these stackings also, excitons with very delocalized 3D distribution, dominate the higher energy range (∼1.5 eV above the absorption onset). The distribution in this case resembles that shown in Fig. 3.14 for the AA′ configuration.

Summarizing the stacking-exciton relationship

In this subsection we summarize the types of excitations that can appear in bulk h-BN, and discuss their appearance by symmetry considerations. By varying the stacking arrangement of the individual layers we selected these types of e-h distribution (see Fig. 3.19) that basically cover all possibilities (see subsection 3.3.3).

Table 3.4: Representation of the different excitonic distributions shown in Fig. 3.19 that can appear in specific region either within the absorption onset (named region A) or in the broad hump above it (named region B) or ∼1.2 eV above the absorption onset (named region C) in each arrangement.

Str. arrangements		Region A		Region B		Region C	Region B
Stackings	Inver. sym.	2D$-l$	3D$-l$	2D$-d$	3D$-d$	3D$-vd$	CT
AA′	√	√	X	X	√	√	√
AA	X	√	X	√	X	√	X
AB	X	√	X	√	X	√	√
A′B	√	X	√	X	√	√	X
AB′	√	X	√	X	√	√	X

The 2D exciton can be localized (2D$-l$) in the in-plane direction or delocalized (2D$-d$)[4] as typical of higher-energy excitons in monolayer h-BN [42]. In bulk h-BN, e-h pair distribution can be extended in the vertical direction to the neighboring layers making 3D excitons. This exciton can be found in three level of extension, either localized (3D$-l$) or delocalized (3D$-d$) or very delocalized in all space as K-S distribution (3D$-vd$) (see Fig. 3.19). In case where the hole and the associated electron sit on different h-BN layers CT exciton is formed.

Depending on the stacking arrangements, the absorption onset of bulk h-BN is dominated by the localized ones either with 2D$-l$ or 3D$-l$ distributions (see Table 3.4) reflecting their bound character. While the lowest-energy excitons in AA′, AA, and AB configurations exhibit a 2D$-l$ character in A′B and AB′ stacking, this exciton is extended in the

[4]In addition to the abbreviation used for the different distributions such as 2D, 3D$-l$ and 3D$-d$, and CT excitons, here, in order to summarize and distinguish between the different types of excitons we refer to the localized (delocalized) 2D exciton by 2D$-l$(2D$-d$) and to the Kohn-Sham like very delocalized exciton by 3D$-vd$.

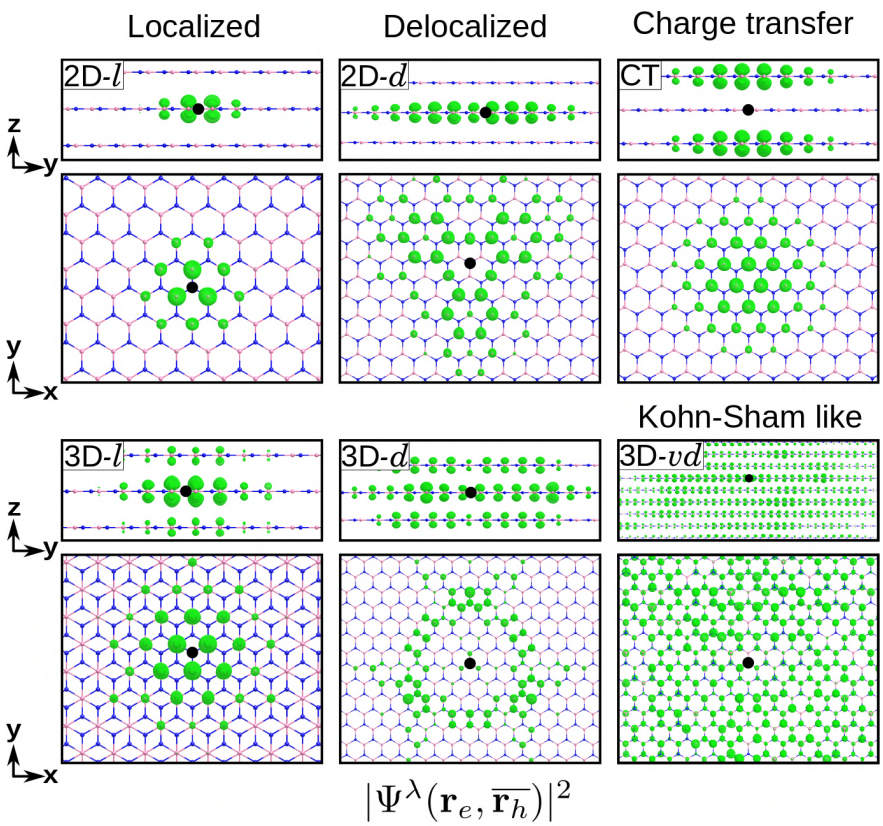

Figure 3.19: Three-dimensional projections of the electron component (green isosurface) of the e-h wave-functions, with the position of the fixed hole marked by the black dot. The different e-h type are classified depending on the dimensionality of the their distribution (2D, 3D, CT), either localized ($-l$) or delocalized ($-d$) or very delocalized in all the space ($-vd$) as Kohn-Sham states.

vertical direction to form 3D$-l$ distribution. This extension is due to the mixed character (transitions from the VB-1/VB to the CB in A'B stacking and from the VB to CB/CB+1 in AB' configuration) reflecting their wave-function distributions (see Fig. 3.15). This is a direct consequence of the vertical alignment of the same atomic species in A'B (here B atoms) and in AB' (here N atoms) stackings. The delocalized excitons either with 2D or 3D distribution dominate the high energy range of the spectrum (the broad hump). Their delocalization reflect the corresponding lower binding energy compared to the localized ones. The 2D$-d$ exciton in AA and AB stackings, where the inversion symmetry is absent, is due to the layer selectivity of the electronic distribution of the involved bands, preventing its extension in the vertical direction. However, 3D$-d$ excitons dominate the broad hump of the AA', A'B, and AB' stacking where the inversion symmetry is present. This exciton arises from transitions outside the H-K path in the BZ where the electronic distribution of the bands spread over all layers. 3D excitations with very delocalized distribution in the in-plane and the vertical direction (3D$-vd$) appear in all stackings at the end of the broad hump ($\sim$1.2 eV above the absorption onset). They arise from mixed transitions outside the K-H path in the BZ. Owing to their resonant character of band-to-band transitions, their distribution resembles (delocalized) Kohn-Sham states (see Fig. 3.19).

Finally, CT exciton can appear under specific conditions. In AA' stacking, it is bright only in the out-of-plane polarization. However, it is optically allowed in the in-plane polarization in the AB stacking. This exciton is a direct result of the layer selectivity of the involved bands at H point (see Fig. 3.15). The common point also between these stackings (AA' and AB) is that atoms of the same species never lie on to of each others. Under these conditions CT exciton appears. The CT e-h pairs are particularly intriguing in view of generating photocurrents [205, 206].

3.4 Tunability in other vdW layered materials

The exciting effect of the stacking arrangement in h-BN can be generalized also to other vdW materials in order to tune their intrinsic properties. We expect that such tunability can be found in most other materials. However, the conditions can differ from one material to others depending on their specific properties and structures. The argument is straightforward for stacked monolayers formed by binary compounds [124, 126, 127]. The same line of reasoning can be applied also to TMDs, where, also additional degrees of freedom arise from spin-orbit coupling and direct-indirect band-gap transitions that are known to occur in these systems upon increasing number of layers [123]. As example, it is found that interlayer (charger transfer) excitons exist only in an inversion symmetric bulk TMDs semiconductor [138]. For monoatomic 2D systems such as graphene, silicene, and germanene, the situation is apparently simpler. Different arrangements can be obtained in these materials only by tuning relative layer displacements, giving rise only to two possible sequences, namely AA and AB. Also, these 2D materials are typically semi-metallic, with this property being preserved independently of the layer stacking [207, 208]. More significant effects can appear once these systems are tailored into one- or zero-dimensional nanostructures, where a finite gap is opened by quantum confinement effects [209–212]. Finally, in group-V 2D materials, like phosphorene and arsenene, the size of the band gap and the optical spectrum have been shown to depend critically not only on the number of layers but also on their stacking order [128–135]. Our results can be exploited to further explore the tunability of the electronic and optical properties of these novel systems. Last but not least, it should be mentioned that in this study we have restricted ourselves to two layers in the unit cell and focused only on the ideal case of perfect lattice coincidence. This is a reasonable assumption in vdW bulk crystals, but superlattices and/or Moiré patterns are often observed in heterostructures (see, *e.g.*, Refs. [150, 213] for graphene/h-BN interfaces). Owing to the reduced symmetry of these systems, delocalized 3D excitations, even with extremely extended character, are expected to form more favorably, thereby promoting weakly-bound e-h pairs. These features obviously introduce further complexity and deserve a dedicated research.

4

Graphene/h-BN vdW heterostructures

In this chapter we investigate the structural, electronic, and optical properties including excitonic effects of vdW heterostructures formed by the vertical intercalation of graphene and h-BN nanosheets. These two building blocks exhibit similar structural parameters such as a planar geometry and in-plane hexagonal honeycomb lattice with a small mismatch (<1.7 %). The latter has already triggered several works to employ h-BN as substrate for high-quality graphene [140, 141]. Moreover, the gap opening in graphene by intercalation with h-BN layers has been extensively investigated in order to use it as building block for the next generation optoelectronic devices [43, 92, 145, 146, 214, 215].

Here, we consider vdW heterostructures with a graphene sheet sandwiched between h-BN layers and infinitely replicated by means of periodic boundary conditions. Employing density functional theory and many-body perturbation theory calculations, we address how the tailored combination of these vertically stacked 2D materials can give rise to peculiar optical excitations that are not present in the individual constituents.

4.1 Structures

In graphene/h-BN vdW heterostructures considered in this work, each unit cell contains three layers: one graphene sheet sandwiched between two h-BN layers, as shown in Fig. 4.1.a. In a realistic sample the two constituents are subject to lattice mismatch that in turn gives rise to complicated arrangements including finite twist angles and even Moiré patterns (see subsection 1.2.1). Owing to the difficulties related to simulate such complex systems, we consider that graphene and the two h-BN monolayers are commensurate. As a result, the unit cell which describes these heterostructures includes one unit cell of graphene and one of each h-BN monolayer (see Fig. 4.1.b). With this choice the unit cell contains 2 nitrogen (N), 2 boron (B), and 2 carbon (C) atoms (see Fig. 4.1.b). The swapping of the positions of B and N atoms in h-BN layer as well as their relative displacement (by one bond length) with respect to graphene give rise to twelve different combinations (see Fig. 4.2). We notice that these well defined stacking arrangements can be found locally in realistic systems where the stacking in not homogenous (see subsection 1.2.1). In these

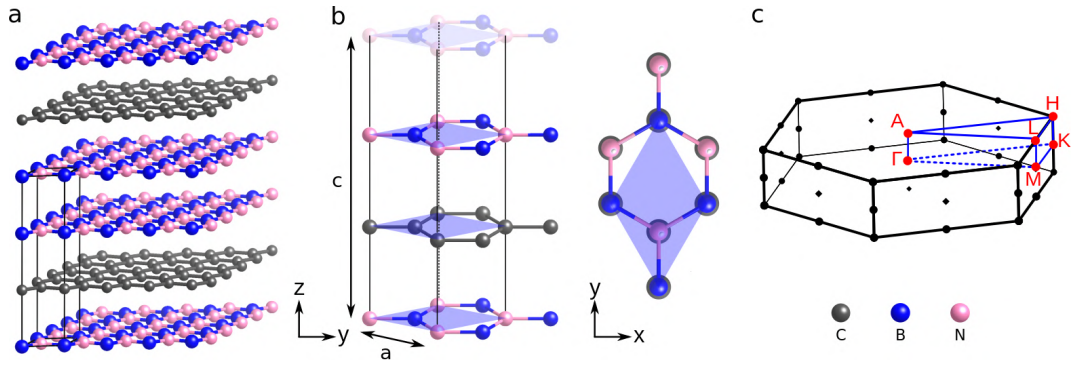

Figure 4.1: (**a**): Sketch of the vdW heterostructure considered in this work where the graphene sheet is sandwiched between h-BN layers and infinitely replicated by means of periodic boundary conditions. The black box indicates the unit cell that describes such a system. (**b**): Top and side view of the unit cell used to simulate the considered heterostructure. The graphene and h-BN are commensurate within one unit cell. The blue areas indicates the in-plane unit cell which contains 2N, 2B, and 2C atoms. The three layers included in the unit cell are shown in the foreground, while periodic image is shaded. (**c**): The corresponding first Brillouinn zone (BZ) with the high-symmetry points marked in red.

considered arrangements the three layers in the unit cell can be staggered and/or eclipsed and the atoms of different constituents are on top of each other and/or occupy the *hollow* positions. Consequently, the interlayer interaction is larger than in cases where the lattice mismatch is present. For this reason we consider that these simplest configurations are the ideal ones to investigate how the interlayer interaction gives rise to new features that are not present in the individual constituents. In addition, the investigation of these different stacking configurations allows to rationalize the structure-property relation in such vdW combinations.

Configurations nomenclature

In order to simplify the discussion, we label the twelve stacking arrangements considered in this work. We refer to the h-BN layers by either "A or B or C" to indicate their displacement with respect to the carbon sheet in the in-plane direction. The position of graphene is taken as reference and named "g" in all stackings. The "A", "B", and "C" positions, respectively coincide with the 1st carbon, 2nd carbon, and the hollow position of graphene in the unit cell according to the conventional nomenclature for stacked systems [100]. In these cases, the first atom in the unit cell of the corresponding h-BN layer is boron. If N atom occupy the first position in h-BN layer we add prime to the labels (A′, B′ and C′) (see Fig. 4.2)

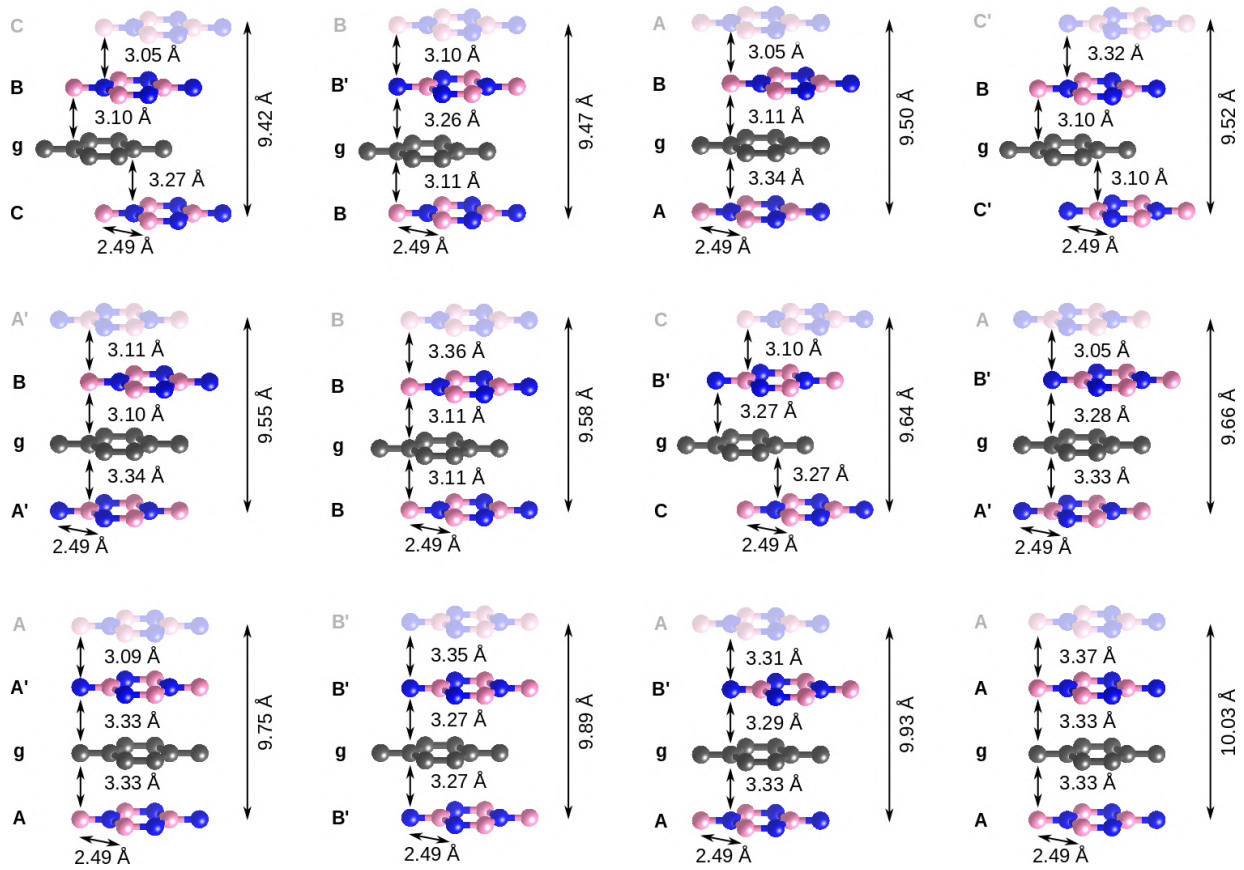

Figure 4.2: Sketch of the twelve considered stacking arrangements given by layer sliding by one bond length and/or swapping the positions of the atomic species within h-BN layers. The three layers included in the unit cell are shown in the foreground, while periodic images are shaded. The corresponding nomenclature of different configurations are also shown. The values of in- and out-of-plane lattice parameters are indicated together with black arrows. We notice that these configurations are ordered according to their out-of-plane *c* parameters. The B, N, and C atoms are pink, blue, and gray, respectively.

4.1.1 Lattice parameters

The twelve obtained stacking arrangements are shown in Fig. 4.2 together with their structural parameters. We notice that these parameters are given by groundstate DFT calculations using the GGA-PBE approximation [176] and the DFT-D2 approach [185] to account for vdW interactions.

In-plane lattice parameter

Since the unit cells of graphene and h-BN are commensurate within one unit cell in the considered graphene/h-BN vdW heterostructures, their in-plane lattice parameters should be the same (see Fig. 4.1). This condition can be realized by applying a strain to one of these layers. The in-plane lattice parameters of pristine graphene and bulk h-BN are around 2.46 Å and 2.50 Å, respectively. Consequently, the resulting lattice mismatch in this case is: $100(a_{h-BN} - a_{Graphene})/a_{h-BN} = 1.6\%$.

In vdW heterostructures, the in-plane lattice parameter is close to the one of h-BN, being 2.49 Å. This result indicates that the graphene sheet is more able to the in-plane strain than the h-BN sheet. We notice that the value of the in-plane lattice parameter remain constant in all considered stacking configurations. As a result, the weak interlayer interaction has no impact on the in-plane lattice parameter with respect to the strong in-plane bonding which dictate such distance.

Out-of-plane lattice parameter

The out-of-plane *c* parameter is strongly related to the stacking arrangement of the layers as shown in Fig. 4.2. It represents the sum of three interlayer distances between the three subunits. The vdW forces in our systems are responsible for keeping the layers at a given distance. However, by changing the stacking arrangement the interlayer distances change. This is a direct consequence of the different interactions between the vertically aligned atomic species [192, 196]. In Fig. 4.2, the twelve considered stacking arrangement are ordered according to their *c* parameters. We notice that this parameter is smaller in those stackings where the N atoms are not vertically aligned with N and C atoms of the neighboring layers. We have found that the interlayer distance between graphene and h-BN layers is smaller in the case where the B (N) atoms are vertically aligned with C atoms (occupy the *hollow* position in graphene). The largest ones are found in the case where the graphene and the h-BN layers are eclipsed which means that the B (N) atoms are vertically aligned with C (C) atoms. Likewise, the interlayer distance between h-BN layers is smaller in case where the N atoms are not vertically aligned as discussed in subsection 3.1.4.

The resulting smallest *c* parameter found in the C-g-B configuration reflects its atomic arrangement. In this case the N atoms of different h-BN layers do not lie on top of each other. In addition, the C atoms of graphene sheet coincide with B atoms of the h-BN layer above it and with N atoms of the h-BN layers below it. Consequently, the interlayer distance between graphene and the h-BN above it as well as between the h-BN layers are minimized giving rise to the smallest *c* parameter, being 9.42 Å.

The large *c* parameter (10.03 Å) is found in the A-g-A stackings where all layers are eclipsed. This means that all the corresponding atoms are vertically aligned which maximize the interlayer distances (see Fig. 4.2). Elsewhere, the c parameter range between the 9.42 Å and 10.03 Å. In those cases, the interlayer distances are maximized in between some layer and/or minimized in others depending on the vertical alignment of the atomic species.

4.1.2 Electronic charge density

In order to understand how the vertical alignment of the atomic species gives rise to different interlayer distances, we plot in Fig. 4.3 the in- and the our-of-plane projection

of the electronic charge density by taking C-g-B stacking as example. First, we notice that the excess of electronic charge in the vicinity of the N atoms is due to the enhanced electronegativity compared to the B atoms (see also subsection 3.1.3). As a result, the atomic centers of N (B) atoms are negatively (positively) partially charged, giving rise to a polar-like B-N bound [122, 192, 195, 196]. Secondly, the in-plane distribution of the electronic charge presented in Fig. 4.3.a shows that it is homogenous within the graphene layer. This distribution reflects the non-polar homo-nuclear C-C bonds [196].

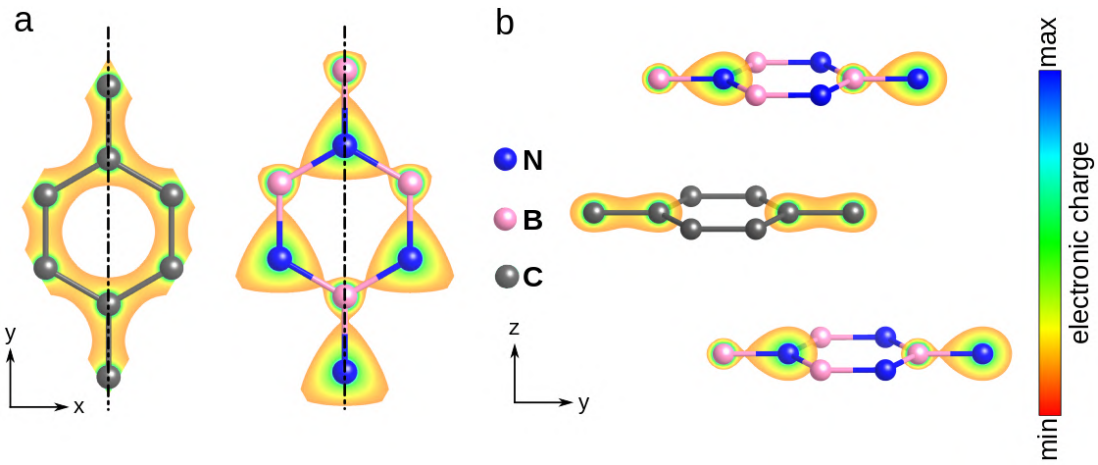

Figure 4.3: Electronic charge density in the C-g-B configuration. (**a**): In-plane projection within graphene and h-BN layers. (**b**): The out-of-plane projection within the layer indicated by dotted-dashed line in (**a**).

From the charge distribution around the graphene and h-BN atomic species (see Fig. 4.3), we can understand that the different interlayer distances shown in Fig. 4.2 reflect the electrostatic interaction between their corresponding vertically aligned atomic species as discussed in subsection 3.1.4 [192, 196, 198, 201]. We notice that the interlayer distance between graphene and h-BN layers is larger when the C and N atoms lie on to of each other. In this case, in addition to the electrostatic repulsion that arises from partial negative charge, the Pauli repulsion between overlapping electron clouds of C and N atoms leads to maximize such distance [201]. This distance is smaller in the case where the C and B atoms lie on top of each other since the atomic centers of B atoms are surrounded by a partial positive charges.

4.1.3 Stability

To understand the structure-stability relationship, we report the structural parameters of the twelve configuration in Table 4.1 together with the binding energy (E_b) given by:

$$E_b^{hetero.}(eV) = E_{tot}^{hetero.} - [E_{tot}^{Graphene} + 2E_{tot}^{h-BN}], \tag{4.1}$$

where E_{tot} represent the total energy per unit cell of the corresponding system (heterostructure, isolated graphene and isolated h-BN sheet). We notice that the values reported in Table 4.1 allow only to order and discuss the more favorable configurations. However, the stability in realistic system can be deduced from phonon investigation which goes beyond the scope of this work and will be addressed in a dedicated study. The different configurations are ordered according to their out-of-plane c parameter. From Table 4.1, we can see clearly that the most favorable configurations are the ones that exhibit a smaller c parameters. The reduced electrostatic and Pauli repulsions between the partially charged atomic centers leads to reduce the interlayer distance, showing a better stability. Since these repulsions can be modulated by vertical alignment of the atomic species, the interlayer distance and stability are strongly related to the stacking arrangements (see Table 4.1). Hence, in the inhomogenous stacking in realistic system larger stability is to be expected compared to our ideal arrangements, where the interlayer interactions are maximized (see subsection 1.2.1).

Table 4.1: Structural parameters and binding energies of different stacking configurations of graphene/h-BN vdW heterostructure considered in this work.

Stackings	Lattice constant(Å)		Binding energy (eV)
	a	c	E_b
C g B	2.49	9.42	-0.80
B g B′	2.49	9.47	-0.79
A g B	2.49	9.50	-0.79
C′g B	2.49	9.52	-0.78
A′g B	2.49	9.55	-0.78
B g B	2.49	9.58	-0.78
C g B′	2.49	9.64	-0.76
A′g B′	2.49	9.66	-0.76
A g A′	2.49	9.75	-0.75
B′g B′	2.49	9.89	-0.72
A g B′	2.49	9.93	-0.72
A g A	2.49	10.03	-0.71
Graphene	2.46		
h-BN	2.50		

4.2 Electronic properties

The vdW heterostructures considered in this work are constructed by combining a large band gap material (h-BN) with a semi-metal (graphene). The first questions that we can ask are on the character of the resulting electronic properties as well as the impact of the layer patterning on these properties. To answer these questions we plot the resulting electronic band structure of graphene/h-BN vdW heterostructure in C-g-B configuration given by the DFT-GGA method in Fig. 4.4. To ease the discussion, in the same figure,

we plot the electronic band structure of the individual constituents which are graphene and bulk h-BN in the AB stacking arrangements. The choice of the AB stacking for the bulk h-BN is due to the fact that the h-BN layers in C-g-B configuration exhibit an AB arrangement.

4.2.1 From building blocks to vdW heterostructures

After combining these building blocks in C-g-B configuration, the resulting band structure looks like a superposition of the individual constituents ones. We notice that all graphene and h-BN characteristics of the bands are basically preserved. This result reflects the nature of this assembly which preserves the individual layers without any modifications.

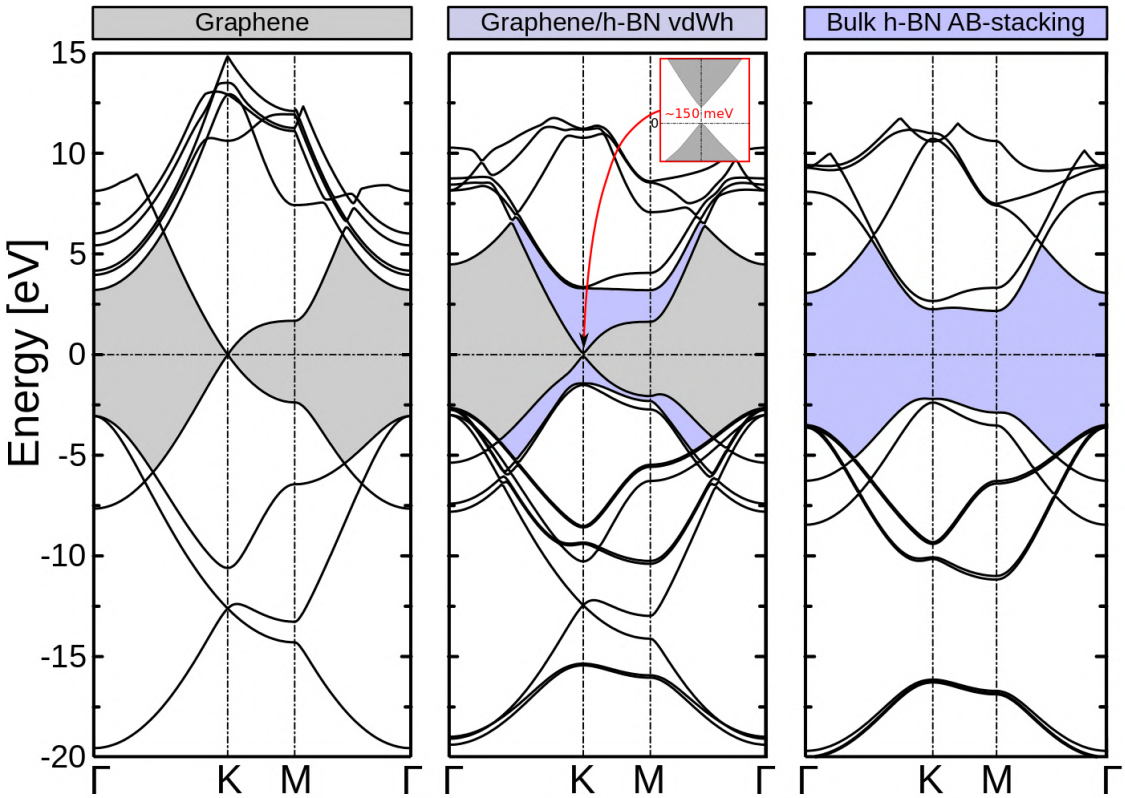

Figure 4.4: Electronic band structure, along the Γ-K-M-Γ path in the BZ (see Fig. 4.1.c), of graphene (left), graphene/h-BN vdW heterostructure in the C-g-B configuration (center), and bulk h-BN in AB stacking (right). The zoom of the band structure of the vdW combination around the K point is shown in the red box. The maximum of the valence band is set to zero. The blue and gray shaded areas indicate the large gap in h-BN and the zero gap in graphene, respectively.

We noticed new features related to the mixed character of some bands specifically around the gap region as well as the opening of small gap between graphene bands. First, the mixed character of the bands is a direct consequence of the weak interaction between layers (hybridization). Second, the band gap opening between graphene band

is also due to such interlayer interaction. At the K point in the BZ, the VB/CB bands of graphene have π/π^*-like character from both inequivalent C atoms in the unit cell. This means that their corresponding orbitals exhibit the same energy at the K points. However, the intercalation of graphene between h-BN layers breaks the symmetry within the layer such that each C atom in the unit cell is in different environment (different neighboring atoms). In this configuration (C-g-B stacking) the two C atoms are under two different environment. In one hand, the first C atoms of graphene in the unit cell is vertically aligned with N atoms of the h-BN layer below it and with the *hollow* position of the h-BN layer above it (see Fig. 4.5. left). On the other hand, the second C atom is vertically aligned with B atom of the h-BN layer above it and with the *hollow* position of the h-BN layer below it. Consequently, the two inequivalent C atoms of graphene in the unit cell are under two different potential generated by oppositely and partially charged atomic centers of, respectively, N and B atoms in the vertical direction. As a result, the corresponding VB/CB bands are now energetically split at the K point in the BZ (see red box in Fig. 4.4). In addition, each band is now dominated by only one C atom such that the CB (VB) band is dominated by the first (second) C atom which is vertically aligned with N (B) atom. This splitting is due to the additional (minus) energy, induced by the different vertical potential of N (B) which shift up (down) the CB (VB) band. This shift defines the size of the band gap in graphene which is around 150 meV in C-g-B case (see Fig. 4.5). This heterostructure, which is a semiconductor, exhibits a *straddling* band alignment since the graphene band gap is inside the h-BN one. This *type I* electronic configuration is exploited for applications such as lasers and light-emitting diodes (LEDs) [220]. As discussed above the character of the bands is basically preserved. The VB-1/VB-1 (CB+1/CB+2) bands are dominated by the N (B) atoms as in bulk h-BN. In these cases we neglect the very small contribution from the C atoms. Likewise, the VB/CB bands which are dominated by C atoms in graphene preserve their character. Here we notice that the VB band is also dominated by the N atoms outside the K-H path in the BZ. This mixed character reflects the small hybridization due to weak interlayer interaction.

4.2.2 Electronic band structure vs. stacking arrangement

Now, we consider C′-g-B stacking arrangements where all layers are staggered and the two inequivalent C atoms have the same neighboring atoms (see Fig. 4.5). Since the C atoms are in the same environment the corresponding VB/CB bands exhibit the same energy at the K point in the BZ, preventing the opening of the gap. This result shows that the opening of the band gap in graphene can be controlled through the layer patterning. We notice that the VB-2/VB-1 bands are now split along the K-H path in the BZ. This is a direct consequence of the arrangement of the h-BN layers, where the N atoms lie on top of each other, as in bulk AB′ configuration (more detail can be found in subsection 3.3.1.

Now, we consider the twelve stacking arrangements in order to understand its effect

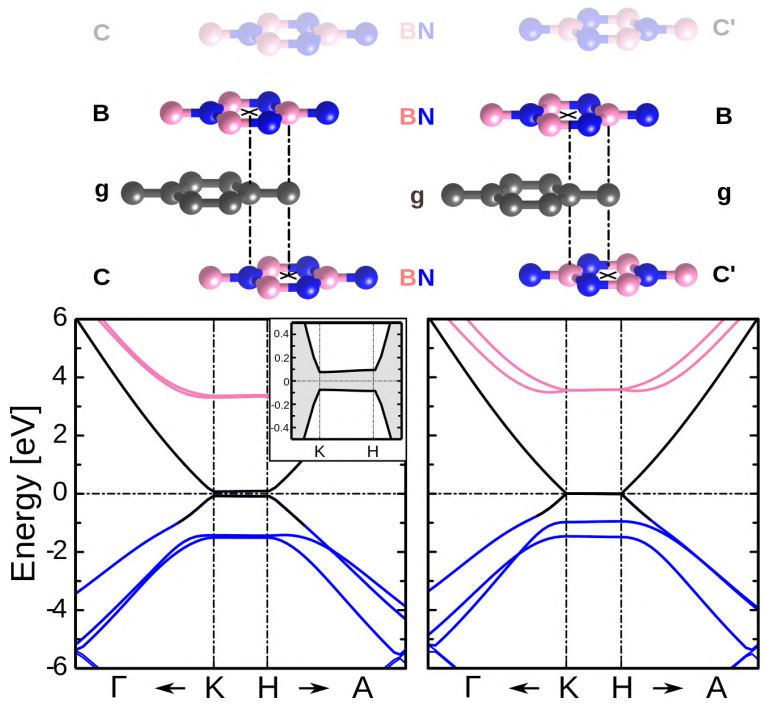

Figure 4.5: Electronic band structures in the vicinity of the K-H path in the BZ of C-g-B (left) and C′-g-B (right) configurations. The dotted-dashed lines in the structures above indicate the different (same) neighboring atoms of the two inequivalent C atoms in C-g-B (C′-g-B) stacking. The character of the bands is indicated by the atomic color code. The B, N, and C atoms are pink, blue, and gray, respectively.

on the electronic band structure (see Fig. 4.6). According to their band gap the configurations are classified into semiconducting (within the green box) and semi metallic (within the red box). The resulting band structures of different configurations given by DFT-GGA method are quit similar. This result shows that the vdW combination basically preserves the intrinsic bands of the constituents even if the stacking is changed. However, the degeneracy and the splitting of these bands along the K-H path in the BZ can be strongly tuned by layer patterning. The N-like bands (VB-2/VB-1) and the B-like bands (CB+1/CB+2) are split (degenerate) along the K-H path when the atoms of the same species are (not) on top of each other. This energy splitting reflects the weak electrostatic interaction between atoms of the same species from the two inequivalent h-BN layers in the unit cell. This result observed in bulk h-BN (see subsection 3.3.1) is also preserved in these heterostructures. So far, focusing on the band gap opening between graphene bands the layer patterning have a strong impact on it. In all the semiconducting configurations the two inequivalent C atoms exhibit a different neighboring atoms (different environment) as discussed for Fig. 4.5. Consequently, the VB/CB band split at the K point in the BZ, giving rise to a small band gap. However, in case where the two inequivalent C atoms are in similar environmental (similar neighboring atoms) the corresponding VB/CB bands are degenerate at the K point giving rise to the semi metallic configurations (see Fig. 4.6).

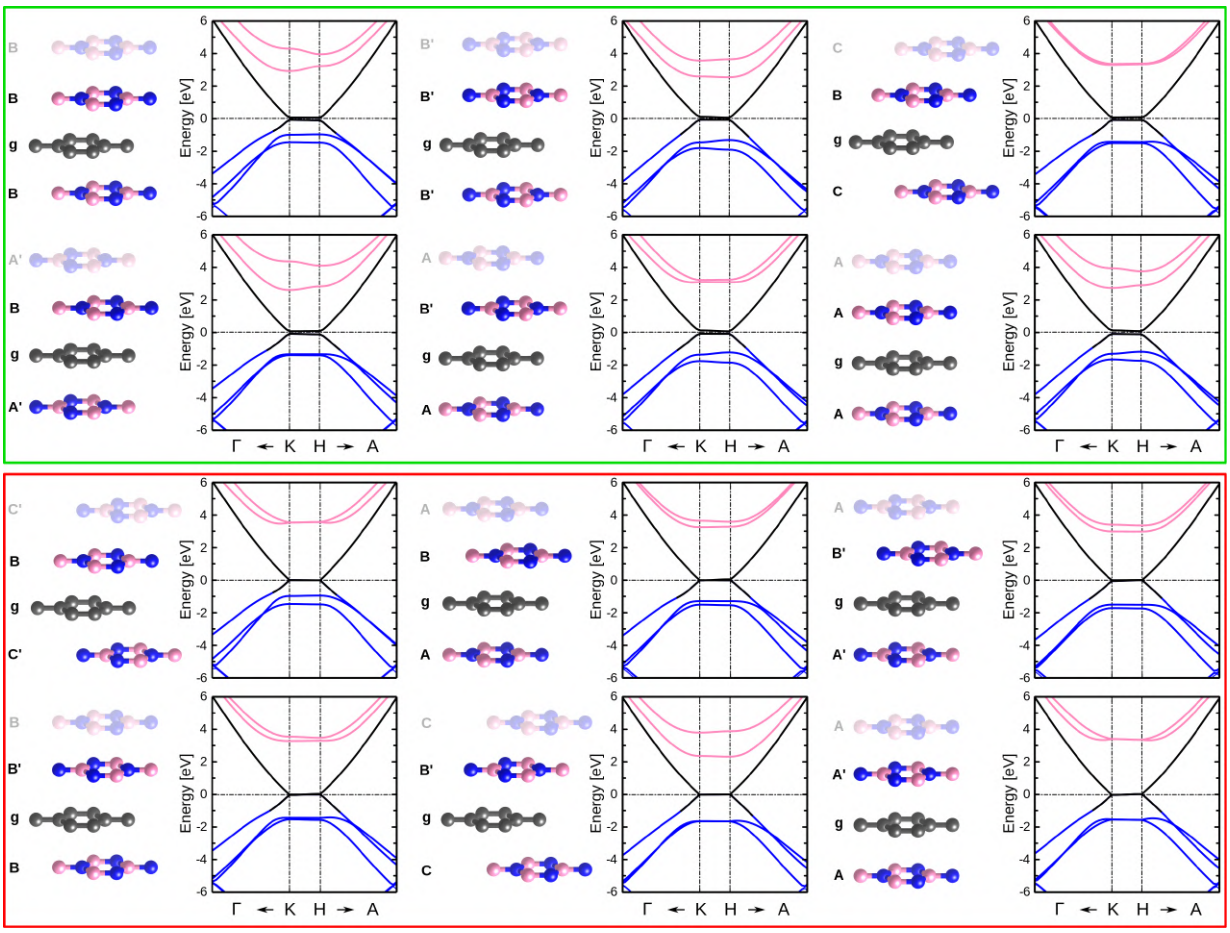

Figure 4.6: Electronic band structures of the twelve considered stacking arrangements of graphene/h-BN vdW heterostructures around the K-H path in the BZ. The green and the red boxes include the semiconducting and the semi-metallic configurations, respectively. The character of the bands is indicated using the atomic color code. The B, N, and C atoms are pink, blue, and gray, respectively.

To sum up, the considered graphene/h-BN vdW heterostructures preserve the electronic properties of the individual constituents to a large extend. It gives rise to new features due to the weak interlayer interaction such as the mixed character of some bands and the opening of the gap between graphene bands. This latter makes such vdW combinations useful for optoelectronic applications. We have shown that this characteristic can be tuned by layer patterning depending on the neighboring atoms that lie with the two inequivalent C atoms (see Fig. 4.5).

4.3 Semi-conducting configurations

In this section we investigate the effect of the stacking arrangement on the electronic properties of the semiconducting configurations of graphene/h-BN vdW heterostructures. From DFT and MBPT investigation we focus on the size and character of the resulting band gap as well as the wave-function distribution of the QP states along the K-H that in

the BZ (gap region).

4.3.1 Tuning the size of the band gap by layer patterning

As presented in Fig. 4.6, we have 6 semiconducting combinations which fulfill the condition that the two inequivalent C atoms exhibit a different neighboring atoms. In Table 4.2 we report the DFT and the QP gaps of the different semiconducting configurations (ordered from the smallest to the largest QP gap). The size of the DFT gap ranges between 125 and 180 meV depending on the stacking arrangement. The G_0W_0 correction leads to increase these gaps to range between 245 and 325 meV.

Table 4.2: Electronic band gaps of the semiconducting stackings given by DFT-GGA and G_0W_0 approach.

Stackings	DFT gap (meV)	G_0W_0 gap (meV)
B g B-stacking	131	248
B'g B'-stacking	126	262
C g B-stacking	151	263
A'g B-stacking	157	275
A g B'-stacking	156	295
A g A-stacking	177	322

The large value of the QP band gap is found in A-g-A stacking where the first (second) C atom is vertically aligned between two B (N) atoms in the unit cell. The two inequivalent C atoms in this case are under two different maximized electrostatic potential generated by oppositely and partially charged atomic centers of B and N atoms. Consequently, the CB (VB) band at the K point is energetically shifted up (down) with maximal value, giving rise to the largest QP band gap ($\sim$ 320 eV). The smallest band gap is found in the B-g-B arrangement. One inequivalent C atom in the unit cell occupies, in this case, the *hollow* position of the two neighboring h-BN layers and the second C atom is vertically aligned with B atoms of both h-BN layers. As a result, only CB band is shifted up due to the weak interaction with B atoms giving rise to the smallest QP band gap ($\sim$ 250 eV).

4.3.2 Quasi-particle band structure

From now on, we consider only the two semiconducting B-g-B and the C-g-B configurations in order to investigate the following properties. These to configurations are considered as the most favorable semiconducting ones (see Table 4.1). In Fig. 4.7, we present their electronic band structures given by DFT-GGA and G_0W_0@GGA approach, along the full path in the BZ (see Fig. 4.1.c). By setting the maximum of the valence band to zero we can see clearly that the G_0W_0 corrections (red line) lead to shift up all the conduction bands with respect to the DFT ones (black line). In addition, we notice that the other valence bands (VB-1/VB-2/...) are also shifted down.

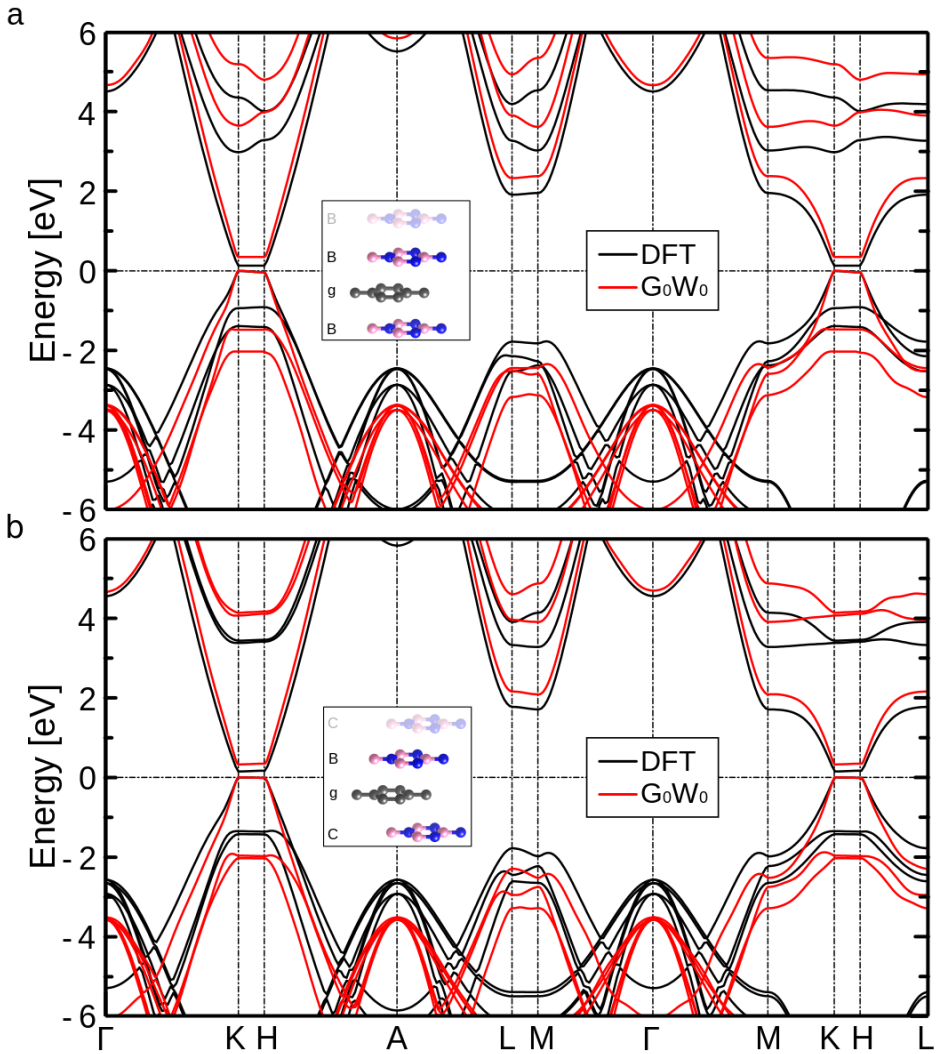

Figure 4.7: DFT (black) and quasi-particle (red) band structure of (**a**) B-g-B and (**b**) C-g-B heterostructures along the full path in the BZ (see Fig. 4.1.c). The valence-band maximum is set to zero. The B, N, and C atoms are pink, blue, and gray, respectively.

The value of this shift depends on the bands since they exhibit different origin and character. In both configurations the graphene-like CB bands, given by the G_0W_0 approximation, are shifted up with a very small value (around 120 meV) along the K-H path in the BZ. However, the N-like (VB-1/VB-2) and the B-like (CB+1/CB+2) bands are shifted down and up, respectively, with larger values (around 0.7 eV up and 0.7 eV down) along the K-H path in the BZ. The large shift in the h-BN-like bands reflect the significant e-e interaction due to weak screening effect in such materials. However, the small shift in garphene-like bands is due to the pronounced screening effect in graphene. This means that the electrons are close to the uniform electron gas picture which is captured quite well already in the DFT-GGA level.

In these vdW combinations the simple scissor operator, which represents the value needed to shift the DFT bands to the QP ones, cannot be used since the shift value depends on the bands and the **k**-points. Focusing on the differences between the band

structures of these two configurations we notice that the VB-2/VB-1 and the CB+1/CB+2 bands are split in the B-g-B stacking and degenerated in the C-g-B configuration along the K-H path in the BZ. This is dictated by the vertical alignment of the N and B atoms (see subsection 4.2.2) consistent with that found for bulk h-BN in their corresponding AA and AB stackings, respectively (see Fig. 3.15).

Renormalization of the h-BN QP gap

In order to analyze in detail the changes in the electronic structure produced by introducing graphene between h-BN layers, we compare the resulting gap between the VB-1 and CB+1 bands in the C-g-B stacking with that found in bulk h-BN in the corresponding AB arrangement (see Fig. 4.8). By introducing graphene sheet, the DFT gap between h-BN bands in the heterostructure increases with respect to that found in bulk h-BN system. At the K point in the BZ, the difference between the DFT gap (between the h-BN-like VB-1/CB+1 bands) in the C-g-B heterostructure and the gap in bulk h-BN (AB stacking), is: ΔE_g^{DFT}=4.72 - 4.45 = 0.27 eV. At this level, all changes are induced due to structure relaxations and electrostatic interactions caused by weak hybridization between graphene and h-BN electronic states.

In contrast to DFT results, the G_0W_0 band gap between h-BN like (VB-1/CB+1) bands is getting lower in heterostructure than in bulk h-BN system ($\Delta E_g^{G_0W_0}$=6.01-6.17=-0.16 eV). We ascribe the reduces of the QP gap in the heterostructure to the so-called charge image effect (polarization effect) [221–223] induced by the dynamical charge fluctuation, within graphene sheet, on the neighboring h-BN layers. Owing to the non-local nature of such interactions, the renormalization of the h-BN like bands cannot be captured by the DFT method. For this reason, this effect is observed only at the G_0W_0 level, where the non-local interactions are also considered. As a result, in order to evaluate the shift induced by the polarization on the h-BN like bands in the heterostructures (Δ_p), we neglect the weak hybridization between electronic states found at the DFT level by subtracting the ΔE_g^{DFT} from the $\Delta E_g^{G_0W_0}$ as follow:

$$\Delta_p = \Delta E_g^{G_0W_0} - \Delta E_g^{DFT} = -0.16 - 0.27 \sim -0.4\text{eV}. \tag{4.2}$$

At the H point, we found similar value of the renormalization of the h-BN-like bands. We notice that the renormalization values of the h-BN bands found in other vdW configurations are quit similar to that found here in the C-g-B stacking which is around 0.4 eV. Such a renormalization in the band gap is also observed in h-BN monolayer physisorbed on a graphite substrate [221, 222], which have been extensively discussed also for molecules and polymers adsorbed on graphene [223]. This non-local interaction is essentially dominated by the correlation term as reported in Ref. [224].

To sum up, for predicting the electronic structure of the considered vdW heterostructures the methodology that goes beyond DFT is required due to the importance of the

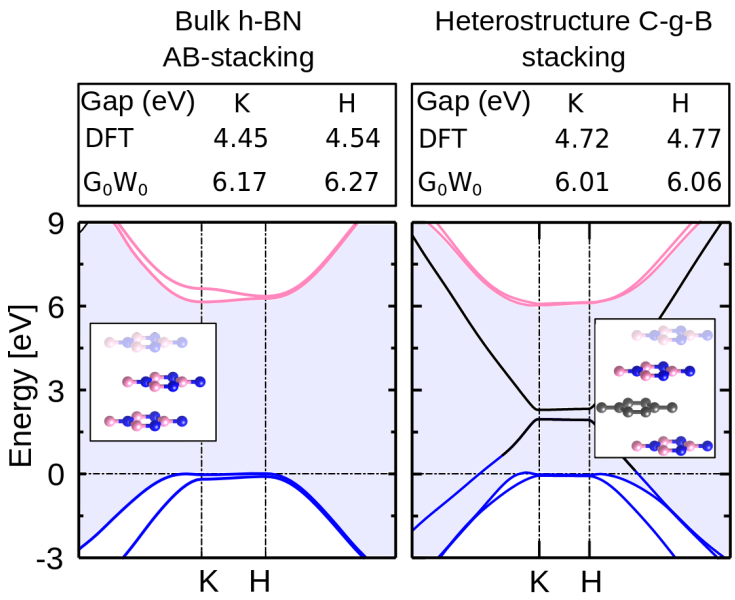

Figure 4.8: Quasi-particle band structure in the vicinity of the K-H path of the Bulk h-BN in the AB stacking (left) and C-g-B heterostructure (right). The shaded area indicates the gap between the h-BN bands. In the C-g-B stacking, the VB-1 bands is set to zero. The values of the the gap at K and H point are indicated above the corresponding band structure. The character of the band is indicated using the atomic color code. The B, N, and C atoms are pink, blue, and gray, respectively.

non-local correlations.

4.3.3 Distribution of Kohn-Sham states

In order to ease the study of the effect of the stacking arrangement on the character of the resulting bands in the gap region, we plot the electronic wave-function distribution of the VB-2/VB-1/VB as well as the CB/CB-1/CB+2 bands at K and H points in the BZ (see Fig. 4.9). This choice is due to the fact that most excitations in the following study arise from transitions between QP states around the gap region. In the B-g-B stacking the VB-2/VB-1 (CB+1/CB+2) bands are split along the K-H path since the N (B) atoms of the inequivalent h-BN layers lie on top of each other. However in the case of C-g-B stacking these bands are almost degenerate since their corresponding atoms are not vertically aligned, avoiding any electrostatic interaction. In this case the small splitting (around 80 meV) of the VB-2/VB-1 (CB+1/CB+2) bands is due to the different neighboring atoms of the two inequivalent N (B) atoms in the unit cell as reported for the bulk AB stacking (see details in subsection 3.3.1). We notice that the VB bands of both stackings are dominated by the C and N atoms outside the K-H path in the BZ. This mixed character reflects the weak interlayer interaction between graphene and h-BN layers.

At the K point in the BZ the C-like VB/CB bands exhibit a π/π^*-like character and distributed over different C atoms (inequivalent C atoms in the unit cell). In pristine graphene these bands are degenerate at the K point and dominated by both C atoms

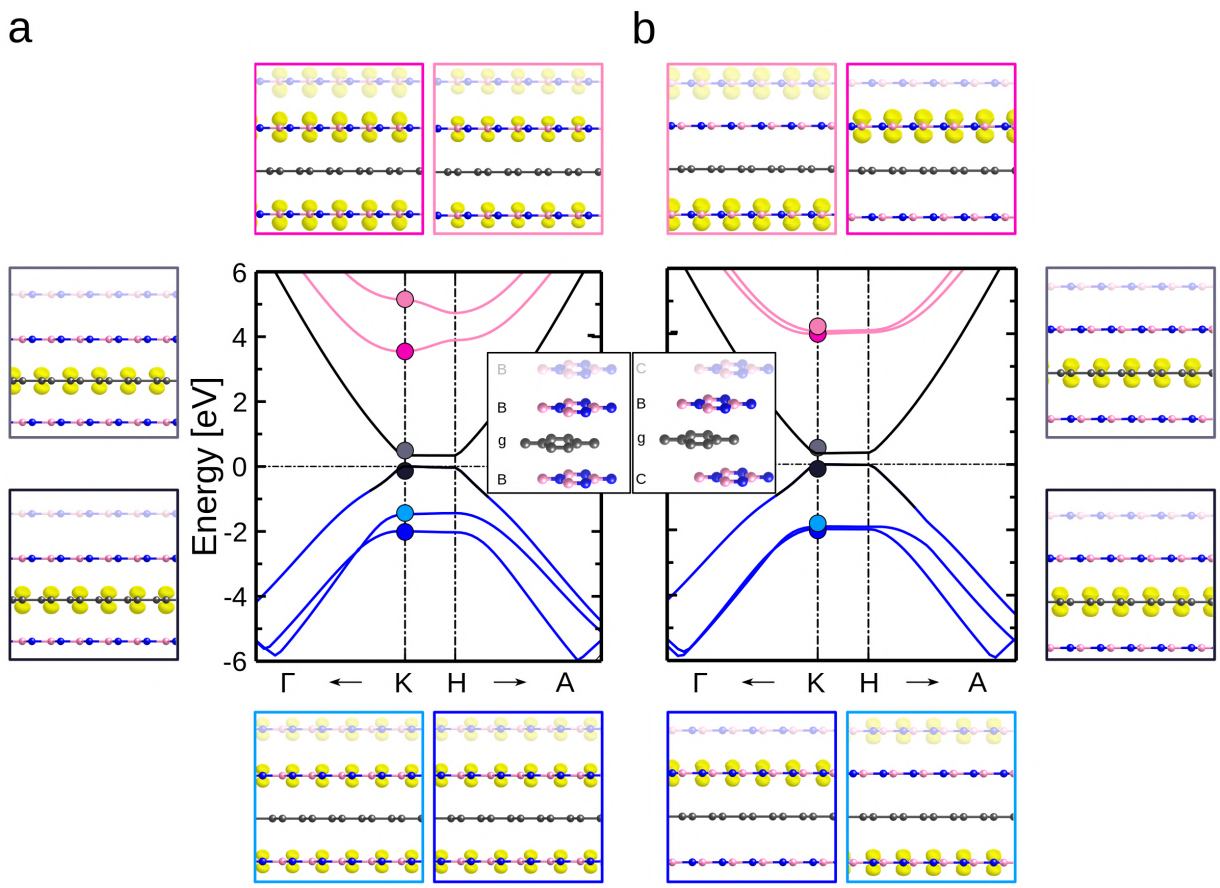

Figure 4.9: Quasi-particle band structure in the vicinity of the K-H path and electron probability density at K of the three highest occupied and the three lowest unoccupied Kohn-Sham states of the B-g-B (**a**) and the C-g-B (**b**) heterostructures. The three layers included in the unit cell are shown in the foreground, while periodic images are shaded. The band character is indicated by the color code of the corresponding atomic species (B: pink, N: blue, and C: gray), while the box frame points to the corresponding electronic states marked in the band structures. The valence-band maximum is set to zero.

in the unit cell. However, due to the different neighboring atoms of the inequivalent C atoms, their corresponding VB/CB bands split at the K point. This result is valid for all semiconducting stackings and consistent with our discussion about the opening of the gap between these bands in subsection 4.2.1. Outside the K-H path in the BZ we notice that the VB/CB bands are dominated by both inequivalent C atoms.

Now focusing on the N (B)-like VB-2/VB-1 (CB+1/CB+2) bands we notice that they preserve a similar distribution as in bulk h-BN at the corresponding stacking (see Fig. 3.15.c). In B-g-B configuration the VB-2/VB-1 bands are split at the K point and exhibit a π/π^*-like character. They are distributed over N atoms of both h-BN layers. This case corresponds to the AA stacking arrangement of bulk h-BN. The same is happened for the CB+1/CB+2 bands where they are distributed over B atoms of both h-BN layers. However, in the C-g-B stacking the VB-2/VB-1 bands are split at the K point and each one is distributed over N atoms of only one inequivalent h-BN layers. This result is also similar to that found in the corresponding AB stacking of bulk h-BN (see Fig. 3.15.c). The same

also is happened for the CB+1/CB+2 bands, they are distributed over B atoms of only one h-BN layers.

To summarize, the B-g-B and C-g-B configurations can be seen as an intercalation of graphene and h-BN bulk in AA and AB stacking arrangement, respectively. The electronic wave-function distribution found in bulk h-BN are preserved in the heterostructures. In addition to the character, the degeneracy or splitting of these bands is also preserved and dictated by the vertical alignment of the N and B atoms as discussed in the previous chapter. This layer selectivity of the electronic distribution is expected to play an important role in the resulting optical excitation discussed in the following.

4.4 Optical properties

In this section we present the resulting optical properties of the graphene/h-BN vdW heterostructure. We focus on the new features that can appear in this combination that are not present in the individual constituents. By solving the Bethe-Salpeter equations on top of the QP states we analyze the origin and nature of the main peaks in the absorption spectrum. We focus on the character and the spatial distribution of the resulting e-h pairs. In addition, by considering the different semiconducting configurations, we discuss the effect of the layer patterning on the resulting excitations.

4.4.1 From constituents to vdW heterostructures

First, in order to analyze the origin of each peak, we compare the resulting absorption spectrum given by solving the full BSE Hamiltonian of the graphene/h-BN vdW heterostructures with the spectra of the individual constituents. We take as example the B-g-B configuration which can be seen as intercalating of graphene sheet between bulk h-BN layers in AA stacking arrangement. In order to identify the character of each peak we plot the corresponding IQPA spectra (which neglects the excitonic effects) of each system. As shown in Fig. 4.10.a, the absorption spectrum of graphene[1] is dominated by a zero-energy resonance in near-IR region, reflecting its semi-metallic nature. This peak is formed by band-to-band transitions since it is also captured by the IQPA calculation, as reported in Ref. [219]. In addition to several excitations such as excitons and plasmons that occur at UV frequencies [94, 216–218], graphene is rather featureless in the visible region [219]. We notice that, by showing the low intensity part (see Fig. 4.10.a, inset), our result are in good agreement with that reported in Refs. [94, 219]. On the other hand, the absorption spectrum of bulk h-BN in the AA stacking is dominated by strong excitonic

[1]We notice that this spectrum is given by solving the full BSE Hamiltonian using the scissor operator in order to open the gap in graphene. Then, we redshift the spectrum by the same value used for the scissor. The sampling of the BZ used for such calculation is 42x42x1 shifted **k**-mesh from the Γ point. The broadening used in this case is approximately 0.1 eV

peak in the near-UV region (see Fig. 4.10.b). This peak is formed by strongly bound e-h pairs as reported in the last chapter.

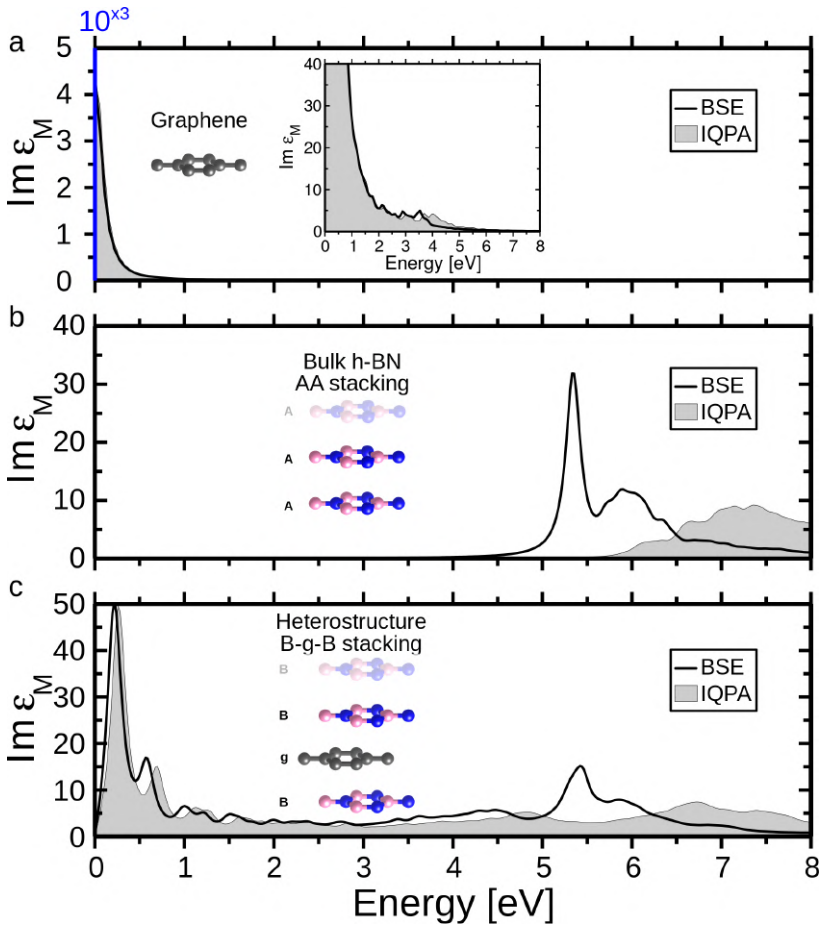

Figure 4.10: In-plane component of the imaginary part of the macroscopic dielectric function of (**a**) graphene sheet, (**b**) bulk h-BN in AA stacking, and (**c**) graphene/h-BN vdW heterostructure in B-g-B arrangement (insets), computed by including (BSE, solid line) and by neglecting (IQPA, shaded area) excitonic effects. The broadening used in all spectra is 0.1. The C, N, and B atoms are gray, blue, and pink, respectively

The vdW combination of these two constituents to build the B-g-B heterostructures gives rise to absorption spectrum shown in Fig. 4.10.c. This heterostructures absorb light over a broad frequency range from the near-IR up to the UV region. By comparing the main peaks with the individual feature of the constituents, we notice that the sharp peak in the near-IR region is originated from graphene sheet. However, instead of the zero-energy divergence that dominate the absorption spectrum of graphene (see Fig. 4.10.a) the peak being blue-shifted in this case due to the opening of the gap between graphene bands. In the near-UV region the sharp peak that appears in the heterostructures exhibits an excitonic character and can be seen by comparing to the IQPA spectrum (without excitonic effects). This peak is mainly originated from the h-BN layers as reported for bulk h-BN in the AA stacking arrangement (see Fig. 4.10.b). Now, focusing on the differences, we notice that this heterostructures absorb the light in the visible ∼(1.6 to 3.2 eV) and the near-UV range below the sharp excitonic peak. This characteristic is not observed in bulk

h-BN nor in the graphene sheet which are featureless in this range [219].

To sum up, this vdW combination preserves the intrinsic optical characteristic of the constituents since their electronic bands are basically preserved. It gives access to new features that are not present in the individual constituents such as the absorption of the visible light as well as the blue shift of the zero energy peak of graphene. This new features reflect the weak interlayer interaction between these constituents which are observed also in the resulting electronic properties. In the next section we analyze each region of the spectrum, focusing on the character and the origin of the resulting excitations.

4.4.2 Stacking arrangement vs. absorption spectra

In this subsection we present the effect of the stacking arrangement of the constituents on the resulting absorption spectrum of the graphene/h-BN vdW heterostructure. To do so, in Fig. 4.11 we plot the absorption spectrum of each semiconducting configurations computed by including (BSE, solid line) and by neglecting (IQPA, shaded area) excitonic effects.

The first remark is that all the spectra features of the B-g-B stacking presented in Fig. 4.10.c are also found in other configurations. The sharp peak in the near-IR region exhibits the same shape as in all configurations. We notice a very small difference in the excitation energy due to the different QP gap between graphene bands found in these stackings (see Table. 4.2).

The sharp excitonic peaks near UV region is also preserved in all stackings while the main differences is related to its shape and excitation energy. Owing to the different arrangement of h-BN layers the corresponding VB-2/VB-1 and CB+1/CB+2 bands are either degenerate or split in the gap region. The QP gap between these bands is affected by the layer patterning (see Fig. 4.6). Consequently, these differences are reflected in the shape of the resulting excitonic peak as well as the excitation energy. This tunability of the excitonic peak is also reported for bulk h-BN (see Fig. 3.16).

Overall, all the spectra looks quit similar since all the configurations absorb the visible light and the intensity of the main peaks are also comparable. Despite the small effect of the stacking arrangement on the spectra shape we expect a large tunability of the resulting optical excitations as shown in the following subsections.

4.4.3 Excitons in graphene/h-BN vdW heterostructures

By considering B-g-B configuration, we investigate the resulting excitations in each spectral region of the graphene/h-BN vdW heterostructure. We analyze their character and distribution in the real and the reciprocal space. To ease our analysis we plot again the resulting absorption spectrum of the B-g-B configurations computed by including (BSE, solid line) and by neglecting (IQPA, shaded area) excitonic effects in Fig. 4.12. We high-

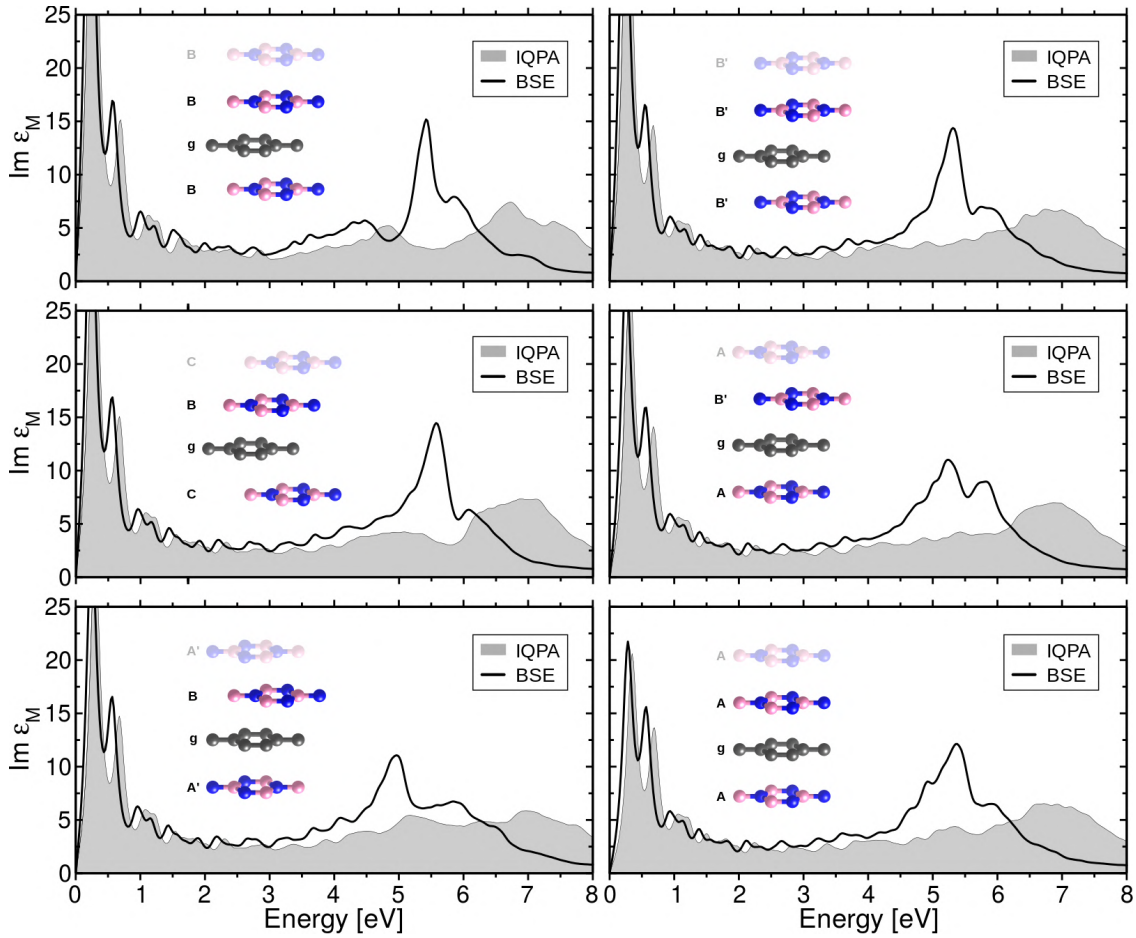

Figure 4.11: In-plane component of the imaginary part of the macroscopic dielectric function of all the considered semiconducting configurations (inset) of the graphene/h-BN vdW heterostructure, computed by including (BSE, solid line) and by neglecting (IQPA, shaded area) excitonic effects. The C, N, and B atoms are gray, blue, and pink, respectively..

light the selected excitations that dominate each spectral region using different color to indicate the graphene-like (red), visible (green), and UV-like (magenta) spectral regions. We notice that these selected excitations exhibit a specific character and are not necessarily the most intense ones. However, all the BSE solutions (E^{λ} eigenvalues in Eq. 2.45) and their relative oscillator strength (t_{λ} in Eq. 2.49) are presented together with the absorption spectrum in Appendix B (Fig. B.3.a).

As reported for bulk h-BN (see subsection 3.2.4), the resulting excitations shown in Fig. 4.12 are doubly degenerate owing to the symmetry of the system. In order to ease the representation, the intensity of the excitations highlighted in Fig. 4.12 represent their relative oscillator strength given by t_{λ} (see Eq. 2.49).

In the low-frequency part of the spectrum (up to 1 eV) we select the two intense excitations, named (I) and (II) that dominate the sharp peak and its shoulder. Likewise, in the near-UV region we analyze the intense one that dominates the sharp excitonic peak (V) and another one from the broad hump above it (VI). In the visible and near-UV regions we

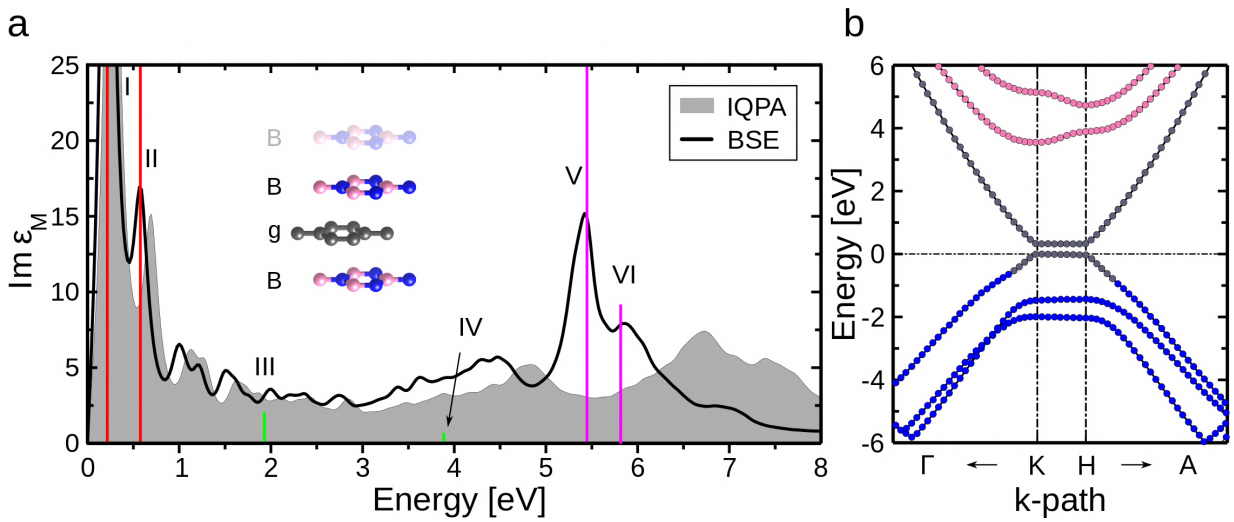

Figure 4.12: (**a**) In-plane component of the imaginary part of the macroscopic dielectric function of a B-g-B stacked h-BN/graphene/h-BN heterostructure (inset), computed by including (BSE, solid line) and by neglecting (IQPA, shaded area) excitonic effects. (**b**) Quasi-particle (QP) electronic structure of the system around the K-H path in the BZ. The band character is indicated using the color code of the atomic species (C: gray, N: blue, B: pink).

select two other excitations labeled III and IV. In the following, since these excitations are twofold degenerate, the electronic distribution of each exciton with the hole being fixed, is given by the averaged densities of the degenerated BSE solutions. The corresponding individual plots of these degenerate excitons can be found in Appendix B (Fig.B.4).

Graphene-like excitations in IR region

As discussed in subsection 4.4.1, the sharp peak in the near-IR region is originated from the graphene sheets. This peak is formed by the sharp one dominated by excitation (I) at 220 meV and its shoulder centered by excitation (II) at 600 meV[2] (see Fig. 4.13). The corresponding first peak in the IQPA spectrum is located at around 250 meV which coincides with the QP gap found in this configuration. Owing to the inclusion of the excitonic effects, the energy of the first excitation is redshifted with respect to the IQPA one. This means that the binding energy of the e-h pair in this case is around 30 meV. As shown in Fig. 4.13 both excitations arise from transitions between graphene-like VB/CB bands along (for excitation I) and in the vicinity (for excitation II) the K-H path in the BZ (see Fig. 4.13). By fixing the hole on the inequivalent C atom that dominates the VB band (see Fig. 4.9.a), these excitations are characterized by a delocalized π^*-like distribution of the associated electron over the second inequivalent C atoms within the graphene sheet (see

[2]We notice that the energy of the sharp peak centered by excitation (I) and its shoulder centered by (II) converge to the same value, as in graphene sheet (see Fig. 4.10.a). Owing to the enhanced numerical complexity of this system, the mesh is limited to $30 \times 30 \times 4$ shifted **k**-point and then interpolated onto a $60 \times 60 \times 4$ mesh, using the double grid method [188, 189]. The convergence tests and the details of this interpolation can be found in Appendix B.

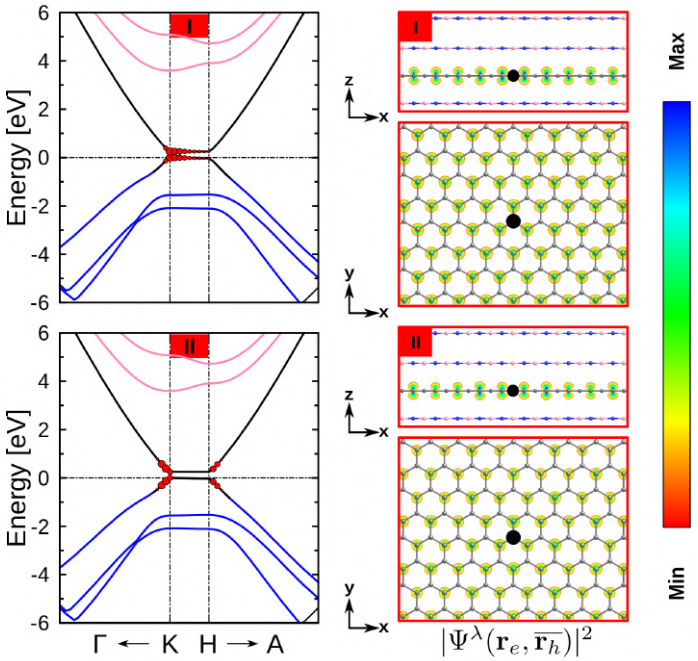

Figure 4.13: (left): Band contributions to the graphene-like excitations (I and II) highlighted in the spectra of the B-g-B heterostructure in Fig. 4.12. The size of the colored circles are quantitatively representative of the weight of the corresponding quasi-particle states (see Eq. 2.50). The band character is indicated by the color code of the atomic species (C: grey, N: blue, B: pink). The valence band maximum is set to zero. (right): The corresponding two-dimensional projections of the electron component of the e-h wavefunctions. The position of the hole is marked by a black dot.

Fig. 4.13). The band-to-band delocalized character of these e-h pairs reflects their week binding energy (around 30 meV). We notice that the resulting distribution is given by the average density of the degenerated solutions while the individual plots can be found in Appendix B (see Fig. B.4.a).

To summarize, the near-IR region of the spectrum (up to 1 eV) is dominated by the band-to-band graphene-like excitations. The sharp peak in the the IQPA spectrum coincides with the QP gap opened in graphene while the inclusion of the e-h interaction leads to redshift this peak by around 30 meV. This value which represents the e-h binding energy reflects its delecolized character within graphene sheet.

h-BN-like bound exciton in UV region

As found in bulk h-BN, the sharp peak in the near-UV region of the B-g-B heterostructure appears only by including the excitonic effects. This peak is centered by excitation (V). We have also selected the excitation (VI) which is located in the broad hump above the sharp peak. As shown in Fig. 4.14, these excitations stem from transitions between h-BN-like VB-2/CB+1 bands along the K-H path in the BZ. We notice that the origin of these excitations is consistent with that found for bulk h-BN in the corresponding AA stackings (see Fig. 3.17).

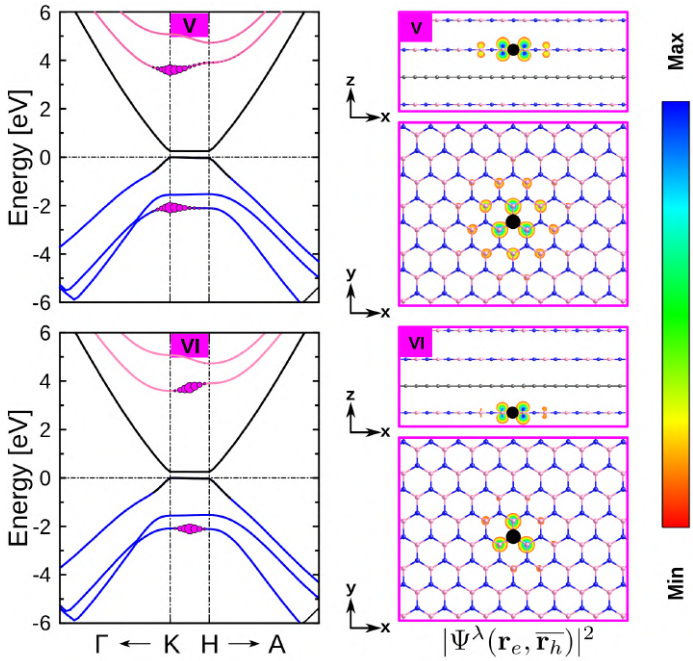

Figure 4.14: The same analysis, as in Fig. 4.13, is done for h-BN like excitons (V and VI) highlighted in the spectra of the B-g-B heterostructure in Fig. 4.12.

As shown in Fig. 4.14 the electronic distribution of these excitons with the hole being fixed on the N atom, is spread over the neighboring B atoms within the h-BN layer. The resulting trigonal shape reflects the hexagonal symmetry of the lattice as reported also for bulk h-BN (see Fig. 3.17). We notice that since these excitons are twofold degenerate, the resulting trigonal shape is given by the averaged densities of the degenerated solutions as reported in Ref. [40] for bulk h-BN (the individual plots can be found in Appendix B, Fig. B.4.c). The localized nature of these excitons reflect their strong binding energy. In these cases the binding energy cannot be quantified with respect to the fundamental gap given by the graphene bands. However, the comparison between the BSE and the IQPA spectra indicates that the two main excitations (V and VI) stem from the manifold of interband transitions between 6 and 8 eV (see Fig. 4.12). With this comparison we estimate the binding energy of excitation (V) to be on the order of 1 eV. We notice that in Fig. 4.14 we have visualized these two localized excitons on different h-BN layers in the unit cell. Since the electronic distribution of the VB-2/CB+1 bands are spread over both h-BN layers in the unit cell (see Fig. 4.9.a) these excitons can appear uniformly in both h-BN layers as reported for bulk h-BN in AA stacking (see Fig. 3.17). These results show that this vdW combination preserves also the contributing bands and the spatial distribution of the excitons as in the individual constituents.

Charge-transfer excitations in the visible region

Beside the intrinsic features of the constituents shown above, the graphene/h-BN vdW heterostructures exhibit a new characteristic in the visible region where the individuals

constituent are featureless. The excitations found in this region are originated from both constituents. As shown in Fig. 4.15, the excitation located at around 2 eV (labeled III in Fig. 4.12) arises from transition between VB-1 and CB around the K point in the BZ. These bands are dominated, respectively, by N and C atoms which stem from different layers (see Fig. 4.9.a). By fixing the hole on top of the N atom in the h-BN layer, the corresponding electronic distribution spreads over one inequivalent C atoms within the graphene sheet. This character is named charge transfer exciton since the hole and the associated electron sit on different layers. The weak binding energy in this case (around 0.1 eV) evaluated by comparison to the IQPA spectrum reflects the delocalization character of this exciton. The oscillator strength of this excitation is significantly lower than that in the in-plane graphene-like excitations due to the weak $\pi - \pi^*$ interaction between the layers.

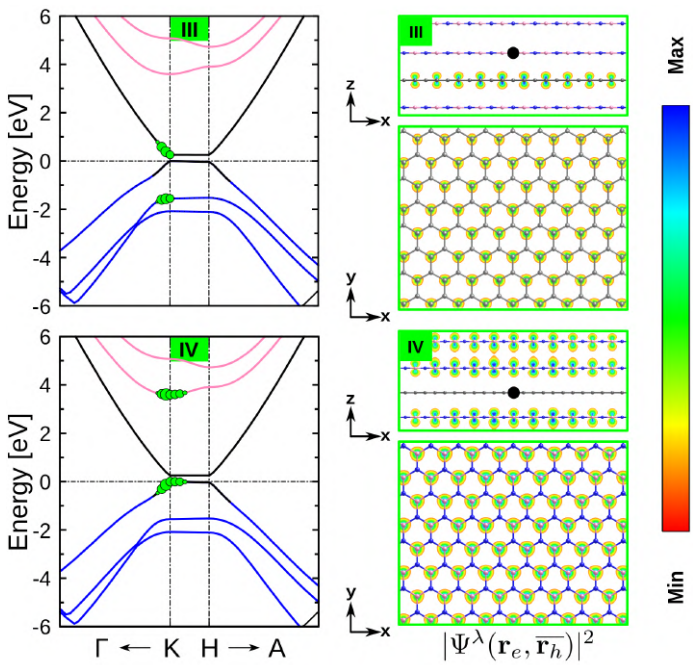

Figure 4.15: The same analysis, as in Fig. 4.13, is done for the charge transfer excitations (III and IV) highlighted in the spectra of the B-g-B heterostructure in Fig. 4.12.

We notice that since the electronic distribution of the VB-1 band at the K point is spread over both h-BN layers in the unit cell (see Fig. 4.9.a) the hole can be fixed also in the h-BN layer below graphene (see Fig. 4.15).

Likewise, the excitation (IV) located at around 4 eV exhibit a charge transfer like character. It stems from transitions between the VB and the CB+1 bands around the K point in the BZ. These bands are dominated, respectively, by C and B atoms which come from different layers (see Fig. 4.9.a). Consequently, by fixing the hole on top of the corresponding inequivalent C atom, the electronic distribution spreads over B atoms of both inequivalent h-BN layers. Due to the weak e-h binding energy (around 0.1 eV) the resulting spatial distribution is delocalized as KS states (see Fig. 4.9.a). In this case the

weak oscillator strength is due also the weak wave-function overlap between graphene and h-BN states. To sum up, in the visible and near-UV range where the spectra of the constituents are rather featureless we find the actual fingerprints of the heterostructure represented by the charge transfer e-h pairs. It can be formed by transitions from h-BN to graphene bands in the visible region and from graphene to h-BN bands in the near-UV region. While this type of excitons is more known for the *type* II band alignment where the band gaps are staggered [50], the *type* I straddling band alignment between the graphene and h-BN gaps gives rise also to such excitons.

4.5 Stacking effects on the electron-hole distribution

Now, let's see what happens to the e-h distributions discussed above if we change the stacking arrangement of the layers. First, we have shown in Fig. 4.11 that the main effect of the stacking arrangement on the absorption spectrum of the graphene/h-BN vdW heterostructures is in the shape of the excitonic peak near UV region which is also reported for bulk h-BN (see Fig. 3.16). This result reflects the differences between their electronic band structures (see Fig. 4.6). Second, by focusing on the electronic wave-functions distribution, we have shown in Fig. 4.9 that the corresponding h-BN bands in the C-g-B stacking are almost degenerate and distributed over only one h-BN layer in the unit cell along the K-H path in the BZ. For these reasons, in order to analyze the effect of the stacking arrangement we consider the C-g-B configuration which can be obtained by sliding one h-BN layer in the unit cell of the B-g-B arrangement.

As shown in Fig. 4.16, the low energy part (up to 1 eV) of the resulting spectrum of the C-g-B configuration is also characterized by graphene-like excitations. This part of the spectrum is unaffected by layer patterning (see in Fig. 4.12). However, the energy of the excitation I (about 225 meV) is smaller than that found in the B-g-B stacking (220 meV) due to the different QP gaps (see Table 4.2). Now, by comparing the region of the weak absorption up to 4 eV with that of the B-g-B stacking (see in Fig. 4.12), we notice a small difference in the shape reflecting the differences in the N-like (VB-2/VB-1) and B-like (CB+1/CB+2). These differences are also reflected in the resulting shape of the excitonic peak between 5 and 6 eV.

To visualize the effect of the stacking arrangement on the e-h pairs distribution we plot also the real and reciprocal distribution of the excitons highlighted in the C-g-B spectrum in Fig. 4.16. The graphene-like (I and II) excitations exhibit a similar origin and spatial distribution as found in the B-g-B stacking (see Fig. 4.13) since the electronic distribution of the VB/CB bands is unaffected by layer patterning. Now, we examine the visible/near-UV region where the charge-transfer excitations (III and IV) appear. To be consistent with the previous analysis we select the analogous features as excitations (III) and (IV) in the B-g-B heterostructure, in this region. The contributing bands to these excitations show that the hole and the associated electron sit on different layers (see Fig. 4.17). Excitation

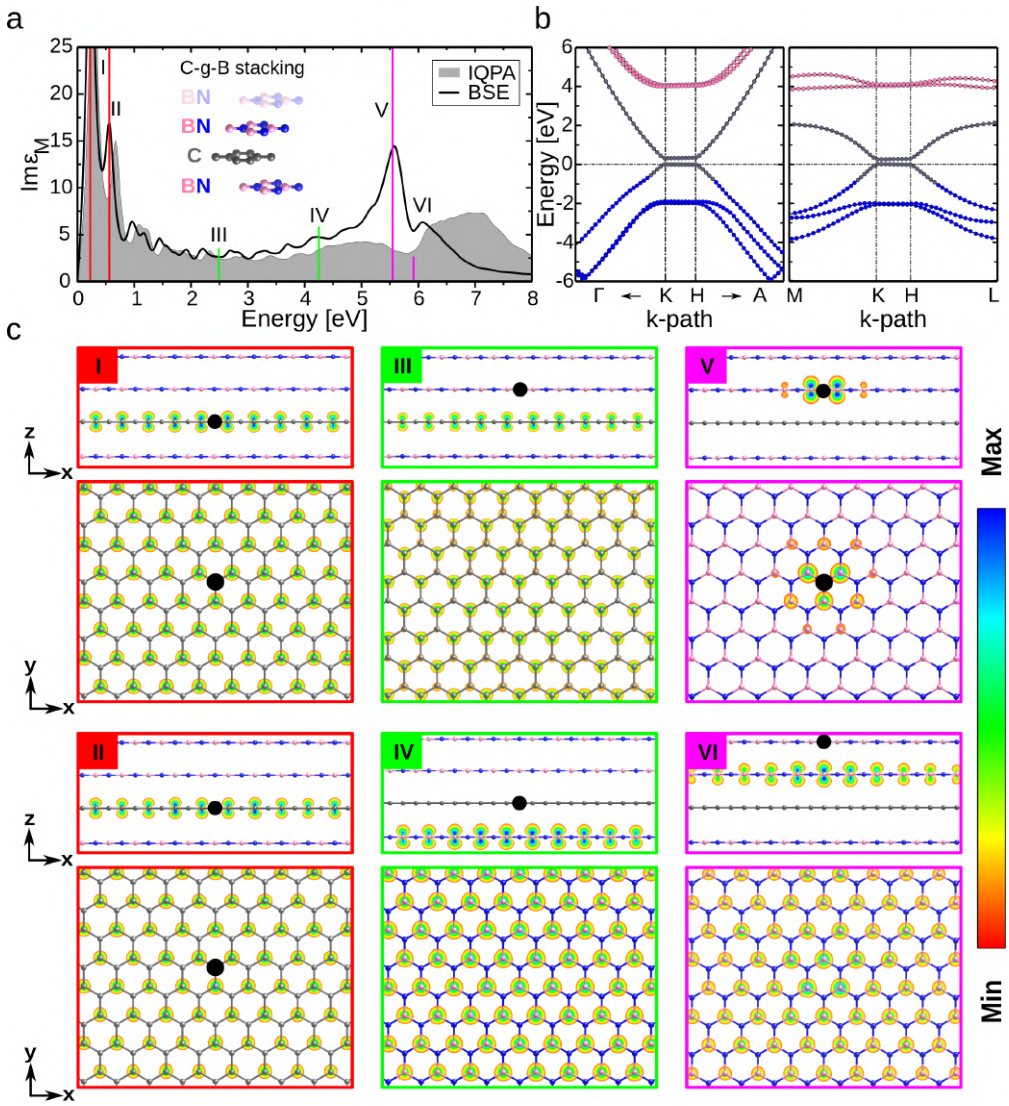

Figure 4.16: (**a**) In-plane component of the imaginary part of the macroscopic dielectric function of a C-g-B stacked h-BN/graphene/h-BN heterostructure (inset), computed by including (BSE, solid line) and by neglecting (IQPA, shaded area) excitonic effects. (**b**) Quasi-particle electronic structure of the system in the vicinity of the high-symmetry points K and H, approached from two different directions. The band character is indicated using the color code of the atomic species (C: gray, N: blue, B: pink). The VBM is set to zero. (**c**) Two-dimensional projections of the electron component of the e-h wavefunctions highlighted in the spectrum in panel (**a**). The corresponding position of the hole is marked by a black dot.

III around 2.5 eV is twofold degenerate and originates from transitions between the VB-2/CB bands at the K path in the BZ. Unlike the B-g-B configuration the position of the hole, in this case, should be on specific h-BN layer (the one above graphene) according to the electronic distribution of the VB-2 band (see Fig. 4.9.b). The resulting electronic distribution of excitation (III) is uniformly delocalized over graphene sheet with π^*-like distribution (see Fig. 4.16). The binding energy in this case is similar to that found for the corresponding excitation in the B-g-B stacking, being 0.1 eV.

The resulting excitation (IV) highlighted in the spectrum at around 4.2 eV stems from

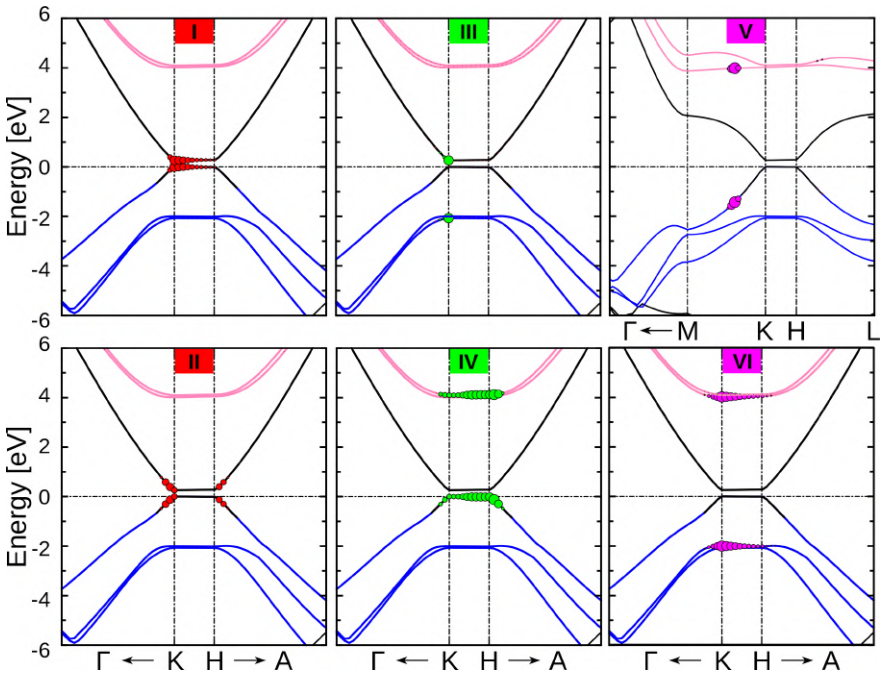

Figure 4.17: Band contributions to the main excitations in the spectra of C-g-B heterostructure shown in Fig. 4.16. The size of the colored circles are quantitatively representative of the weight of the corresponding quasi-particle states (see Eq. 2.50). The band character is indicated by the color code of the atomic species (C: grey, N: blue, B: pink). The valence band maximum is set to zero.

transitions between the C-like VB and the B-like CB+2 bands along the K-H path in the BZ (see Fig. 4.17). By fixing the hole on top of the corresponding inequivalent C atom within the graphene sheet, the associated electronic distribution spreads over B atoms of the h-BN layer below it. We notice that, in a situation where an excitation (not shown) arises from transitions between the C-like VB and the B-like CB+1 bands the corresponding associated electronic distribution spreads over the h-BN layer above graphene (see Fig. 4.9.b). The difference with respect to the B-g-B heterostructure should be noted at this point. The electron distribution of excitation IV in the B-g-B stacking spreads over both inequivalent h-BN layers (see Fig. 4.15). However, it is restricted only to one h-BN layer in the C-g-B configuration with the hole being fixed on graphene sheet (see Fig. 4.16). These results reflect the layer-selectivity of the electronic wave-functions distribution of the N- and B-like bands when involving the layer patterning (see Fig. 4.9). As a consequently, the distribution of the resulting charge transfer excitons is very sensitive to the stacking sequence.

Within the sharp excitonic peak in the near-UV region we select two different excitations (V and VI). The intense one (V) around 5.5 eV arises from transitions involving N-like VB and B-like CB+1 bands in the middle of M-K path in the BZ. By fixing the hole on top of the N atom, the associated electronic distribution spreads over the neighboring B atoms within the same h-BN layer. This trigonal shape is similar to that found in the B-g-B stacking and in bulk h-BN as well (see Fig. 4.14 and 3.17). The effect of the stacking

arrangement in this region can be seen in excitation (VI) (see Fig. 4.16). It stems from transitions between the VB-1 and CB+1 bands along the K-H path in the BZ. At the K point these bands are spread over N and B atoms, respectively, on different h-BN layers in the unit cell (see Fig. 4.9.b). Thus, the hole and the associated electron sit on different h-BN layers making the charge transfer like exciton. The lower intensity of this exciton compared to the in-plane exciton (V) is due to its interlayer character, reflecting the weak wave-function overlap between the involving states. We notice that this charge transfer character is reported also for bulk h-BN in the corresponding AB stacking. However, the in-plane distribution of the charge transfer exciton in this case is more extended (embrace about 14 unit cells) than in the AB stacking (around 5 unit cells), reflecting its weak binding energy (around 0.1 eV).

5 Conclusions and outlooks

In this thesis we have provided a detail analysis of the structural, electronic, and optical properties of bulk h-BN and periodic graphene/h-BN vdW heterostructures, focusing on the resulting e-h pairs distribution. We have shown how the stacking arrangement of the 2D layers may control and tune the resulting properties. By varying the stacking sequence in bulk h-BN, a significant variability in the band structure is obtained. The minimum direct QP gap ranges between 5.05 eV and 6.33 eV, with the highest (lowest) occupied (unoccupied) bands has N (B)-like character and becoming degenerate depending on vertical alignment of the atomic species. This characteristic is directly related with the real-space distribution of the corresponding wave-functions. Such electronic modulation is reflected in the optical spectra and in the character of the resulting e-h pairs. The energy and the intensity of the absorption onset in bulk h-BN which is dominated by a pronounced excitonic peak, depends crucially on the layer patterning. By modifying the stacking, energy, intensity, and character of the resulting e-h pairs can be selectively modulated. Depending on the dimensionality of e-h distribution we found a prototype of three kinds of excitons, namely 2D (localized or delocalized), 3D (localized or delocalized), and CT-like character. We found that the 2D excitons appear in all stacking, and can be extended to form the 3D distribution in the presence of inversion symmetry. On the other hand, remarkably, charge-transfer excitons appear in those stackings where atoms of the same species never lie on top of each other.

By combining graphene and h-BN in periodic vdW heterostructures, we have found that these assemblies absorb light over a large frequency range, going from the near-IR to the UV. While the electronic band structures of the constituents are basically preserved, their weak interlayer interaction leads to open a small band gap in graphene ($\sim$ 300 meV). This property is driven by layer stacking such that the two inequivalent C atoms should be aligned with different neighboring atoms to open this gap. Such electronic features are reflected in the optical spectrum. Instead of the zero-energy divergence that dominates the absorption spectrum of pristine graphene, the resulting shape peak below 1 eV in the heterostructure is blue shifted from the zero-energy due to the opening of the band gap. This peak is dominated by π/π^* interband graphene-like transitions. In addition,

the sharp excitonic peak found in the near-UV region is dominated by strongly bound e-h pair within the h-BN layers. Besides these intrinsic features of the constituents, we found the fingerprint of this vdW combination in the visible and near-UV region (between 1.6 and 5 eV) represented in charge-transfer excitations. In this case the electron and hole distributions spread over different constituents (graphene and h-BN). While the delocalized character reflect the weak interlayer e-h interaction, the reduced intensity of these excitations is due to the weak wave function overlap of the involving QP states. By modifying the stacking arrangement we have shown that the spatial distribution of such excitations can be selectively modulated.

Our findings, obtained within a first-principles DFT and many-body perturbation theory, and the interpretation that we provide represent a valuable starting point to better understand the interplay between structure-properties in vdW layered systems. As such, they open fascinating perspectives in view of predicting their optical behavior and designing novel vdW layered materials and heterostructures with customized characteristics achieved through layer patterning.

A

Convergence tests of bulk h-BN calculations

In Tables A.1 and A.2 we show how the quasi-particle (QP) gap of the AA′ stacking at the H point in the Brillouin zone varies with respect to the number of empty bands and of k-points, respectively. We carried out these tests independently, by converging the number of empty bands on a 9x9x4 k-mesh, and by converging the size of the k-grid fixing to 50 the number of empty bands. Although the absolute values reported in Tables A.1 and A.2 below are obviously affected by this choice, the indicated trends are unaltered in case enhanced parameters are used. The results in Table A.1 indicate the increase of the QP gap at increasing number of empty bands. An accuracy of 10 meV is reached for the chosen number of 250 empty bands.

Table A.1: Convergence behavior of the QP gap of the AA′ stacking of h-BN at increasing number of empty bands on a uniform 9x9x4 k-grid.

Empty bands	QP gap at H [eV]
50	6.22
100	6.30
150	6.35
200	6.38
250	6.41
300	6.42

The convergence tests over the k-grid indicate instead an opposite trend, with the QP decreasing by employing a denser mesh (see Table A.2). Our results in Table A.2 show that the adopted 18x18x6 **k**-mesh ensures an accuracy of the QP gap of the order of 10 meV. It should be noted that for an appropriate sampling of the Brillouin zone (BZ), explicitly including the high-symmetry points M (0.5, 0.5, 0.0), K (0.66, 0.33, 0.00), and H (0.66, 0.33, 0.50), k-grids with a number of points that is a multiple of 6 (2) along the in-plane (out-of-plane) directions has been chosen. It is worth noting that the GW results presented in the manuscript are obtained with a 18x18x6 k-mesh shifted from the Γ point at (0,0,0) to a very closer point, in order to employed all the k-point (18x18x6=1944 k-points). This consideration improves the quality of the BZ sampling also in the subsequent BSE calculations of the optical properties. Based on the results of the tests presented

in Tables A.1 and A.2 we can claim an accuracy for the QP gap of the order of 20 meV.

Table A.2: Convergence behavior of the QP gap of the AA′ stacking of h-BN at increasing number of **k**-points including 50 empty bands. Uniform non-shifted grids giving rise to a reduced number of **k**-points have been employed for these convergence tests.

k-grid	Reduced number of **k**-points	QP gap at H [eV]
3x3x2	6	6.62
6x6x2	14	6.22
9x9x4	36	6.22
12x12x4	57	6.18
15x15x4	108	6.19
18x18x6	148	6.18

In BSE calculations the **k**-point grid and the number of bands included in the construction and diagonalization of the BSE Hamiltonian are relevant parameters for numerical convergence of the spectra. The results of our convergence tests, presented in Fig. A.1, clearly demonstrate that the chosen 24x24x8 k-mesh shifted from the Γ-point ensures converged spectra in the considered energy range. Likewise, including transitions between 4 occupied and 4 unoccupied bands is sufficient to capture all spectral features in the region of interest.

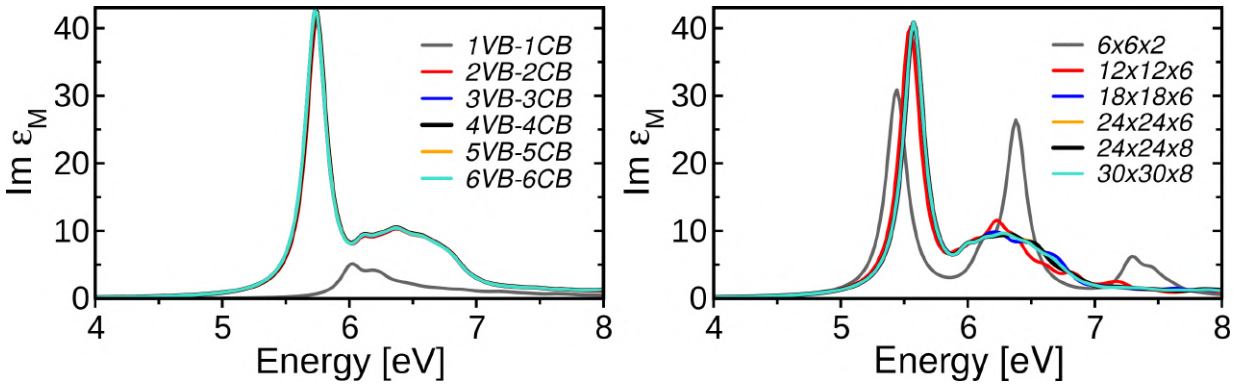

Figure A.1: BSE convergence for the optical spectrum of h-BN, AA′ stacking. Left: Convergence with respect to the number of valence and conduction bands (VB and CB, respectively) obtained on a 18x18x6 **k**-mesh shifted from the Γ-point. These calculations are performed on top of the Kohn-Sham band-structure by applying a scissors operator. Right: Convergence with respect to the size of the **k**-mesh considering transitions from 4 occupied to 4 unoccupied bands. These calculations are performed on top of the QP band structure.

These parameters ensure an accuracy on the excitation energy of the first two BSE solutions of at least 10 meV, as shown in Table A.3 for the AA′ stacking.

The **k**-point sampling adopted in BSE calculations is directly related to the real-space extension of the excitonic wave-functions (see Eq. 2.51), that are non-periodic objects. For an optimal visualization of the physical characteristics of the excitons, in chapter 2, we zoom in the region where the electron exhibits a finite distribution for a fixed hole

Table A.3: Convergence behavior with respect to the **k**-mesh of the excitation energy of the first doubly degenerate excitons (the first four solutions of the BSE) in the AA′ stacking of h-BN. Transitions between the 4 highest occupied and the 4 lowest unoccupied bands are considered.

Shifted k-grid	Energy λ=(1,2) (dark) [eV]	Energy λ=(3,4) (bright) [eV]
6x6x2	5.40	5.44
12x12x4	5.47	5.55
18x18x6	5.51	5.58
24x24x6	5.51	5.58
24x24x8	5.50	5.57

position. We have constructed a supercell with in-plane lattice parameter being 14 times larger the one of the corresponding unit cell (see Fig. A.2). In the vertical direction the supercell parameter is 4 times larger than the unit cell one. This choice correspond to 8 vertically stacked layers always included in the visualization box. In all such plots presented in Fig. A.2 and in chapter 2, the position of the hole is fixed according to the composition of the exciton and the correlated electron distribution is visualized by the green isosurface. In order to ensure the visualization of the whole extension of the very delocalized exciton shown in Fig. 3.19, a supercell with in-plane parameter equal to 22a is used (see A.3). The adopted k-point sampling and the related supercell size are sufficient to ensure a meaningful representation of all types of e-h pairs shown in chapter 2. We notice that the adopted isovalues to plot such excitons is around 12% of the maximum values.

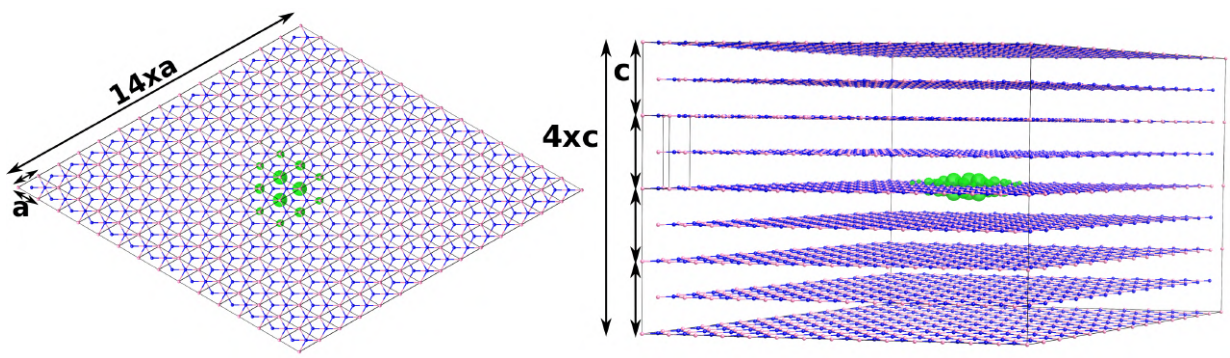

Figure A.2: Real-space distribution of the 2D exciton of the AA′ stacking shown in Fig. 3.11 in the main text. Left: Top view, with the in-plane unit cell parameter "a" and supercell parameter 14a highlighted. Right: Side view, with the out-of-plane unit cell parameter "c" and supercell lattice parameter 4c highlighted. The electron distribution for a fixed hole position is given by the green isosurface.

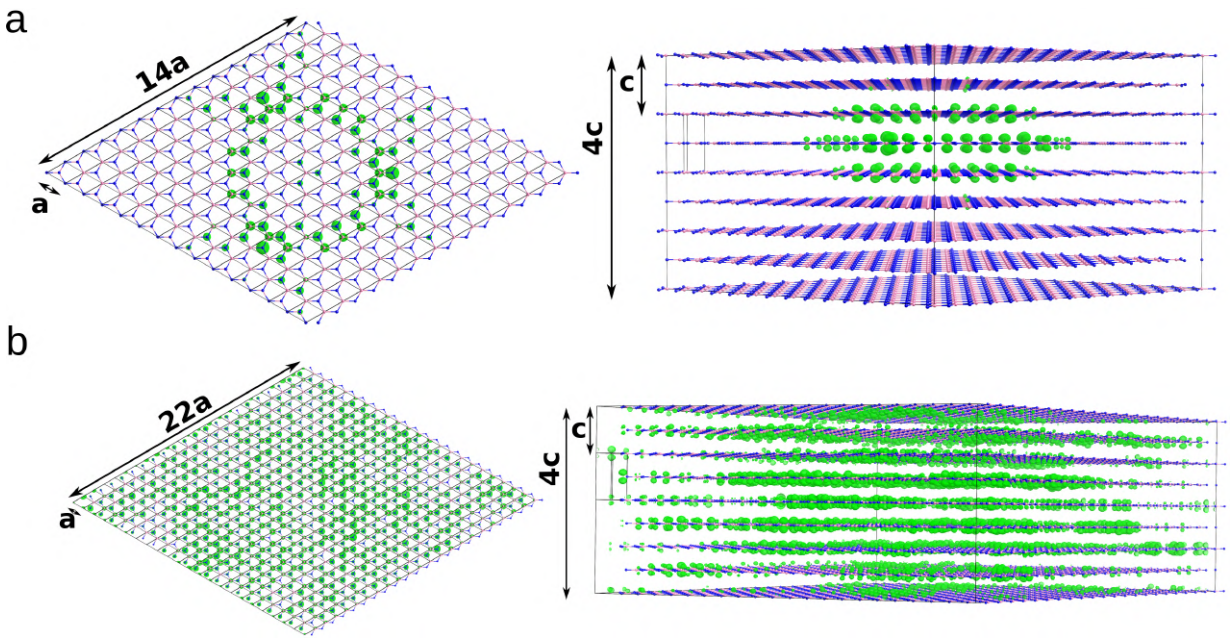

Figure A.3: Real-space distribution of the 3D$-d$ exciton (**a**) and the K-S like very delocalized 3D e-h pair (**b**) of the AA′ stacking shown in Figs. 3.13 and 3.14, respectively, in subsection 3.2.5. Left: Top view, with the in-plane unit cell parameter "a" and supercell parameter 14a highlighted. The in-plane supercell parameter is increased to 22a to ensure the very delocalized character of the exciton shown in Fig. 3.14 in subsection 3.2.5. Right: Side view, with the out-of-plane unit cell parameter "c" and supercell lattice parameter 4c highlighted. The electron distribution for a fixed hole position is given by the green isosurface.

B

Computational details of graphene/h-BN vdW heterostructures

In Table B.1 and B.2 we show how the quasi-particle (QP) gap between the graphene bands along the K-H path in the BZ varies with respect to the number of empty bands and of **k**-points, respectively. We consider here the B-g-B heterostructure as an example. We carried out these tests independently, by converging the number of empty bands on a 9x9x2 **k**-mesh, and by converging the size of the k-grid using the converged value of the latter which is 250 empty bands. The results in Table B.1 indicate that the 250 empty bands ensure an accuracy less than 10 meV on the band gap.

Table B.1: Convergence test of the QP gap along the K-H path in the BZ of the B-g-B configuration at increasing number of empty bands on a uniform 9x9x2 k-grid.

Empty bands	QP gap [eV]
25	0.350
50	0.339
100	0.325
200	0.317
250	0.316
300	0.315

Our results in Table B.2 show that the adopted 18x18x4 **k**-mesh ensures an accuracy of the QP gap less than 40 meV. We notice that for an appropriate sampling of the Brillouin zone (BZ), the used mesh includes the high-symmetry points M (0.5, 0.5, 0.0), K (0.66, 0.33, 0.00), and H (0.66, 0.33, 0.50) since it is a multiple of 6 (2) along the in-plane (out-of-plane) directions. It is worth noting that the GW results presented in the manuscript are obtained with a 18x18x4 k-mesh shifted from the Γ point in order to employ all the k-point (18x18x4=1296 k-points). This consideration improves the quality of the BZ sampling also in the subsequent BSE calculations of the optical properties.

In BSE calculations the **k**-point grid and the number of bands included in the construction and diagonalization of the BSE Hamiltonian are relevant parameters for numerical convergence of the spectra. The results of our convergence tests, presented in Fig. B.1.a,

Table B.2: Convergence test of the QP gap of the B-g-B stacking at increasing number of **k**-points including 250 empty bands. Uniform non-shifted grids giving rise to a reduced number of **k**-points have been employed for these convergence tests.

k-grid	Reduced number of **k**-points	QP gap [eV]
3x3x2	8	2.1
6x6x2	20	0.615
12x12x4	93	0.364
15x15x4	138	0.287
18x18x4	192	0.248

clearly demonstrate that the inclusion of transitions between 3 occupied and 3 unoccupied bands is sufficient to capture all spectral features in the region of interest. Likewise, the chosen 30x30x4 **k**-mesh, shifted from the Γ-point, ensures converged spectra by interpolating it onto the 60x60x4 mesh (see Fig. B.1.b) using the double grid method [188, 189], discussed in the following. We notice that the differences between the spectra shown in Fig. B.1.a,b is due to the different k-mesh used. However, the red-shift of the position of excitonic peak around 5.5 eV shown in Fig. B.1.b reflects the small value of the scissor operator used in Fig. B.1.a. Since the value of the scissor operator depends on character of the bands (see subsection 4.3.2) in this case we have chosen the one given by graphene bands. Consequently, the sharp peak given by h-BN bands is red-shifted to the 4 eV in Fig. B.1.a.

The sharp peak in the low energy part of the spectrum shown in Fig. B.1.b, is given by graphene-like transitions within the Dirac cone. Consequently, the use of a denser **k**-mesh in order to sample the linear dispersion in this region is requested to converge such peak. As in graphene, the sharp peak below 0.5 eV and its shoulder around 0.5 eV (see Fig. B.1.b) converge to only one peak using a denser mesh, as reported in Ref. [219]. Due to the enhanced numerical complexity of our system we have fixed the interpolated mesh onto the 60x60x4 grid. We rule out from this choice any artifact produced in this region. We notice also that the character of the resulting excitations in this region is nonetheless consistent with the existing literature [94, 219].

As shown in Fig. B.2.c for the B-g-B configuration, the double grid method consists of calculating four BSE spectrum at different **k**-grid. As example, we present this method for 3x3 in-plane mesh to ease the discussion (black point in Fig. B.2.b). This mesh is then shifted to the blue **k**-points. Staring from the blue **k**-points we construct three other 3x3 grids with different shift. The origin (Γ point) of the different grids is linked by the displacement vector (1/2,1/2,0) within one grid cell (see Fig. B.2.b). Looking now at the all colored **k**-points, the resulting **k**-grid coincides with that of the 6x6 **k**-mesh (see the dotted-dashed lines in Fig. B.2.b). Based on this result, the average of the four BSE spectrum given by the different 3X3 **k**-grids represents the interpolated BSE spectrum onto the 6x6 **k**-mesh (see Refs. [188, 189] for all details). In our case, we construct four 30x30x4 **k**-grids that differ the shift from the Γ point, as discussed above. The average

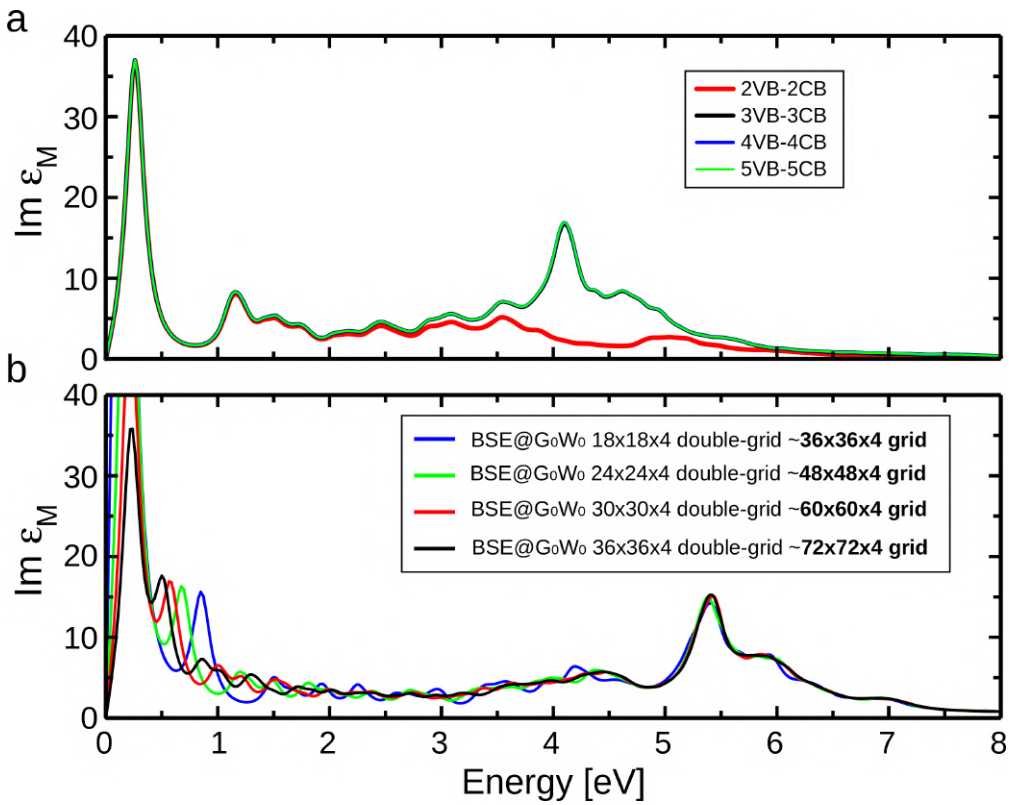

Figure B.1: BSE convergence tests for the optical spectrum of the B-g-B stacking. (**a**): Convergence with respect to the number of valence and conduction bands (VB and CB, respectively) obtained on a 18x18x4 shifted k-mesh. These calculations are performed on top of the Kohn-Sham band-structure by applying a scissors operator that reproduces the QP gap of only graphene. (**b**): Convergence with respect to the **k**-mesh considering transitions from 3 occupied and 3 unoccupied bands. These calculations are performed on top of the QP band structure using the double grid method discussed in the following.

of the resulting BSE spectra represents the interpolated spectrum onto the 60x60x4 grid shown in Chapter 4.

The resulting BSE spectra given by different shifted 30x30x4 grids are very sensitive to the value of the adopted shift. As shown in Fig. B.2.a, the shift of the mesh from Γ point means that we shift from the K, M, and all other high-symmetry points with the same value. Since the sharp peak in the low energy range of the spectrum arises from transitions between VB/CB gaphene bands around the K point (Dirac cone), the use of large value for this shift leads to lose such transitions (see Fig. B.2.d). Consequently, the only considered transitions are the ones arising from outside the gap region, far from the K point. For this reason, the resulting sharp peak in the green, orange, and magenta spectra are blue-shifted above the QP gap (see Fig. B.2.c). We notice that the similarity between these spectra reflects the independence of the other spectral region on the value of the shift. In case of small shift (see blue **k**-points in Fig. B.2.b), the resulting **k**-grid is very close to include the Γ, K, and other high-symmetry points in the BZ (see blue dotted line in Fig. B.2.d). Consequently, the band transitions around the K point are included, giving rise to the intense sharp peak in the corresponding blue spectrum in Fig. B.2.c.

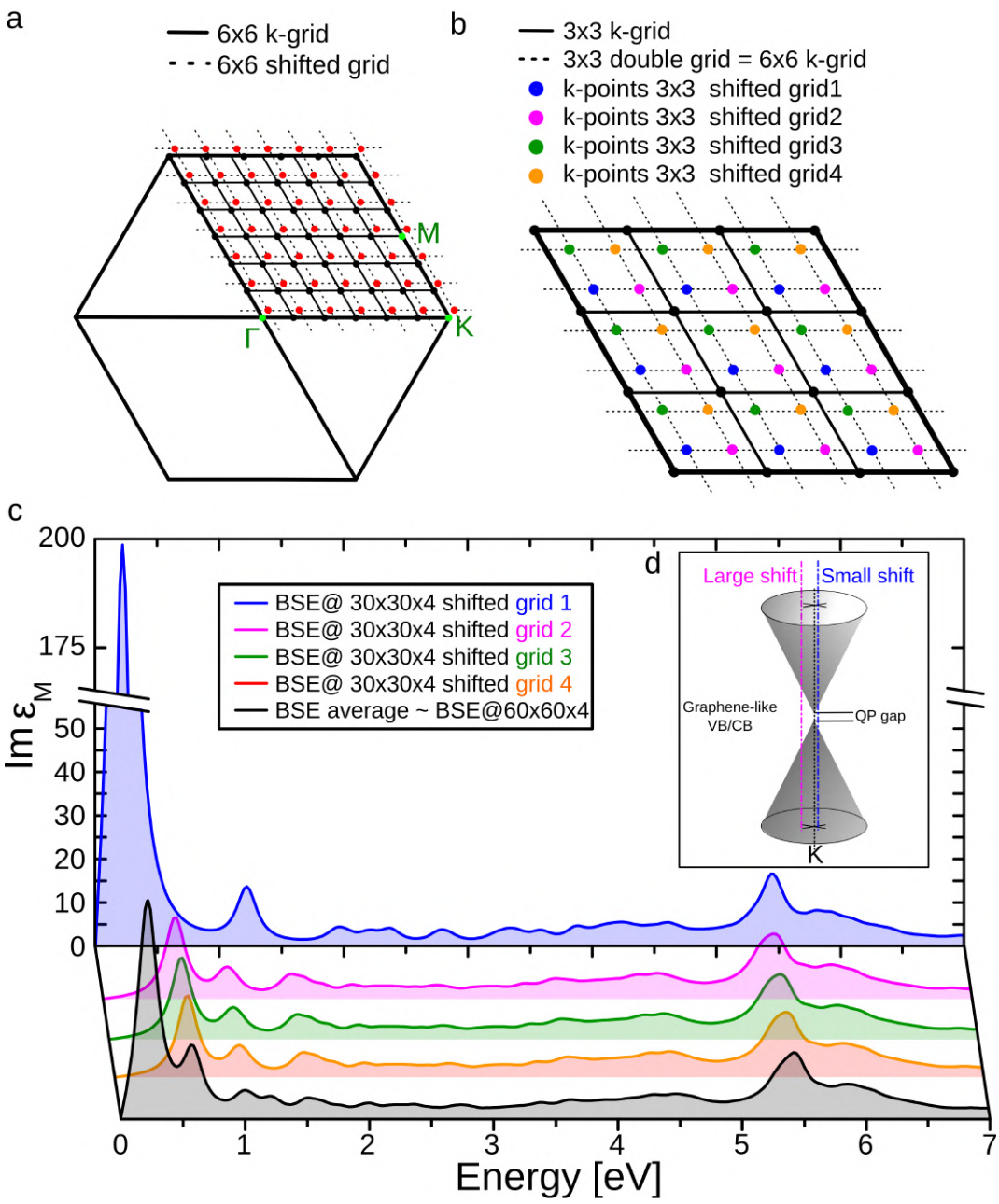

Figure B.2: Schematic representation of the (**a**): 6x6 uniform (black points) and shifted (red points) **k**-mesh as well as (**b**): the double grid method which request four different 3x3 shifted **k**-mesh (blue, magenta, green, and orange **k**-points) that builds the resulting interpolated 6x6 shifted **k**-mesh. (**c**): The resulting BSE spectra of the B-g-B configuration given by different 30x30x4 meshes that are built following the example shown in (**b**). The color code of the spectra corresponds to that of the different **k**-point shown in (**b**). The average of the four BSE spectra gives the resulting interpolated BSE spectrum onto the 60x60x4 **k**-mesh (black line). (**d**): Schematic representation of the graphene Dirac cone, where the band gap is opened (case of our heterostructures). The dashed-dotted lines represent the meshes that includes the K point (black), slightly shifted (blue) and largely shifted (magenta). The color of the dashed dotted line correspond to the color code of the spectra.

As a result, the energy of the peak is now within the QP gap and the one given by the independent QP approximation coincide exactly with the value of the QP gap (see the

IQPA spectrum of the B-g-B stacking shown in Chapter 4, Fig. 4.12). We notice that, in our case, the value of this small shift from the Γ (0,0,0) point is (0.166x10^{-3}, 0.833x10^{-4}, 0.375x10^{-2}).

Together with the in-plane component of the imaginary part of the macroscopic dielectric function, in Fig. B.3 we show the oscillator strength of the corresponding BSE solutions (E^{λ} eigenvalues in Eq. 2.45) for the B-g-B and B-g-C stacking arrangements discussed in Chapter 4. In these configurations, we have selected excitations with specific character, not necessarily corresponding to the most intense ones. Specifically, in the visible region we have selected the well defined interlayer excitons. However, most of the spectral intensity in this region is also given by a several transitions between the three highest-occupied bands and the graphene-like CB band. In order to ease this representation, we notice that the intensity of the red bars represent the relative oscillator strength which correspond to the $|\mathbf{t}_{\lambda}|$ (see Eq. 2.49).

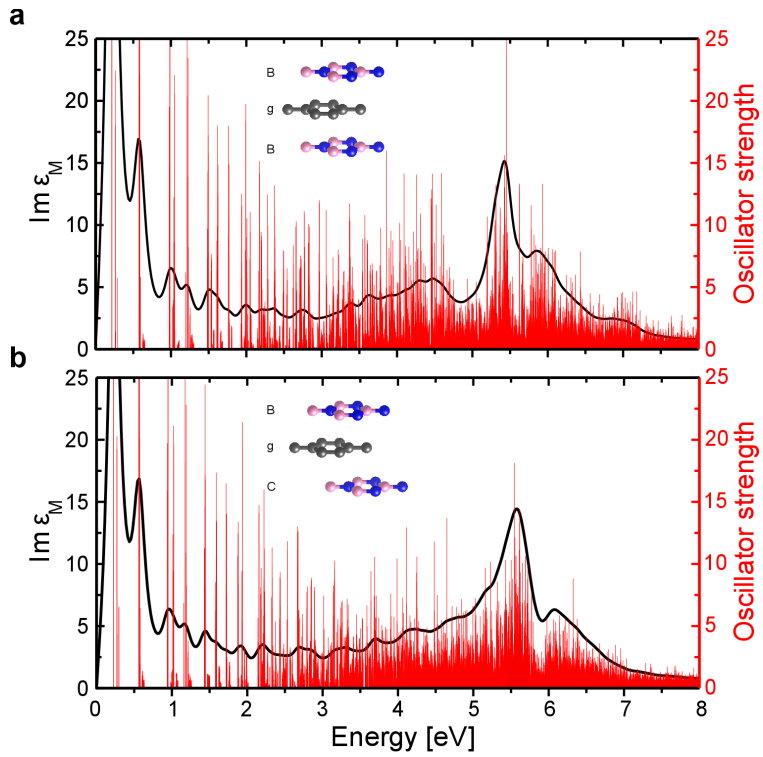

Figure B.3: In-plane component of the imaginary part of the macroscopic dielectric function (black solid line) and oscillator strength (red bars) of the corresponding BSE solutions (E^{λ} eigenvalues in Eq. 2.45) of B-g-B (**a**) and B-g-C (**b**) heterostructures

These excitations are double-degenerate due to the in-plane hexagonal symmetry of our systems, as reported also for bulk h-BN in Ref. [40]. Consequently, by fixing the hole positions, the associated electronic distribution of each excitons, is given by the averaged densities of each degenerated BSE solutions. In Fig. B.4, we plot the individual electronic distribution of each degenerate exciton reported in the B-g-B and C-g-B heterostructures. The first two distributions in this figure are referred to the degenerate graphene-like excitations (labeled I and II in Figs. 4.12 and 4.16) as well as to the in-plane distribution

within the graphene sheet of the charge transfer excitations labeled (III). The second ones are refereed to the electronic distribution within the h-BN layer (see Fig. B.4.b) of the degenerate charge transfer excitons (labeled IV in Figs. 4.12 and 4.16). The final two distributions represent the degenerate bound exciton within the h-BN layer (labeled V in Chapter 4). The average of these two densities gives rise to the trigonal shape of that exciton. These distributions are also valid for the twofold degenerate exciton of bulk h-BN shown in Chapter 3, and in good agreement with that reported in Ref. [40].

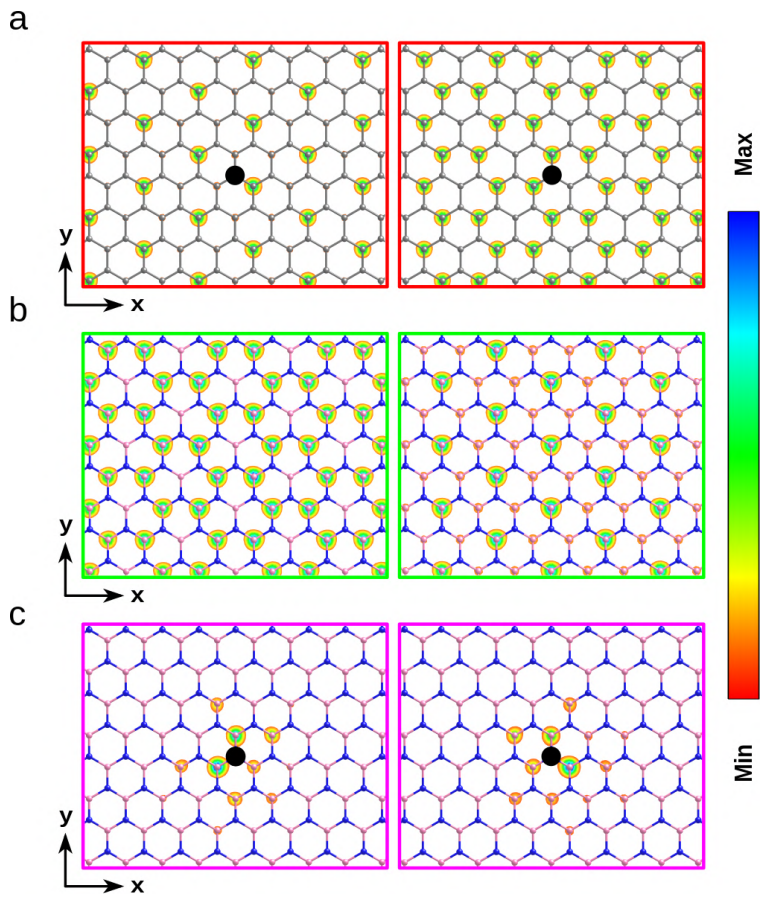

Figure B.4: Two-dimensional projections of the probability density associated to the electron component of the electron-hole pairs of double-degenerate excitations presented in Chapter 4 with (a) graphene delocalized character, (b) h-BN delocalized and (c) localized character. The corresponding position of the hole is marked by a black dot

In order to plot the electronic distribution of the excitons, the physical position of the hole has to be taken into account. Considering the charge transfer exciton found in the B-g-B configurations as example (labeled III in Chapter 4), in Fig. B.5 we show how the chosen position of the hole impacts the resulting electronic distribution of such e-h pair.

The charge transfer exciton in the B-g-B stacking arises from transitions between the N-like VB-1 and C-like CB bands around the K point in the BZ (see Fig. 4.15). Since the electronic wave-functions distribution of VB-1 band is spread over both inequivalent h-BN layers (see Fig. 4.9.a), the position of the hole can be fixed on top of the N atom of both h-BN layers in the unit cell. The resulting electronic distribution spread over graphene

sheet (see Fig. B.5, left). Now, by moving the hole position along the N-B bond towards the B atom, the associated electronic distribution within the graphene sheet is almost vanishing (see Fig. B.5, right). This result reflects the N-like character of the involved VB-1 states. Since the VB band exhibits a π-like character, the same test is done (not shown) in the vertical direction in order to evaluate the best vertical position of the hole on top of the N atom in Fig. B.5, left. We find that shifting by 0.4 a.u. in the z direction from that N atom is enough to capture the maximal electronic isovalue.

Now, by fixing the electron position on top of the corresponding inequivalent C atoms that dominated the CB bands, we report also the spatial distribution of the associated hole in B-g-B stackings (see Fig. B.6.a). With this representation we can clearly see that the hole is distributed over N atoms of both h-BN layers. In addition, by comparing the spatial distribution of the electron and the hole shown, respectively, in Figs.B.5.left and B.6.a the charge-transfer character, from h-BN layers to graphene, can be seen easily.

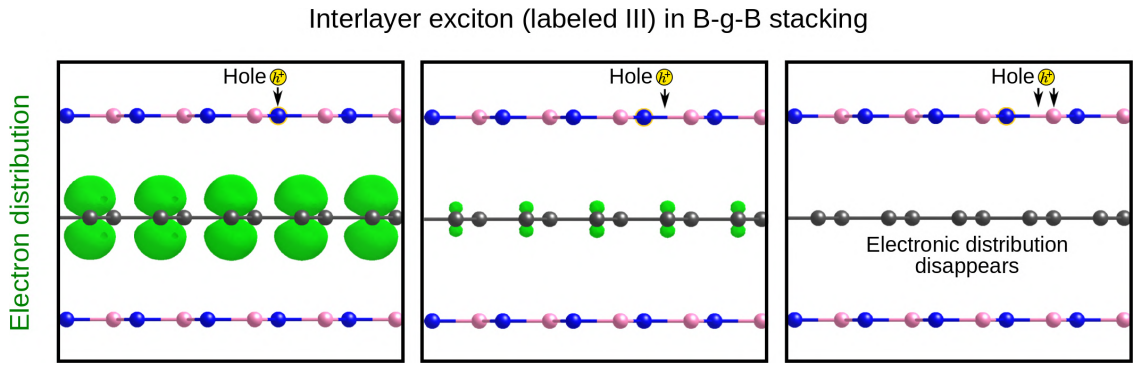

Figure B.5: Electronic distribution (green isosurface) vs. hole position (yellow circle) of excitation labeled III in the B-g-B stacking shown in Chapter 4. The position of the hole is moved from the physical position on top of the N atom towards the B atom (see from left to right). In the different panels we have used the same minimal isovalue. This minimal value is equal to 12% of the maximal isovalue found in the left panel.

We notice that the effect of the layer arrangement on the charge transfer excitation labeled (IV in Chapter 4) is more clear in the main text by comparing directly the associated electronic distribution in the B-g-B and the C-g-B configurations (see Figs. 4.15 and 4.16).

However, the effect of the stacking arrangement on the charge transfer excitation, labeled III, can be seen by plotting the hole distribution in both stackings. As shown in Fig. B.6, fixing the electron on top of the corresponding inequivalent C atom, the spatial distribution of the hole spread over both h-BN layers in the B-g-B stacking and over only one h-BN layer in the C-g-B arrangement. This result reflects the layer selectivity of the KS states shown in Fig. 4.9. As a result, the spatial distribution of the e-h pairs can be controlled through the layer patterning.

The 3D visualization of these excitons can be found in YouTube azt this link:

http://youtu.be/tQrAPuFqFh8. In addition, the input and output files of our calculations

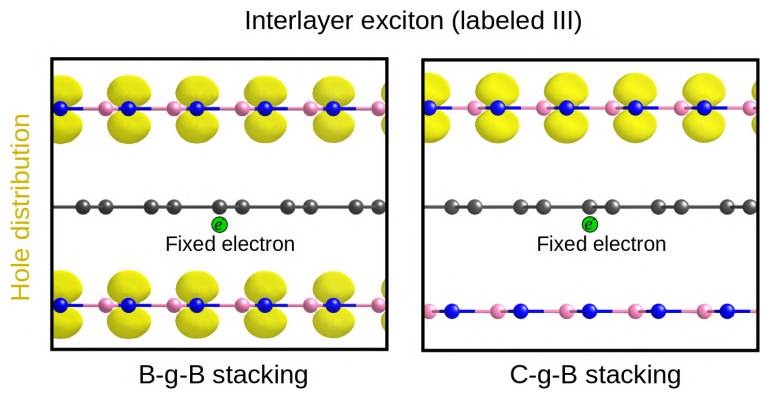

Figure B.6: The spatial distribution of the associated hole (yellow isosurface) with the electron being fixed on top of C atoms (green circle) of excitation labeled III in Chapter 4 of B-g-B (**a**) and C-g-B (**b**) configurations.

presented in Chapter 4 for the B-g-B and C-g-B stackings can be downloaded from the NOMAD repository at this link:

http://dx.doi.org/10.17172/NOMAD/2017.03.16-1

Bibliography

[1] A. Geim et al., Nature (London) **499**, 419 (2013).

[2] K. S. Novoselov et al., Science. **306**, 666 (2004).

[3] A. K. Geim et al., Nature Materials. **6**, 183 (2007).

[4] K. Watanabe et al., Nature Materials. **3**, 404 (2004).

[5] W. Auwarter et al., Chem. Mater. **16**, 343 (2004).

[6] L. Song et al., Nano Letters. **10**, 3209 (2010).

[7] A. Splendiani et al., Nano Letters. **10**, 1271 (2010).

[8] J.-K. Huang et al., ACS Nano. **8**, 923 (2014).

[9] K. Mak et al., Phys. Rev. Lett. **105**, 136805 (2010).

[10] Q. Wang et al., Nature Nanotech. **7**, 699 (2012).

[11] M. Chhowalla et al., Nature Chemistry. **5**, 263 (2013).

[12] H. Liu et al., ACS Nano. **8**, 4033 (2014).

[13] L. Li et al., Nature Nanotech. **9**, 372 (2014).

[14] A. H. Woomer et al., ACS Nano. **9**, 8869 (2015).

[15] K. S. Novoselov et al., Proc. National Acad. Sci. **102**, 10451 (2005).

[16] C. Lee et al., Science. **328**, 76 (2010).

[17] J. N. Coleman et al., Science. **331**, 568 (2011).

[18] H. Zhang, ACS Nano. **9**, 9451 (2015).

[19] B. Aufray et al., Appl. Phys. Lett. **96**, 183102 (2010).

[20] D. M. E. et al., New J. Phys. **16**, 095002 (2014).

[21] Q. Wang et al., Chem. Rev. **112**, 4124 (2012).

[22] R. Ma et al., Advanced Materials. **22**, 5082 (2010).

[23] I. C. Smith et al., Angewandte Chemie. **126**, 11414 (2014).

[24] D. H. Cao et al., J. American Chem. Soc. **137**, 7843 (2015).

[25] L. Dou et al., Science. **349**, 1518 (2015).

[26] J. Song et al., Adv. Materials. **28**, 4861 (2016).

[27] G. Grancini et al., Nature Communications. **8**, 15684 (2017).

[28] A. C. Ferrari et al., Nanoscale. **7**, 4598 (2015).

[29] S. Z. Butler et al., ACS Nano. **7**, 2898 (2013).

[30] M. Xu et al., Chem. Rev. **113**, 3766 (2013).

[31] H. Wang et al., Nanoscale. **6**, 12250 (2014).

[32] A. Ferrari et al., Nanoscale. **7**, 4598 (2015).

[33] T. Niu et al., Prog. Surf. Sci. **90**, 21 (2015).

[34] M.-Y. Li et al., Materials Today. **19**, 322 (2016).

[35] K. S. Novoselov et al., Science. **353**, aac9439 (2016).

[36] W. Zhang et al., 2D Mater. **3**, 022001 (2016).

[37] Y. Kubota et al., Science. **317**, 932 (2007).

[38] B. Arnaud et al., Phys. Rev. Lett. **96**, 026402 (2006).

[39] L. Wirtz et al., Phys. Rev. Lett. **96**, 126104 (2006).

[40] L. Wirtz et al., Phys. Rev. Lett. **100**, 189701 (2008).

[41] S. Galambosi et al., Phys. Rev. B. **83**, 081413 (2011).

[42] T. Galvani et al., Phys. Rev. B. **94**, 125303 (2016).

[43] R. Quhe et al., NPG Asia Materials **4**, e6 (2012).

[44] Y. Sakai et al., Phys. Rev. B. **89**, 115424 (2014).

[45] Y. Sakai et al., J. Phys. Soc. Jpn. **84**, 121002 (2015).

[46] Q. Wang et al., Nature Nanotech. **7**, 699 (2012).

[47] G. Bhimanapati et al., ACS Nano **9**, 11509 (2015).

[48] Q. Zeng et al., Small. **11**, 1868 (2015).

[49] G. Fiori et al., Nature Nanotech. **9**, 768 (2014).

[50] K. S. Thygesen et al., 2D Mater. **4**, 022004 (2017).

[51] F. Xia et al., Nature Photon. **8**, 899 (2014).

[52] A. Ramasubramaniam, Phys. Rev. B. **86**, 115409 (2012).

[53] Q. H. Wang et al., Nature Nanotech.**7**, 699 (2012).

[54] V. Tran et al., Phys. Rev. B. **89**, 235319 (2014).

[55] A. Chernikov et al., Phys. Rev. Lett. **113**, 076802 (2014).

[56] K. He et al., Phys. Rev. Lett. **113**, 026803 2014.

[57] S. Latini et al., Phys. Rev. B. **92**, 245123 (2015).

[58] D. Qiu et al., Phys. Rev. Lett. **111**, 216805 (2013).

[59] W. Wei et al., Phys. Rev. B **87**, 085202 2013.

[60] W. Wei et al., Phys. Rev. B. **88**, 045203 2013.

[61] H. Shu et al., Phys. Chem. Chem. Phys. **17**, 4542 (2015).

[62] P. Cudazzo et al., Phys. Rev. Lett. **116**, 066803 2016.

[63] M. Osada et al., Adv. Mater. **24**, 210 (2012).

[64] F. Koppens et al., Nature Nanotech. **9**, 780 (2014).

[65] J. Y. Lee et al., Nanomaterials. **6** (2016).

[66] A. H. Neto et al., Rev. Mod. Phys. **81**, 109 (2009).

[67] C. Lee et al., Science. **321**, 385 (2008).

[68] R. R. Nair et al., Science. **320**, 1308 (2008).

[69] A. Balandin et al., Nano Letters. **8**, 902 (2008).

[70] J. Wang et al., Materials Today Phy. **2**, 6 (2017).

[71] X. Huang et al., Small. **7**, 1876 (2011).

[72] F. Bonaccorso et al., Nature Photonics. **4**, 611 (2010).

[73] V. Chabot et al., Energy Environ. Sci. **7**, 1564 (2014).

[74] D. Chen et al., Chem. Soc. Rev. **39**, 3157 (2010).

[75] Y. Wang et al., Trends in Biotech. **29**, 205 (2011).

[76] A. K. Geim, Science. **324**, 1530 (2009).

[77] S. Bae et al., Nature Nanotechnology. **5**, 574 (2010).

[78] X. Wang et al., Nano Letters. **8**, 323 (2008).

[79] W. Choi et al., Criti. Rev. in Soli. Stat. and Mater. Sci. **35**, 52 (2010).

[80] W. Ren et al., Nature Nanotechnology. **9**, 726 (2014).

[81] Materials Today. **15**, 564 (2012).

[82] X. Li et al., Science. **319**, 1229 (2008).

[83] K. T. et al., Progr. in Mater. Sci. **57**, 1061 (2012).

[84] V. Georgakilas et al., Chemical Reviews. **112**, 6156 (2012).

[85] J. Sofo et al., Phys. Rev. B. **75**, 153401 (2007).

[86] R. Balog et al., Nature Materials. **9**, 315 (2010).

[87] P. Cudazzo et al., Phys. Rev. Lett. **104**, 226804 (2010).

[88] H. Liu et al., J. Mater. Chem. **21**, 3335 (2011).

[89] W. Aggoune et al., Phys. Status Solidi B. **253**, 712 (2016).

[90] Z. Ni et al., ACS Nano. **2**, 2301 (2008).

[91] S. Y. Zhou et al., Nature Materials. **6**, 770 (2007).

[92] G. Giovannetti et al., Phys. Rev. B. **76**, 073103 (2007).

[93] P. Trevisanutto et al., Phys. Rev. Lett. **101**, 226405 (2008).

[94] P. Trevisanutto et al., Phys. Rev. B. **81**, 121405 (2010).

[95] A. Ramasubramaniam et al., Nano Lett. **11**, 1070 (2011).

[96] Z.-G. Chen et al., Nature Communications. **5**, 4461 (2014).

[97] F. Withers et al. Nature materials. **14**, 301 (2015).

[98] L. Wang et al., Science. **342**, 614 (2013).

[99] D. Golberg et al., ACS Nano. **4**, 2979 (2010).

[100] J. Bernal, Proc. R. Soc. London A. **106**, 749 (1924).

[101] Y. Lin et al., Nanoscale. **4**, 6908 (2012).

[102] G. Cassabois et al., Nature Photonics. **10**, 262 (2016).

[103] R. Bourrellier et al., ACS Photon. **1**, 857 (2014).

[104] F. V. A. et al., Sov. Phys. Solid State. **13**, 754 (1971).

[105] A. Zunger et al., Phys. Rev. B. **13**, 5560 (1976).

[106] C. L. G. et al., J. of Phys. D: Appl. Phys. **15**, 1143 (1982).

[107] C. Tarrio et al., Phys. Rev. B. **40**, 7852 (1989).

[108] A. I. Lukomskii et al., J. Appl. Spectrosc. **57**, 607 (1992).

[109] V.L. Solozhenko et al., J. Phys. Chem. Solids. **62**, 1331 (2001).

[110] E. D. A. et al., J. Phys.: Cond. Matter. **20**, 075233 (2008).

[111] E. J. H. et al., J. of Crys. Growth. **403**, 110 (2014).

[112] X. Blase et al., Phys. Rev. B. **51**, 6868 (1995).

[113] L. Wirtz et al., https://arxiv.org/abs/cond-mat/0508421 (2005).

[114] S.-P. Gao, Solid State Commun. **152**, 1817 (2012).

[115] J. Warner et al., ACS Nano **4**, 1299 (2010).

[116] C.-J. Kim et al., Nano Lett. **13**, 5660 (2013).

[117] A. Shmeliov et al., Nanoscale. **5**, 2290 (2013).

[118] M. H. Khan et al., Nanoscale. **8**, 15926 (2016).

[119] M. H. Khan et al., Materials Today. **20**, 611 (2017).

[120] H. Henck et al., Appl. Phys. Lett. **110**, 023101 (2017).

[121] Y. J. L. et al., Physica B: Conden. Matter. **406**, 2293 (2011).

[122] L. Liu et al., Phys. Rev. B. **68**, 104102 (2003).

[123] J. He et al., Phys. Rev. B. **89**, 075409 (2014).

[124] A. H. Reshak et al., RSC Adv. **4**, 11967 (2014).

[125] J. Yan et al., Nano Lett. **15**, 8155 (2015).

[126] H. Zheng et al., Phys. Rev. B. **92**, 115307 (2015).

[127] Z. Xu et al., Physica E. **79**, 198 (2016).

[128] J. Dai et al., J. Phys. Chem. Lett. **5**, 1289 (2014).

[129] S. Lei et al., Nano Letters. **16**, 1317 (2016), pMID: 26799596.

[130] P. Kumar et al., Phys. Rev. B. **93**, 195428 (2016).

[131] D. Koda et al., J. Phys. Chem. C. **121**, 3862 (2017).

[132] H.-F. Lin et al., J. Mater. Chem. C **5**, 2291 (2017).

[133] D. Çakır et al., Phys. Rev. B. **92**, 165406 (2015).

[134] D. Kecik et al., Phys. Rev. B. **94**, 205410 (2016).

[135] Y. Mogulkoc et al., Comp. Mater. Sci. **124**, 23 (2016).

[136] N. R. Wilson et al., Sci. Adv. **3** (2017).

[137] E. Torun et al., https://arxiv.org/abs/1803.05483 (2018).

[138] A. Arora et al., Nature Comm. **8**, 639 (2017).

[139] S. Latini et al., Nano Lett. **17**, 938 (2017).

[140] C. R. Dean et al., Nature Nanotech. **5**, 722 (2010).

[141] A. Mayorov et al., Nano Lett. **11**, 2396 (2011).

[142] N. Kharche et al., Nano Lett. **11**, 5274 (2011).

[143] X. Zhong et al., Nanoscale. **4**, 5490 (2012).

[144] J. Wang et al., RSC Adv. **7**, 16801 (2017).

[145] Q. Li et al., Small. **12**, 32 (2016).

[146] L. Britnell et al., Science. **335**, 947 (2012).

[147] Z.-G. Chen et al., Nature Comm. **5**, 4461 (2014).

[148] D. S. L. Abergel et al., New. J. Phys. **15**, 123009 (2013).

[149] R. Decker et al., Nano Letters. **11**, 2291 (2011).

[150] C. R. Woods et al., Nature Phys. **10**, 451 (2014).

[151] M. M. van Wijk et al., Phys. Rev. Lett. **113**, 135504 (2014).

[152] G. Argentero et al., Nano Letters. **17**, 1409 (2017).

[153] M. Yankowitz et al., Nature Physics. **8**, 382 (2012).

[154] G. J. Slotman et al., Phys. Rev. Lett. **115**, 186801 (2015).

[155] W. Yang et al., Nature Materials. **12** (2013).

[156] L. H. Thomas, Mathematical Proceedings of the Cambridge Philosophical Society. **23**, 542–548 (1927).

[157] E. Fermi, Zeitschrift für Physik. **48**, 73 (1928).

[158] H. Hohenberg et al., Phys. Rev. **136**, B864 (1964).

[159] K. W. et al., Phys. Rev. **140**, A1133 (1965).

[160] D. M. Ceperley et al., Phys. Rev. Lett. **45**, 566 (1980).

[161] J. P. Perdew et al., Phys. Rev. B. **23**, 5048 (1981).

[162] J. F. Janak, Phys. Rev. B. **18**, 7165 (1978).

[163] M. Levy et al., Phys. Rev. A. **30**, 2745 (1984).

[164] C.-O. Almbladh et al., Phys. Rev. B. **31**, 3231 (1985).

[165] G. Strinati, La Rivista del Nuovo Cimento (1978-1999). **11**, 1 (1988).

[166] S. Albrecht et al., Phys. Rev. Lett. **80**, 4510 (1998).

[167] G. Onida et al., Rev. Mod. Phys. **74**, 601 (2002).

[168] L. Hedin, Phys. Rev. **139**, A796 (1965).

[169] S. Sagmeister, Ph.D. thesis, Karl-Franzens-Universität Graz, http://exciting-code.org (2009).

[170] M. Rohlfing et al., Phys. Rev. B. **62**, 4927 (2000).

[171] H. Lehmann, Il Nuovo Cimento (1943-1954). **11**, 342 (1954).

[172] M. Hybertsen et al., Phys. Rev. B. **34**, 5390 (1986).

[173] M. van Schilfgaarde et al., Phys. Rev. Lett. **96**, 226402 (2006).

[174] D. Nabok et al., Phys. Rev. B. **94**, 035118 (2016).

[175] H. Jiang et al., Comput. Phys. Commun. **184**, 348 (2013).

[176] J. P. Perdew et al., Phys. Rev. Lett. **77**, 3865 (1996).

[177] B. Cunningham et al., Phys. Rev. Materials. **2**, 034603 (2018).

[178] A. Gulans et al., J. Phys. Condens. Matter. **26**, 363202 (2014).

[179] P. P. et al., Phys. Rev. B **66**, 165105 (2002).

[180] J. C. Slater, Phys. Rev. **51**, 846 (1937).

[181] O. Andersen et al., Phys. Rev. B. **12**, 3060 (1975).

[182] E. Sjöstedt et al., Solid State Commun. **114**, 15 (2000).

[183] http://exciting-code.org .

[184] R. H. Byrd et al., SIAM Journal on Scientific Computing. **16**, 1190 (1995).

[185] S. Grimme, J. Comput. Chem. **27**, 1787 (2006).

[186] A. Tkatchenko et al., Phys. Rev. Lett. **102**, 073005 (2009).

[187] S. Sagmeister et al., Phys. Chem. Chem. Phys. **11**, 4451 (2009).

[188] Y. Gillet et al., Phys. Rev. B. **88**, 094305 (2013).

[189] D. Kammerlander et al., Phys. Rev. B. **86**, 125203 (2012).

[190] K. Momma et al., J. Appl. Cryst. **44**, 1272 (2011).

[191] Pease R. S., Nature. **165**, 722–723 (1950).

[192] N. Marom et al., Phys. Rev. Lett. **105**, 046801 (2010).

[193] V. Solozhenko et al., Solid State Commun. **96**, 1 (1995).

[194] T. Bučko et al., Phys. Rev. B. **87**, 064110 (2013).

[195] R. M. Ribeiro et al., Phys. Rev. B. **83**, 235312 (2011).

[196] O. Hod, J. Chem. Theory. Comput. **8**, 1360 (2012).

[197] T. Bučko et al., J. Phys. Chem. A. **114**, 11814 (2010), pMID: 20923175.

[198] G. Constantinescu et al., Phys. Rev. Lett. **111**, 036104 (2013).

[199] R. S. Pease, Acta Crystallogr. **5**, 356 (1952).

[200] N. McDougall et al., Microscopy and Microanalysis. **20**, 1053–1059 (2014).

[201] I. Leven et al., J. Chem. Theory. Comput. **12**, 2896 (2016).

[202] N. Berseneva et al., Phys. Rev. B. **87**, 035404 (2013).

[203] R. Mamy et al., J. Phys. Lett.-Paris. **42**, 473 (1981).

[204] F. Paleari et al., https://arxiv.org/abs/1803.00982 (2018).

[205] C. Deibel et al., Adv. Mater. **22**, 4097 (2010).

[206] X. Hong et al., Nature Nanotech. **9**, 682 (2014).

[207] M. Aoki et al., Solid State Commun. **142**, 123 (2007).

[208] Y. Xu et al., Nanotechnol. **21**, 065711 (2010).

[209] B. Sahu et al., Phys. Rev. B. **78**, 045404 (2008).

[210] N. Kharche et al., ACS Nano. **5**, 6096 (2011).

[211] K. Gundra et al., Phys. Rev. B. **84**, 075442 (2011).

[212] M. De Corato et al., J. Phys. Chem. C. **118**, 23219 (2014).

[213] M. Yankowitz et al., Nature Phys. **8**, 382 (2012).

[214] L. Britnell et al., Nano Lett. **12**, 1707 (2012).

[215] A. Mishchenko et al., Nature Nanotech. **9**, 808 (2014).

[216] C. Kramberger et al., Phys. Rev. Lett. **100**, 196803 (2008).

[217] V. Despoja et al., Phys. Rev. B. **87**, 075447 (2013).

[218] P. Wachsmuth et al., Phys. Rev. B. **88**, 075433 (2013).

[219] L. Yang et al., Phys. Rev. Lett. **103**, 186802 (2009).

[220] K. M. Lau et al., Ultralow threshold quantum well lasers (San Diego, CA: Academic., 1993).

[221] J. B. Neaton et al., Phys. Rev. Lett. **97**, 216405 (2006).

[222] F. Hüser et al., Phys. Rev. B. **87**, 235132 (2013).

[223] P. Puschnig et al., Phys. Rev. B. **86**, 085107 (2012).

[224] Q. Fu et al., Phys. Chem. Chem. Phys. **19**, 6196 (2017).

Papers

- ***Enhanced light–matter interaction in graphene/h-bn van der waals heterostructures***, Wahib Aggoune, Caterina Cocchi, Dmitrii Nabok, Karim Rezouali, Mohamed Akli Belkhir, and Claudia Draxl, J. Phys. Chem. Lett., **8**, 1464 (2017). Link: https://pubs.acs.org/doi/abs/10.1021/acs.jpclett.7b00357
- ***Strong excitonic effects in hydrogen–graphene–fluorine janus graphene***, Wahib Aggoune, Karim Rezouali, and Mohamed Akli Belkhir, Phys. Status Solidi B, **253**, 712 (2016). Link: http://onlinelibrary.wiley.com/doi/10.1002/pssb.201552431/full
- ***Dimensionality of excitons in stacked van der Waals materials: The example of hexagonal boron nitride***, Wahib Aggoune, Caterina Cocchi, Dmitrii Nabok, Karim Rezouali, Mohamed Akli Belkhir, and Claudia Draxl, submitted for publication.
- ***Structural, electronic, and optical properties of graphene/h-BN vdW heterostructures***, Wahib Aggoune, Caterina Cocchi, Dmitrii Nabok, Karim Rezouali, Mohamed Akli Belkhir, and Claudia Draxl, in preparation.

THE JOURNAL OF PHYSICAL CHEMISTRY Letters

Letter

pubs.acs.org/JPCL

Enhanced Light−Matter Interaction in Graphene/h-BN van der Waals Heterostructures

Wahib Aggoune,[†,‡] Caterina Cocchi,[*,†,§] Dmitrii Nabok,[†,§] Karim Rezouali,[‡] Mohamed Akli Belkhir,[‡] and Claudia Draxl[†,§]

[†]Institut für Physik and IRIS Adlershof, Humboldt-Universität zu Berlin, 12489 Berlin, Germany

[‡]Laboratoire de Physique Théorique, Faculté des Science Exactes, Université de Bejaia, 06000 Bejaia, Algeria

Supporting Information

ABSTRACT: By investigating the optoelectronic properties of prototypical graphene/hexagonal boron nitride (h-BN) heterostructures, we demonstrate how a nanostructured combination of these materials can lead to a dramatic enhancement of light−matter interaction and give rise to unique excitations. In the framework of ab initio many-body perturbation theory, we show that such heterostructures absorb light over a broad frequency range, from the near-infrared to the ultraviolet (UV), and that each spectral region is characterized by a specific type of excitations. Delocalized electron−hole pairs in graphene dominate the low-energy part of the spectrum, while strongly bound electron−hole pairs in h-BN are preserved in the near-UV. Besides these features, characteristic of the pristine constituents, charge-transfer excitations appear across the visible region. Remarkably, the spatial distribution of the electron and the hole can be selectively tuned by modulating the stacking arrangement of the individual building blocks. Our results open up unprecedented perspectives in view of designing van der Waals heterostructures with tailored optoelectronic features.

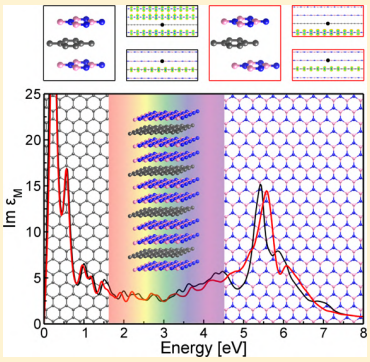

Van der Waals (vdW) heterostructures are a new frontier of materials science.[1] The possibility of stacking atomically thin layers with nanoscale precision has opened unprecedented opportunities to create materials with customized characteristics. New properties can be accessed through a combination of the constituents, which maintain their intrinsic features.[2,3] This perspective is particularly appealing in the field of optoelectronics. The response of materials to electromagnetic radiation, consisting of a multitude of diversified phenomena, is extremely sensitive to their atomic structure and, consequently, to their electronic properties. Systems efficiently absorbing over a broad frequency range can be designed through an engineered stacking of single layers. Charge-transfer excitations, with the electron and the hole delocalized on different layers, can be created at the interface.[4−9] At the same time, the spatial separation of the electron−hole pairs can be enhanced through a systematic modulation of the structural properties.[10−12]

Graphene and hexagonal boron nitride (h-BN) monolayers are ideal candidates to achieve this goal as they exhibit a complementary behavior when interacting with light. The optical spectrum of graphene, a peculiar semi-metal,[13] is dominated by a zero-energy resonance, while it is rather featureless in the visible region.[14] Collective excitations, such as excitons and plasmons, occur only at ultraviolet (UV) frequencies.[15−18] On the other hand, h-BN is a large-band-gap material transparent to visible light, which exhibits unique optical properties in the near-UV range[19,20] related to the presence of strongly bound excitons.[21−23] Combining these two materials to form a vdW heterostructure enables one to benefit from their individual characteristics and to access new features.[24] The small mismatch between their lattices has already triggered a number of pioneering studies in this direction,[25−28] further boosted by the opportunity to exploit h-BN in view of opening a band gap in graphene.[29−31] When interacting with light, graphene/h-BN vdW heterostructures are expected to show all their potential,[32] as recently demonstrated also for plasmonic excitations.[33−35]

In this work, we study the optoelectronic properties of prototypical periodic graphene/h-BN heterostructures. Through detailed analysis of the spectra, enabled by a highly precise state-of-the-art ab initio many-body approach, we demonstrate that different types of excitations coexist in such a system, each of them dominating a well-defined frequency range. We focus on charge-transfer excitations that are created at the interface and show that a selective modulation of the stacking of h-BN layers with respect to each other and to graphene can tune the spatial distribution of the electron−hole (e−h) pairs. As such, our results pave the way for selectively enhancing light−matter interaction through nanopatterning.

To perform this study, we consider a periodic heterostructure with a graphene sheet sandwiched between four h-BN layers. Such a system is modeled by a trilayer unit cell (h-BN/graphene/h-BN), infinitely replicated by means of periodic boundary conditions. In this configuration, each h-BN layer

Received: February 14, 2017
Accepted: March 15, 2017
Published: March 15, 2017

 © XXXX American Chemical Society

DOI: 10.1021/acs.jpclett.7b00357
J. Phys. Chem. Lett. 2017, 8, 1464−1471

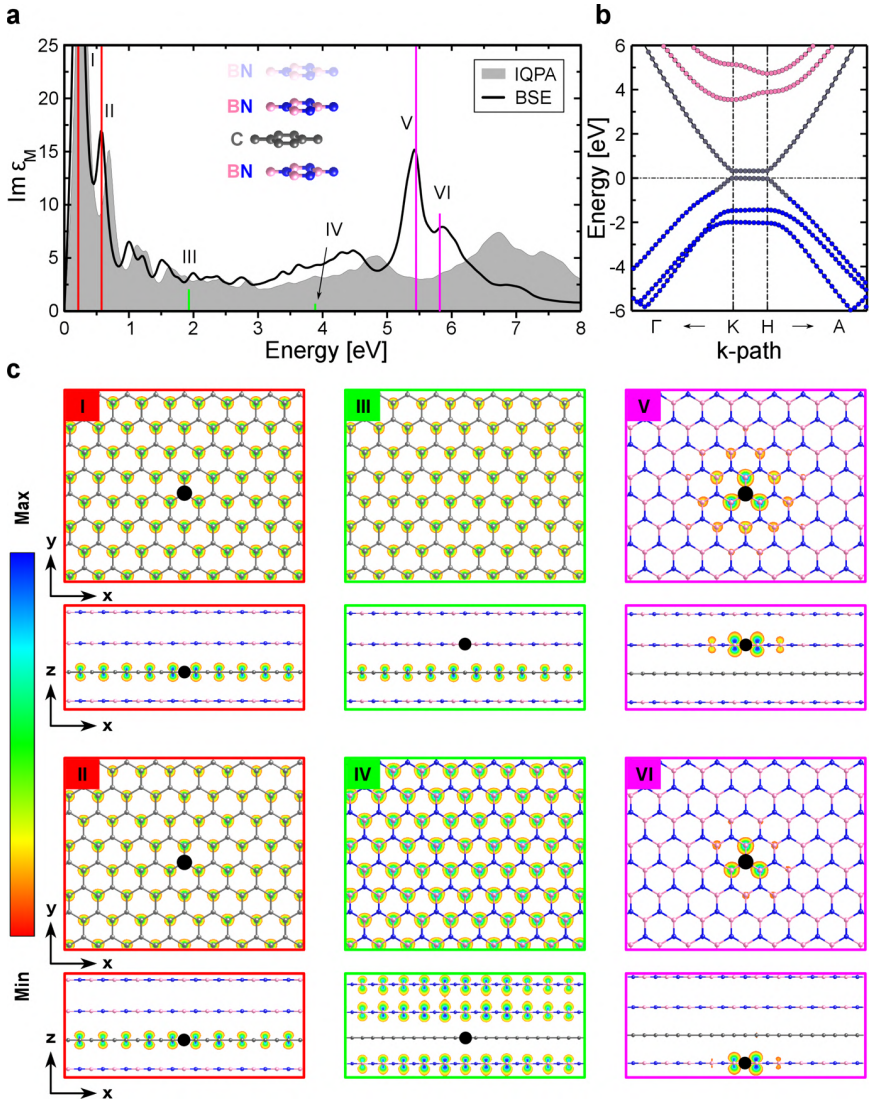

Figure 1. (a) In-plane component of the imaginary part of the macroscopic dielectric function of a B−g−B stacked h-BN/graphene/h-BN heterostructure (inset), computed by including (BSE, solid line) and by neglecting (IQPA, shaded area) excitonic effects. (b) Quasi-particle (QP) electronic structure of the system. The band character is indicated using the color code of the atomic species (C: gray, N: blue, B: pink). The valence band maximum is set to zero. (c) Two-dimensional projections of the electron component of the e−h wave functions highlighted in the spectrum in panel (a). The corresponding position of the hole is marked by a black dot.

directly interacts with both graphene and another h-BN sheet. An important parameter is represented by the stacking arrangement of the layers in the in-plane directions. Here we focus on a structure where h-BN layers are displaced with respect to graphene such that the N atoms are located on hollow sites with respect to the hexagonal carbon lattice (Figure 1a, inset). We refer to this configuration as the B−g−B stacking, where g stands for graphene and B indicates the displacement of the h-BN layers with respect to the carbon sheet, according to the conventional nomenclature for stacked systems.[36] More details on the structural properties of the heterostructure are provided in the Supporting Information (SI).

The electronic and optical properties of the B−g−B heterostructure are summarized in Figure 1. The interaction with h-BN, although weak, is sufficient to open a quasi-particle (QP) gap of 250 meV in graphene along the K−H path of the Brillouin zone (BZ). This result is in good agreement with previous studies based on density functional theory (DFT)[37−39] and many-body perturbation theory[40−42] performed on analogous systems. On the other hand, the interaction with graphene tends to reduce the intrinsic band gap of h-BN, which in this heterostructure amounts to 5.15 eV at the high-symmetry point K (see Figure 1b). This value is about 0.5 eV smaller than the quasi-particle gap reported for bulk boron nitride in the corresponding stacking sequence.[43,44] Such a band gap reduction is mainly ascribed to polarization effects, which have been extensively discussed for molecules and polymers adsorbed on graphene[45−47] and which turn out to be non-negligible even in the case of interacting monolayer insulators such as h-BN and carbon fluoride.[48] The electronic properties of the heterostructure are reflected in the optical spectrum (Figure 1a), as well as in the wealth of excitations dominating specific energy regions (Figure 1c). Among them, we immediately identify three main types, depending on their spatial extension along the in-plane and out-of-plane directions:

DOI: 10.1021/acs.jpclett.7b00357
J. Phys. Chem. Lett. 2017, 8, 1464−1471

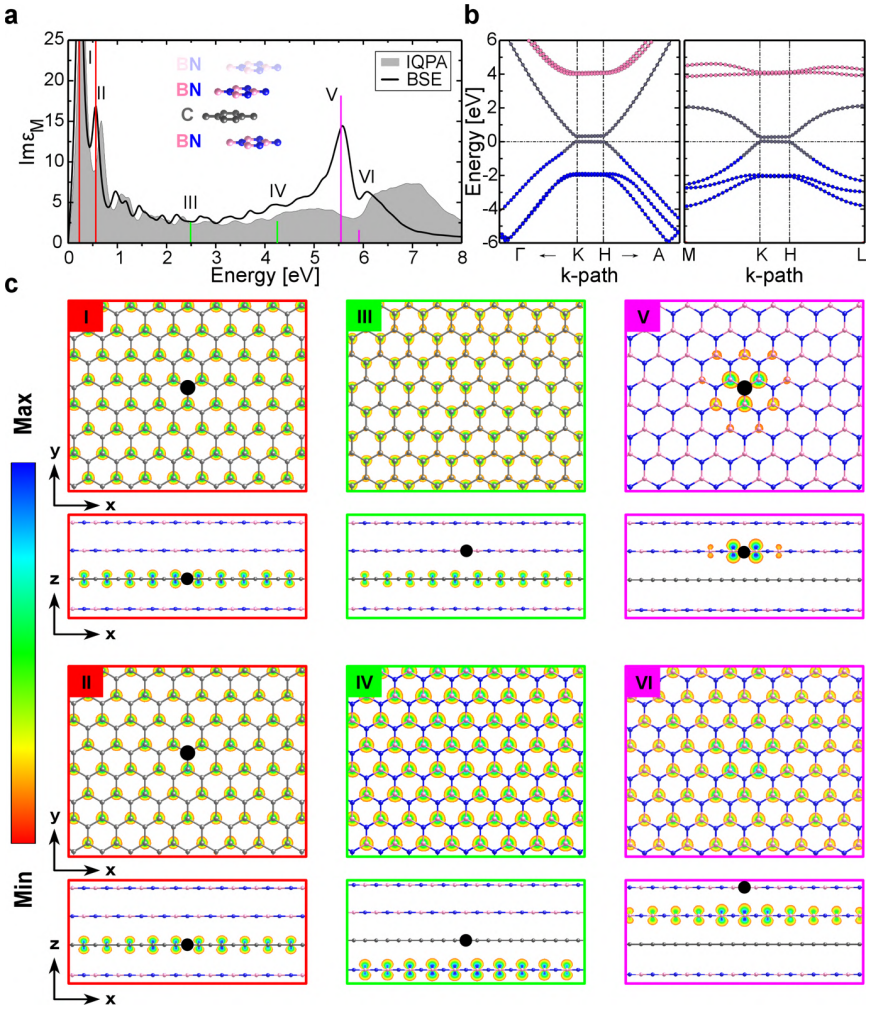

Figure 2. (a) In-plane component of the imaginary part of the macroscopic dielectric function of a B−g−C stacked h-BN/graphene/h-BN heterostructure (inset), computed by including (BSE, solid line) and by neglecting (IQPA, shaded area) excitonic effects. (b) Quasi-particle electronic structure of the system in the vicinity of the high-symmetry points K and H, approached from two different directions. The band character is indicated using the color code of the atomic species (C: gray, N: blue, B: pink). The VBM is set to zero. (c) Two-dimensional projections of the electron component of the e−h wave functions highlighted in the spectrum in panel (a). The corresponding position of the hole is marked by a black dot.

delocalized excitations with both the electron and the hole in the same (I and II) or in different layers (III and IV) as well as localized excitons in the h-BN layer (V and VI). In the following, we discuss in detail each spectral region and the excitation types characterizing it.

The low-frequency part of the spectrum, up to 1 eV, is dominated by interband transitions within the graphene layer, consistent with optical conductivity measurements.[49,50] Due to the symmetry of the honeycomb carbon lattice, the first peak (I) and its shoulder (II) are double-degenerate (more details are given in the SI, Figure S4a). These excitations exhibit $\pi-\pi^*$ character, as shown in Figure 1c by the corresponding correlated probability of finding the electron for a fixed hole position. Specifically, the first absorption maximum (I) at 220 meV comes from a transition along the K−H path of the BZ, while II has major contributions in the vicinity of K, where the electronic wave functions of valence band maximum (VBM) and conduction band minimum (CBM) are located on inequivalent carbon atoms in the unit cell (see also Figures S2a and S5). These intense peaks at IR frequencies are generated by the finite band gap induced by the interaction of the carbon monolayer with the neighboring h-BN sheets.[29] Consequently, the zero-energy divergence dominating the absorption spectrum of graphene, as an effect of its semimetallic character,[14,16] disappears in the heterostructure, with the peak being blue-shifted due to the presence of the quasi-particle gap.[51]

The interband character of the graphene-derived excitations is confirmed by the appearance of analogous absorption maxima in the spectrum computed within the independent quasi-particle approximation (IQPA). The e−h interaction does not affect the spectral shape nor the nature of the excitations, characterized by a delocalized π^*-like distribution of the electron in one inequivalent carbon atom in the unit cell, with the hole being located on the other carbon atom within the graphene layer (Figure 1c). Excitonic effects essentially red shift the peak position by 30 meV with respect to the gap, which coincides with the onset of the IQPA spectrum at 250 meV. Also, the peculiar nature of the highest occupied band, with C-like character in the vicinity of K−H and with N-like character elsewhere in the BZ, is directly determined by the periodic alternation of the monolayers. In the UV region, between 5 and

DOI: 10.1021/acs.jpclett.7b00357
J. Phys. Chem. Lett. 2017, 8, 1464−1471

6 eV, we find the spectroscopic signatures of h-BN, mainly related to the excitonic peak centered at 5.4 eV. A double-degenerate bound exciton dominates the spectrum of the bulk material,[21−23] with its characteristics being preserved in the heterostructure. In the latter case, the exciton binding energy cannot be quantified with respect to the fundamental gap, which is given by the graphene bands (Figure 1b). However, comparison between the BSE and the IQPA spectra indicates that the two main excitations (V and VI) stem from the manifold of interband transitions between 6 and 8 eV (Figure 1a). Considering the absorption maximum of the broad hump between 6 and 8 eV in the IQPA spectrum, we estimate the binding energy of excitation V to be on the order of 1 eV. In this region, the dipole coupling between the single-particle transitions generates spatially confined e−h pairs with large oscillator strength (Figure 1c). At the same time, the e−h Coulomb interaction shifts the spectral weight to lower energy. The correlated electron distribution of these excitons is confined within a triangular region that spreads over a few unit cells around the fixed hole position, in analogy with the excitations predicted for bulk h-BN.[21−23] In Figure 1c, we report the corresponding averaged densities, while individual plots are shown in the SI (Figure S4c). The electron and the hole sit on the same layer, making both V and VI intralayer excitons. This property comes directly from the character of the electronic states contributing to these excitations. Along the K−H path, the N-like VBM-1 and VBM-2, as well as the B-like states above the CBM, namely CBM+1 and CBM+2, are uniformly distributed on both h-BN layers in the unit cell (Figure S2a). The stacking arrangement of neighboring boron nitride sheets thus directly influences their interaction. For this reason, regardless of the position of the hole in both excitons, the corresponding electron is always found in the same h-BN layer. The peak centered at 5.4 eV is formed by a number of excitations with the same character as V (Figure S3a). On the other hand, the weaker peak at 6 eV, in addition to exciton VI, embraces several excitations with rather mixed character, corresponding to delocalized e−h pairs.

In the visible and near-UV range, where the spectra of the constituents are rather featureless, we find the actual fingerprints of the heterostructure. The oscillator strength between 1.6 and 5 eV is weak compared to that in other spectral regions, owing to the charge-transfer character of most of the excitations that take place in this frequency window. With the hole located on h-BN and the electron on the carbon layer, or vice versa, the wave function overlap is significantly lower than that in the in-plane excitations discussed above but still nonzero, thanks to the $\pi-\pi^*$ interaction between the layers. In the visible region, between approximately 1.6 and 3.2 eV, the excitations mainly stem from transitions from the N-like VBM−1/VBM−2 to the graphene-like CBM. An exemplary excitation of this kind is the one labeled by III (double-degenerate; see Figure S4a), which contributes to the peak at 1.9 eV, as shown in Figure 1a. Regardless of whether the hole is fixed on h-BN above or below graphene, the electron distribution has π^* character and is spread over the carbon sheet. At higher energies, between 3.5 and 5 eV, we find e−h pairs with the hole stemming from the graphene VBM and the electron promoted to the boron-like CBM+1 and CBM+2. As discussed above, the wave functions associated with the B-like CBM+1 and CBM+2 are spread over all h-BN layers. For this reason, the electron distribution of the charge-transfer excitation IV (also double-degenerate; see Figure S4b) is delocalized in both in-plane and out-of-plane directions (Figure 1c). The presence of the corresponding peaks also in the IQPA spectrum indicates the interband nature of both III and IV. Similar to the graphene-related $\pi-\pi^*$ transitions (I and II), excitonic effects push these peaks to lower energies. In this case, the red shift amounts to about 0.1 eV. The relatively weak binding of these charge-transfer excitations is expected to ease the dissociation of the corresponding e−h pairs.

The spatial extension of the excitations can be further tuned by modifying the stacking arrangement of the boron nitride layers with respect to the carbon sheet. For this purpose, we consider another heterostructure with B−g−C stacking arrangement. In this case, the two h-BN layers in the unit cell are laterally displaced with respect to each other and to graphene. In this way, the boron atom of one h-BN sheet and the nitrogen atom of the other one are at the hollow site of the carbon honeycomb lattice (Figure 2a, inset). Overall, the spectrum shown in Figure 2a does not exhibit significant differences compared to its counterpart in the B−g−B heterostructure. Clearly, also the quasi-particle band structure is similar to the one of the B−g−B system. In Figure 2b, we plot the band dispersion in the vicinity of the high-symmetry points K and H, approached from two different directions (see also Figure S1e). This is relevant for the later discussion about the excitation character. A band gap of about 260 meV is opened in graphene due to its interaction with the neighboring boron nitride layers, while the energy separation between the highest occupied and lowest unoccupied bands with N- and B-like character, respectively, is approximately 6 eV. As in the case of the B−g−B heterostructure discussed above, the quasi-particle gap of h-BN is reduced by polarization effects due to the interaction with graphene. The renormalization with respect to the bulk material with the same stacking sequence amounts to 0.1 eV.[43,44] The relative displacement of the h-BN layers with respect to each other affects the distribution along the K−H path of the electronic wave functions in both the valence and the conduction regions.[52] In fact, in the B−g−C heterostructure, the VBM−1 and the VBM−2 as well as the CBM+1 and the CBM+2 are separated by about 80 meV along the K−H path. The corresponding electronic wave functions are thus distributed only on one individual h-BN sheet in the unit cell and exhibit either N-like (valence) or B-like (conduction) character (see also Figure S2b in the SI).

These peculiar electronic characteristics significantly influence the interlayer excitations involving h-BN layers, namely, the charge-transfer transitions in the visible/near-UV region as well as the excitons above 5 eV. The excitations in the near-IR, dominated by the graphene $\pi-\pi^*$ transitions (I and II), are obviously unaffected by the stacking arrangement. We examine first the visible/near-UV region where the charge-transfer excitations, III and IV, appear. To be consistent with the previous analysis of the B−g−B heterostructure, we inspect here the analogous features. Excitation III at about 2.5 eV is again double-degenerate (Figure S4a) and stems from transitions between the N-like VBM−2 to the graphene-like CBM (Figure S6 in the SI). The electron is uniformly delocalized on graphene, exhibiting a π^*-like distribution, with the hole located on the h-BN layer directly above the carbon sheet, where the probability density of VBM−2 is the maximal (see Figure S2b in the SI). Likewise, excitation IV is given by an e−h pair generated by transitions from the highest-occupied graphene band, VBM, and the boron-like CBM+2. In this case, the hole is on the carbon layer and the electron is distributed

DOI: 10.1021/acs.jpclett.7b00357
J. Phys. Chem. Lett. 2017, 8, 1464−1471

over the h-BN sheet directly below it (Figure 2c). At a few hundreds of meV lower and higher in energy compared to III and IV, other excitations are present (not shown), exhibiting again interlayer nature but different e−h distribution, consistent with the character of the h-BN bands (Figure S2b). A difference with respect to the B−g−B heterostructure should be noted at this point. In the latter system, the electron distribution of excitation III is in graphene, regardless of whether the hole sits on the h-BN layer directly above or below it. Instead, in the B−g−C stacked system, the correlated hole probability associated with excitation III is limited to one boron nitride sheet with the corresponding electron being again spread over the carbon lattice. Likewise, in this heterostructure, the electron distribution of excitation IV is restricted only to one h-BN layer, with the correlated hole sitting on graphene. These results indicate that the distribution of the e−h pairs appears to be very sensitive to the stacking sequence.

In a similar fashion, also the h-BN excitons are significantly affected by the layer stacking. In this case, even the shape of the corresponding peak in the spectrum is modified compared to the B−g−B heterostructure. The absorption maximum, centered at 5.6 eV, is formed by a number of excitations (Figure S3b) with the same character as the double-degenerate exciton V, that is, exhibiting intralayer character, analogous to their counterparts in the B−g−B stacking (Figure 2c). However, different from the B−g−B heterostructure, exciton V in the B−g−C stacked system arises from transitions between the N-like VBM and the B-like CBM+1 away from the K−H path in the direction of the high-symmetry point M (see Figure S6). In addition, a charge-transfer exciton between the h-BN sheets (VI) appears at 6 eV, within a peak formed by several excitations with mixed composition and spatial delocalization. Due to its interlayer character, VI has lower intensity compared to the in-plane exciton V. With the hole being located on one h-BN layer, the correlated electron distribution of exciton VI is delocalized over the other inequivalent h-BN sheet in the unit cell; with an in-plane envelope modulation embracing about 14 unit cells in real space (see Figure 2c), this exciton arises from transitions between the N-like VBM−1 and the B-like CBM+1 along the K−H path (see Figure S6 in the SI), which are distributed on the h-BN sheet below and above graphene, respectively (Figure S2b). Such a feature appears only in the B−g−C heterostructure due to the lateral displacement of the two h-BN layers in the unit cell. The interplay between the stacking arrangement and electronic wave function delocalization evidently affects also "pure" h-BN excitations. Although less relevant from a technological viewpoint, this result is additional confirmation of the potential tunability of the optical properties of graphene/h-BN heterostructures.

The graphene/h-BN heterostructures considered in this work are semiconductors exhibiting a straddling band alignment. This type I electronic configuration is optimal for stimulated emission and is thus exploited for applications such as lasers and light-emitting diodes (LEDs).[53] A prototypical LED formed by vdW-stacked graphene, h-BN, and MoS_2 layers was indeed produced recently through a well-defined arrangement of metallic, insulating, and direct-gap seminconducting monolayers, respectively.[12] Here, in a simpler system, consisting of a graphene/h-BN vdW heterostructure, we have demonstrated that further modulation of the electronic and optical properties can be achieved by selectively varying the stacking displacements of the h-BN sheets.

Before concluding, it is worth considering the results presented in this work in the context of the existing research on graphene/h-BN heterostructures. One of the main aspects to take into account is the slight lattice mismatch between the two materials, which triggers the formation of Moiré patterns.[54−61] Depending on the growth conditions, specifically whether either graphene or h-BN acts as a substrate, different patterns can be obtained.[62] Locally, the stacking arrangement may vary substantially and even coincide with the sequences considered here. The formation of Moiré patterns affects also optical properties.[63−70] New spectral features may appear above the absorption onset, with decreasing intensity at increasing magnitude of the mismatch angle.[71] The heterostructures considered in this work, with perfect lattice matching between the individual monolayers, are obviously idealized structures. Nonetheless, the analysis of their optical fingerprints presented here is an essential step forward in view of identifying and understanding the features of real systems, where not only Moiré-like superlattices but also buckling and distortions typically appear and impact light−matter interaction processes.

To summarize, we have shown that periodic graphene/h-BN heterostructures absorb electromagnetic radiation over an extended frequency range, going from the near-IR to the UV. While the electronic and optical properties of the constituents are essentially preserved, the interaction driven by layer stacking promotes new features in the visible/near-UV region. Due to the interaction with the neighboring h-BN sheets, a gap is opened in graphene, with intense $\pi-\pi^*$ interband transition below 1 eV. In the visible window and beyond, between 1.6 and 5 eV, a number of weakly bound charge-transfer excitations appear, with the corresponding electron and hole distributed on either graphene or h-BN. The e−h separation can be selectively tuned by modifying the stacking arrangement, which impacts the wave function overlap and thus leads to an increased absorption intensity. The versatile interplay between structural, electronic, and photoresponse properties in graphene/h-BN heterostructures makes such materials ideal candidates and an exceptional playground for optoelectronics.

■ THEORETICAL METHODS AND COMPUTATIONAL DETAILS

Ground-state properties are computed in the framework of DFT, within the generalized gradient approximation for the exchange−correlation functional (Perdew−Burke−Ernzerhof parametrization[72]). The DFT-D2 approach proposed by S. Grimme[73] is adopted to account for van der Waals interactions between the layers. Optical spectra are obtained in the framework of many-body perturbation theory. QP energies are computed within the G_0W_0 approximation.[74,75] Optical spectra are obtained from the solution of the Bethe−Salpeter equation (BSE), an effective two-body equation for the e−h two-particle Green's function.[76,77] The BSE Hamiltonian reads $H^{BSE} = H^{diag} + 2H^{x} + H^{dir}$, where the first term H^{diag} accounts for vertical transitions, while the other two terms incorporate electron−hole exchange (H^{x}) and the screened Coulomb interaction (H^{dir}). The excitation energies E^{λ} are the eigenvalues of the secular equation associated with the BSE Hamiltonian: $\sum_{v'c'\mathbf{k}'} H^{BSE}_{vc\mathbf{k},v'c'\mathbf{k}'} A^{\lambda}_{v'c'\mathbf{k}'} = E^{\lambda} A^{\lambda}_{vc\mathbf{k}}$, where v and c indicate valence and conduction states, respectively. The eigenvectors A^{λ} provide information about the intensity of the excitation, through the oscillator strength, given by the square modulus of $\mathbf{t}_{\lambda} = \sum_{vc\mathbf{k}} A^{\lambda}_{vc\mathbf{k}} \frac{\langle v\mathbf{k}|\hat{p}|c\mathbf{k}\rangle}{\epsilon_{c\mathbf{k}} - \epsilon_{v\mathbf{k}}}$. Moreover, they

DOI: 10.1021/acs.jpclett.7b00357
J. Phys. Chem. Lett. 2017, 8, 1464−1471

indicate the character and the composition of excitations, being the coefficients of the two-particle wave functions $\Psi^{\lambda}(\mathbf{r}_e,\mathbf{r}_h) = \sum_{vck} A^{\lambda}_{vck}\phi_{ck}(\mathbf{r}_e)\phi^{*}_{vk}(\mathbf{r}_h)$. Absorption spectra are represented by the imaginary part of the macroscopic dielectric function $\mathrm{Im}\,\varepsilon_M = \frac{8\pi^2}{\Omega}\sum_{\lambda}|\mathbf{t}_{\lambda}|^2\delta(\omega - E^{\lambda})$, where Ω is the unit cell volume.

All calculations are performed using **exciting**,[78] an all-electron full-potential code, implementing the family of linearized augmented plane-wave plus local orbitals methods. In the ground-state calculations, a basis set cutoff of $R_{MT}G_{max} = 7$ is used. For all atomic species involved (C, B, and N) a muffin-tin radius of $R_{MT} = 1.3$ bohr is adopted. The sampling of the BZ is performed with a 30 × 30 × 8 **k** grid. Both lattice constants and internal coordinates are optimized until the residual forces on each atom are smaller than 0.003 eV/Å. Calculations of QP corrections to the Kohn−Sham eigenvalues within the G_0W_0 approximation[79] include 250 empty states, and a BZ sampling with a 18 × 18 × 4 shifted **k** mesh is adopted. For the solution of the BSE[80] within the Tamm−Dancoff approximation, a cutoff of $R_{MT}G_{max} = 6$ and a 30 × 30 × 4 shifted **k** point mesh are adopted and then interpolated onto a 60 × 60 × 4 mesh using the so-called double-grid method.[81,82] In the calculation of the response function and the screened Coulomb potential, 100 empty bands are included. In the construction and diagonalization of the BSE Hamiltonian, three occupied and three unoccupied bands are considered. Local field effects are taken into account, by including 41 $|\mathbf{G} + \mathbf{q}|$ vectors. For the resulting spectra, a Lorentzian broadening of 0.1 eV is applied. Atomic structures and isosurfaces are produced with the VESTA software.[83]

■ ASSOCIATED CONTENT

Supporting Information

The Supporting Information is available free of charge on the ACS Publications website at DOI: 10.1021/acs.jpclett.7b00357.

Structural and electronic properties of the considered heterostructures as well as additional details on the character and the composition of the optical excitations (PDF)

■ AUTHOR INFORMATION

Corresponding Author

*E-mail: caterina.cocchi@physik.hu-berlin.de.

ORCID

Caterina Cocchi: 0000-0002-9243-9461

Claudia Draxl: 0000-0003-3523-6657

Notes

The authors declare no competing financial interest.

§C.C., D.N., and C.D. are also affiliated with the European Theoretical Spectroscopic Facility (ETSF).

■ ACKNOWLEDGMENTS

The authors are grateful to A. Gulans, S. Lubeck, P. Pavone, Q. Fu, and S. Tillack for fruitful discussions. This work was partly funded by the German Research Foundation (DFG), through the Collaborative Research Centers 658 and 951. W.A. acknowledges financial support from the Algerian Ministry of High Education and Scientific Research. C.C. acknowledges financial support from the Berliner Chancengleichheitsprogramm (BCP) and from IRIS Adlershof.

■ ADDITIONAL NOTE

Input and output files of our calculations can be downloaded from the NOMAD repository at this link: http://dx.doi.org/10.17172/NOMAD/2017.03.16-1.

■ REFERENCES

(1) Geim, A. K.; Grigorieva, I. V. Van der Waals heterostructures. *Nature (London, U. K.)* **2013**, *499*, 419−425.

(2) Osada, M.; Sasaki, T. Two-Dimensional Dielectric Nanosheets: Novel Nanoelectronics From Nanocrystal Building Blocks. *Adv. Mater.* **2012**, *24*, 210−228.

(3) Xu, M.; Liang, T.; Shi, M.; Chen, H. Graphene-like two-dimensional materials. *Chem. Rev.* **2013**, *113*, 3766−3798.

(4) Hong, X.; Kim, J.; Shi, S.-F.; Zhang, Y.; Jin, C.; Sun, Y.; Tongay, S.; Wu, J.; Zhang, Y.; Wang, F. Ultrafast charge transfer in atomically thin MoS2/WS2 heterostructures. *Nat. Nanotechnol.* **2014**, *9*, 682−686.

(5) Ceballos, F.; Bellus, M. Z.; Chiu, H.-Y.; Zhao, H. Ultrafast charge separation and indirect exciton formation in a MoS2−MoSe2 van der Waals heterostructure. *ACS Nano* **2014**, *8*, 12717−12724.

(6) Rivera, P.; Schaibley, J. R.; Jones, A. M.; Ross, J. S.; Wu, S.; Aivazian, G.; Klement, P.; Seyler, K.; Clark, G.; Ghimire, N. J.; et al. Observation of long-lived interlayer excitons in monolayer $MoSe_2$−WSe_2 heterostructures. *Nat. Commun.* **2015**, *6*, 6242.

(7) Latini, S.; Olsen, T.; Thygesen, K. S. Excitons in van der Waals heterostructures: The important role of dielectric screening. *Phys. Rev. B: Condens. Matter Mater. Phys.* **2015**, *92*, 245123.

(8) Haastrup, S.; Latini, S.; Bolotin, K.; Thygesen, K. S. Stark shift and electric-field-induced dissociation of excitons in monolayer MoS_2 and *h*BN/MoS_2 heterostructures. *Phys. Rev. B: Condens. Matter Mater. Phys.* **2016**, *94*, 041401.

(9) Latini, S.; Winther, K. T.; Olsen, T.; Thygesen, K. S. Interlayer excitons and Band Alignment in MoS2/hBN/WSe2 van der Waals Heterostructures. *Nano Lett.* **2017**, *17*, 938−945.

(10) Bernardi, M.; Palummo, M.; Grossman, J. C. Extraordinary sunlight absorption and one nanometer thick photovoltaics using two-dimensional monolayer materials. *Nano Lett.* **2013**, *13*, 3664−3670.

(11) Fang, H.; Battaglia, C.; Carraro, C.; Nemsak, S.; Ozdol, B.; Kang, J. S.; Bechtel, H. A.; Desai, S. B.; Kronast, F.; Unal, A. A.; et al. Strong interlayer coupling in van der Waals heterostructures built from single-layer chalcogenides. *Proc. Natl. Acad. Sci. U. S. A.* **2014**, *111*, 6198−6202.

(12) Withers, F.; Del Pozo-Zamudio, O.; Mishchenko, A.; Rooney, A.; Gholinia, A.; Watanabe, K.; Taniguchi, T.; Haigh, S.; Geim, A.; Tartakovskii, A.; et al. Light-emitting diodes by band-structure engineering in van der Waals heterostructures. *Nat. Mater.* **2015**, *14*, 301−306.

(13) Castro Neto, A.; Guinea, F.; Peres, N. M.; Novoselov, K. S.; Geim, A. K. The electronic properties of graphene. *Rev. Mod. Phys.* **2009**, *81*, 109.

(14) Yang, L.; Deslippe, J.; Park, C.-H.; Cohen, M. L.; Louie, S. G. Excitonic effects on the optical response of graphene and bilayer graphene. *Phys. Rev. Lett.* **2009**, *103*, 186802.

(15) Kramberger, C.; Hambach, R.; Giorgetti, C.; Rümmeli, M.; Knupfer, M.; Fink, J.; Büchner, B.; Reining, L.; Einarsson, E.; Maruyama, S.; et al. Linear plasmon dispersion in single-wall carbon nanotubes and the collective excitation spectrum of graphene. *Phys. Rev. Lett.* **2008**, *100*, 196803.

(16) Trevisanutto, P. E.; Holzmann, M.; Côté, M.; Olevano, V. Ab initio high-energy excitonic effects in graphite and graphene. *Phys. Rev. B: Condens. Matter Mater. Phys.* **2010**, *81*, 121405.

(17) Despoja, V.; Novko, D.; Dekanić, K.; Šunjić, M.; Marušić, L. Two-dimensional and π plasmon spectra in pristine and doped graphene. *Phys. Rev. B: Condens. Matter Mater. Phys.* **2013**, *87*, 075447.

(18) Wachsmuth, P.; Hambach, R.; Kinyanjui, M.; Guzzo, M.; Benner, G.; Kaiser, U. High-energy collective electronic excitations in free-standing single-layer graphene. *Phys. Rev. B: Condens. Matter Mater. Phys.* **2013**, *88*, 075433.

DOI: 10.1021/acs.jpclett.7b00357
J. Phys. Chem. Lett. 2017, 8, 1464−1471

(19) Watanabe, K.; Taniguchi, T.; Kanda, H. Direct-bandgap properties and evidence for ultraviolet lasing of hexagonal boron nitride single crystal. *Nat. Mater.* **2004**, *3*, 404−409.
(20) Kubota, Y.; Watanabe, K.; Tsuda, O.; Taniguchi, T. Deep ultraviolet light-emitting hexagonal boron nitride synthesized at atmospheric pressure. *Science* **2007**, *317*, 932−934.
(21) Arnaud, B.; Lebegue, S.; Rabiller, P.; Alouani, M. Huge excitonic effects in layered hexagonal boron nitride. *Phys. Rev. Lett.* **2006**, *96*, 026402.
(22) Wirtz, L.; Marini, A.; Grüning, M.; Attaccalite, C.; Kresse, G.; Rubio, A. Comment on "Huge excitonic effects in layered hexagonal boron nitride". *Phys. Rev. Lett.* **2008**, *100*, 189701.
(23) Galambosi, S.; Wirtz, L.; Soininen, J.; Serrano, J.; Marini, A.; Watanabe, K.; Taniguchi, T.; Huotari, S.; Rubio, A.; Hämäläinen, K. Anisotropic excitonic effects in the energy loss function of hexagonal boron nitride. *Phys. Rev. B: Condens. Matter Mater. Phys.* **2011**, *83*, 081413.
(24) Sakai, Y.; Saito, S.; Cohen, M. L. First-Principles Study on Graphene/Hexagonal Boron Nitride Heterostructures. *J. Phys. Soc. Jpn.* **2015**, *84*, 121002.
(25) Britnell, L.; Gorbachev, R.; Jalil, R.; Belle, B.; Schedin, F.; Mishchenko, A.; Georgiou, T.; Katsnelson, M.; Eaves, L.; Morozov, S.; et al. Field-effect tunneling transistor based on vertical graphene heterostructures. *Science* **2012**, *335*, 947−950.
(26) Britnell, L.; Gorbachev, R. V.; Jalil, R.; Belle, B. D.; Schedin, F.; Katsnelson, M. I.; Eaves, L.; Morozov, S. V.; Mayorov, A. S.; Peres, N. M.; et al. Electron tunneling through ultrathin boron nitride crystalline barriers. *Nano Lett.* **2012**, *12*, 1707−1710.
(27) Mishchenko, A.; Tu, J.; Cao, Y.; Gorbachev, R.; Wallbank, J.; Greenaway, M.; Morozov, V.; Morozov, S.; Zhu, M.; Wong, S.; et al. Twist-controlled resonant tunnelling in graphene/boron nitride/graphene heterostructures. *Nat. Nanotechnol.* **2014**, *9*, 808−813.
(28) Li, Q.; Liu, M.; Zhang, Y.; Liu, Z. Hexagonal Boron Nitride−Graphene Heterostructures: Synthesis and Interfacial Properties. *Small* **2016**, *12*, 32−50.
(29) Giovannetti, G.; Khomyakov, P. A.; Brocks, G.; Kelly, P. J.; van den Brink, J. Substrate-induced band gap in graphene on hexagonal boron nitride: Ab initio density functional calculations. *Phys. Rev. B: Condens. Matter Mater. Phys.* **2007**, *76*, 073103.
(30) Dean, C. R.; Young, A. F.; Meric, I.; Lee, C.; Wang, L.; Sorgenfrei, S.; Watanabe, K.; Taniguchi, T.; Kim, P.; Shepard, K.; et al. Boron nitride substrates for high-quality graphene electronics. *Nat. Nanotechnol.* **2010**, *5*, 722−726.
(31) Mayorov, A. S.; Gorbachev, R. V.; Morozov, S. V.; Britnell, L.; Jalil, R.; Ponomarenko, L. A.; Blake, P.; Novoselov, K. S.; Watanabe, K.; Taniguchi, T.; et al. Micrometer-scale ballistic transport in encapsulated graphene at room temperature. *Nano Lett.* **2011**, *11*, 2396−2399.
(32) Gao, G.; Gao, W.; Cannuccia, E.; Taha-Tijerina, J.; Balicas, L.; Mathkar, A.; Narayanan, T.; Liu, Z.; Gupta, B. K.; Peng, J.; et al. Artificially stacked atomic layers: toward new van der Waals solids. *Nano Lett.* **2012**, *12*, 3518−3525.
(33) Zhang, K.; Yap, F. L.; Li, K.; Ng, C. T.; Li, L. J.; Loh, K. P. Large scale graphene/hexagonal boron nitride heterostructure for tunable plasmonics. *Adv. Funct. Mater.* **2014**, *24*, 731−738.
(34) Woessner, A.; Lundeberg, M. B.; Gao, Y.; Principi, A.; Alonso-González, P.; Carrega, M.; Watanabe, K.; Taniguchi, T.; Vignale, G.; Polini, M.; et al. Highly confined low-loss plasmons in graphene−boron nitride heterostructures. *Nat. Mater.* **2015**, *14*, 421−425.
(35) Jia, Y.; Zhao, H.; Guo, Q.; Wang, X.; Wang, H.; Xia, F. Tunable plasmon−phonon polaritons in layered graphene−hexagonal boron nitride heterostructures. *ACS Photonics* **2015**, *2*, 907−912.
(36) Bernal, J. The structure of graphite. *Proc. R. Soc. London, Ser. A* **1924**, *106*, 749−773.
(37) Ramasubramaniam, A.; Naveh, D.; Towe, E. Tunable band gaps in bilayer graphene-BN heterostructures. *Nano Lett.* **2011**, *11*, 1070−1075.
(38) Zhong, X.; Amorim, R. G.; Scheicher, R. H.; Pandey, R.; Karna, S. P. Electronic structure and quantum transport properties of trilayers formed from graphene and boron nitride. *Nanoscale* **2012**, *4*, 5490−5498.
(39) Sakai, Y.; Saito, S.; Cohen, M. L. Lattice matching and electronic structure of finite-layer graphene/h-BN thin films. *Phys. Rev. B: Condens. Matter Mater. Phys.* **2014**, *89*, 115424.
(40) Kharche, N.; Nayak, S. K. Quasiparticle band gap engineering of graphene and graphone on hexagonal boron nitride substrate. *Nano Lett.* **2011**, *11*, 5274−5278.
(41) Quhe, R.; Zheng, J.; Luo, G.; Liu, Q.; Qin, R.; Zhou, J.; Yu, D.; Nagase, S.; Mei, W.-N.; Gao, Z.; et al. Tunable and sizable band gap of single-layer graphene sandwiched between hexagonal boron nitride. *NPG Asia Mater.* **2012**, *4*, e6.
(42) Hüser, F.; Olsen, T.; Thygesen, K. S. Quasiparticle GW calculations for solids, molecules, and two-dimensional materials. *Phys. Rev. B: Condens. Matter Mater. Phys.* **2013**, *87*, 235132.
(43) Bourrellier, R.; Amato, M.; Galvao Tizei, L. H.; Giorgetti, C.; Gloter, A.; Heggie, M. I.; March, K.; Stéphan, O.; Reining, L.; Kociak, M.; et al. Nanometric resolved luminescence in h-BN flakes: excitons and stacking order. *ACS Photonics* **2014**, *1*, 857−862.
(44) A strictly quantitative comparison with the results of ref 43 can hardly be made due to the different **k** meshes adopted for the calculations of the quasi-particle band structure. In this work, we use a shifted 18 × 18 × 4 grid, while in ref 43, a 6 × 6 × 2 mesh was adopted. Nonetheless, the band gap renormalization of h-BN in the presence of graphene is qualitatively confirmed.
(45) Neaton, J. B.; Hybertsen, M. S.; Louie, S. G. Renormalization of Molecular Electronic Levels at Metal-Molecule Interfaces. *Phys. Rev. Lett.* **2006**, *97*, 216405.
(46) Puschnig, P.; Amiri, P.; Draxl, C. Band renormalization of a polymer physisorbed on graphene investigated by many-body perturbation theory. *Phys. Rev. B: Condens. Matter Mater. Phys.* **2012**, *86*, 085107.
(47) Fu, Q.; Cocchi, C.; Nabok, D.; Gulans, A.; Draxl, C. Graphene-modulated photo-absorption in adsorbed azobenzene monolayers. *Phys. Chem. Chem. Phys.* **2017**, *19*, 6196−6205.
(48) Fu, Q.; Nabok, D.; Draxl, C. Energy-Level Alignment at the Interface of Graphene Fluoride and Boron Nitride Monolayers: An Investigation by Many-Body Perturbation Theory. *J. Phys. Chem. C* **2016**, *120*, 11671−11678.
(49) Mak, K. F.; Sfeir, M. Y.; Wu, Y.; Lui, C. H.; Misewich, J. A.; Heinz, T. F. Measurement of the optical conductivity of graphene. *Phys. Rev. Lett.* **2008**, *101*, 196405.
(50) Peres, N. Colloquium: The transport properties of graphene: An introduction. *Rev. Mod. Phys.* **2010**, *82*, 2673.
(51) In graphene, the excitation energies of peaks I and II converge to the same value. Such a behavior is expected also in this system but not perfectly reproduced due to the enhanced numerical complexity of the superlattice. The character of these excitations is nonetheless consistent with the existing literature,[14,16] to which we refer for a detailed analysis of the optical spectrum of graphene. Thus, the essence of our results is unaffected.
(52) Liu, L.; Feng, Y.; Shen, Z. Structural and electronic properties of h-BN. *Phys. Rev. B: Condens. Matter Mater. Phys.* **2003**, *68*, 104102.
(53) Lau, K.; Zory, P. *Ultralow threshold quantum well lasers*; Academic, San Diego, CA, 1993; pp 198−203.
(54) Xue, J.; Sanchez-Yamagishi, J.; Bulmash, D.; Jacquod, P.; Deshpande, A.; Watanabe, K.; Taniguchi, T.; Jarillo-Herrero, P.; LeRoy, B. J. Scanning tunnelling microscopy and spectroscopy of ultra-flat graphene on hexagonal boron nitride. *Nat. Mater.* **2011**, *10*, 282−285.
(55) Yankowitz, M.; Xue, J.; Cormode, D.; Sanchez-Yamagishi, J. D.; Watanabe, K.; Taniguchi, T.; Jarillo-Herrero, P.; Jacquod, P.; LeRoy, B. J. Emergence of superlattice Dirac points in graphene on hexagonal boron nitride. *Nat. Phys.* **2012**, *8*, 382−386.
(56) Ponomarenko, L.; Gorbachev, R.; Yu, G.; Elias, D.; Jalil, R.; Patel, A.; Mishchenko, A.; Mayorov, A.; Woods, C.; Wallbank, J.; et al. Cloning of Dirac fermions in graphene superlattices. *Nature (London, U. K.)* **2013**, *497*, 594−597.

DOI: 10.1021/acs.jpclett.7b00357
J. Phys. Chem. Lett. 2017, 8, 1464−1471

(57) Woods, C.; Britnell, L.; Eckmann, A.; Ma, R.; Lu, J.; Guo, H.; Lin, X.; Yu, G.; Cao, Y.; Gorbachev, R.; et al. Commensurate-incommensurate transition in graphene on hexagonal boron nitride. *Nat. Phys.* **2014**, *10*, 451−456.
(58) Yankowitz, M.; Xue, J.; LeRoy, B. J. Graphene on hexagonal boron nitride. *J. Phys.: Condens. Matter* **2014**, *26*, 303201.
(59) Chen, Z.-G.; Shi, Z.; Yang, W.; Lu, X.; Lai, Y.; Yan, H.; Wang, F.; Zhang, G.; Li, Z. Observation of an intrinsic bandgap and Landau level renormalization in graphene/boron-nitride heterostructures. *Nat. Commun.* **2014**, *5*, 4461.
(60) Ni, G.; Wang, H.; Wu, J.; Fei, Z.; Goldflam, M.; Keilmann, F.; Özyilmaz, B.; Castro Neto, A.; Xie, X.; Fogler, M.; et al. Plasmons in graphene moire superlattices. *Nat. Mater.* **2015**, *14*, 1217−1222.
(61) Gao, T.; Song, X.; Du, H.; Nie, Y.; Chen, Y.; Ji, Q.; Sun, J.; Yang, Y.; Zhang, Y.; Liu, Z. Temperature-triggered chemical switching growth of in-plane and vertically stacked graphene-boron nitride heterostructures. *Nat. Commun.* **2015**, *6*, 6835.
(62) Leven, I.; Maaravi, T.; Azuri, I.; Kronik, L.; Hod, O. Inter-Layer Potential for Graphene/h-BN Heterostructures. *J. Chem. Theory Comput.* **2016**, *12*, 2896−2905.
(63) Sachs, B.; Wehling, T.; Katsnelson, M.; Lichtenstein, A. Adhesion and electronic structure of graphene on hexagonal boron nitride substrates. *Phys. Rev. B: Condens. Matter Mater. Phys.* **2011**, *84*, 195414.
(64) San-Jose, P.; Gutiérrez-Rubio, A.; Sturla, M.; Guinea, F. Electronic structure of spontaneously strained graphene on hexagonal boron nitride. *Phys. Rev. B: Condens. Matter Mater. Phys.* **2014**, *90*, 115152.
(65) Mucha-Kruczyński, M.; Wallbank, J.; Fal'Ko, V. Heterostructures of bilayer graphene and h-BN: Interplay between misalignment, interlayer asymmetry, and trigonal warping. *Phys. Rev. B: Condens. Matter Mater. Phys.* **2013**, *88*, 205418.
(66) Wallbank, J.; Patel, A.; Mucha-Kruczyński, M.; Geim, A.; Fal'ko, V. Generic miniband structure of graphene on a hexagonal substrate. *Phys. Rev. B: Condens. Matter Mater. Phys.* **2013**, *87*, 245408.
(67) Wallbank, J.; Mucha-Kruczyński, M.; Fal'ko, V. Moiré minibands in graphene heterostructures with almost commensurate 3 × 3 hexagonal crystals. *Phys. Rev. B: Condens. Matter Mater. Phys.* **2013**, *88*, 155415.
(68) van Wijk, M.; Schuring, A.; Katsnelson, M.; Fasolino, A. Moire patterns as a probe of interplanar interactions for graphene on h-BN. *Phys. Rev. Lett.* **2014**, *113*, 135504.
(69) Slotman, G.; van Wijk, M.; Zhao, P.-L.; Fasolino, A.; Katsnelson, M.; Yuan, S. Effect of structural relaxation on the electronic structure of graphene on hexagonal boron nitride. *Phys. Rev. Lett.* **2015**, *115*, 186801.
(70) Wallbank, J. R.; Mucha-Kruczyński, M.; Chen, X.; Fal'ko, V. I. Moiré superlattice effects in graphene/boron-nitride van der Waals heterostructures. *Ann. Phys.* **2015**, *527*, 359−376.
(71) Abergel, D. S.; Wallbank, J.; Chen, X.; Mucha-Kruczyński, M.; Fal'ko, V. I. Infrared absorption by graphene−hBN heterostructures. *New J. Phys.* **2013**, *15*, 123009.
(72) Perdew, J. P.; Burke, K.; Ernzerhof, M. Generalized Gradient Approximation Made Simple. *Phys. Rev. Lett.* **1996**, *77*, 3865−3868.
(73) Grimme, S. Semiempirical GGA-type density functional constructed with a long-range dispersion correction. *J. Comput. Chem.* **2006**, *27*, 1787−1799.
(74) Hedin, L. New method for calculating the one-particle Green's function with application to the electron gas problem. *Phys. Rev.* **1965**, *139*, A796−A823.
(75) Hybertsen, M. S.; Louie, S. G. First-Principles Theory of Quasiparticles: Calculation of Band Gaps in Semiconductor and Insulators. *Phys. Rev. Lett.* **1985**, *55*, 1418−1421.
(76) Hanke, W.; Sham, L. J. Many-particle effects in the optical spectrum of a semiconductor. *Phys. Rev. B: Condens. Matter Mater. Phys.* **1980**, *21*, 4656−4673.
(77) Strinati, G. Application of the Green Functions Method to the Study of the Optical Properties of Semiconductors. *Riv. Nuovo Cimento* **1988**, *11*, 1−86.
(78) Gulans, A.; Kontur, S.; Meisenbichler, C.; Nabok, D.; Pavone, P.; Rigamonti, S.; Sagmeister, S.; Werner, U.; Draxl, C. exciting: a full-potential all-electron package implementing density-functional theory and many-body perturbation theory. *J. Phys.: Condens. Matter* **2014**, *26*, 363202.
(79) Nabok, D.; Gulans, A.; Draxl, C. Accurate all-electron G_0W_0 quasiparticle energies employing the full-potential augmented planewave method. *Phys. Rev. B: Condens. Matter Mater. Phys.* **2016**, *94*, 035118.
(80) Sagmeister, S.; Ambrosch-Draxl, C. Time-Dependent Density Functional Theory versus Bethe−Salpeter equation: An All-Electron Study. *Phys. Chem. Chem. Phys.* **2009**, *11*, 4451−4457.
(81) Gillet, Y.; Giantomassi, M.; Gonze, X. First-principles study of excitonic effects in Raman intensities. *Phys. Rev. B: Condens. Matter Mater. Phys.* **2013**, *88*, 094305.
(82) Kammerlander, D.; Botti, S.; Marques, M. A.; Marini, A.; Attaccalite, C. Speeding up the solution of the Bethe-Salpeter equation by a double-grid method and Wannier interpolation. *Phys. Rev. B: Condens. Matter Mater. Phys.* **2012**, *86*, 125203.
(83) Momma, K.; Izumi, F. *VESTA3* for three-dimensional visualization of crystal, volumetric and morphology data. *J. Appl. Crystallogr.* **2011**, *44*, 1272−1276.

DOI: 10.1021/acs.jpclett.7b00357
J. Phys. Chem. Lett. 2017, 8, 1464−1471

SUPPORTING INFORMATION

Enhancing Light-Matter Interaction in Graphene/h-BN van der Waals heterostructures

Wahib Aggoune,[†,‡] Caterina Cocchi,[*,†,¶] Dmitrii Nabok,[†,¶] Karim Rezouali,[‡] Mohamed Akli Belkhir,[‡] and Claudia Draxl[†,¶]

†*Institut für Physik and IRIS Adlershof, Humboldt-Universität zu Berlin, 12489 Berlin, Germany*

‡*Laboratoire de Physique Théorique, Faculté des Sciences Exactes, Université de Bejaia, 06000 Bejaia, Algeria*

¶*European Theoretical Spectroscopic Facility (ETSF)*

E-mail: caterina.cocchi@physik.hu-berlin.de

Graphene/h-BN Periodic Heterostructures: Structural and Electronic Properties

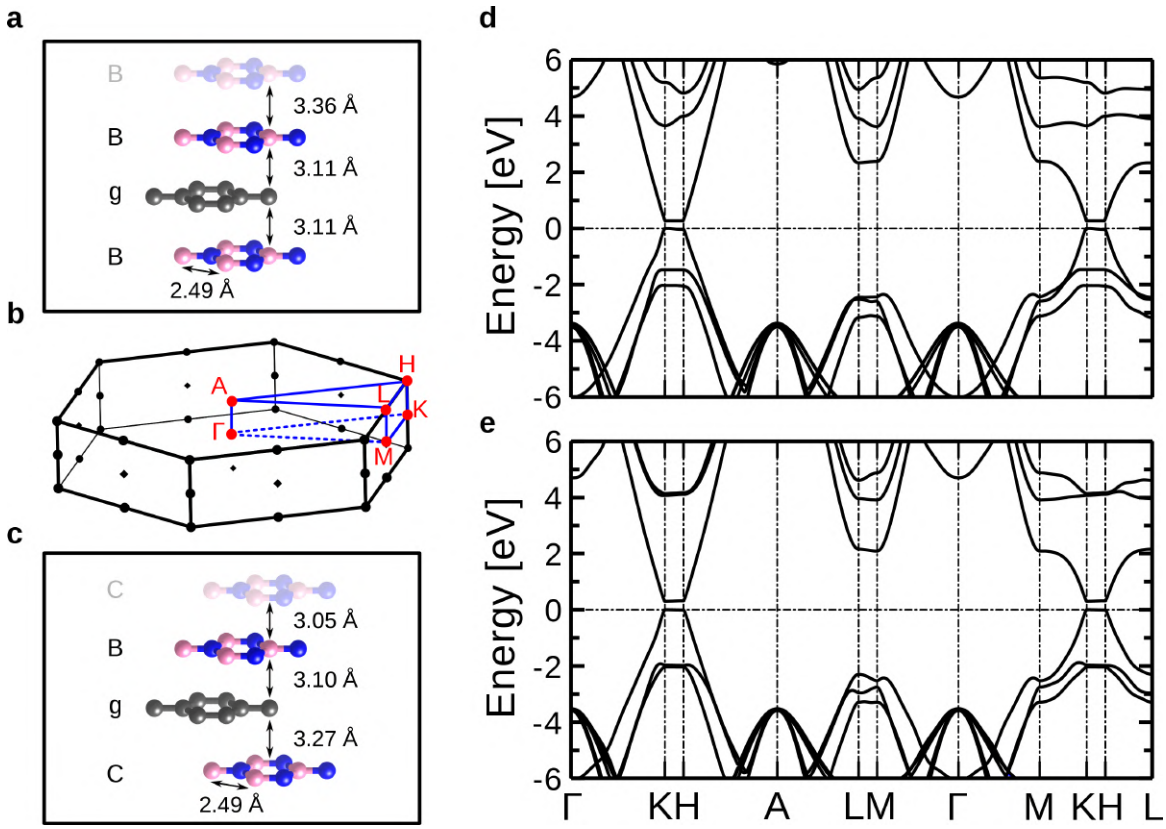

Figure S1: Stacking arrangements of the two heterostructures considered in this work, with B-g-B and B-g-C stacking arrangements (a and c, respectively). The corresponding Brillouin zone (BZ) is also shown (b), with the high-symmetry points marked in red. Quasi-particle band structures of (d) B-g-B and (e) B-g-C heterostructures along the path in the BZ highlighted in (b), with the valence-band maximum set to zero.

The unit cells of the graphene/h-BN heterostructures considered in this work contain 6 atoms, and have in-plane lattice parameter a=2.49 Å. In the B-g-B stacking arrangement (Fig. S1a), c=9.58 Å. In this configuration, the graphene layer is separated by 3.11 Å from the h-BN ones, while two neighboring h-BN sheets are at a vertical distance of 3.36 Å. In the B-g-C heterostructure c=9.42 Å. In this system, the distance between graphene and the h-BN layers in stacking position B and C is 3.10 Å and 3.27 Å, respectively. In this stacking sequence, the distance between two neighboring boron nitride sheets is 3.05 Å.

In Figs. S1d-e we show the full band structure of the graphene/h-BN periodic heterostructures along the **k**-point path highlighted in Fig. S1b. These plots are obtained by Wannier interpolation starting from a calculation using a 12×12×4 **k**-mesh. The systems exhibit a quasi-particle gap of 250 meV (B-g-B) and 260 meV (B-g-C) between the graphene-like highest-occupied and lowest-unoccupied bands along the K-H path. Along the L-M path the separation between the N-like valence-band maximum (VBM) and the C-like conduction-band minimum (CBM) is significantly larger, being 4.7 eV in B-g-B and 4.5 eV in B-g-C.

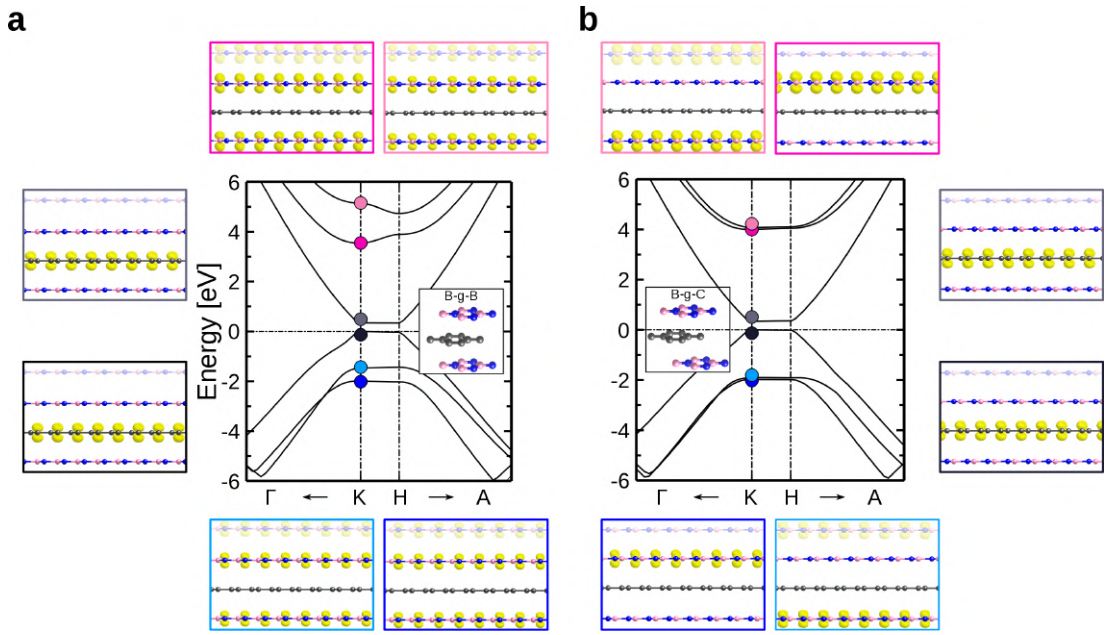

Figure S2: Quasi-particle band structure in the vicinity of the K-H path and electron probability density at K of the three highest occupied and the three lowest unoccupied Kohn-Sham states of the B-g-B (a) and the B-g-C (b) heterostructures. The three layers included in the unit cell are shown in the foreground, while periodic images are shaded.

In Fig. S2 we show the spatial extension of the electron density associated with the three lowest occupied and unoccupied Kohn-Sham (KS) states at the high-symmetry point K. Regardless of the stacking order, the VBM and the CBM are purely graphene-like π and π^* states, respectively, exhibiting their typical delocalized distribution on the two inequivalent carbon atoms in the unit cell. In the B-g-B system, VBM-1 and VBM-2 are extended N

states, while CBM+1 and CBM+2 show a boron-like character. In both cases, the electron distribution is uniformly spread over both h-BN layers included in the unit cell. This is a direct consequence of the equivalent arrangement of the h-BN sheets with respect to each other. On the other hand, in the B-g-C heterostructure VBM-1 and VBM-2 as well as CBM+1 and CBM+2 are almost degenerate at K and their corresponding electron density is distributed on one inequivalent h-BN layer.

Graphene/h-BN Heterostructures: Optical Properties

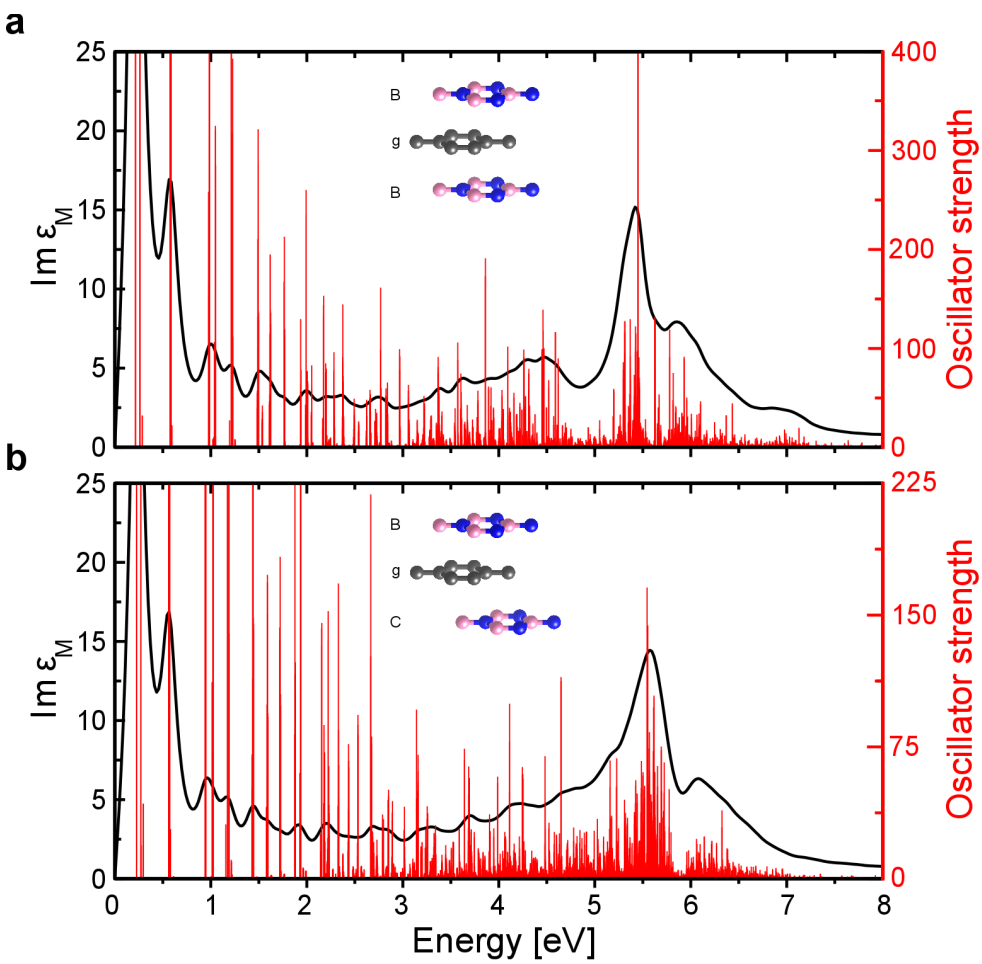

Figure S3: In-plane component of the imaginary part of the macroscopic dielectric function (black solid line) and oscillator strength of the corresponding solution of the BSE (red bars) of B-g-B (a) and B-g-C (b) heterostructures.

In Fig. S3 we show the in-plane component of the imaginary part of the macroscopic dielectric function and the oscillator strength of the corresponding solutions of the Bethe-Salpeter equation (BSE) for the B-g-B and B-g-C stacking arrangements. In main text (Figs. 1a and 2a) we highlight only selected excitations with specific character, not necessarily corresponding to the most intense ones. Specifically, in the visible region, most of the spectral intensity comes from excitations formed by a mixture of transitions between the three highest-occupied bands to the graphene-like CBM. As discussed in main body of the article, many excitations are double-degenerate for symmetry reasons. As such, the correlated probability density associated to the electron, with the hole being fixed, is a linear combination of the single contribution of the degenerate BSE solutions. Significant examples, corresponding to each type of excitation discussed in the main text is shown in Fig. S4. It is worth noting, in particular, that the correlated electron distribution of the intralayer exciton in the h-BN layer (Fig. S4c) is consistent with the results reported in Ref. 1.

Exciton Analysis in k-Space

In this section, we provide an additional analysis of the excitations highlighted in Figs. 1 and 2 in the main text. Specifically we consider here the **k**-resolved contributions of individual quasi-particle bands to the electron-hole pairs. To do so, we introduce the *weight* of each transition between valence and conduction states at a given **k**-point, defined as:

$$w^{\lambda}_{v\mathbf{k}} = \sum_{c} |A^{\lambda}_{vc\mathbf{k}}|^2, \;\; w^{\lambda}_{c\mathbf{k}} = \sum_{v} |A^{\lambda}_{vc\mathbf{k}}|^2. \tag{1}$$

In Figs. S5 and S6 these quantities are plotted as colored circles, whose size is representative of the **k**-resolved band contributions, independently of the oscillator strength of the corresponding excitation.

In Fig. S5 we show the most relevant contributions to the excitations in the spectra of graphene/h-BN heterostructures with B-g-B stacking sequence. Excitations are labeled

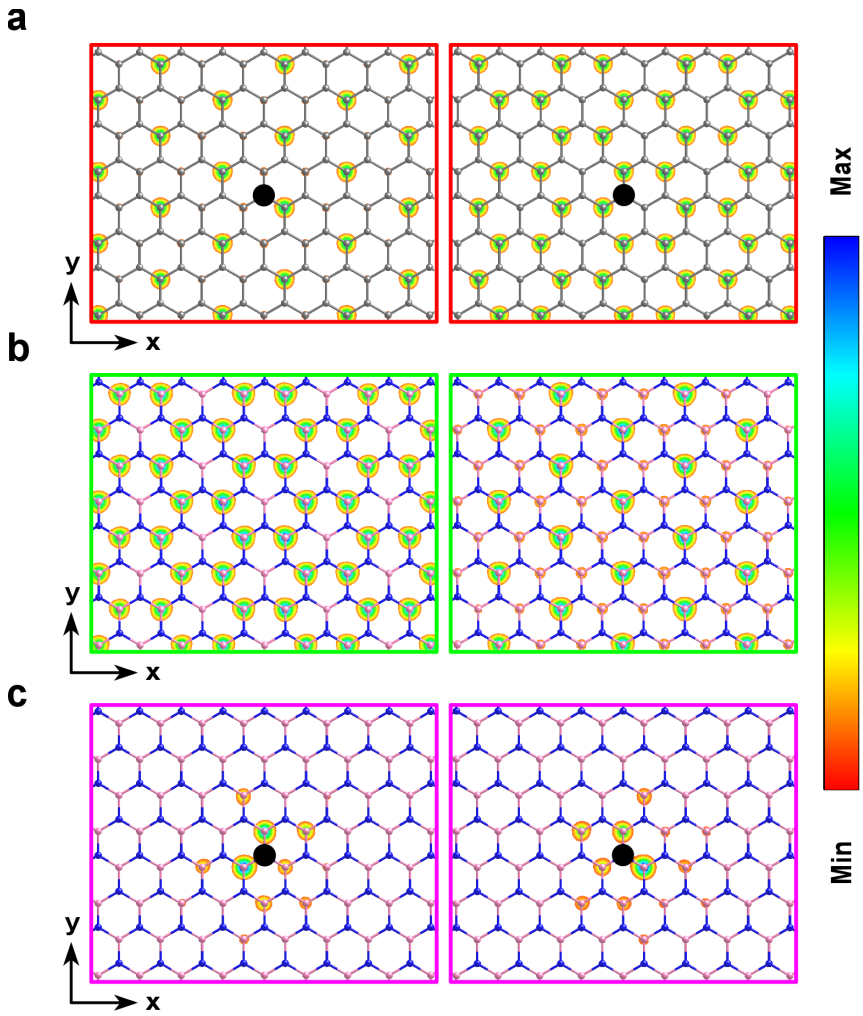

Figure S4: Two-dimensional projections of the probability density associated to the electron component of the electron-hole pairs of double-degenerate excitations with (a) graphene delocalized character, (b) h-BN delocalized and (c) localized character. The corresponding position of the hole is marked by a black dot.

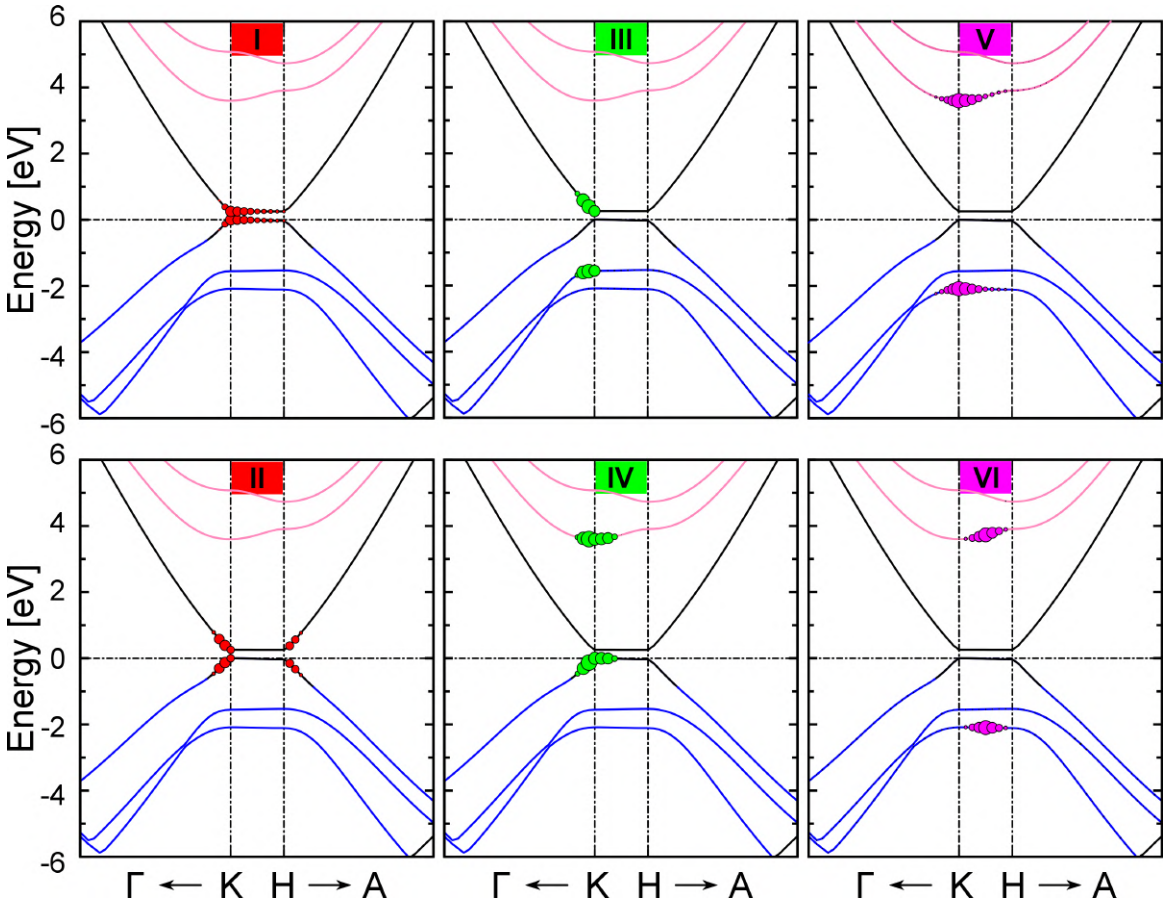

Figure S5: Band contributions to the main excitations in the spectra of the B-g-B heterostructure, given by the corresponding weights (Eq. 1). The size of the colored circles are quantitatively representative of the weight of the corresponding quasi-particle states. The band character is indicated by the color code of the atomic species (C: grey, N: blue, B: pink).

according to the notation introduced in the main text. For both heterostructures, the first excitations (I and II) are graphene interband transitions occurring along the K-H path (I) or in its vicinity (II). Excitations III and IV have charge-transfer character with the electron and the hole being situated on either graphene or h-BN layer. Specifically, excitation III stems from the N-like VBM-1 targeting the lowest unoccupied graphene band, regardless of the position of the hole above or below graphene. Excitation IV is characterized by transitions from the highest occupied graphene band to the B-like CBM+1. Excitons V and VI stem purely from the h-BN bands, within the K-H path.

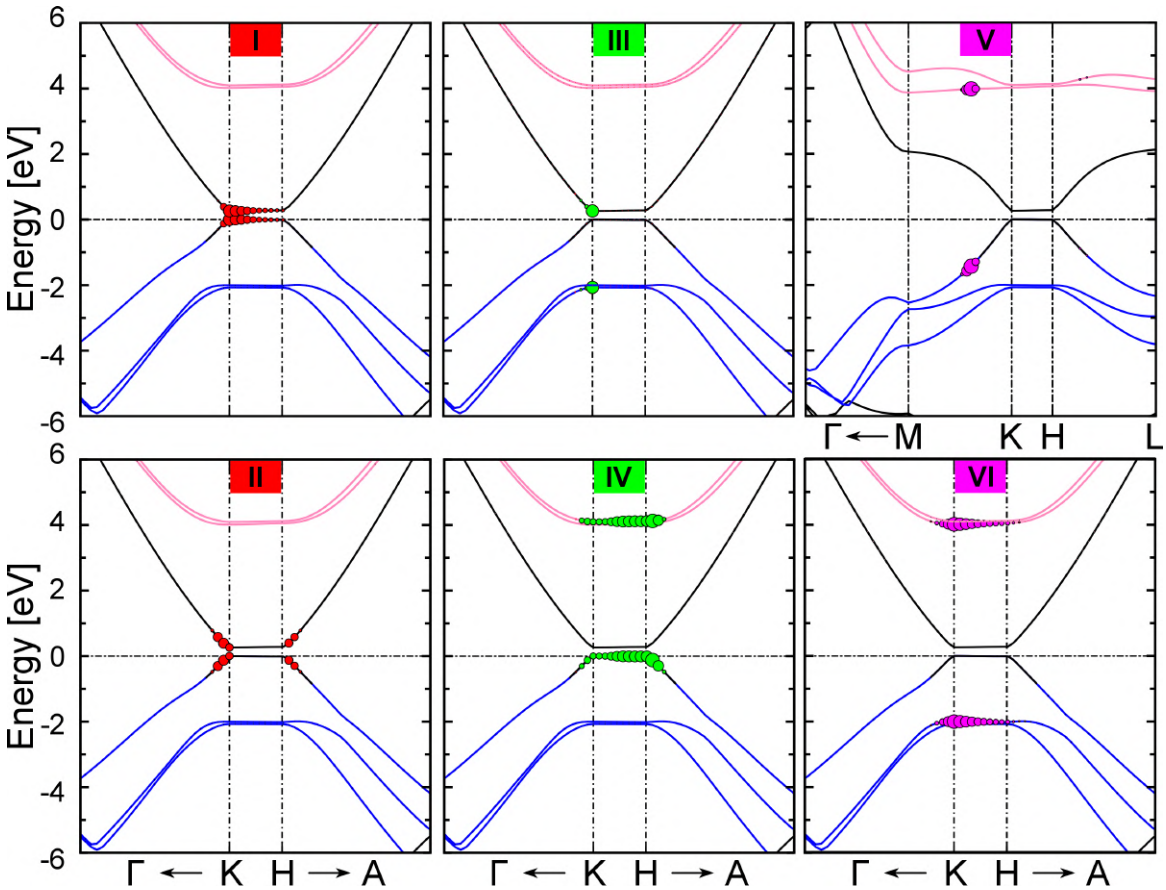

Figure S6: Band contributions to the main excitations in the spectra of B-g-C heterostructure, given by the corresponding weights (Eq. 1). The size of the colored circles are quantitatively representative of the weight of the corresponding quasi-particle states. The band character is indicated by the color code of the atomic species (C: grey, N: blue, B: pink).

In Fig. S6 we show the corresponding plots referred to the B-g-C heterostructure. No

significant differences appear regarding the interband transitions in graphene (excitations I and II). Conversely, the effects of the different stacking arrangements on the electronic wave-functions in the h-BN layers are reflected in the optical excitations where these states are involved. The interlayer excitations III and IV are again given by transition from h-BN to graphene bands (III) and from graphene to h-BN levels (IV). However, in this case, the distribution in **k**-space is slightly modified, as a consequence of the character of the h-BN bands, VBM-2/VBM-1 and CBM+1/CBM+2, along the K-H path (see also Fig. S2b). Even more pronounced differences appear in the h-BN excitons V and VI. Especially the former comes primarily from a region in the BZ between the high-symmetry points K and M.

References

(1) Wirtz, L.; Marini, A.; Grüning, M.; Attaccalite, C.; Kresse, G.; Rubio, A. *Phys. Rev. Lett.* **2008**, *100*, 189701.

Wiley Online Library
Early View publication on www.wileyonlinelibrary.com
(issue and page numbers not yet assigned;
citable using Digital Object Identifier – **DOI**)

Phys. Status Solidi B, 1–6 (2015) / **DOI** 10.1002/pssb.201552431

physica status solidi b
www.pss-b.com
basic solid state physics

Strong excitonic effects in hydrogen–graphene–fluorine janus graphene

W. Aggoune, K. Rezouali, and M. A. Belkhir*

Laboratoire de Physique Théorique, Faculté des sciences exactes, Université de Bejaia, 06000 Bejaia, Algérie

Received 28 June 2015, revised 21 October 2015, accepted 10 November 2015
Published online 9 December 2015

Keywords computational physics, density functional theory, excitons, graphene, optical absorption

* Corresponding author: e-mail muhend.belkhir@gmail.com, Phone/Fax: 213 34 21 59 86

We present a first-principles many-body Green's function method (GW approximation and Bethe–Salpeter equation) of the electronic and optical properties of recently predicted hydrogen–graphene–fluorine janus graphene. Significant self-energy corrections, of more than 50%, to the Kohn–Sham bandgap from the local density approximation (LDA) calculations are found. Moreover, the optical absorption spectrum of this janus graphene is dominated by enhanced excitonic effects with formation of a bound exciton with considerable binding energy. The reduced spatial separation of excited electrons and holes gives rise to extremely short radiative lifetimes, preventing condensation.

© 2015 WILEY-VCH Verlag GmbH & Co. KGaA, Weinheim

1 Introduction Graphene [1], a single sheet of carbon atoms arranged in a honeycomb pattern, has a lot of special properties likely to be used as a building block for future applications. However, graphene suffers from its gapless state which constitutes a serious limitation for its use in optoelectronics. As a consequence, many efforts have been devoted to tune its electronic properties for modern electronics. In particular, bandgap engineering through chemical modification including hydrogenation [2], fluorination [3, 4], and chlorination [5, 6] has been regarded as an attractive route because of its simplicity, scalability, and inexpensiveness. Recent synthesis of graphane [2] and fluorographene [3, 4] opens up an important route to designing potential systems for applications in electronics by taking advantage of the exceptional properties these materials offer such as quantum size confinement, less efficient electronic screening, and so on. These properties explain the recent explosion of scientific activity around these systems giving rise to several studies addressing some of their intriguing electronic structures [3, 7–15]. For example, it was shown that these materials are wide-direct-bandgap insulators, making them appealing for applications in high-power electronics and light-emitting diodes [16, 17]. Furthermore, theoretical work predicted strong charge-transfer excitonic effects and Bose–Einstein exciton condensate in graphane [8], and high-temperature superconductivity in hole-doped graphane [18].

Recently, significant research activity on graphene chemistry has been focused on the bifacially asymmetric modification via covalently attaching different functional groups. Several janus nanostructures are theoretically predicted [19] and experimentally confirmed [20]. For example, a more recent theoretical work has proven that attaching the two sides of graphene with hydrogen and fluorine (H–CC–F) breaks its symmetric restriction, leading to a stable and robust bandgap material. In addition, a proof of the existence of piezoelectricity in this graphene derivative, comparable to that present in bulk piezoelectric material, has been reported in the literature [21–23].

Despite this importance in science and technology, the knowledge of the optical properties of this janus material is still lacking. Moreover, reports available are restricted to a few studies on its electronic and piezoelectric properties.

In this work, we study the changes in the electronic structure of graphene after the codecoration with H and F atoms. It is well established that the impact of many-body effects on the electronic structure is important in reduced-dimensional materials. In particular, the electron–hole interaction is of great importance for a trustworthy optical absorption spectrum [24, 25]. Therefore, it is of considerable interest to explore the impact of low dimensionality on excitonic effects in H–CC–F. The present work will provide the fundamental parameters for nanodevice design based on

© 2015 WILEY-VCH Verlag GmbH & Co. KGaA, Weinheim

this fascinating material. We found significant self-energy corrections of about 50% to the LDA bandgap. Moreover, the optical absorption of H–CC–F is dominated by enhanced excitonic effects with formation of a bound exciton with large binding energy. The paper is organized as follows. Descriptions of the computational methods are given in Section 2. In Section 3, we report and discuss our results, and finally we summarize our main conclusions.

2 Numerical details All calculations described in the present work were conducted by combining the ABINIT and YAMBO codes [26, 27]. We first compute the wave functions of the valence bands and a large number of conduction bands by using density functional theory (DFT) [28, 29] within the norm-conserving pseudopotentials [30] and a plane-wave basis set. The exchange-correlation potential has been approximated by local density approximation (LDA) using the Teter functional [31]. A plane-wave energy cutoff of 60 Ry is used together with the Brillouin-zone sampling of a 16 × 16 × 1 Monkhorst–Pack grid [32]. The boundary condition in the direction parallel to the surface vector is maintained by introducing enough vacuum between neighboring supercells (13 Å). This technique is also used to avoid spurious interactions that may arise between the successive images. Both lattice constant and internal coordinates of structures were fully optimized until the residual forces on each atom are less than 0.002 eV Å^{-1}.

Secondly, quasiparticle calculations were performed on the top of the LDA wave functions at the optimized geometry by solving the Dyson equation [25, 33]:

$$\left[-\frac{\nabla^2}{2} + V_{\text{ext}} + V_{\text{Hartree}} + \Sigma(E_m^{\text{QP}})\right]\psi_m^{\text{QP}} = E_m^{\text{QP}}\psi_m^{\text{QP}},$$

where the electron self-operator Σ is written using the Hedin's GW approximation. The calculations were performed without self-consistency in the Green's function (G) and the screened Coulomb interaction (W) ($\Sigma = iG_0W_0$ approximation scheme). We used 100 bands for expanding the Green's function, 816.34 eV (6303 G-vectors) for the exchange part and 103.54 eV (800 G-vectors) for the correlation part of the self-energy. A 30 × 30 × 1 uniform k-point grid was necessary for computing the converged self-energy. The LDA eigenvalues and eigenfunctions were used in the construction of G_0 while the dynamical screening effect in W is taken into account through the generalized plasmon pole model.

Finally, the calculations of excitonic spectra have been done by solving the equation of motion of the two particles Green's function, known as the Bethe–Salpeter equation (BSE) on top of the G_0W_0 quasiparticle spectrum [25, 33]:

$$(E_{\text{ck}}^{\text{QP}} - E_{\text{vk}}^{\text{QP}})A_{\text{vck}}^{\text{S}} + \sum_{\text{v}'\text{c}'} K_{(\text{e-h})\text{vck},\text{v}'\text{c}'\text{k}}(\Omega^S)A_{\text{v}'\text{c}'\text{k}}^{\text{S}} = \Omega^{\text{S}}A_{\text{vck}}^{\text{S}},$$

where $A_{\text{vck}}^{\text{S}}$, Ω^{S}, and $K_{(\text{e-h})}$ are the exciton amplitudes, excitation energie, and the kernel describing the interaction between excited electrons and holes, respectively. We made use of the Tamm–Dancoff approximation [34] and the static electron–hole interaction approximation. The electron–hole interaction kernel was evaluated on a 30 × 30 × 1 k-grid to get a much better convergence of the optical spectrum. We include 100 bands in the optical absorption spectra. To eliminate the mirror effect between neighboring supercells, we truncate the Coulomb force [35] in the out-of-plane direction for both the GW and BSE calculations. A Gaussian broadening of 0.1 eV was applied to the frequency values.

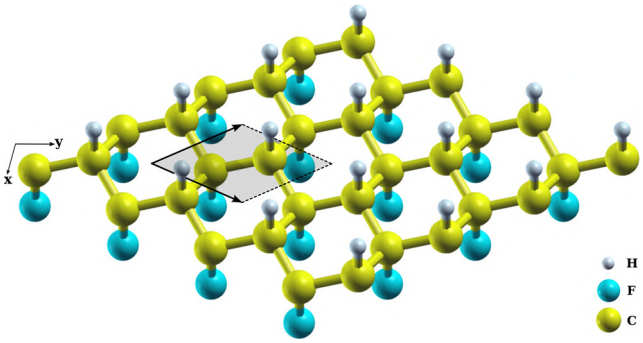

Figure 1 Unit cell and base of hydrogen–graphene–fluorine (H–CC–F). Yellow, blue, and white balls represent carbon, fluorine, and hydrogen atoms, respectively.

3 Results and discussion

3.1 Structural properties When we begin to construct the H–CC–F sheet, it is natural for us to pay special attention to the previous works [19, 21, 23]. With these references, we consider model systems where fluorine and hydrogen atoms are alternately attached to carbon atoms of graphene in a chairlike configuration that has been proved to be more energetically favorable than other configurations [19]. Moreover, comparison of its formation energy (−1.15 eV) to those of the already synthesized materials: graphane (−0.25 eV) and fluorographene (−2.05 eV) suggests clearly that this material is stable and can be realized in experiment. The ground-state geometry of H–CC–F is shown in Fig. 1. As can be seen, the flat structure of graphene transforms to puckered geometry upon the codecoration with H and F atoms. During this reconstruction, the carbon atom attached to an H atom (F atom) moves upward (downward) leading to a buckling of about 0.47 Å, such a value is comparable to the buckling of graphane (0.45 Å) and fluorographene (0.49 Å) [11]. This structural transformation can be qualitatively guessed as a transformation from an sp^2- to an sp^3-bonded system.

The calculated average bond lengths and bond angles are shown in Table 1. As can be seen, the C–H and C–F bond lengths are calculated to be about 1.11 Å and 1.38 Å, respectively. It is worth noting that these values are comparable to the corresponding bonds in graphane and fluorographene [11–13]. The C–C bond length of the tetrahedral structure is calculated to be about 1.54 Å. The ∠HCC and ∠FCC angles (107.75°) are quite close to the ideal tetrahedral angle

© 2015 WILEY-VCH Verlag GmbH & Co. KGaA, Weinheim

Table 1 Calculated average bond lengths and bond angles.

	lattice constant (Å)	bond length (Å)			angle (degrees)			gap-DFT (eV)
		C–C	C–H	C–F	∠ FCC	∠ HCC	∠ CCC	
our results	2.54	1.54	1.11	1.38	107.75	107.75	111.13	2.97
Ref. [19]	2.57	1.56	1.11	1.40	107.53	107.57	111.34	3.34
Ref. [22]		1.54	1.11	1.37	107.77	107.77	111.12	
Ref. [14]	2.55		1.11	1.38				2.82

of 109.5°, confirming the transformation to an sp^3-bonded system. It is worth noting that our structural predictions are in good agreement with previous works [14, 19, 22].

3.2 Electronic properties The calculated LDA band structure and quasiparticle corrections are summarized in Fig. 2a, indicating that sp^3 hybridization of carbon orbitals causes a gap opening of graphene. In other words, the partially filled bonding π band and the filled σ bands of graphene transform into sp^3 σ bands with filled bonding and empty antibonding states. This causes a large bandgap opening of about 2.97 eV with respect to graphene; a value between the graphane's DFT gap [8, 11] and that of fluorographene [10, 11]. It is noteworthy that the evaluated bandgap agrees well qualitatively with results reported in the literature (see Table 1). The gap is calculated as the difference between the energies of the lowest unoccupied molecular orbitals (LUMO) and the highest occupied molecular orbitals (HOMO). The band structure still indicates that both conduction and valence bands near the Fermi level are nearly perfect parabolas over a large fraction of the Brillouin zone, which indicate that graphene loses its high Fermi velocities after the chemical modification. This material is predicted to have a direct gap at Γ point, with doubly degenerated valence bands, a property that is quite desirable for applications in high-power electronics and light-emitting diodes.

The character of the lowest unoccupied molecular orbitals (LUMO) and the highest occupied molecular orbitals (HOMO) is examined by plotting the partial density of states (PDOS) displayed in Fig. 2b. The PDOS curves show that the valence band is essentially composed of F p_{x+y} with small contributions from the orbitals of carbon and hydrogen atoms. The conduction band is made up essentially of a heavy mixture of the s and p states of C atoms with small contributions of the orbitals of F and H atoms. The C p_{x+y} states especially dominate the upper valence-band edge, whereas the C p_z states dominate the lower conduction band edge. These features have not been reported elsewhere.

Once the electron–electron self-energy effects are included using the G_0W_0 approximation, the band structure is strongly modified. The direct bandgap increases from 2.97 to 5.96 eV, suggesting an enhancement of the electron–electron interactions, in good agreement with recent calculations (6.0 eV) [23]. The particularly large quasiparticle corrections to the DFT-LDA energy gap are a consequence of the enhanced electron–electron interaction due to the confinement effect and a weaker electronic screening in reduced-dimensional semiconducting materials. In addition, the low screening leads to excitonic effects well below the

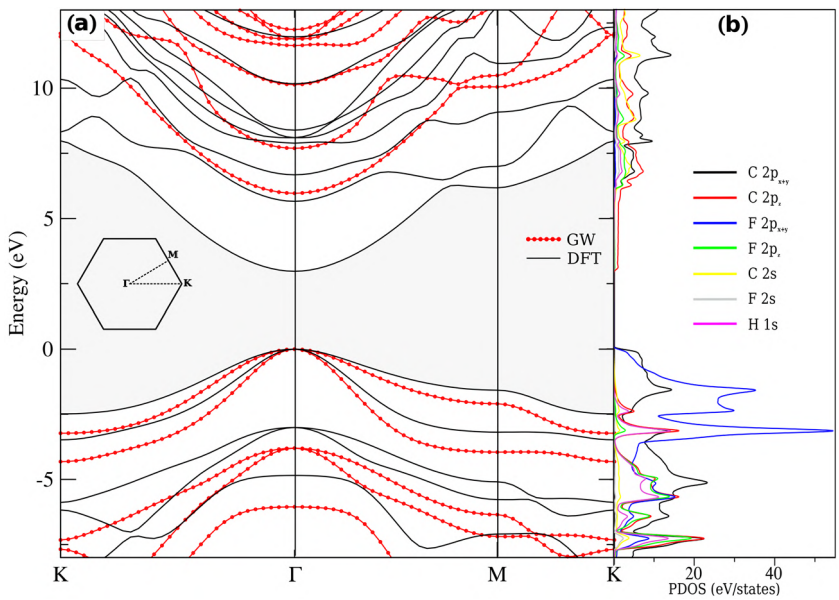

Figure 2 (a) The band structure of H–CC–F in LDA (full line) and GW approximation (red circles) and (b) the projected density of states (PDOS). The band structure was calculated in hexagonal structure along the high-symmetry line K−Γ−M−K; the zero indicates the highest occupied state.

© 2015 WILEY-VCH Verlag GmbH & Co. KGaA, Weinheim

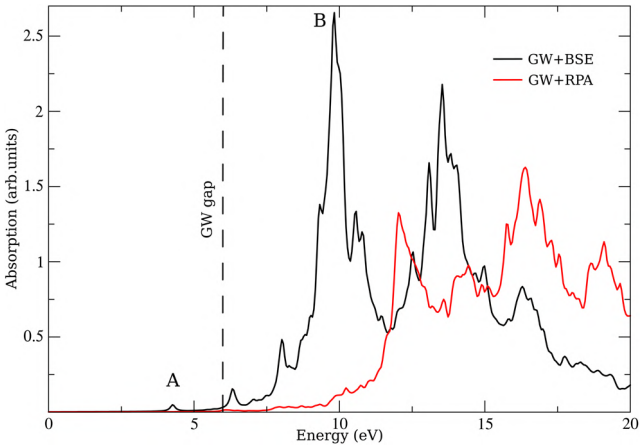

Figure 3 Imaginary part of the macroscopic dielectric function for light polarized along the H–CC–F plane. The dashed line indicates the position of the GW gap.

quasiparticle bandgap. This point will be discussed in the next section. We also notice that the quasiparticle correction is half-way between the graphane's GW gap (5.4 eV) [8] and that of fluorographene (7.01 eV) [10]. The larger quasiparticle correction in fluorographene is mainly a consequence of its denser charge distribution near fluorine atoms due to the strong electronegativity of fluorine [10]. Because of this inhomogeneous charge distribution, the valence band consists mainly of fluorine p orbitals, while the conduction band is essentially composed of C p_z orbitals. These orbitals are not confined to the sheet, but extended into the vacuum region. Due to the weak dynamical screening for the electric field perpendicular to the sheet (depolarization effect), the many-body interaction effects in these bands would be less screened. As a consequence, both valence and conduction bands would have a larger quasiparticle correction and hence a larger difference between the quasiparticle energies and LDA eigenvalues. In H–CC–F, the presence of an H layer in one side compensates the charge transfer from carbon to fluorine atoms and in turn makes the delocalization of the charge density less pronounced. Consequently, the quasiparticle correction in H–CC–F is smaller than that of fluorographene [10] but larger than that of graphane [8].

3.3 Optical properties Starting from the quasiparticle states and solving the Bethe–Salpeter equation (BSE), the imaginary part of the macroscopic dielectric function $\mathrm{Im}\epsilon_{\mathrm{M}}(\omega)$ is presented in Fig. 3. It is worth noting that only the spectrum for light propagating along the H–CC–F plane in the x-direction is considered. The spectrum with out-of-plane components is not discussed here because of the huge depolarization effect. This effect, known in low-dimensional systems with confined geometry, reduces mainly the magnitude of the out-of-plane component of the $\mathrm{Im}\epsilon_{\mathrm{M}}(\omega)$, and enhances the optical anisotropy. The resulting absorption spectrum is compared to the $\mathrm{Im}\epsilon_{\mathrm{M}}(\omega)$ calculated at GW-RPA, that is the random phase approximation (RPA) on the top of GW quasiparticle corrections.

The GW-RPA absorption spectrum (GW+RPA curve in Fig. 3) does not show any significant feature near to the GW bandgap (5.96 eV), reflecting a small spatial overlapping of the wave functions of the top-valence and bottom-conduction states. The absorption spectrum is strongly modified after the inclusion of electron–hole interaction in addition to electron–electron effects (GW + BSE curve in Fig. 3). Our calculation shows a redshift of the whole spectrum, with the appearance of a number of pronounced excitonic resonances. In particular, we have identified that the major peak (labeled with B in Fig. 3) is originated from a large number of transitions around 9.80 eV from the top of the valence band to the bottom of the conduction band.

In the low-energy region below the GW gap, the absorption spectrum shows an optically active (bright) bound exciton at 4.26 eV with a large binding energy of 1.7 eV (see Fig. 3). The binding energy of exciton A, which is between the theoretical one of graphane (1.6 eV) [8] and that of fluorographene (1.96 eV) [10], would have a vital role in the photoluminescence of H–CC–F. We attribute the increase of binding energy as one moves from graphane to fluorographene to the decrease of screening, predominantly by the valence electrons. The strong screening leads to a weaker Coulomb interaction between electrons and holes, and hence a reduced exciton binding energy. In graphane, many-body interaction effects on the valence electrons corresponding to the in-plane C–C σ bands are significantly screened. In the case of fluorographene, due to the strong electronegativity of fluorine, the valence band is associated with orbitals that extend into the vacuum region from the sheet. Consequently, the screening effects on those bands would be less significant. The hydrogene–graphene–fluorine is an intermediate case between graphane and fluorographene. The valence-band electrons are confined on fluorine atoms but also in a carbon-atom network, making the screening in this material in between that of graphane and that of fluorographene.

This exciton, which is twofold degenerate, is related to a large number of transitions from the top of the valence band (twofold degenerate at Γ) to the bottom of the conduction band around the Γ-point.

So as to describe how the excited quasielectrons and quasiholes are correlated in real space, we plot the electron density for the excitons A and B with the hole (black spot) pinned at a C–C bond as displayed in Fig. 4. As can be seen, the wave functions of the excitons show that the electron orbitals distribute on nearest-neighbor carbon atoms and adjacent fluorine atoms in the vicinity of the hole. Since the hole is fixed at the C–C bond, the creation of such excitons corresponds to a charge transfer toward the carbon-atom network and the side layer on top of the fluorine atoms, leading to insufficient spatial separation of the charge. This strong overlap between electron and hole wave functions is a clear indication of shorter excitonic lifetimes. Exciton A exhibits a fast damping character indicating the stronger binding nature between quasielectrons and quasiholes governed by the ex-

© 2015 WILEY-VCH Verlag GmbH & Co. KGaA, Weinheim

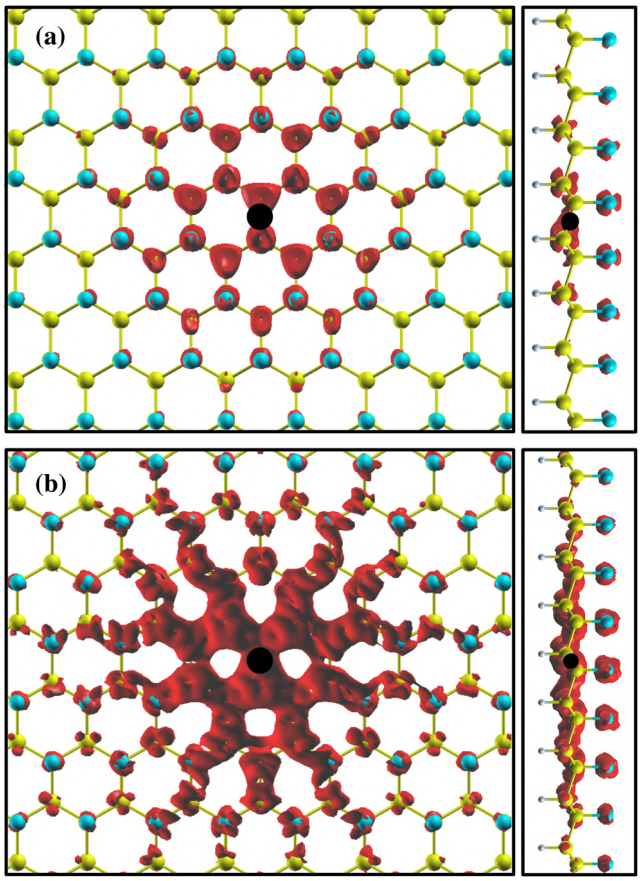

Figure 4 Top and side views of the energy wave functions of the bound exciton A (a) and exciton B (b) for a fixed position of the hole (black spot) in a C–C bond.

citonic effects, while the charge distribution of exciton B has an extended feature due to its resonant nature. The relatively small spatial extension of the exciton A is a consequence of its delocalization in reciprocal space. On the other hand, the charge distribution is shown to be correlated with the binding energy. As the binding energy decreases, the exciton gradually acquires extended features. In graphane, the large binding energy, coupled with strong localization in the excitonic state, and sufficient spatial separation may allow the observation of an excitonic Bose–Einstein condensate by continuous optical pumping of excitons. In H–CC–F, the lower spatial separation of the charge gives rise to extremely short radiative lifetimes, preventing condensation.

4 Conclusions In summary, we studied the electronic and optical properties of a hydrogen–graphene–fluorine janus graphene by means of a first-principles many-body Green's function method. The quasiparticle bandgap increases from 2.97 to 5.96 eV, suggesting an enhanced electron–electron interaction. Moreover, strong charge-transfer excitonic effects dominate the optical response, giving rise to a bound exciton. Although the exciton indicate a large binding energy and small spatial extension, the strong overlap between electron and hole wave functions gives rise to extremely short radiative lifetimes, preventing condensation.

References

[1] K. S. Novoselov, A. K. Geim, S. V. Morosov, D. Jiang, Y. Zhang, S. V. Dubonos, I. V. Grigorieva, and A. A. Firsov, Science **306**, 666 (2004).
[2] D. C. Elias, R. R. Nair, T. M. G. Mohiuddin, S. V. Morozov, P. Blake, M. P. Halsall, A. C. Ferrari, D. W. Boukhvalov, M. I. Katsnelson, A. K. Geim, and K. S. Novoselov, Science **323**, 610 (2009).
[3] R. R. Nair, W. Ren, R. Jalil, I. Riaz, V. G. Kravets, L. Britnell, P. Blake, F. Schedin, A. S. Mayorov, S. Yuan, M. I. Katsnelson, H.-M. Cheng, W. Strupinski, L. G. Bulusheva, A. V. Okotrub, I. V. Grigorieva, A. N. Grigorenko, K. S. Novoselov, and A. K. Geim, Small **6**, 2877 (2010).
[4] J. T. Robinson, J. S. Burgess, C. E. Junkermeier, S. C. Badescu, T. L. Reinecke, F. K. Perkins, M. K. Zalalutdniov, J. W. Baldwin, J. C. Culbertson, P. E. Sheehan, and E. S. Snow, Nano Lett. **10**, 3001 (2010).
[5] J. Wu, L. Xie, Y. Li, H. Wang, Y. Ouyang, J. Guo, and H. Dai, J. Am. Chem. Soc. **133**, 19668 (2011).
[6] X. Zhang, A. Hsu, H. Wang, Y. Song, J. Kong, M. S. Dresselhaus, and T. Palacios, ACS Nano **7**(8), 7262 (2013).
[7] J. O. Sofo, A. S. Chaudhari, and G. D. Barber, Phys. Rev. B **75**, 153401 (2007).
[8] P. Cudazzo, C. Attaccalite, I. V. Tokatly, and A. Rubio, Phys. Rev. Lett. **104**, 226804 (2010).
[9] D. K. Samarakoon, Z. Chen, C. Nicolas, and X.-Q. Wang, Small **7**, 965 (2011).
[10] W. Wei and T. Jacob, Phys. Rev. B **87**, 115431 (2013).
[11] H. Sahin, M. Topsakal, and S. Ciraci, Phys. Rev. B **83**, 115432 (2011).
[12] F. Karlicky and M. Otyepka, J. Chem. Theory Comput. **9**, 4155 (2013).
[13] M. Klintenberg, S. Lebgue, M. I. Katsnelson, and O. Eriksson, Phys. Rev. B **81**, 085433 (2010).
[14] F. Li and Y. Li, J. Mater. Chem. C **3**, 3416 (2015).
[15] Y. Liang and L. Yang, MRS Proc. **1370**, 137 (2011).
[16] Y. Zhang, T.-T. Tang, C. Girit, Z. Hao, M. C. Martin, A. Zettl, M. F. Crommie, Y. R. Shen, and F. Wang, Nature (London) **459**, 820 (2009).
[17] F. Withers, M. Dubois, and A. K. Savchenko, Phys. Rev. B **82**, 073403 (2010).
[18] G. Savini, A. C. Ferrari, and F. Giustino, Phys. Rev. Lett. **105**, 037002 (2010).
[19] R. Singh and G. Bester, Phys. Rev. B **84**, 155427 (2011).
[20] L. Zhang, J. Yu, M. Yang, Q. Xie, H. Peng, and Z. Liu, Nature Commun. **4**, 1443 (2013).
[21] M. T. Ong, K. A. N. Duerloo, and E. J. Reed, J. Phys. Chem. C **117**, 3615 (2013).
[22] Y. Yang, W. Ren, and L. Bellaiche, Phys. Rev. B **89**, 245439 (2014).
[23] H. J. Kim, M. Noor-A-Alam, J. Y. Son, and Y. Shin, Chem. Phys. Lett. **603**, 62 (2014).
[24] M. S. Hybertsen and S. G. Louie, Phys. Rev. B **34**, 5390 (1986).
[25] M. Rohlfing and S. G. Louie, Phys. Rev. B **62**, 4927 (2000).

© 2015 WILEY-VCH Verlag GmbH & Co. KGaA, Weinheim

[26] X. Gonze, B. Amadon, P.-M. Anglade, J.-M. Beuken, F. Bottin, P. Boulanger, F. Bruneval, D. Caliste, R. Caracas, M. Cote, T. Deutsch, L. Genovese, Ph. Ghosez, M. Giantomassi, S. Goedecker, D. R. Hamann, P. Hermet, F. Jollet, G. Jomard, S. Leroux, M. Mancini, S. Mazevet, M. J. T. Oliveira, G. Onida, Y. Pouillon, T. Rangel, G.-M. Rignanese, D. Sangalli, R. Shaltaf, M. Torrent, M. J. Verstraete, G. Zerah, and J. W. Zwanziger, Comput. Phys. Commun. **180**, 2582 (2009).
[27] A. Marini, C. Hogan, M. Grüning, and D. Varsano, Comput. Phys. Commun. **180**, 1392 (2009).
[28] P. Honenberg and W. Kohn, Phys. Rev. **136**, B864 (1964).
[29] W. Kohn and L. J. Sham, Phys. Rev. **140**, A1133 (1965).
[30] N. Troullier and J. L. Martins, Phys. Rev. B **43**, 1993 (1991).
[31] S. Goedecker, M. Teter, and J. Huetter, Phys. Rev. B **54**, 1703 (1996).
[32] H. J. Monkhorst and J. K. Pack, Phys. Rev. B **13**, 5188 (1976).
[33] G. Onida, L. Reining, and A. Rubio, Rev. Mod. Phys. **74**, 601 (2002).
[34] A. Fetter and J. D. Walecka, Quantum Theory of Many Particle Systems (McGraw-Hill, San Francisco, 1971), p. 538.
[35] C. A. Rozzi, D. Varsano, A. Marini, E. K. U. Gross, and A. Rubio, Phys. Rev. B **73**, 205119 (2006).

© 2015 WILEY-VCH Verlag GmbH & Co. KGaA, Weinheim

Dimensionality of excitons in stacked van der Waals materials: The example of hexagonal boron nitride

Wahib Aggoune,[1,2] Caterina Cocchi,[1,3] Dmitrii Nabok,[1,3]
Karim Rezouali,[2] Mohamed Akli Belkhir,[2] and Claudia Draxl[1,3]

[1] *Institut für Physik and IRIS Adlershof, Humboldt-Universität zu Berlin, Berlin, Germany*
[2] *Laboratoire de Physique Théorique, Faculté des Sciences Exactes, Université de Bejaia, 06000 Bejaia, Algeria*
[3] *European Theoretical Spectroscopic Facility (ETSF)*

(Dated: May 9, 2018)

With the example of h-BN, we demonstrate how the character of electron-hole pairs in van der Waals bound low-dimensional systems is driven by layer stacking. Four types of excitons appear, with either two- or three-dimensional spatial extension. Electron and hole distributions are either overlapping or exhibit charge-transfer nature. We discuss under which structural and symmetry conditions they appear and are either dark or bright. This analysis provides the key elements to identify, predict, and possibly tailor the character of e-h pairs in van der Waals materials.

Two-dimensional (2D) systems and layered weakly-bound structures thereof are considered the materials of the 21st century. Their wealth of intriguing properties is widely explored from a fundamental scientific point of view but also in view of a plethora of possible applications [1, 2]. Hexagonal boron nitride (h-BN) is one of these materials, consisting of covalently bound sheets that are held together by van der Waals (vdW) forces [3]. h-BN is a wide-gap semiconductor, exhibiting pronounced excitonic effects in its optical excitations that are present irrespective of the material's dimensionality [4–11]. Owing to the flat geometry of its in-plane hexagonal lattice, h-BN is often chosen as a building block in vdW heterostructures [12–15]. Combining different 2D systems, quantum confinement effects allow for tailoring their opto-electronic properties [16–18]. This not only concerns level alignment at the interface [19–26] but also the way the system interacts with light, i.e., quantum efficiency, as well as the character and spatial distribution of electron-hole (e-h) pairs [14, 15, 27–32].

In this Letter, we show that the nature and dimensionality of excitons can also be governed in a single vdW-bound bulk material, taking h-BN as an example. This seems surprising at a first glance as e-h pairs in this material have been found to exhibit basically the same character and extension in bulk [6–8], monolayers [10], as well as in interfaces with graphene [14]. Here we demonstrate how strongly stacking impacts the optical excitations of a vdW crystal at the absorption onset and beyond. By varying the arrangement of individual h-BN layers, we find in total four types of electron-hole pairs, of two-dimensional, three-dimensional (3D), and charge-transfer character, and discuss their appearance by symmetry considerations. We focus on the five structures that are obtained by including four inequivalent atoms in the unit cell, allowing only rigid translation by one bond length and/or exchanged positions between the two atomic species. We employ density-functional theory [33, 34] and many-body perturbation theory (MBPT, including G_0W_0 [35, 36] and the Bethe-Salpeter equation [37–40]), implemented in the all-electron framework of the `exciting` code [41–43].

Prototypes of the four kinds of excitations that can appear in h-BN are displayed in Fig. 1. There, the electronic distribution surrounding a fixed position of the hole is plotted. The first type is a 2D exciton, i.e., with the electron and hole on the same layer. Such e-h pairs are typical of atomically-thin sheets [10], but may also dominate the absorption onset of multilayer crystals [6–8, 25, 44]. We notice that these excitons are very localized, extending only up to three lattice parameters in the in-plane direction. The trigonal shape of the excitonic wave-function reflects the hexagonal symmetry of the monolayer. As extensively discussed in earlier works on h-BN based on MBPT [6, 7], this exciton is twofold degenerate, and its shape results from the averaged densities of the two degenerate contributions [7].

In multilayer structures, e-h pairs can also be extended in the vertical direction, with the electron and/or the hole spreading over neighboring layers. This is the case of *charge-transfer* (CT) excitons, where the electron and the hole sit on different layers and their extension is limited to a few (here up to five) lattice parameters in the in-plane direction. Viewed from the top, also this e-h pair exhibits clear trigonal symmetry (see Fig. 1). CT excitons are particularly intriguing in view of generating photocurrents [28, 45] or, if characterized by large binding energies, even Bose-Einstein condensates [46–50].

The other two types of excitons shown in Fig. 1 exhibit a 3D distribution, that can be either localized in the in-plane direction (3D$-l$) or delocalized over the whole space (3D$-d$). In both cases, the electron distribution overlaps with the hole distribution and further extends uniformly and symmetrically to the adjacent layers. In the 3D$-l$ e-h pairs, the electron probability density is significantly enhanced in the layer where the hole resides. This e-h pair exhibits a trigonal in-plane shape with an extension similar to the one of 2D excitons. In addition

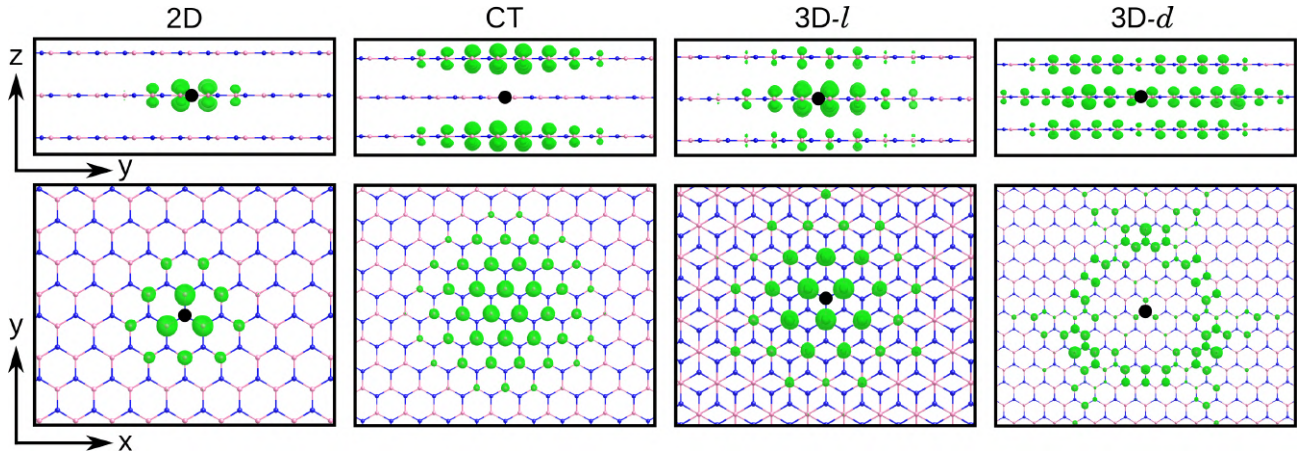

FIG. 1: (Color online) Real-space distribution (side and top view) of the four types of excitons that can appear in bulk h-BN upon different layer stacking. From left to right: 2D exciton, with the electron and the hole sitting on the same layer; charge-transfer (CT) exciton, with the electron and the hole on different layers; 3D exciton with localized (3D$-l$) and delocalized (3D$-d$) in-plane extension. The hole is indicated by the black dot and the electron distribution by the green isosurface. B atoms are pink and N atoms blue.

to the specific arrangement of the atoms, as discussed in the following, the 3D$-l$ excitons appear in configurations where the neighboring layers are linked by inversion symmetry. 3D$-d$ excitons appear above the absorption onset and are characterized by a delocalized spatial distribution in the three directions. In the h-BN structures considered here these e-h pairs extend up to twelve lattice parameters in the in-plane directions and across three layers in the stacking direction [51]. While reflecting resonant character and reduced crystal symmetry, such excitons exhibit a triangular-like shape, typical of higher-energy excitons in monolayer h-BN [10].

In order to relate the exciton characters described above with symmetry and atomic arrangement of the considered stackings, it is instructive to inspect more closely the corresponding geometries and analyze their electronic structure and optical spectra. In the simplest configuration, all atoms of the two inequivalent layers are aligned on top of each other (AA stacking). In the AB or Bernal stacking, every second atoms lies on the *hollow* site. These patterns, initially defined for monoatomic stacks of graphitic layers [52], can be further modulated by the positions of the two atomic species. The AA configuration results in the AA' stacking if B and N atoms of alternating layers lie on top of each other. We note in passing that this is considered to be the most stable h-BN arrangement [3, 53, 54]. The A'B and AB' stackings are obtained from the AB configuration: instead of alternating B and N atoms on the *hollow* site, as in the AB pattern, in the A'B (AB') arrangement only N (B) atoms occupy the *hollow* position. While the AB configuration has been reported for bilayer structures [55], other arrangements are observed only locally in few-layer stacks [56–60]. Complex modulated patterns have been achieved in combination with graphene [61–66] while transitions from a stacking sequence to another one have been shown upon morphological deformation [9]. These different layer stackings combined with the atomic arrangements in the vertical direction strongly impact the electronic structure (Fig. 2, right panel) and the optical spectra accordingly. In the following, we discuss how this structure-property relation determines the conditions under which different types of e-h pairs are formed.

In Fig. 2 we display the optical spectra (left panel) together with the quasi-particle (QP) band structures (right panel). Our results are in good agreement with available experimental data for the AA' stacking [67, 68], see also [51]. First, we consider the character of the first bright exciton in each configuration (green bars). The contributions of individual electronic states to the e-h pairs are indicated by the green circles drawn on top of the QP band structures [51]. Regardless of the stacking, the direct QP gap of bulk h-BN is always along or in the vicinity of the K-H path in the Brillouin zone (BZ). Hence, all excitations comprised within the first peak and up to $\sim$1 eV above, it always stem from transitions between QP states in the gap region. The two uppermost valence bands (VB, VB-1) and the two lowest conduction bands (CB, CB+1) are energetically very close to each other, due to the presence of two atoms of the same species in the unit cell. These bands have well-defined N and B character (highlighted in color in Fig. 2), which is related to the atomic structure of the constituting species and thus independent of the layer stacking.

The first bright e-h pair has 2D character in the AA', AA, and AB configurations. In the AA' stacking, it is twofold degenerate, owing to the symmetry of the lattice. Due to the parity of the exciton with respect to the inversion symmetry of the crystal, a double degenerate dark exciton with 2D distribution appears lowest

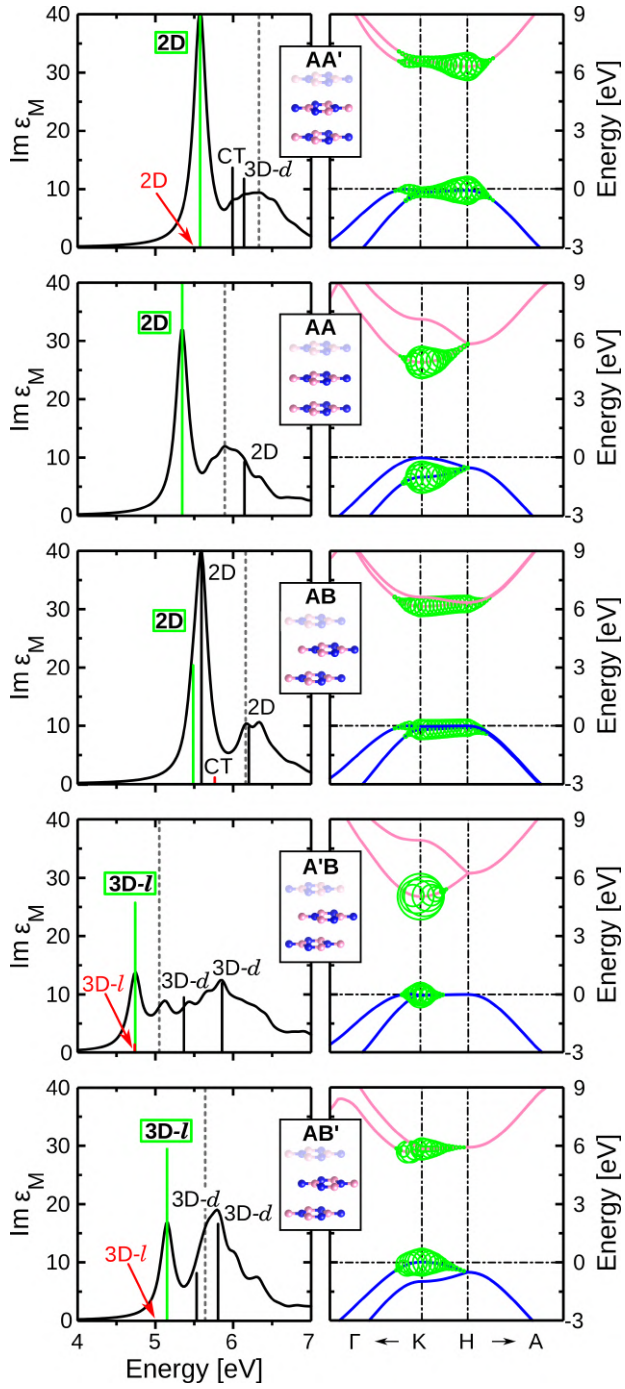

FIG. 2: (Color online) Left: Optical absorption spectra, given by the imaginary part of the macroscopic dielectric function, of the five considered stacking arrangements of h-BN (insets). The character of selected excitations is indicated following the nomenclature in Fig. 1. The height of the vertical bars is indicative of their relative intensity [51]. The first bright exciton is marked by a green bar with the corresponding label framed in green. Dark exciton at lowest energy are indicated by red arrows. A Lorentzian broadening of 0.1 eV is applied to all spectra. Direct QP gaps are marked by dashed gray lines. Right: Reciprocal-space distribution of the first bright exciton with band character highlighted in color: blue for N and pink for B. The size of the green circles indicate the **k**-resolved band contributions to the corresponding excitation (green bar) [51]. Fermi energy set to zero at the VBM and marked by a dashed-dotted line.

in energy (here at 5.50 eV, for comparison with experiments see [51]). These findings are in agreement with earlier studies of this h-BN phase [7, 69]. The 2D character of the first bright exciton in these arrangements is closely related to the electronic structure. In the AA' and AB stackings, where atoms of the same species never lie on top of each other, VB-1 and VB (and likewise CB and CB+1) are (almost) degenerate along the entire K-H path, as reported also in Refs. [6, 53, 70]. At the high-symmetry point H the Kohn-Sham wave-functions sit on one inequivalent layer only. In the AB configuration the same behavior is found also at K, with the consequence that in this stacking hole and electron of the 2D exciton are always localized within one specific h-BN sheet. Conversely, in the AA' and AA arrangements, electronic wave-functions tend to be delocalized over all layers towards the high-symmetry point K. As a result, the 2D exciton appears with the same probability in any layer [51, 71].

The lowest-energy exciton is optically allowed in those stackings that lack inversion symmetry between the layers. This is the case of the AB arrangement, where the absence of inversion symmetry allows for the presence of two optically-active e-h pairs, both twofold degenerate and encompassed within the first peak (see Fig. 2). Likewise, in the AA stacking the lowest-energy exciton is optically-allowed and bares 2D distribution. It dominates the absorption onset giving rise to a sharp peak. Conversely, in the AA' stacking, exhibiting inversion symmetry, the first exciton is dark. Overall, the spectra of these three structures look quite similar: They are characterized by an intense excitonic peak around 5.5 eV, followed by a broader and less intense hump at higher energies. The binding energy of the first optically-active exciton ranges between 0.50 eV and 0.75 eV, depending on the specific structure [51]. We define the binding energy as the difference between the excitation energy computed with the e-h interaction included (by solving the Bethe-Salpeter equation) and neglected (independent QP approximation) [51]. This definition is general and holds for any excitation independent of its position in the spectrum. For the first bright excitons discussed above, it coincides with the often adopted definition of binding energy as the difference between fundamental and optical gaps.

In the A'B and AB' configurations the lowest-energy bright exciton has a 3D$-l$ nature. This e-h pair has the same in-plane extension as the 2D one, but the electron is vertically spread over two neighboring layers to the one hosting the hole. This distribution can be once again traced back to symmetry and character of the electronic states near the gap that contribute to it. As discussed above, in the A'B (AB') stackings layers are staggered with B (N) atoms vertically aligned on top of each other. This makes the CB (VB) energetically split from the CB+1 (VB-1). The wave-functions of these bands

along the K-H path are therefore delocalized within all layers [51]. Under these conditions, the resulting e-h pairs extend to the neighboring layers.

The inversion symmetry in these structures is responsible for the presence of a forbidden exciton lowest in energy: In the A'B lattice, the first dark e-h pair has the same energy as the first bright 3D$-l$ exciton, while in the AB' stacking it is found at approximately 5 eV. The intensity of the first peak is considerably lower compared to the other arrangements, due to reduced wave-function overlap between the QP states contributing to it. In the A'B arrangement, the direct QP gap and thus the absorption onset are significantly red-shifted compared to the AA' stacking, up to 1.3 eV and 0.8 eV, respectively. Depending on the stacking arrangement, only 2D or 3D$-l$ excitons can appear at the absorption onset and are always associated with intense peaks. Their oscillator strength is related to the symmetry conditions as well as to the large overlap between the π/π^* wave-functions of the bands involved in the corresponding transitions. Their spatial localization, in turn, reflects the bound character of these e-h pairs. On the other hand, CT and 3D$-d$ e-h pairs emerge only at higher energies and, especially the former, upon strict symmetry and structural requirements, reflecting the layer-selective distribution of the contributing bands. In fact, CT excitons can appear only in the AA' and AB stackings, since in these structures the condition that atoms of the same species are aligned on top of each other is never satisfied. In the AA' arrangement, the CT exciton marked in the spectrum of Fig. 2 originates from transitions between the VB-1 and the CB+1, and between the VB and the CB, at the H point in the BZ. Here, these bands are degenerate and the corresponding electronic wave-functions are spread over N and B atoms belonging to different h-BN layers. The CT exciton is dipole-allowed only in the out-of-plane polarization direction and does not exhibit any degeneracy. As a result, the in-plane distribution of this e-h pair differs form the one shown in Fig. 1 [51]. In the spectrum of the AB arrangement, we find a double-degenerate CT exciton with in-plane polarization, stemming from transitions between the VB and the CB in the vicinity of the K point. According to the wave-function distribution of these bands, the hole and the electron sit on different layers, giving rise to the CT character of this exciton. Its weak oscillator strength is due to the small overlap between the electron and hole wave-functions [51].

Delocalized 3D excitons characterize mainly the high-energy window of the optical spectra. They only appear when inversion symmetry is present. In the AA' configuration the 3D$-d$ exciton marked above 6 eV is twofold degenerate and has a binding energy of 0.2 eV. Viewed from the side (Fig. 1), this type of exciton extends symmetrically to the nearest-neighboring layers in the vertical direction. This in-plane distribution appears in the h-BN monolayer [10] and is apparently preserved also in multilayer structures. Also in the A'B and AB' configurations 3D$-d$ excitons are present in the high energy-range, but they exhibit a different in-plane distribution that reflects the structural arrangement [51]. It is worth noting that in the AA and AB configurations, where inversion symmetry is absent, delocalized 2D excitons with triangonal shape appear in the high energy-range. Remarkably, they resemble higher-energy excitons in monolayer h-BN [10, 51].

Finally, above 1 eV from the absorption onset of each stacking very delocalized excitations appear (not shown, see also [51]). They stem from a number of mixed transitions between electronic states far from the QP gap and do not correspond to any type of exciton depicted in Fig. 1. Due to their resonant character of band-to-band transitions, their delocalized distribution resembles that of Kohn-Sham states. Such 3D excitations with extremely extended character are expected to form more favorably in vdW crystals and heterostructures exhibiting superlattices and/or Moiré patterns. These complex structural arrangements, that are observed in realistic samples (see, *e.g.*, Refs. [72–74] for graphene/h-BN interfaces), tend to decrease the symmetry of the system, thereby promoting weakly-bound e-h pairs.

In summary, we have analyzed the four types of excitations that appear in different stacking arrangements of bulk h-BN, considered here as a prototypical vdW material. We have shown that localized e-h pairs with purely 2D character appear in all configurations. Charge-transfer excitons occur only if specific structural and symmetry conditions are fulfilled. 3D excitons with more or less extended spatial distribution are also present at the absorption onset and/or above it, depending on the layer stacking. Our results demonstrate the interplay between structural arrangements and optical properties in stacked vdW materials, providing the key elements to assess, foresee, and tune the character of their e-h pairs. The general arguments underpinning the presented analysis can be directly extended to other vdW materials and their heterostructures, complementing recent studies on the effects of stacking on optical properties [75–77] and interlayer excitons [31, 78–84]. As such, our findings contribute to the fascinating perspectives of designing vdW heterostructures with customized characteristics, achieved through a controlled modulation of the electronic structure via layer patterning.

Acknowledgment

Work supported by the Algerian Ministry of High Education and Scientific Research under the PNE programme. Partial funding by the German Research Foundation (DFG), through the Collaborative Research Center 951, HIOS, is appreciated. W. A. thanks F. Paleari for fruitful discussions.

[1] G. Bhimanapati, Z. Lin, V. Meunier, Y. Jung, J. Cha, S. Das, D. Xiao, Y. Son, M. Strano, V. Cooper, et al., ACS Nano **9**, 11509 (2015).
[2] C. Tan, X. Cao, X.-J. Wu, Q. He, J. Yang, X. Zhang, J. Chen, W. Zhao, S. Han, G.-H. Nam, et al., Chem. Rev. **117**, 6225 (2017).
[3] Pease R. S., Nature **165**, 722723 (1950).
[4] K. Watanabe, T. Taniguchi, and H. Kanda, Nature Mat. **3**, 404 (2004).
[5] Y. Kubota, K. Watanabe, O. Tsuda, and T. Taniguchi, Science **317**, 932 (2007).
[6] B. Arnaud, S. Lebegue, P. Rabiller, and M. Alouani, Phys. Rev. Lett. **96**, 026402 (2006).
[7] L. Wirtz, A. Marini, M. Grüning, C. Attaccalite, G. Kresse, and A. Rubio, Phys. Rev. Lett. **100**, 189701 (2008).
[8] S. Galambosi, L. Wirtz, J. Soininen, J. Serrano, A. Marini, K. Watanabe, T. Taniguchi, S. Huotari, A. Rubio, and K. Hämäläinen, Phys. Rev. B **83**, 081413 (2011).
[9] R. Bourrellier, M. Amato, L. H. Galvo Tizei, C. Giorgetti, A. Gloter, M. I. Heggie, K. March, O. Stphan, L. Reining, M. Kociak, et al., ACS Photon. **1**, 857 (2014).
[10] T. Galvani, F. Paleari, H. P. C. Miranda, A. Molina-Sánchez, L. Wirtz, S. Latil, H. Amara, and F. m. c. Ducastelle, Phys. Rev. B **94**, 125303 (2016).
[11] J. Koskelo, G. Fugallo, M. Hakala, M. Gatti, F. Sottile, and P. Cudazzo, Phys. Rev. B **95**, 035125 (2017).
[12] C. R. Dean, A. F. Young, I. Meric, C. Lee, L. Wang, S. Sorgenfrei, K. Watanabe, T. Taniguchi, P. Kim, K. Shepard, et al., Nature Nanotech. **5**, 722 (2010).
[13] J. Yan, K. W. Jacobsen, and K. S. Thygesen, Phys. Rev. B **86**, 045208 (2012).
[14] W. Aggoune, C. Cocchi, D. Nabok, K. Rezouali, M. A. Belkhir, and C. Draxl, J. Phys. Chem. Lett. **8**, 1464 (2017).
[15] S. Latini, K. T. Winther, T. Olsen, and K. S. Thygesen, Nano Lett. **17**, 938 (2017).
[16] A. K. Geim and I. V. Grigorieva, Nature (London) **499**, 419 (2013).
[17] K. Novoselov, A. Mishchenko, A. Carvalho, and A. C. Neto, Science **353**, aac9439 (2016).
[18] D. Jariwala, T. J. Marks, and M. C. Hersam, Nature Mat. **16**, 170 (2017).
[19] J. Kang, S. Tongay, J. Zhou, J. Li, and J. Wu, Appl. Phys. Lett. **102**, 012111 (2013).
[20] M.-H. Chiu, C. Zhang, H.-W. Shiu, C.-P. Chuu, C.-H. Chen, C.-Y. S. Chang, C.-H. Chen, M.-Y. Chou, C.-K. Shih, and L.-J. Li, Nature Comm. **6**, 7666 (2015).
[21] V. O. Özçelik, J. G. Azadani, C. Yang, S. J. Koester, and T. Low, Phys. Rev. B **94**, 035125 (2016).
[22] Q. Fu, D. Nabok, and C. Draxl, J. Phys. Chem. C **120**, 11671 (2016).
[23] Y. Guo and J. Robertson, Appl. Phys. Lett. **108**, 233104 (2016).
[24] C. Zhang, C. Gong, Y. Nie, K.-A. Min, C. Liang, Y. J. Oh, H. Zhang, W. Wang, S. Hong, L. Colombo, et al., 2D Mater. **4**, 015026 (2016).
[25] K. S. Thygesen, 2D Mater. **4**, 022004 (2017).
[26] Q. Fu, C. Cocchi, D. Nabok, A. Gulans, and C. Draxl, Phys. Chem. Chem. Phys. **19**, 6196 (2017).
[27] M. Milko, P. Puschnig, P. Blondeau, E. Menna, J. Gao, M. A. Loi, and C. Draxl, J. Phys. Chem. Lett. **4**, 2664 (2013).
[28] X. Hong, J. Kim, S.-F. Shi, Y. Zhang, C. Jin, Y. Sun, S. Tongay, J. Wu, Y. Zhang, and F. Wang, Nature Nanotech. **9**, 682 (2014).
[29] F. Ceballos, M. Z. Bellus, H.-Y. Chiu, and H. Zhao, ACS Nano **8**, 12717 (2014).
[30] L. Li, R. Long, and O. V. Prezhdo, Chem. Mater. **29**, 2466 (2016).
[31] M. Baranowski, A. Surrente, L. Klopotowski, J. Urban, N. Zhang, D. K. Maude, K. Wiwatowski, S. Mackowski, Y.-C. Kung, D. Dumcenco, et al., Nano Letters **17**, 6360 (2017).
[32] Z. Guan, C.-S. Lian, S. Hu, S. Ni, J. Li, and W. Duan, J. Phys. Chem. C **121**, 3654 (2017).
[33] P. Hohenberg and W. Kohn, Phys. Rev. **136**, B864 (1964).
[34] W. Kohn and L. J. Sham, Phys. Rev. **140**, A1133 (1965).
[35] L. Hedin, Phys. Rev. **139**, A796 (1965).
[36] M. S. Hybertsen and S. G. Louie, Phys. Rev. Lett. **55**, 1418 (1985).
[37] W. Hanke and L. J. Sham, Phys. Rev. B **21**, 4656 (1980).
[38] G. Strinati, Riv. Nuovo Cimento **11**, 1 (1988).
[39] M. Rohlfing and S. G. Louie, Phys. Rev. B **62**, 4927 (2000).
[40] P. Puschnig and C. Ambrosch-Draxl, Phys. Rev. B **66**, 165105 (2002).
[41] A. Gulans, S. Kontur, C. Meisenbichler, D. Nabok, P. Pavone, S. Rigamonti, S. Sagmeister, U. Werner, and C. Draxl, J. Phys. Condens. Matter. **26**, 363202 (2014).
[42] S. Sagmeister and C. Ambrosch-Draxl, Phys. Chem. Chem. Phys. **11**, 4451 (2009).
[43] D. Nabok, A. Gulans, and C. Draxl, Phys. Rev. B **94**, 035118 (2016).
[44] A. Molina-Sánchez, K. Hummer, and L. Wirtz, Surf. Sci. Rep. (Netherlands) **70**, 554 (2015).
[45] C. Deibel, T. Strobel, and V. Dyakonov, Adv. Mater. **22**, 4097 (2010).
[46] H. Min, R. Bistritzer, J.-J. Su, and A. MacDonald, Phys. Rev. B **78**, 121401 (2008).
[47] M. Y. Kharitonov and K. B. Efetov, Phys. Rev. B **78**, 241401 (2008).
[48] P. Cudazzo, C. Attaccalite, I. V. Tokatly, and A. Rubio, Phys. Rev. Lett. **104**, 226804 (2010).
[49] A. Perali, D. Neilson, and A. R. Hamilton, Phys. Rev. Lett. **110**, 146803 (2013).
[50] M. Fogler, L. Butov, and K. Novoselov, Nature Comm. **5**, 4555 (2014).
[51] See Supplemental Material at http:/link.aps.org/ for computational details and as well as additional information about structural, electronic and optical properties of all considered stackings, including comparison with experiments, when available. Refs. [85–100] are additionally cited therein.
[52] J. Bernal, Proc. R. Soc. London A **106**, 749 (1924).
[53] L. Liu, Y. Feng, and Z. Shen, Phys. Rev. B **68**, 104102 (2003).
[54] G. Constantinescu, A. Kuc, and T. Heine, Phys. Rev. Lett. **111**, 036104 (2013).
[55] J. H. Warner, M. H. Rummeli, A. Bachmatiuk, and

B. Buchner, ACS Nano **4**, 1299 (2010).
[56] C.-J. Kim, L. Brown, M. W. Graham, R. Hovden, R. W. Havener, P. L. McEuen, D. A. Muller, and J. Park, Nano Lett. **13**, 5660 (2013).
[57] A. Shmeliov, J. S. Kim, K. B. Borisenko, P. Wang, E. Okunishi, M. Shannon, A. I. Kirkland, P. D. Nellist, and V. Nicolosi, Nanoscale **5**, 2290 (2013).
[58] M. H. Khan, G. Casillas, D. R. G. Mitchell, H. K. Liu, L. Jiang, and Z. Huang, Nanoscale **8**, 15926 (2016).
[59] M. H. Khan, H. K. Liu, X. Sun, Y. Yamauchi, Y. Bando, D. Golberg, and Z. Huang, Materials Today **20**, 611 (2017).
[60] H. Henck, D. Pierucci, Z. Ben Aziza, M. G. Silly, B. Gil, F. Sirotti, G. Cassabois, and A. Ouerghi, Appl. Phys. Lett. **110**, 023101 (2017).
[61] S. M. Kim, A. Hsu, P. Araujo, Y.-H. Lee, T. Palacios, M. Dresselhaus, J.-C. Idrobo, K. K. Kim, and J. Kong, Nano Lett. **13**, 933 (2013).
[62] S. Tang, H. Wang, Y. Zhang, A. Li, H. Xie, X. Liu, L. Liu, T. Li, F. Huang, X. Xie, et al., Sci. Rep. **3**, 2666 (2013).
[63] T. Gao, X. Song, H. Du, Y. Nie, Y. Chen, Q. Ji, J. Sun, Y. Yang, Y. Zhang, and Z. Liu, Nature Comm. **6**, 6835 (2015).
[64] A. Khanaki, H. Tian, Z. Xu, R. Zheng, Y. He, Z. Cui, J. Yang, and J. Liu, Nanotechnol. **29**, 035602 (2017).
[65] J. M. Wofford, S. Nakhaie, T. Krause, X. Liu, M. Ramsteiner, M. Hanke, H. Riechert, and J. M. J. Lopes, Sci. Rep. **7**, 43644 (2017).
[66] R. Zheng, A. Khanaki, H. Tian, Y. He, Y. Cui, Z. Xu, and J. Liu, Appl. Phys. Lett. **111**, 011903 (2017).
[67] R. Mamy, J. Thomas, G. Jezequel, and J. Lemonnier, J. Phys. Lett.-Paris **42**, 473 (1981).
[68] C. Tarrio and S. E. Schnatterly, Phys. Rev. B **40**, 7852 (1989).
[69] F. Paleari, T. Galvani, H. Amara, F. Ducastelle, A. Molina-Snchez, and L. Wirtz, arXiv preprint arXiv:1802.01856 (2018).
[70] S.-P. Gao, Solid State Commun. **152**, 1817 (2012).
[71] For consistency with the other structures, also the AA stacking is represented in a unit cell containing two layer. On account of the resulting band folding, the lowest-energy transition between VB and CB is optically forbidden and the first allowed transition is between VB-1 and CB.
[72] M. Yankowitz, J. Xue, D. Cormode, J. D. Sanchez-Yamagishi, K. Watanabe, T. Taniguchi, P. Jarillo-Herrero, P. Jacquod, and B. J. LeRoy, Nature Phys. **8**, 382 (2012).
[73] C. Woods, L. Britnell, A. Eckmann, R. Ma, J. Lu, H. Guo, X. Lin, G. Yu, Y. Cao, R. Gorbachev, et al., Nature Phys. **10**, 451 (2014).
[74] J. R. Wallbank, M. Mucha-Kruczyński, X. Chen, and V. I. Fal'ko, Ann. Phys. **527**, 359 (2015).
[75] J. He, K. Hummer, and C. Franchini, Phys. Rev. B **89**, 075409 (2014).
[76] A. H. Reshak, S. A. Khan, and S. Auluck, RSC Adv. **4**, 11967 (2014).
[77] J. Yan, J. Xia, X. Wang, L. Liu, J.-L. Kuo, B. K. Tay, S. Chen, W. Zhou, Z. Liu, and Z. X. Shen, Nano Lett. **15**, 8155 (2015).
[78] P. K. Nayak, Y. Horbatenko, S. Ahn, G. Kim, J.-U. Lee, K. Y. Ma, A.-R. Jang, H. Lim, D. Kim, S. Ryu, et al., ACS Nano **11**, 4041 (2017).
[79] B. Miller, A. Steinhoff, B. Pano, J. Klein, F. Jahnke, A. Holleitner, and U. Wurstbauer, Nano Lett. **17**, 5229 (2017).
[80] E. M. Alexeev, A. Catanzaro, O. V. Skrypka, P. K. Nayak, S. Ahn, S. Pak, J. Lee, J. I. Sohn, K. S. Novoselov, H. S. Shin, et al., Nano letters **17**, 5342 (2017).
[81] A. Arora, M. Drüppel, R. Schmidt, T. Deilmann, R. Schneider, M. R. Molas, P. Marauhn, S. M. de Vasconcellos, M. Potemski, M. Rohlfing, et al., Nature Comm. **8**, 639 (2017).
[82] T. Deilmann and K. S. Thygesen, Nano Lett. **18**, 1460 (2018).
[83] M. Okada, A. Kutana, Y. Kureishi, Y. Kobayashi, Y. Saito, T. Saito, K. Watanabe, T. Taniguchi, S. Gupta, Y. Miyata, et al., ACS Nano (2018).
[84] E. Torun, A. Molina-Sánchez, H. P. Miranda, and L. Wirtz, arXiv preprint arXiv:1803.05483 (2018).
[85] J. P. Perdew, K. Burke, and M. Ernzerhof, Phys. Rev. Lett. **77**, 3865 (1996).
[86] A. Tkatchenko and M. Scheffler, Phys. Rev. Lett. **102**, 073005 (2009).
[87] S. Grimme, J. Comput. Chem. **27**, 1787 (2006).
[88] K. Momma and F. Izumi, J. Appl. Cryst. **44**, 1272 (2011).
[89] V. Solozhenko, G. Will, and F. Elf, Solid State Commun. **96**, 1 (1995).
[90] N. Marom, J. Bernstein, J. Garel, A. Tkatchenko, E. Joselevich, L. Kronik, and O. Hod, Phys. Rev. Lett. **105**, 046801 (2010).
[91] O. Hod, J. Chem. Theory. Comput. **8**, 1360 (2012).
[92] X. Blase, A. Rubio, S. G. Louie, and M. L. Cohen, Phys. Rev. B **51**, 6868 (1995).
[93] G. Cassabois, P. Valvin, and B. Gil, Nature Phys. **10**, 262 (2016).
[94] V. Solozhenko, A. Lazarenko, J.-P. Petitet, and A. Kanaev, J. Phys. Chem. Sol. **62**, 1331 (2001).
[95] J. Edgar, T. Hoffman, B. Clubine, M. Currie, X. Du, J. Lin, and H. Jiang, J. Cryst. Growth **403**, 110 (2014).
[96] D. A. Evans, A. G. McGlynn, B. M. Towlson, M. Gunn, D. Jones, T. E. Jenkins, R. Winter, and N. R. J. Poolton, J. Phys. Condens. Matter. **20**, 075233 (2008).
[97] N. Berseneva, A. Gulans, A. V. Krasheninnikov, and R. M. Nieminen, Phys. Rev. B **87**, 035404 (2013).
[98] B. Cunningham, M. Grüning, P. Azarhoosh, D. Pashov, and M. van Schilfgaarde, Phys. Rev. Materials **2**, 034603 (2018).
[99] L. Museur, G. Brasse, A. Pierret, S. Maine, B. Attal-Tretout, F. Ducastelle, A. Loiseau, J. Barjon, K. Watanabe, T. Taniguchi, et al., Phys. Status Solidi RRL **5**, 214 (2011).
[100] K. Watanabe and T. Taniguchi, Phys. Rev. B **79**, 193104 (2009).

SUPPLEMENTAL MATERIAL

Dimensionality of excitons in stacked van der Waals materials: The example of hexagonal boron nitride

Wahib Aggoune,[1,2] Caterina Cocchi,[1,3] Dmitrii Nabok,[1,3]

Karim Rezouali,[2] Mohamed Akli Belkhir,[2] and Claudia Draxl[1,3]

[1] *Institut für Physik and IRIS Adlershof, Humboldt-Universität zu Berlin, Berlin, Germany*

[2] *Laboratoire de Physique Théorique, Faculté des Sciences Exactes, Université de Bejaia, 06000 Bejaia, Algeria*

[3] *European Theoretical Spectroscopic Facility (ETSF)*

Theoretical Methods and Computational Details

Ground-state properties are computed in the framework of density functional theory (DFT), within the generalized gradient approximation for the exchange-correlation functional with the Perdew-Burke-Ernzerhof parameterization [1]. The Tkatchenko-Scheffler (vdW-TS) approach [2] is adopted to account for van der Waals interactions between layers. The DFT-D2 method by S. Grimme [3] is used to estimate binding energies. Optical spectra are obtained in the framework of many-body perturbation theory. Quasi-particle (QP) energies are computed within the G_0W_0 approximation [4, 5]. Optical spectra are obtained from the solution of the Bethe-Salpeter equation (BSE), an effective two-body equation for the electron-hole two-particle Green's function [6, 7]. The BSE Hamiltonian reads $H^{BSE} = H^{diag} + 2H^x + H^{dir}$, where the first term H^{diag} accounts for *vertical* transitions, while the other two terms incorporate electron-hole *exchange* (H^x) and the screened Coulomb interaction (H^{dir}). The excitation energies E^λ are the eigenvalues of the secular equation associated to the BSE Hamiltonian

$$\sum_{v'c'\mathbf{k}'} H^{BSE}_{vc\mathbf{k},v'c'\mathbf{k}'} A^\lambda_{v'c'\mathbf{k}'} = E^\lambda A^\lambda_{vc\mathbf{k}}, \tag{1}$$

where v and c indicate valence and conduction states, respectively. The eigenvectors A^λ enter the expression of the transition coefficient of each excitation λ:

$$\mathbf{t}_\lambda = \sum_{vc\mathbf{k}} A^\lambda_{vc\mathbf{k}} \frac{\langle v\mathbf{k}|\widehat{\mathbf{p}}|c\mathbf{k}\rangle}{\epsilon_{c\mathbf{k}} \; - \; \epsilon_{v\mathbf{k}}}. \tag{2}$$

This quantity carries information about the polarization of the excitation in each direction. The oscillator strength of a given excitation corresponds to the absolute square of $\mathbf{t}_\lambda$. This quantity is represented in Fig. S3c together with all spectra. On the other hand, in Fig. 2 (main text) and in Figs. S5, S6, the height of the bars corresponds to $|\mathbf{t}_\lambda|$. This representation is adopted to ease the display of the oscillator strength of the selected excitations within the spectra. $\mathbf{t}_\lambda$ also enters the expression of the imaginary part of the macroscopic dielectric function,

$$\text{Im } \varepsilon_M \;=\; \frac{8\pi^2}{\Omega} \sum_\lambda |\mathbf{t}_\lambda|^2 \delta(\omega - E^\lambda), \tag{3}$$

where Ω is the unit cell volume. The BSE eigenvectors A^λ also contain information about the $\mathbf{k}$-resolved contributions of individual QP bands to the electron-hole pairs, expressed by the coefficients

$$w^\lambda_{v\mathbf{k}} = \sum_c |A^\lambda_{vc\mathbf{k}}|^2, \tag{4}$$

$$w^\lambda_{c\mathbf{k}} = \sum_v |A^\lambda_{vc\mathbf{k}}|^2. \tag{5}$$

for valence and conduction bands, respectively. These coefficients, also called here *exciton weights*, are visualized by green circles in the band-structure plots of Fig. 2, main text, and in Figs. S5, S6 below. Their size is representative of the contribution of a specific transition to the corresponding exciton. BSE eigenvectors A^λ also provide information about character and spatial extension of excitons in real space, acting as coefficients in the expression of the two-particle excitonic wave-functions:

$$\Psi^\lambda(\mathbf{r}_e, \mathbf{r}_h) = \sum_{vc\mathbf{k}} A^\lambda_{vc\mathbf{k}} \phi_{c\mathbf{k}}(\mathbf{r}_e) \phi^*_{v\mathbf{k}}(\mathbf{r}_h). \tag{6}$$

Different from the Kohn-Sham states that retain the crystal periodicity, excitonic wave-functions are non-periodic. Their finite extension needs to be properly resolved numerically through the $\mathbf{k}$-point sampling.

All calculations are performed using **exciting** [8], an all-electron full-potential code, implementing the family of linearized augmented planewave plus local orbitals methods. In the ground-state calculations, a basis-set cutoff $R_{MT}G_{max}$=7 is used. For both atomic species involved, namely boron (B) and nitrogen (N), a muffin-tin radius R_{MT}=1.3 bohr is adopted. The sampling of the Brillouin zone (BZ) is performed with a 36 × 36 × 14 **k**-grid. Lattice constants and internal coordinates are optimized until the residual forces on each atom are smaller than 0.003 eV/Å. Calculations of the QP correction to the Kohn-Sham eigenvalues within the G_0W_0 approximation [9] are performed with 250 empty states and a BZ sampling with a 18 × 18 × 6 shifted **k**-mesh is adopted. These parameters ensure a numerical accuracy over the QP gap at the high-symmetry point H of about 20 meV. For the solution of the BSE [10] a plane-wave cutoff $R_{MT}G_{max}$=6 is employed. In the calculation of the response function and of the screened Coulomb potential 100 empty bands are included. In the construction and diagonalization of the BSE Hamiltonian 4 occupied and 4 unoccupied bands are considered and a 24 × 24 × 8 shifted **k**-point mesh is adopted (see Fig. S1a below for some convergence tests). This choice ensures well converged spectra and an accuracy on the energy of the first exciton of at least 10 meV. Local-field effects are taken into account by including 25 $|\mathbf{G}+\mathbf{q}|$ vectors. A Lorentzian broadening of 0.1 eV is applied to the resulting spectra. Atomic structures and isosurfaces are visualized with the VESTA software [11]. For the real-space visualization of the electron-hole pairs (Eq. 6), a supercell with in-plane lattice parameter of $14a$ and out-of-plane lattice parameter of $4c$ has been used, with a and c being the lattice vectors of the corresponding unit cell (see Fig. S1b). In this way, eight layers are always included in the stacking direction for visualizing the excitons. In all such plots presented here and in the main text, the position of the hole is fixed according to the composition of the exciton, and the correlated electron distribution is visualized by the isosurface (green). The adopted **k**-point sampling and the related supercell size are sufficient to ensure a meaningful representation of the types of e-h pairs depicted in Fig. 1 of the main text and in Figs. S5 and S6 below. For representing the real-space distribution of all excitons we adopt isolvalues of 12% of the maximum values.

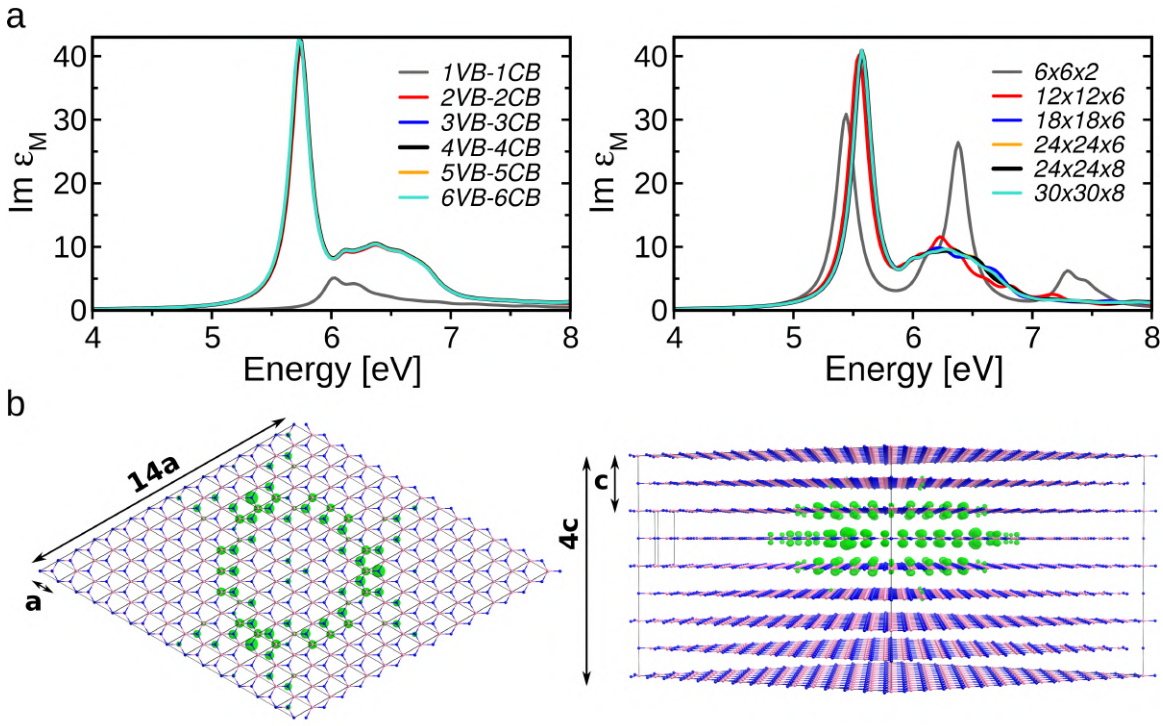

FIG. S1: **a**: BSE convergence for the optical spectrum of h-BN, AA' stacking. Left: Convergence with respect to the number of valence and conduction bands (VB and CB, respectively) obtained on a 18×18×6 **k**-mesh shifted from the Γ-point. These calculations are performed on top of the Kohn-Sham band-structure by applying a scissors operator. Right: Convergence with respect to the size of the **k**-mesh considering transitions from 4 occupied to 4 unoccupied bands. These calculations are performed on top of the QP band structure. **b**: Real-space distribution of the 3D-d exciton of the AA' stacking shown in Fig. 1 in the main text. Left: Top view, with the in-plane unit cell parameter a and supercell parameter $14a$ highlighted. Right: Side view, with the out-of-plane unit cell parameter c and supercell lattice parameter $4c$ highlighted. The electron distribution for a fixed hole position is given by the green isosurface.

Structural and Electronic Properties

In Table S1, we summarize stability and structural parameters of bulk h-BN, in different stacking arrangements. The AA stacking can be characterized by only one layer periodically repeated in the out-of-plane direction. Here, we consider on purpose for this system a unit cell with two layers in order to study the effects of stacking consistently with all other arrangements. The in-plane lattice parameter a=2.50 Å remains constant for all structures, while the

h-BN bulk		AA'	AA	AB	A'B	AB'
Lattice parameter (Å)	a	2.50	2.50	2.50	2.50	2.50
	c	6.60	6.84	6.58	6.48	6.86
Inversion symmetry	i	√	X	X	√	√
Binding energy (eV)	E_b	0.355	0.260	0.360	0.340	0.270

TABLE S1: Lattice parameters and binding energies of bulk h-BN in the considered stacking arrangements

out-of-plane one, c, strongly depends on the layer stacking. The structural parameter of the AA' stacking (given by vdW-TS method) are in agreement with the experimental one reported in Ref. [12].

Due to the enhanced electronegativity compared to the B atoms, there is an excess of charge in the vicinity of the N atoms, enhancing the polarity of the B-N bond (see Fig. S2b). As a result, in addition to the vdW forces which anchor the layers at fixed distance [13], the electrostatic interactions between the vertically aligned atomic centers play an

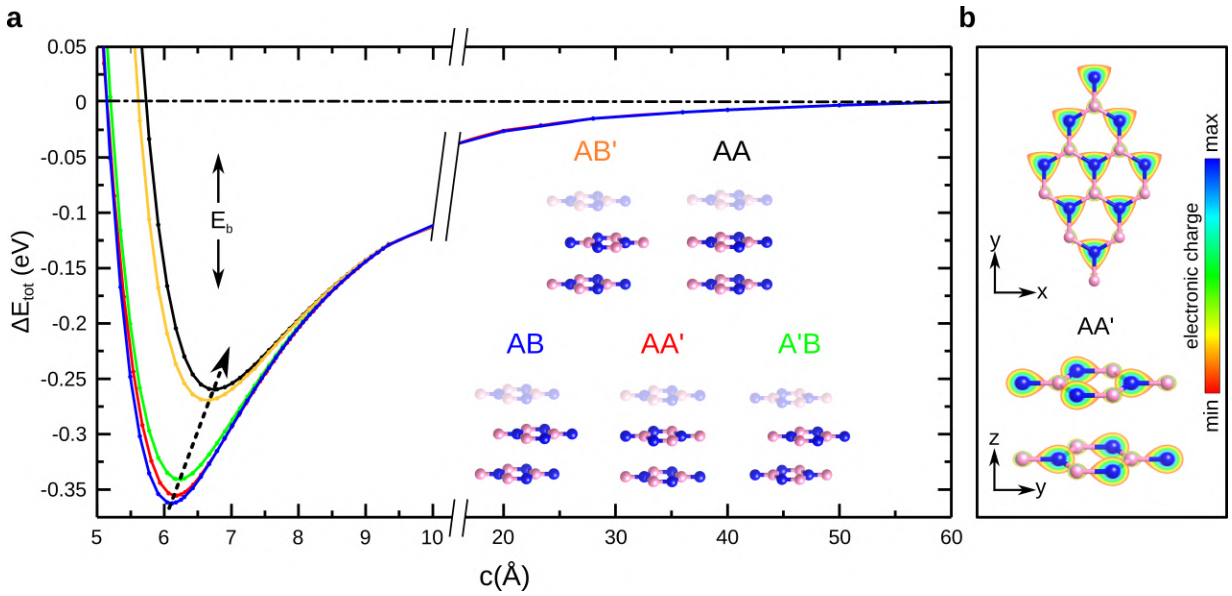

FIG. S2: **a**: Binding energies of the five considered h-BN stackings (structures shown as insets) evaluated as the total energy per unit cell at different interlayer distances along the c direction. The total energy of $c = 60$ Å is set to zero for reference. Different stackings are identified by different colors. **b**: In- and out-of-plane projection of the electronic charge density in AA' arrangement.

important role in the interlayer distance of different stackings [14]. For this reason, the AA (with N over N and B over B) and AB' (with N over N) stackings exhibit a larger c lattice parameter compared to the other configurations, due to the large electrostatic repulsion (see Fig. S3). We notice that the Pauli repulsion between the more delocalized electron clouds of the N atoms further contributes to increase the interlayer distance [14], which is also reflected in the smaller binding energies (trend indicated by the dashed arrow in Fig. S2a). The most unstable configuration is indeed the AA stacking, followed by the AB' one. In the AA', AB, and A'B arrangements, where the N atoms are not aligned on top of each other, electrostatic repulsion forces are weaker giving rise to the largest binding energies. Moreover, since N and B atoms are vertically aligned in the AA' and AB arrangements, the electrostatic attraction between the oppositely charged atomic centers make them the most favorable configurations, as found in Ref. [15, 16], with binding energy up to $\sim$0.36 eV (see Table S1 and Fig. S2). We notice that, since bulk h-BN crystallizes in the AA' configuration [15–17], the larger binding energy found in the AB arrangement with respect to the AA' stacking is due to the accuracy limits of our method [13–15]. The AB arrangement has been reported to appear in bilayer h-BN [18]. Recently, even the other stackings considered in this work have been probed experimentally in few-layer h-BN structures [19–24]. A more detailed investigation of structural properties and stability of these systems goes beyond the scope of this work and will be addressed in a dedicated study.

In the first column of Fig. S3 we show a sketch of the unit cells of the five considered h-BN stackings and in second column their corresponding QP band structures. While the QP band structures of different stackings look quite similar to each other, we notice two important differences. The first one concerns the character and the size of the band gap. As reported in Table S2, depending on the stacking the difference between the electronic and the direct (optical) gap can be more or less pronounced. An indirect band gap of 5.83 eV between the valence-band maximum (VBM) near the K point and the conduction-band minimum (CBM) at the M point is found in the AA' stacking of h-BN. Our result is in agreement with the previous theoretical findings based on MBPT [25–28]. While the reported experimental band gaps range between 3.6 and 7.1 eV [29], the size and the indirect nature of the band gap is in

h-BN bulk		AA'	AA	AB	A'B	AB'
Electronic gap (eV)	DFT	4.22	3.30	4.35	3.48	3.43
	G_0W_0	5.83	4.84	6.00	5.03	4.96
Minimum direct gap (eV)	DFT	4.63	4.16	4.46	3.50	4.00
	G_0W_0	6.33	5.89	6.16	5.05	5.64
Excitation energy (eV)	1st exciton ($\times$2)	**5.50**	5.34	5.48	**4.73**	**5.04**
	2st exciton ($\times$2)	5.57	5.71	5.59	4.74	5.14

TABLE S2: Electronic and direct QP gaps of h-BN bulk in the five considered stacking arrangements as well as the excitation energy of the first and the second exciton, with ($\times$2) to indicate that they are doubly degenerate. Dark excitons are in bold.

agreement with recent experimental observations [30–32]. We also notice that the reported band gaps of AA' and other stackings are in good agreement with the GW results in Refs. [27, 28]. Also, comparing the gaps of the different structures we notice a relevant decrease in those stackings where atoms of the same species are vertically aligned. This is the case of the A'B and AB' configurations, as well as of the AA one. It is worth noting here that the latter structure is formed by only one inequivalent h-BN layer. As mentioned in the main text, we simulate this system including two layers in the unit cell to treat this arrangement consistently with all the others. As a result, the first optically allowed transition is the one between the second uppermost valence band (VB-1) and the lowest conduction band (CB). In Table S2 we report the value of 5.89 eV (4.16 eV), corresponding of the minimum direct QP (DFT) gap between the VB-1 and the CB at the high-symmetry point K, consistent with that given by the IQPA spectrum, as shown in the following. This value is in agreement with Ref. [21].

The second difference in the electronic properties of the considered arrangements is related to the energy separation between VB-1 and VB, as well as CB and CB+1 along the K-H path. Since all the unit cells contain 2 B and 2 N atoms, the N-like bands (VB-1/VB) and the B-like bands (CB/CB+1) are split (degenerate) along the K-H path when the atoms of the same species in unit cell are (not) on top of each other. This energy splitting reflects the weak

electrostatic interaction between atoms of the same species.

To visualize the effect of layer arrangement on the band structure of h-BN, we plot the real-space distribution of the VB-1/VB and CB/CB+1 at the K and H points (see Fig. S4). At the H point the VB-1/VB and the CB/CB+1, with N- and B-like character, respectively, are degenerate in all stackings. The corresponding electronic distribution of each band is spread over only one h-BN layer in unit cell. At the K point, the VB-1/VB and the CB/CB+1 are either energetically degenerate or split, depending on the stacking. The electronic distribution of these bands is spread uniformly over both h-BN layers in the unit cell of all stackings, except for the AB arrangement. Here, the VB-1/VB and the CB/CB+1 are split at the K point and are therefore spread over only one h-BN layer in unit cell, like at the H point.

Optical Properties

The differences in the structural and electronic properties between the stackings are reflected in the optical spectra. The in-plane and out-of-plane component of the imaginary part of the macroscopic dielectric function are shown for each system in the third column of Fig. S3. We notice that in all stackings a sharp excitonic peak appears in the in-plane spectra, followed by a broad hump formed by inter-band transitions, and thus visible also in the independent QP spectra. In the AA', A'B and AB' arrangements, which exhibit inversion symmetry, the first peak is given by the second twofold degenerate bright exciton (see Table S2). The first exciton is also twofold degenerate and optically-forbidden due to its parity with respect to the inversion symmetry operation. Due to the lack of inversion symmetry in the AB stacking, the first peak in the corresponding spectrum embraces degenerate lowest-energy bright excitons. Also in AA arrangement, the first exciton is twofold degenerate optically allowed and gives rise to the intense excitonic peak dominating the absorption onset. While the intensities of the low-energy peak in the AA, AA', and AB stackings are similar, their energies differ due to the varying direct QP gap (see Table S2). In the A'B and

AB' stackings the spectrum is red-shifted compared to the other structures. Concomitantly, the lower symmetry of these two configurations and the reduced wavefunction overlap between the contributing QP states are responsible for the weaker peak intensities and for the larger number of allowed excitations. The corresponding solutions of the BSE (red bars in Fig. S3) are mainly dipole-active but have weak intensity, in contrast with the AA, AA', and AB stackings, where most excitations are either very intense or forbidden. The out-of plane component of the imaginary part of the macroscopic dielectric function is given by a dotted-dashed line (Fig. S3). While these spectra are rather featureless in the relevant energy-region for this study, in the AA' stacking a relatively intense peak appears around 6 eV. It corresponds to the non-degenerate charge-transfer exciton discussed in the main text.

In Fig. S5 we report the absorption spectra of the AA', AA and AB stackings together with the corresponding real- and **k**-space distribution of the main excitons. As discussed in main body of the article, most excitations are double-degenerate for symmetry reasons. As such, the correlated probability density associated to the electron, with the hole being fixed, is a linear combination of the single contributions of degenerate BSE solutions. With the excitonic spatial distribution given by the square modulus of the electron-hole wave-functions (see Eq. 6), here, we report the corresponding averaged densities, consistent with the results reported in Ref. [33]. The twofold degenerate 2D exciton that gives rise to the sharp peak in the AA' stacking, comes from transitions between the QP states along the K-H path in the BZ. In Fig. S5 we show the **k**-space distribution of this exciton along the M-K-H-L path. In addition to the K-H path, the most relevant contribution comes from the M-K path in the BZ, consistent with the results on h-BN monolayer published in Ref. [34]. The CT exciton in the AA' stacking is dipole-allowed only in the perpendicular polarization direction and does not exhibit any degeneracy. The corresponding in-layer distribution of this exciton differs from the one shown in the main text, which is twofold degenerate and referred to the AB stacking. In the AA arrangement, in addition to the 2D exciton that dominates the absorption onset, about $\sim$1 eV above the absorption onset we find a delocalized 2D exciton with trigonal symmetry as in monolayer h-BN [34]. The electronic distribution of the bands contributing to it (VB-1 and CB, around the H point) prevents the vertical extension of

this exciton, giving rise to its 2D delocalized character. In the AA' stacking it has instead 3D$-d$ distribution. At higher energy ($\sim$1.2 eV above the absorption onset), we find a very delocalized 3D exciton (see Fig. S5). It arises form mixed transitions between QP states outside the gap. Due to their resonant character, their distribution resembles delocalized Kohn-Sham states, which can appears in all stackings at higher energy range. As discussed above, in these stackings (AA' and AA), the 2D excitons that dominates the absorption onset, can appear uniformly in both h-BN layer in the unit cell since the electronic distribution of the contributing bands along the K-H path is spread over all layers (see Fig. S4). Differently, in AB arrangement, the excitons are localized on one specific layer in the unit cell according to the wave function distribution of the contributing bands along the K-H path (see Fig. S4). The 2D exciton that forms the sharp peak and the lowest-energy one are localized on different h-BN layers, as confirmed by the electronic wave-function distribution shown in Fig. S4. They come, respectively, form VB $\rightarrow$ CB+1 and VB-1 $\rightarrow$ CB transitions along the K-H path in the BZ. The CT exciton, characterized by a weak oscillator strength, stems from transitions between the VB and the CB, which are spread over N and B atoms, respectively, belonging to different layers in the unit cell (see Fig. S4). At higher energies, above 6 eV, a weakly delocalized e-h pair appears with 2D character. In contrast to the AA' stacking that exhibits inversion symmetry and where thus the 3D$-d$ is extended to the neighboring layers, here the in-plane nature of this exciton is determined by the electronic distribution of the bands contributing to it: They preserve the trigonal symmetry reported also in the monolayer [34]. At the higher energies ($\sim$1.2 eV above the absorption onset) excitons with very delocalized 3D distribution appear, resembling the delocalized Kohn-Sham states appearing in this stacking. They stem from mixed transitions between QP states outside the gap region.

In Fig. S6 the same analysis is presented for the A'B and AB' configurations. Since the electronic distribution of the QP states along the K-H path is spread over both staggered h-BN layers in the unit cell (the layers are linked by inversion symmetry) and due to the reduced wave-function overlap between the QP states, these stackings exhibit a large number of weak excitations, mostly characterized by a 3D-like distribution. In the spectra of these systems

the absorption onset is dominated by a 3D$-l$ exciton which exhibits an in-layer distribution analogous to the one of the 2D e-h pair in the AA' stacking. Above the sharp excitonic peak, a 3D$-d$ exciton appears. Its in-plane distribution preserves the trigonal symmetry, similar to higher-energy excitons in monolayer h-BN [34]. Furthermore, it extends uniformly and symmetrically over the nearest neighboring layers, as in AA' stacking. This exciton arises form transitions between the VB and the CB outside the K-H path in the BZ, where the bands are split and their corresponding wave-functions are spread over both h-BN layers in the unit cell.

Comparison with experiments

For a final assessment of the quality of our results we briefly discuss them in the context of the experimental literature. Most of the available measurements refer to the most stable AA' stacking configuration of h-BN, which we consider for this analysis. In Fig. S7 we plot our spectra in comparison with two experimental datasets obtained with different techniques and spanning different energy regions. The intensity of the first bright peak is aligned to match the measured values. In both cases our computed spectrum is in agreement with the measurements. All spectral features are accurately resolved, also the relative intensity of each maximum and minimum. In Fig. S7, right panel, the region around the first sharp peak and the subsequent hump is plotted. Experimental data from Ref. [36] are obtained with inelastic X-ray scattering at finite $\mathbf{q}$. The spectrum shown here is taken at $\mathbf{q}$=0.13 Å^{-1} but its similarity to the one at $\mathbf{q}$=0, discussed in the original reference [36] makes this comparison meaningful [37]. The experimental spectrum plotted in Fig. S7, left panel, is obtained by optical absorption measurements and covers a much widers energy range, including also the second pronounced maximum at about 15 eV [35]. All features are correctly resolved in our calculation, including the weak peak at about 12 eV. As a side remark, our spectra are blue-shifted by 0.4 – 0.5 eV to match the experimental onset of both datasets in Fig. S7. In addition to the uncertainty of $\pm$0.2 eV in the experimental spectrum from Ref. [36], we ascribe this difference to the intrinsic underestimation of the gap

given by the single-shot G_0W_0 method compared to a self-consistent treatment [37, 38]. The binding energy of the first bright exciton of about 0.75 eV (see Table S2) further contributes to shift the peak position to lower energy compared to experiment [37]. We rule out any artifact produced by the computational parameters adopted in the G_0W_0 calculations (see also Ref. [28]). On top of this, the nature of the band-gap in bulk h-BN is still under debate. Our G_0W_0 results for the AA' stacking indicate an indirect band gap of 5.83 eV between the VBM near the K point and the CBM at the M point and a direct QP gap of 6.33 eV in the vicinity of M. As mentioned above, this result is in the range of experimental measurements [30–32, 39, 40] and in agreement with a recent G_0W_0 study [27, 28].

[1] J. P. Perdew, K. Burke, and M. Ernzerhof, Phys. Rev. Lett. **77**, 3865 (1996).

[2] A. Tkatchenko and M. Scheffler, Phys. Rev. Lett. **102**, 073005 (2009).

[3] S. Grimme, J. Comput. Chem. **27**, 1787 (2006).

[4] L. Hedin, Phys. Rev. **139**, A796 (1965).

[5] M. S. Hybertsen and S. G. Louie, Phys. Rev. Lett. **55**, 1418 (1985).

[6] W. Hanke and L. J. Sham, Phys. Rev. B **21**, 4656 (1980).

[7] G. Strinati, Riv. Nuovo Cimento **11**, 1 (1988).

[8] A. Gulans, S. Kontur, C. Meisenbichler, D. Nabok, P. Pavone, S. Rigamonti, S. Sagmeister, U. Werner, and C. Draxl, J. Phys. Condens. Matter. **26**, 363202 (2014).

[9] D. Nabok, A. Gulans, and C. Draxl, Phys. Rev. B **94**, 035118 (2016).

[10] S. Sagmeister and C. Ambrosch-Draxl, Phys. Chem. Chem. Phys. **11**, 4451 (2009).

[11] K. Momma and F. Izumi, J. Appl. Cryst. **44**, 1272 (2011).

[12] V. Solozhenko, G. Will, and F. Elf, Solid State Commun. **96**, 1 (1995).

[13] N. Marom, J. Bernstein, J. Garel, A. Tkatchenko, E. Joselevich, L. Kronik, and O. Hod, Phys. Rev. Lett. **105**, 046801 (2010).

[14] O. Hod, J. Chem. Theory. Comput. **8**, 1360 (2012).

[15] G. Constantinescu, A. Kuc, and T. Heine, Phys. Rev. Lett. **111**, 036104 (2013).

[16] L. Liu, Y. Feng, and Z. Shen, Phys. Rev. B **68**, 104102 (2003).

[17] Pease R. S., Nature **165**, 722723 (1950).

[18] J. H. Warner, M. H. Rummeli, A. Bachmatiuk, and B. Buchner, ACS Nano **4**, 1299 (2010).

[19] C.-J. Kim, L. Brown, M. W. Graham, R. Hovden, R. W. Havener, P. L. McEuen, D. A. Muller, and J. Park, Nano Lett. **13**, 5660 (2013).

[20] A. Shmeliov, J. S. Kim, K. B. Borisenko, P. Wang, E. Okunishi, M. Shannon, A. I. Kirkland, P. D. Nellist, and V. Nicolosi, Nanoscale **5**, 2290 (2013).

[21] R. Bourrellier, M. Amato, L. H. Galvo Tizei, C. Giorgetti, A. Gloter, M. I. Heggie, K. March, O. Stphan, L. Reining, M. Kociak, et al., ACS Photon. **1**, 857 (2014).

[22] M. H. Khan, G. Casillas, D. R. G. Mitchell, H. K. Liu, L. Jiang, and Z. Huang, Nanoscale **8**, 15926 (2016).

[23] M. H. Khan, H. K. Liu, X. Sun, Y. Yamauchi, Y. Bando, D. Golberg, and Z. Huang, Materials Today **20**, 611 (2017).

[24] H. Henck, D. Pierucci, Z. Ben Aziza, M. G. Silly, B. Gil, F. Sirotti, G. Cassabois, and A. Ouerghi, Appl. Phys. Lett. **110**, 023101 (2017).

[25] X. Blase, A. Rubio, S. G. Louie, and M. L. Cohen, Phys. Rev. B **51**, 6868 (1995).

[26] B. Arnaud, S. Lebegue, P. Rabiller, and M. Alouani, Phys. Rev. Lett. **96**, 026402 (2006).

[27] S.-P. Gao, Solid State Commun. **152**, 1817 (2012).

[28] F. Paleari, T. Galvani, H. Amara, F. Ducastelle, A. Molina-Snchez, and L. Wirtz, arXiv preprint arXiv:1802.01856 (2018).

[29] V. Solozhenko, A. Lazarenko, J.-P. Petitet, and A. Kanaev, J. Phys. Chem. Sol. **62**, 1331 (2001).

[30] J. Edgar, T. Hoffman, B. Clubine, M. Currie, X. Du, J. Lin, and H. Jiang, J. Cryst. Growth **403**, 110 (2014).

[31] D. A. Evans, A. G. McGlynn, B. M. Towlson, M. Gunn, D. Jones, T. E. Jenkins, R. Winter, and N. R. J. Poolton, J. Phys. Condens. Matter. **20**, 075233 (2008).

[32] G. Cassabois, P. Valvin, and B. Gil, Nature Phys. **10**, 262 (2016).

[33] L. Wirtz, A. Marini, M. Grüning, C. Attaccalite, G. Kresse, and A. Rubio, Phys. Rev. Lett. **100**, 189701 (2008).

[34] T. Galvani, F. Paleari, H. P. C. Miranda, A. Molina-Sánchez, L. Wirtz, S. Latil, H. Amara, and F. m. c. Ducastelle, Phys. Rev. B **94**, 125303 (2016).

[35] R. Mamy, J. Thomas, G. Jezequel, and J. Lemonnier, J. Phys. Lett.-Paris **42**, 473 (1981).

[36] C. Tarrio and S. E. Schnatterly, Phys. Rev. B **40**, 7852 (1989).

[37] B. Cunningham, M. Grüning, P. Azarhoosh, D. Pashov, and M. van Schilfgaarde, Phys. Rev. Materials **2**, 034603 (2018).

[38] N. Berseneva, A. Gulans, A. V. Krasheninnikov, and R. M. Nieminen, Phys. Rev. B **87**, 035404 (2013).

[39] L. Museur, G. Brasse, A. Pierret, S. Maine, B. Attal-Tretout, F. Ducastelle, A. Loiseau, J. Barjon, K. Watanabe, T. Taniguchi, et al., Phys. Status Solidi RRL **5**, 214 (2011).

[40] K. Watanabe and T. Taniguchi, Phys. Rev. B **79**, 193104 (2009).

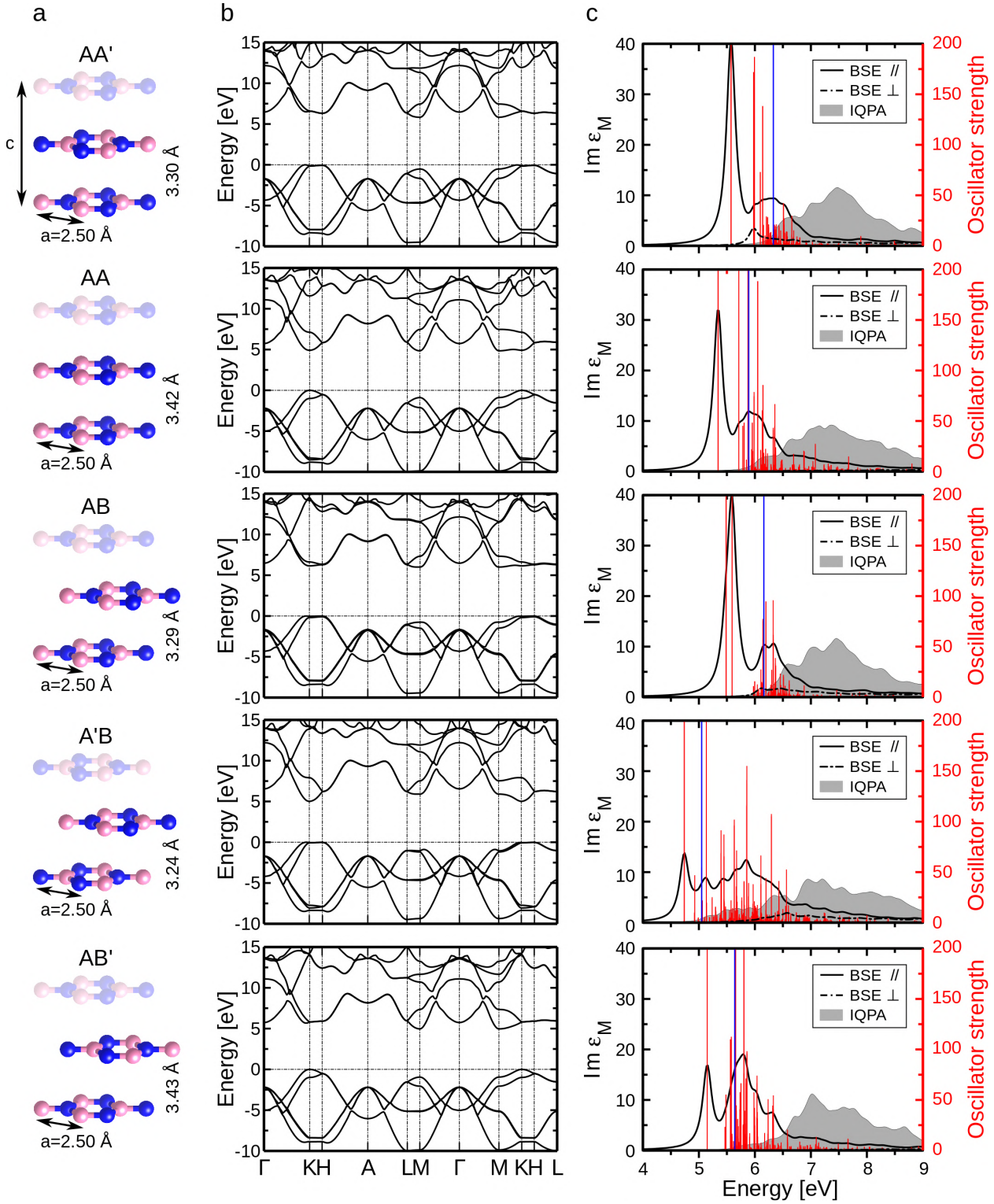

FIG. S3: **a**: Sketch of the unit cells of the five considered stacking arrangements of bulk h-BN. The two layers included in the unit cell are shown in the foreground, while periodic images are shaded. B atoms are pink, N are blue. **b**: Quasi-particle band structures with valence-band maximum set to zero. **c**: Optical spectra computed by including excitonic effects (BSE: solid line for the in-plane component and dotted-dashed line for the out-of-plane one) and neglecting them within the independent QP approximation (IQPA, shaded area). Red bars indicate the full oscillator strength of the BSE solutions (see Eq. 2) and the blue line the direct QP gap.

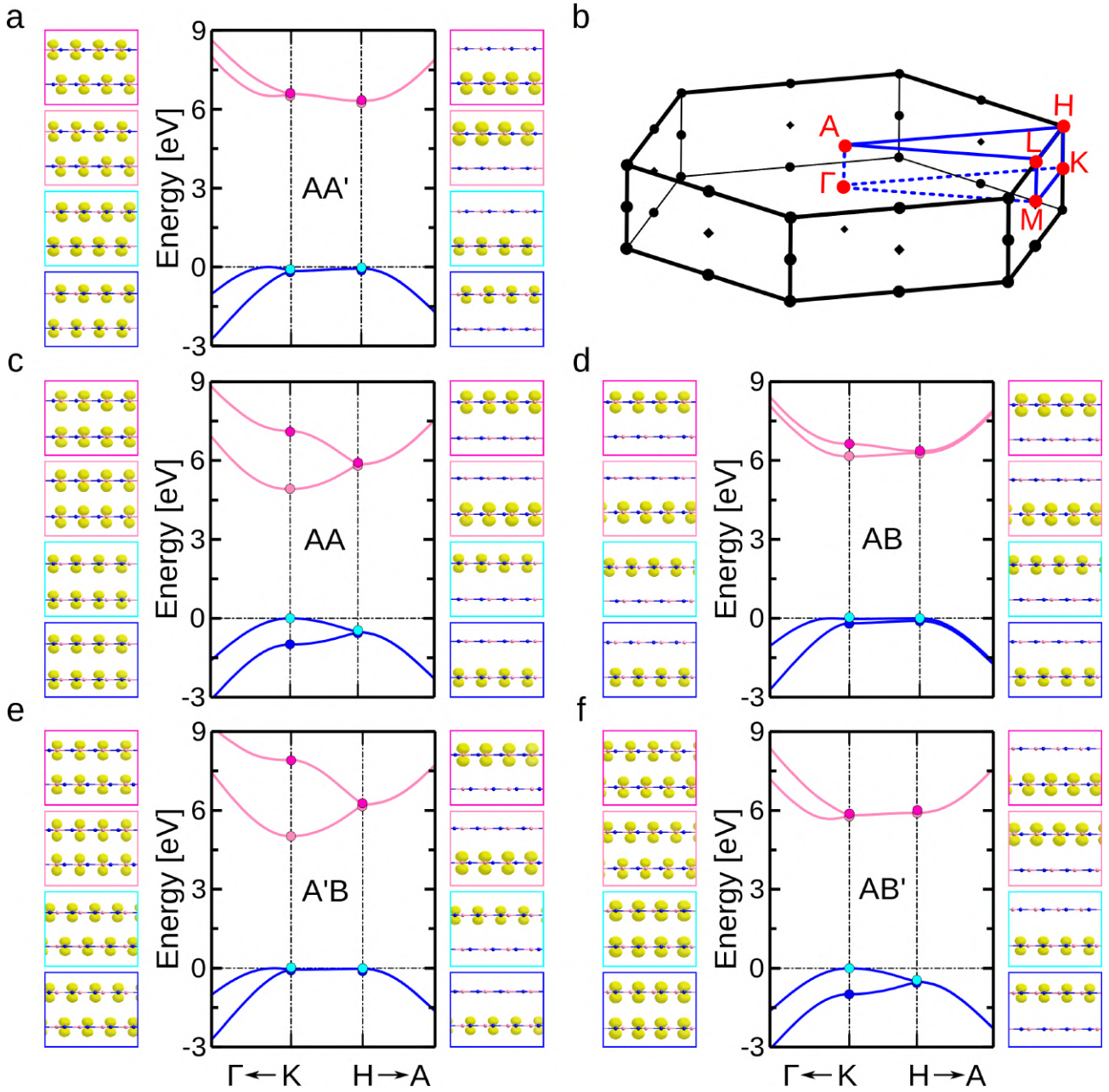

FIG. S4: (a,c,d,e,f) QP band structures in the vicinity of K-H path of the five considered stacking arrangements and real-space distribution of the two highest occupied and the two lowest unoccupied bands at the K (left) and at the H (right) point in the BZ. The band character is indicated by the color code of the corresponding atomic species (B: pink, N: blue), while the box frame points to the corresponding electronic states marked in the band structures. The valence-band maximum is set to zero. (b) Sketch of the Brillouin zone with the high-symmetry points highlighted.

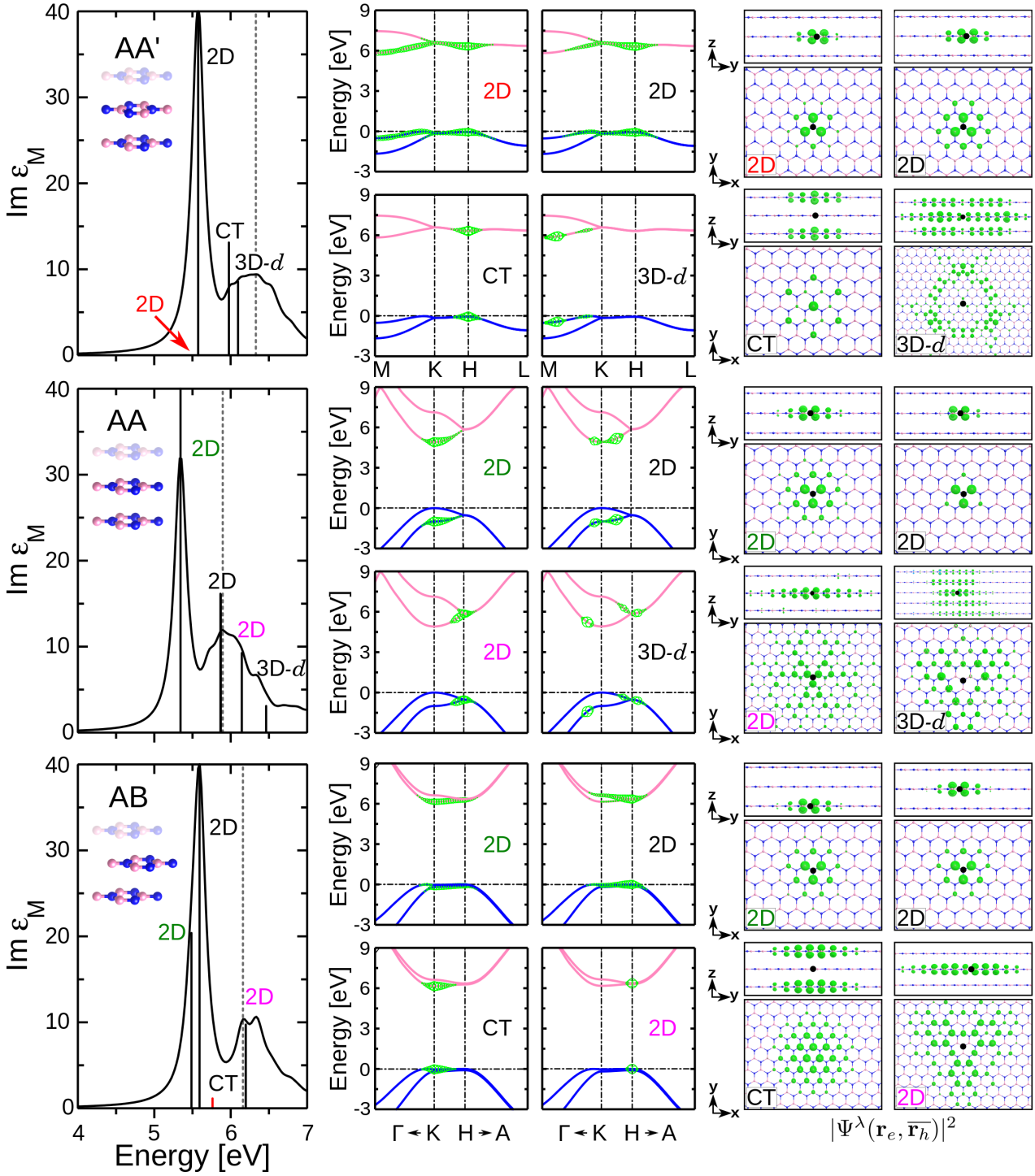

FIG. S5: (Left): Optical spectra of the AA', AA, and AB stacking of h-BN (structures in the inset), computed by including excitonic effects (BSE). A Lorentzian broadening of 100 meV is included. The dotted line indicates the direct QP gap and the intensity of the black bars indicate the relative oscillator strength given by $|t_\lambda|$ (see Eq. 2). (Center): Band contributions to the excitations marked in the spectra: The size of the green circles is representative of the weights (Eq. 5) of the involved QP states. The band character is indicated by the color code of the atomic species (B: pink, N: blue). The valence-band maximum is set to zero. (Right): Three-dimensional projections of the electron component of the e-h wave-functions highlighted in the spectrum, with the position of the fixed hole marked by the black dot.

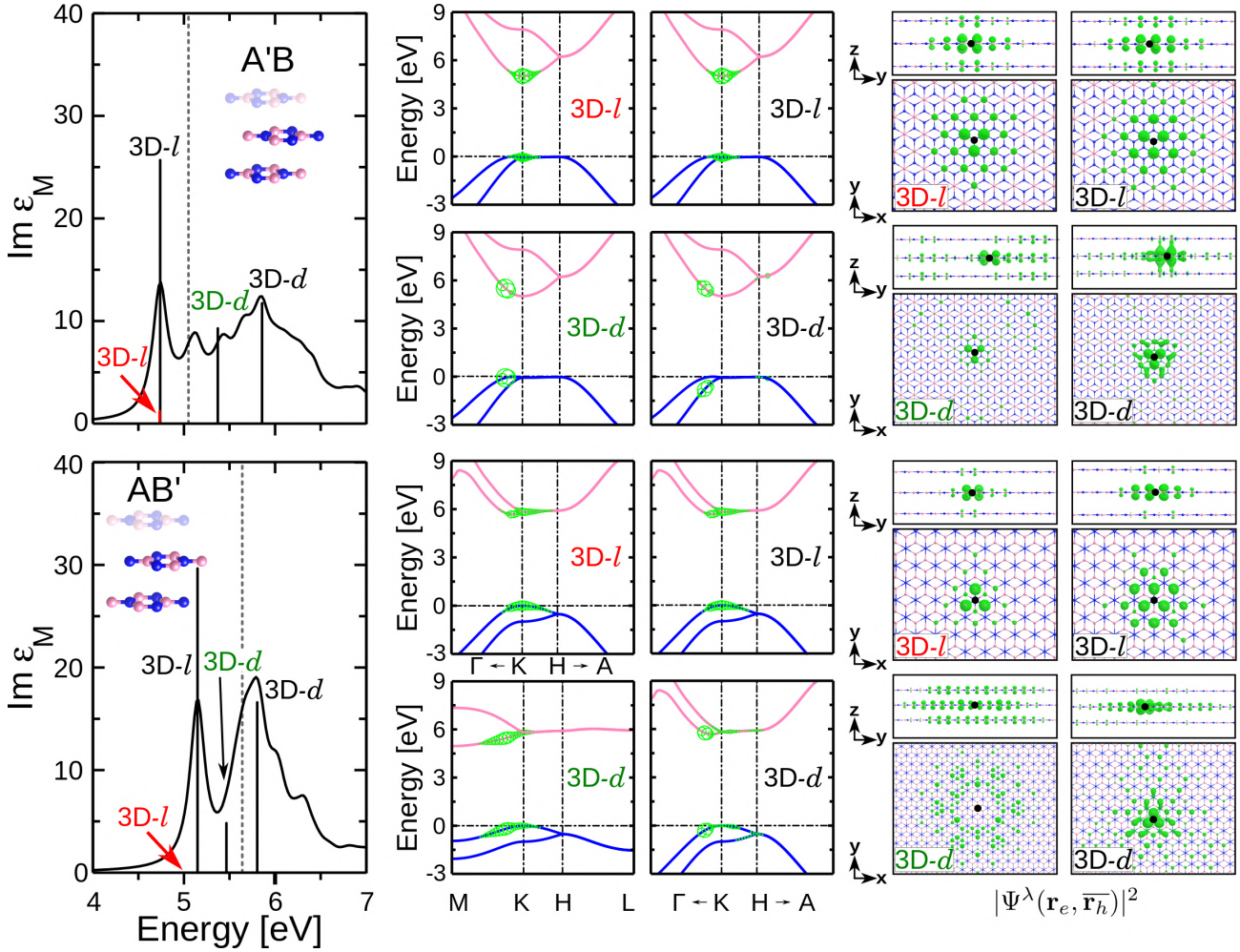

FIG. S6: (Left): Optical spectra of the A'B and AB' stackings of h-BN (structures shown in the inset), computed by including excitonic effects (BSE). A Lorentzian broadening of 100 meV is included. The dotted line indicates the direct QP gap and the intensity of the black bars indicate the relative oscillator strength given by $|t_\lambda|$ (see Eq. 2). (Center): Band contributions to the excitations marked in the spectra: The size of the green circles is representative of the weights (Eq. 5) of the involved QP states. The band character is indicated by the color code of the atomic species (B: pink, N: blue). The valence-band maximum is set to zero. (Right): Three-dimensional projections of the electron component of the e-h wave-functions highlighted in the spectrum, with the position of the fixed hole marked by the black dot.

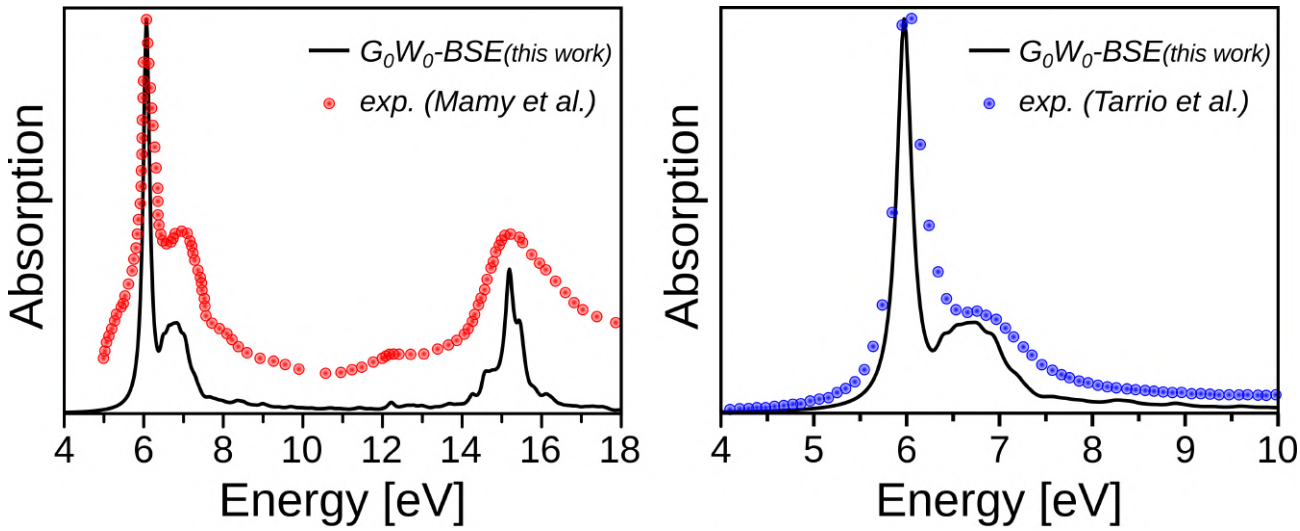

FIG. S7: Calculated optical spectrum of bulk h-BN in the AA' stacking compared with experimental data from (left) Mamy *et al.* [35] and (right) Tarrio and Schnatterly [36]. The computed spectrum is blue-shifted by 0.495 eV (left) and 0.4 eV (right) to align with the measured position of the first peak. The spectral intensity is aligned to the height of the first peak.

List of communications

- ***Electronic gap and optical spectrum of hydrofluorinated graphene : A many-body perturbation theory study***, W. Aggoune, K. Rezouali and M. A. Belkhir, **Meeting**: HoW exciting! Hands-on Workshop on Excitations in Solids, Humboldt Universität zu Berlin, July 31- August 8 (2014), Germany.
  Link: http://exciting-code.org/how-e xciting-2014-hands-on-workshop-berlin

- ***Electronic gap and optical spectrum of hydrofluorinated graphene : A many-body perturbation theory study***, W. Aggoune, K. Rezouali and M. A. Belkhir, **Meeting**: 11éme Congrès Nationale de la Physique et ses Application CNPA, 21-23 Décembre (2014), Blida, Algeria.
  Link: http://www.univ-blida.dz/fs-bulletin-spe-dec-2014Coprs1-min.pdf

- ***Tuning electronic and optical properties of graphene/h-BN heterostructures by layer patterning***, W. Aggoune, C. Cocchi, C. Draxl and M. A. Belkhir, **Meeting**: 13th ETSF Young Researchers' Meeting, 6-10 June (2016), London, United Kingdom.
  Link: https://yrm2016.github.io/

- ***Tunable excitons in graphene/h-BN van der Waals heterostructures*** , C. Cocchi, W. Aggoune, M. A. Belkhir, C. Draxl, **Conference**: Condensed Matter Division of the European Physical Society, 4th-9th September (2016), Groningen, the Netherlands.
  Link: http://www.eps.org/events/EventDetails.aspx?id=751067

- ***Tuning excitons by 3D stacking of hexagonal boron nitride layers***, W. Aggoune, C. Cocchi, D. Nabok, K. Rezouali, M. A. Belkhir and C. Draxl, **Meeting**: Deutsche Physikalische Gesellschaft e.V. (DPG), 19-24 March (2017), Dresden, Germany.
  Link: https://www.dpg-verhandlungen.de/year/2017/conference /dresden/part/ds/session/44/contribution/4

- ***Enhanced light-matter interaction in graphene/h-BN van der Waals heterostructures***, C. Cocchi, W. Aggoune, D. Nabok, K. Rezouali, M. A. Belkhir and C. Draxl,

Meeting: Deutsche Physikalische Gesellschaft e.V. (DPG), 19-24 March (2017), Dresden, Germany.
Link: https://www.dpg-verhandlungen.de/year/2017/conference/ dresden/part/ds/session/50/contribution/1

- ***Excitons in graphene/h-BN van der Waals heterostructures***, W. Aggoune, C. Cocchi, D. Nabok, K. Rezouali, M. A. Belkhir and C. Draxl, **Meeting**: 14th ETSF Young Researchers' Meeting, 5-9 June (2017), Tarragona, Spain.
  Link: https://yrm2017.github.io/

- ***Disclosing the nature of excitons in van der Waals materials: The role of layer stacking in hexagonal boron nitride*** , C. Cocchi, W. Aggoune, D. Nabok, K. Rezouali, M. A. Belkhir and C. Draxl, **Meeting**: Deutsche Physikalische Gesellschaft e.V. (DPG), 11-16 March (2018), Berlin, Germany.
  Link: https://www.dpg-verhandlungen.de/year/2018/conference/berlin/part/ds/session/37/contribution/6

Resumé

L'interaction rayonnement-matière dans les matériaux de van der Waals (vdW), formés par empilement vertical de feuillets bi-dimensionnels (2D), présentent des caractéristiques fascinantes, ce qui en fait des candidats idéaux pour la prochaine génération de dispositifs opto-électroniques. De nos jours, ces matériaux sont intensivement étudiés dans le but de comprendre les principaux paramètres pouvant influencer leurs propriétés et caractéristiques. Dans cette thèse, nous examinons la façon avec laquelle la combinaison de ce type de matériaux empilés verticalement peut donner lieu à des excitations optiques particulières qui ne sont pas présentes dans les constituants individuels. En se basant sur la relation structure-propriété, nous étudions l'impact de l'empilement des couches sur le caractère et la distribution des paires électron-trou (e-h). Avec l'exemple du nitrure de bore hexagonal en phase massive (h-BN), nous démontrons d'abord que les propriétés électroniques et optiques des multicouches de h-BN peuvent être ajustées à travers l'empilement des couches. En modifiant arrangement des couches, l'énergie, l'intensité et caractère des paires e-h peuvent être sélectivement modulées. En se concentrant sur la dimensionnalité des excitons, nous établissons les conditions nécessaire pour l'obtention des excitons avec une distribution purement 2D, transfert de charge ou bien à caractère tridimensionnel (3D). En second lieu, en combinant le graphène et h-BN pour former des hétérostructures vdW périodiques, nous constatons que l'écart de l'ouverture du gap dans le graphène est fortement liée à la structuration des couches. En se concentrant sur les configurations semi-conductrices, nous démontrons que de telles hétérostructures absorbent la lumière sur une large gamme de fréquences s'étalant du proche infrarouge (IR) à l'ultraviolet (UV). La plage de basse énergie du spectre est dominée par des paires e-h délocalisées dans la couche de graphène, tandis la gamme proche UV est dominée par des excitons fortement liés dans les couches h-BN. Outre ces caractéristiques intrinsèques des constituants, des excitations de transfert de charge apparaissent dans la région du visible. Notamment, la distribution spatiale des paires e-h peut être sélectivement syntonisée via une modulation contrôlée de d'empilement des constituants. Nos résultats, obtenus dans le cadre de la théorie fonctionnelle de densité de premier principe (DFT) et de la théorie des perturbations multi-corps (MBPT), ouvre une perspective fascinante via l'exploitation de la relation structure-propriété pour concevoir des matériaux de vdW avec des propriétés opto-électroniques sur mesure.

Abstract

Light-matter interaction in van der Waals (vdW) materials, formed by vertically stacked two-dimensional (2D) sheets, displays fascinating characteristics, making them ideal candidates for the next generation of opto-electronic devices. Nowadays, these materials are intensively investigated in order to understand the main parameters that can affect, tune and customize their resulting properties. In this thesis we address how the vdW combinations of these vertically stacked 2D materials can give rise to peculiar optical excitations that are not present in the individual constituents. Focusing on the structure-property relation, we investigate the impact of layer arrangement on the resulting character and distribution of the electron-hole (e-h) pairs. With the example of bulk hexagonal boron-nitride (h-BN), we first demonstrate that the electronic and optical properties of h-BN multilayers can be tuned through layer stacking. By modifying the layer arrangement, energy, intensity, and character of the e-h pairs can be selectively modulated. Focusing on the dimensionality of the excitons, we summarize the conditions that have to be fulfilled in order to obtain excitons with purely 2D distribution, charge-transfer, or three-dimensional character. Second, by combining graphene and h-BN to form periodic vdW heterostructures, we find that the gap opening in graphene is strongly related to the layer patterning. Focusing on the semiconducting configurations, we show that such heterostructures absorb light over a broad frequency range, from the near-infrared (IR) up to the ultraviolet (UV). The low-energy part of the spectrum is dominated by delocalized e-h pairs in the graphene layer, while strongly bound excitons in h-BN layers dominate the near-UV range. Besides these intrinsic features of the constituents, charge-transfer excitations appear across the visible region. Notably, the spatial distribution of e-h pairs can be selectively tuned through a controlled modulation of the stacking arrangement of the individual building blocks. Our results, obtained within a first-principles density functional theory (DFT) and many-body perturbation theory (MBPT), open a fascinating perspectives to benefit from the structure-property relationship for designing vdW materials and heterostructures with tailored opto-electronic properties.

الملخص

إن التفاعل بين الضوء والمادة في فاندر فالز المواد, المتشكل من التراص الأفقي للطبقات الثنائية الأبعاد التي تمتاز بسُمك ذري, يعرض خصائص مثالية, مما يجعلها واعدة للجيل القادم من الأجهزة الضوئية والإلكترونية. في الوقت الحاضر, يتم دراسة هذه المواد بشكل مكثف لغرض فهم الإعدادات التي يمكن ان تؤثر وتضبط خصائصها الناتجة. في هذه الرسالة, نتناول كيف يمكن أن يؤدي الجمع بين هذه المواد ثنائية الأبعاد لتهيُجات بصرية جديدة غير موجودة في المكونات الأصلية. بالتركيز على العلاقة بين البنية والخصائص الناتجة, نقوم بالتحري عن تأثير ترتيب الطبقات على هيئة و إنتشار الإلكترون المُتهَيج والثقب الناتج عنه (الإزدواج يسمى إكستون). بإختيار بور الآزوت السداسي الصلب (الكتلي) كنموذج مثالي, نثبت أولا أن الخصائص الإلكترونية والضوئية لهذه المادة المتعددة الطبقات يمكن ضبطها من خلال تغيير التراص الأفقي للطبقات. من خلال هذا التغيير, يمكن تعديل طاقة وشدة وإنتشار الإكسيتونات بشكل إنتقائي. بالتركيز على أبعاد إنتشارها في الفضاء أو المجال الحقيقي, نُلخص الشروط البنيوية التي يجب توفيرها من أجل الحصول على إكسيتونات ذات توزيع ثنائي الأبعاد في طبقة واحدة, أو إنتقال الشحنة ما بين طبقتين أو بطابع ثلاثي الأبعاد ليشمل عدد كبير من الطبقات. ثانيا من خلال الجمع بين الجرافين وطبقات بور الآزوت السداسية لتشكيل مواد غير متجانسة مترابطة بتجاذب/تنافر فاندر فالز, نجد أن ظهور الفجوة الإلكترونية في الجرافين مرتبطة ارتباطا قويا مع طريقة رص هذه الطبقات. بالتركيز على البنيات التي تتيح فتح الفجوة الإلكترونية لتشكيل أشباه النواقل, نُظهر أن هذه الهياكل اللامتجانسة تمتص الضوء على مدى واسع للترددات, إنطلاقا من الأشعة القريبة من تحت الحمراء الى غاية الأشعة فوق البنفسجية. يُهيمن على الجزء ذو الطاقة المنخفضة في الطيف, تهيُجات (إكسيتونات) الآتية من طبقة الجرافين, بينما تهيمن الإكسيتونات الشديدة الإرتباط, الآتية من طبقات بور الآزوت السداسية, على التهيُجات التي تصدر من المجال القريب من الأشعة فوق البنفسجية. إلى جانب هذه السمات الأصلية الصادرة من المكونين المختلفين, تظهر تهيُجات ذات طابع مشترك بينهما في المجال المرئي. بحيث أن الإلكترون المتهيج ينتشر في طبقة أحد المكونين والثقب الناتج عنه ينتشر على طبقة المكون الأخر. الجدير بالذكر ان التوزيع المكاني لهذه الإكسيتونات يمكن ضبطه بشكل إنتقائي من خلال تعديل مُنَظم لترتيب التراص لطبقات المكونين, مما يعطي وسيلة مثيرة لإستكشاف خصائص جديدة وتوسيع مجالات إستعمالها. هذه النتائج, والتي تم الحصول عليها إعتمادا على المحاكاة التي تتركز على النظرية الدالية للكثافة ونظرية الإضطراب متعددة الاجسام, تفتح آفاقا واعدة وذلك بإستغلال العلاقة بين البنية الهيكلية للطبقات والخصائص الناتجة لغرض تصميم مواد وهياكل غير متجانسة و بخصائص ضوئية وإلكترونية مثالية وعلى المقاس.